Theoretical and Experimental Investigations of the Friction Behavior of Automotive Shock Absorbers

Dissertation
zur Erlangung des akademischen Grades

Doktoringenieur
(Dr.-Ing.)

vorgelegt der
Fakultät für Maschinenbau der
Technischen Universität Ilmenau

von Herrn
M.Sc. Ludwig Herzog

1. Gutachter:	Prof. Dr.-Ing. Klaus Augsburg
2. Gutachter:	Prof. Dr.-Ing. Jochen Neher
3. Gutachter:	Dr.-Ing. Tomasz Łukasik

Tag der Einreichung:	04.02.2021
Tag der wissenschaftlichen Aussprache:	17.11.2021

DOI: 10.22032/dbt.50596
URN: urn:nbn:de:gbv:ilm1-2021000372

Abstract

Friction in automotive shock absorbers is composed of two friction types: The intended viscous fluid friction generates the speed-dependent counter force to damp the chassis vibrations, while the unwanted solid body friction is generated by the rubbing of the damper's seals and guides during stroking. The latter so-called static friction impairs ride comfort and (at high levels) driving safety. Lowering static friction is therefore a common target in the shock absorber design process. In this dissertation, a friction simulation method is introduced, which allows for the optimization of damper friction early in the design stage, aiming to significantly decrease time and cost for the setup and experimental analysis of real prototypes. To determine the parameters which have a relevant impact on the damper's friction behavior, this dissertation presents the design and setup of novel single friction point test rigs, since existing damper friction measurement setups do not sufficiently resemble the real operating conditions of a full damper. To prove the integrity of this experimental concept, it is validated against full damper friction measurements. The single friction point measurements are analyzed with regard to their friction behavior, on the base of which a friction modeling approach is developed. Since damper friction is highly dependent on geometry, and the variation of the shape of the damper parts is common in the design process, 3D structural FEM is used to determine the deformations of the damper parts resulting from mounting and varying operation conditions. In the respective contact zones, a dynamic friction model is applied to the FEM simulation and parameterized based on the single friction point measurements. Subsequent to the parameterization of the overall friction model with geometry data, operation conditions, material properties and friction model parameters, single friction point simulations are performed, analyzed and validated against both single friction point and full damper measurements. It is shown that the simulation method introduced within this work allows for friction prediction coincident with the above-mentioned requirements. Consequently, its application makes it possible to reliably investigate a wide range of parameters relevant to damper friction with significantly increased development efficiency.

Zusammenfassung

Reibung in Automobil-Schwingungsdämpfern setzt sich aus zwei Reibungstypen zusammen: Die beabsichtigte viskosen Flüssigkeitsreibung dämpft geschwindigkeitsabhängig die Fahrwerksschwingungen, während die ungewollte Festkörperreibung zwischen den aneinander reibenden Dichtungen und Führungen des Dämpfers entsteht. Die letztere, sogenannte statische Reibung beeinträchtigt den Fahrkomfort und (bei hohem Reibniveau) die Fahrsicherheit. Die Verminderung der statischen Reibung ist daher ein übliches Ziel in der Dämpferentwicklung. In dieser Dissertation wird eine Methode zur Reibungssimulation vorgestellt, welche die Optimierung der Dämpferreibung früh im Entwicklungsprozess ermöglicht, wodurch Zeit und Kosten für die Untersuchung realer Prototypen deutlich gesenkt werden können. Zur Ermittlung der Parameter, welche in relevanter Weise das Reibverhalten des Dämpfers mitbestimmen, werden neuartige Einzelreibstellenprüfstände entwickelt und aufgebaut, da bereits existierende Dämpferreibungsprüfstände die tatsächlichen Betriebsbedingungen im Gesamtdämpfer nur unzureichend wiedergeben. Die Integrität dieses Experimentalkonzeptes wird durch Reibmessungen am Gesamtdämpfer validiert. Die Einzelreibstellenmessungen werden ausgewertet, woraufhin ein Ansatz zur Reibmodellierung aufgrund des Reibverhaltens entwickelt wird. Da Dämpferreibung in hohem Maße geometrieabhängig und die Variation von Bauteilgeometrie ein üblicher Konstruktionsprozess ist, wird 3D-FEM-Struktursimulation verwendet, um die Verformung der Dämpferbauteile durch Montage und unter veränderlichen Betriebsbedingungen zu bestimmen. In den jeweiligen Kontaktzonen der FEM-Simulation wird ein dynamisches Reibmodell implementiert und mittels Einzelreibstellenmessungen parametriert. Im Anschluss an die Parametrierung des Gesamtreibmodells mit Geometriedaten, Betriebsbedingung, Materialdaten und Reibmodellparametern werden Einzelreibstellensimulationen durchgeführt, ausgewertet und gegen sowohl Einzelreibstellen- als auch Gesamtdämpfermessungen validiert. Es stellt sich heraus, dass die in dieser Arbeit vorgestellte Simulationsmethode die Vorhersage des Reibverhaltens übereinstimmend mit den anfangs aufgeführten Anforderungen erlaubt. Die Anwendung dieser Methode ermöglicht es somit, ein weites Feld von dämpferreibungsrelevanten Parametern mit signifikant erhöhter Entwicklungseffizienz zuverlässig zu untersuchen.

"Finite Element Analysis makes a good engineer great,

and a bad engineer dangerous."

Robert D. Cook

Professor for Mechanical Engineering

University of Wisconsin-Madison

Acknowledgments

The present dissertation was prepared during my activity as a research fellow in the Automotive Engineering Group at the Technical University Ilmenau. I would like to express my gratitude to all those who gave me the opportunity to complete this thesis.

The first one to be expressly thanked is obviously Prof. Dr.-Ing. Klaus Augsburg, head of the automotive engineering group. His advice on the academic and scientific work, but especially his commitment to a free, independent and productive working environment proved to be decisive for the successful completion of my dissertation. My sincere thanks go to him furthermore for his continued and unconditional support during convalescence after my motorcycle accident, and his great generosity in the process of my planning and enjoying parental leaves.

I am greatly indebted also to Glenn Vercalsteren from formerly Tenneco Inc., now Driv Inc. He was not only the person responsible for the PhD topic from the company side, but was also able to create enthusiasm for the topic of friction, helped to establish contact to internal and external specialists for certain questions, and always ensured good organization. Additionally, Glenn taught me important lessons about work organization and work-life-balance, and shared some (but not enough) great climbing sessions with me.

Particular thanks goes also to Henning Schwanbeck, responsible for the high performance computing in the compute center of the TU Ilmenau, for his infinite patience in listening to my wishes and reconciling them with the possibilities of the compute center and the requirements of the other users.

I am moreover very grateful to my colleagues, both from the research and the laboratory teams, especially Viktor Schreiber for his ongoing support and motivation towards friction simulation specific issues, Vincenzo Ricciardi for his Matlab help, and Sebastian Brettschneider, Achim Kuhne and Michael Posselt for realizing and improving the probe preparation and test rigs.

I also want to thank all students who worked under my supervision in student research projects and on their theses, and who contributed significantly to the overall research project through their dedicated work on their respective subtasks.

Special thanks goes to the CADFEM GmbH support team, where all my questions regarding structural FEM, contact mechanics and implementation of self-written code were always treated and answered efficiently. In particular I am grateful to Dr. Cord Steinbeck-Behrens, who always had an open ear for both specific and vague questions regarding FEM and its realization in Ansys Mechanical.

Technical support going beyond the common level was provided by the team of the tensile tester supplier, Schütz+Licht Prüftechnik GmbH. Their extraordinary help enabled me to implement various sensors to the tensile tester, which made measurement records very straightforward.

Last but not least I want to thank my dear sister Mechthild Roos and my good friend René Gassmöller for their critical review of my writings. Their different professional distance to the dissertation’s topic, their skills in academic writing, and their availability for endless more or less professional discussions proved to be crucial for the successful completion of this thesis.

Table of Contents

Abbreviations

APDL	Ansys Parametric Design Language
CAD	Computer Aided Design
CAE	Computer Aided Engineering
CFD	Computational Fluid Dynamics
CPU	Central Processing Unit
EHL	Elasto-Hydrodynamic Lubrication
EP	Elasto-Plastic friction model
FEM	Finite Element Method
FKM	Fluoroelastomer rubber
FSI	Fluid Structure Interaction
GMS	Generalized Maxwell Slip friction model
GUI	Graphical User Interface
LuGre	Lund Grenoble friction model
NBR	Nitrile Butadiene Rubber
NDA	Non-Disclosure Agreement
NVH	Noise and Vibration Harshness
OEM	Original Equipment Manufacturer
PTFE	Polytetrafluoroethylene
RAM	Random Access Memory
SFP	Single Friction Point
SFP1	Single Friction Point Test Rig (1) – Rod Guide Assembly / Rod and Piston / Tube
SFP2	Single Friction Point Test Rig (2) – Floating Piston / Tube

Symbols

Symbol	Unit	Designation
A	m^2	Area in Square Meters
$\hat{A}$	mm	Actuation Amplitude in Millimeters
$A_{ee}\,;A_{ue}$	μm	Elongation in Micrometers
amp	-	Amplification Factor (dimensionless)
b	N/m^2	Contact Cohesion in Newtons per Square Meter
$c,\ c_i$	N/m	(Element) Spring Stiffness in Newtons per Meter
d	m	Diameter in Meters
E	MPa	Young's Modulus in Megapascals
e	-	Euler's Number – $e \approx 2.71828$
F	N	Force in Newtons
G	GPa	Shear Modulus in Gigapascals
h	m	Lubrication Gap Height in Meters
k	-	Number of Elements or Terms (dimensionless)
n	-	Shaping Factor (dimensionless)
p	Pa	Pressure in Pascals
$p_{diff}\,;\Delta p$	Pa	Pressure Difference in Pascals
s	m	Contact Slip in Meters
$t\,;\Delta t$	s	Time; Time Step Size in Seconds
$v\,;\bar{v}$	m/s	(mean) Speed in Meters per Second
v_S	m/s	Stribeck Velocity in Meters per Second
x	m	Displacement in Meters
z	m	Average Bristle Deflection in Meters

z_{ba}	m	Average Break Away Bristle Deflection in Meters
z_{ss}	m	Average Bristle while Steady State Motion in Meters

α	-	Stribeck Coefficient (dimensionless)
α_i^G	-	Relative Modulus of a Prony Term (dimensionless)
ϵ	mm/mm	Strain in Millimeters per Millimeter
ζ_i	m	Element Displacement in Meters
η	$Pa \cdot s$	Dynamic Viscosity in Pascal Seconds
μ	-	Friction Coefficient (dimensionless)
ν	-	Poisson's Ratio (dimensionless)
π	-	Pi – $\pi \approx 3.14159$
ρ	kg/m^3	Density in Kilograms per cubic Meter
σ	N/mm^2	Stress in Newtons per Square Millimeter
σ_0	N/m	Average Bristle Stiffness in Newtons per Meter
σ_1	$N\,s/m$	Average Bristle Damping Coefficient in Newton Seconds per Meter
σ_2	$N\,s/m$	Viscosity Coefficient in Newton Seconds per Meter
σ_m	MPa	Ultimate Tensile Strength in Megapascals
σ_y	MPa	Yield Strength in Megapascals
τ	N/m^2	Stress in Newtons per Square Meter
τ_i^G	s	Relaxation Time of a Prony Term in Seconds
ϕ	m	Maximum Bristle Deflection in Meters
Ω	N	Inverse Normal Force Sensitivity in Newtons

1 Introduction

Driving a car is a highly sensual and emotional experience. While basic perception and control is recorded with audio-visual senses, accelerations and oscillations recorded by the vestibular system – the sense of balance – are particularly relevant for the general rating of vehicle dynamics and ride comfort. The component of the suspension system mainly responsible for ensuring appropriate ride comfort while simultaneously preserving optimal tire / road contact is the automotive shock absorber. Despite its name its main task is not absorbing shocks, but damping oscillations. The ability to dampen oscillations is illustrated in the force-speed curve in 1.1, which plots dampening force over the speed of oscillations. In order to optimally dampen oscillations the shock absorbers characteristic line should cross the point of origin of this graph, which means zero force at zero speed as depicted with the blue line in 1.1.

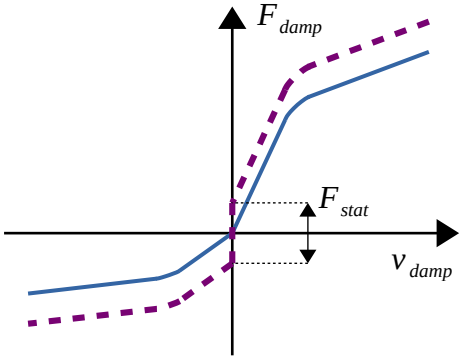

Illustration 1.1: Simplified typical damper curve without (blue line) and with (purple line) static friction

Viscous fluid friction creates exactly this behavior. Consequently today's automotive shock absorbers with only few exceptions are hydraulically damped. Special damper oils are used as working fluids. Consequently, reliably sealed damper designs are required to ensure tightness over a long usage time, which is often planned to be equal to the car's life span. This topic is situated in the wide field of seal design, which is always a compromise of tightness versus friction: The more the seal design process is focused on tightness, the larger is its tension and contacting surface, resulting in higher seal friction. Because this friction is only valid at near-zero speed and small displacements, it is called static friction F_{stat}, while the viscous fluid friction, becoming relevant at larger speeds and gross sliding, is called dynamic friction F_{dyn}. Because of the static friction comfort deteriorates as the smooth zero-crossing of the dynamic friction is overlaid by a more or less sharp step of the static friction as depicted by the purple line in 1.1. This means in reality, that for actuation forces that are smaller than half of F_{stat} the shock absorber acts as a non-deformable part. Since it is usually mounted in parallel to the suspension springs, it deactivates the whole suspension system, resulting in a direct transfer of each transient wheel displacement to the cabin and with that to the driver. This behavior is not

only disturbing the driver and the passengers. It is simultaneously increasing the transient wheel load changes, which deteriorates the tire / road contact, consequently lowers the longitudinal and lateral force transmission potential between tire and road, and therefore deteriorates driving safety in general. Additionally, since modern ride control systems have to consider the static friction within the shock absorber as a contribution to its overall damping behavior, this amount of static friction should be as low as possible, and at least known in its magnitude for optimal control purposes.

While ensuring sufficient tightness of seals is commonly achievable, friction is hard to estimate, especially early in the design stage where prototypes for measurements are not available. This can result in bad design decisions which are recognized only in later prototype or series tests, causing high redesign and delay costs. To alleviate these risks, the main objective of this dissertation can be formulated as follows: In order to improve and enhance the design process for automotive shock absorbers and to take static friction related part design earlier into account, it is necessary to understand friction based on the relevant friction-related parameters. This dissertation seeks to identify and quantify these parameters, and to set up simulations whose sub-models take these parameters into consideration in such a way that the future damper's friction behavior can be estimated even without the current amount of experiments. Additionally the setup and calculation time of these simulations has to be suitable for industrial use.

The documentation of this approach is structured as follows: Chapter 1 introduces the shock absorber with its characteristics and tasks in the car's suspension system and clarifies the general problem description of this work. Chapter 2 is concerned with the tribology background needed to discuss and interpret the results. It also provides an overview of the state of the art of friction simulations on lubricated rubber-metal contacts. Chapter 3 introduces the general research targets which can be derived from the problem description in connection with the state of the art. Chapter 4 documents the experiments developed and performed to characterize the damper's friction behavior and to validate subsequent simulations. The related measurement results are analyzed in Chapter 5, which also validates the chosen measurement approach. Chapter 6 describes the method to determine the seal's material behavior experimentally. Chapter 7 introduces the simulation setup and its parameterization. In Chapter 8 the simulation results are analyzed and the friction simulation model is validated. Chapter 9 sums up this dissertation and provides an outlook on future possibilities of applying and enhancing the created model.

1.1 Application of Automotive Shock Absorbers

To avoid or minimize vertical oscillations in automotive applications is both critical for safety, because of load variations at the tire road contact, as well as for comfort, because of the human body being disturbed by continuously fluctuating accelerations. However, oscillations appear permanently while traveling with a car, be it through longitudinal dynamics (acceleration, deceleration), lateral dynamics (cornering), three-dimensional oscillations (pitching, rolling) or direct excitation by road irregularities, tire non-uniformities or others. To reduce

these oscillations, some boundary conditions must be clarified: For safety and driving dynamics, all wheels of the vehicle have to be damped to minimize wheel load variations. For comfort reasons, mainly the vehicle's body and the driver's and passengers' seats have to be damped. While seat behavior is a topic not covered in this work, both wheel and vehicle body damping is achieved by the shock absorber through it's mounting between each wheel and the vehicle's body. Since the eigenfrequencies of vehicle body and wheel differ, and the human body's eigenfrequency range is just in between (see 1.2) not one specific, but a whole range of amplitudes and frequencies must be taken into account. Corresponding to that a large range of relative speeds is possible, which have to be identified by the suspension designer, who has to adjust the damping characteristics respectively. [1]

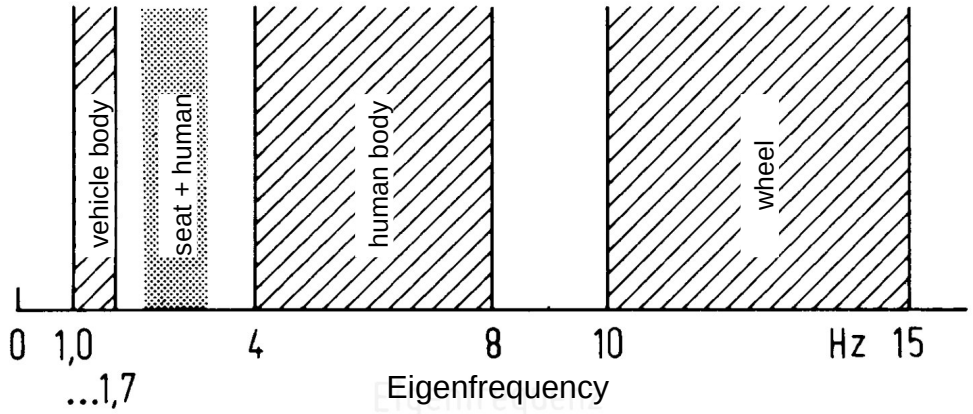

Illustration 1.2: Approximate range of relevant eigenfrequencies in vehicle dynamics; modified from [1]

Yet, there are many competing construction requirements and limitations to automotive shock absorbers. The wheel well is very restricted in terms of available space, some of which is occupied by the other suspension parts, wheel, tire, braking system and others. This leads to an often indirect or at least non-orthogonal damper mounting according to the line of action of the suspension deflection. The damper also performs additional tasks, e.g. as spring guide and spring plate, as wheel guide together with the control arms, as support of braking torques, as support of or to transfer steering torques, as anti-roll bar mount point, as fixation of sensor cables and/or brake hoses and so on. The result in modern cars is a multi-functional suspension component that is highly specialized to its application in a specific car model, both in its core task (damping oscillations adjusted to the car's specific eigenfrequencies) and in its side tasks as written above. [1] [2] [3]

1.1.1 Historical Outline

The history of automotive shock absorbers is directly linked to the history of the automobile itself. Since the suspension of horse-drawn carriages – even in premium models – was quite simple and usually set up by leaf springs, there was no need for a dedicated oscillation damper. The usually low travel speed due to bad road quality, the physical limitations of the

draft animals and the high friction caused by the rubbing of the leaf spring elements against each other during deflection sufficiently limited the sway of wheels and body of the carriage. The much higher power provided by internal combustion engines soon led to much higher drive speeds, and with that increased the need for appropriate damping for safety and comfort reasons. Up to the early 1920s various types of dry friction dampers dominated the market because of their simple, robust and cheap design. This kind of damper came with one inherent disadvantage: Dry friction is nearly independent of speed and because of that forms a sharp step at the zero-crossing of the force-speed-graph which causes a discontinuity of damper force at the return points of the suspension's deflection (see Chapter 2.1). This locks the whole suspension system at small actuation forces and leads to a poor ride on smooth surfaces. This disadvantage was sought to be overcome through several design approaches, e.g. by combinations of different rubbing materials, (adjustable) spring pretension of the rubbing package, or lubrication of the package with oil to lower low-speed friction. With still increasing top speed and comfort needs, from the mid 1920s on the dry friction shock absorbers were no longer able to fulfill the designers' and customers' requirements, and were gradually displaced by hydraulically damped shock absorbers. The design of hydraulic shock absorbers started with lever-actuated rotary dampers but shifted nearly completely to directly actuated telescopic dampers, which are still common today. The further development starting in the 1980s focused more and more on the ride control part: attempts were made to transfer more and more features of theoretical ideal active suspension to the damper. This led to the development of very fast auto-adjusting dampers, which are much cheaper in production and energy consumption than an actual active suspension, which event today represents no practicable solution yet due to high costs and power needs. [2]

1.1.2 Working Principles: Mono Tube / Double Tube Damper

As mentioned above, the main damper type used today is the hydraulically damped telescopic shock absorber. These can be categorized in two main types – the mono tube damper and the double tube damper – which will be introduced in this section. Since this work is not focused on the topic of viscous damping, these listings will be relatively short. For further information please refer to the relevant literature, e.g. [1] [2] [3] on which the following section is based.

The typical forms of hydraulically damped telescopic shock absorber are depicted in 1.3. Their basic function principle is identical: While stroking, i.e. while moving the rod (2) through the damper's upper mount point (1) relative to the pressure tube (4) with the damper's lower mount point (9), the working piston (6) mounted to the rod forces the oil inside the pressure tube to flow through its bores. These bores have a small diameter, which creates a large increase in fluid velocity, leading together with the zero-speed condition on the bore's wall and the oil's viscosity to viscous friction against this movement. Consequently, the kinetic energy from the relative movement of the wheel to the chassis is transformed to heat, thus damping the exciting forces. To adjust the shock absorber to its requirements (see Chapter 1.1), these bores carry more or less complex valving systems, which open or close at certain relative oil pressures, resulting in speed and with that in frequency-dependent damping.

The piston is sealed against the pressure tube with a piston band. To ensure that the oil stays inside and to guide the rod, the shock absorber's upper end is closed with a rod guide assembly (3), carrying both guide and seal elements, where the seal is usually divided into an oil seal and a dust lip (scraper). The guide is either simply a part of the oil seal's housing, or, if higher lateral forces occur in application or lower friction is needed, a dedicated additionally coated bushing (bearing). Depending on the amount of lateral force and tolerable friction, its properties (thickness, guide length, material, coating) are adjusted.

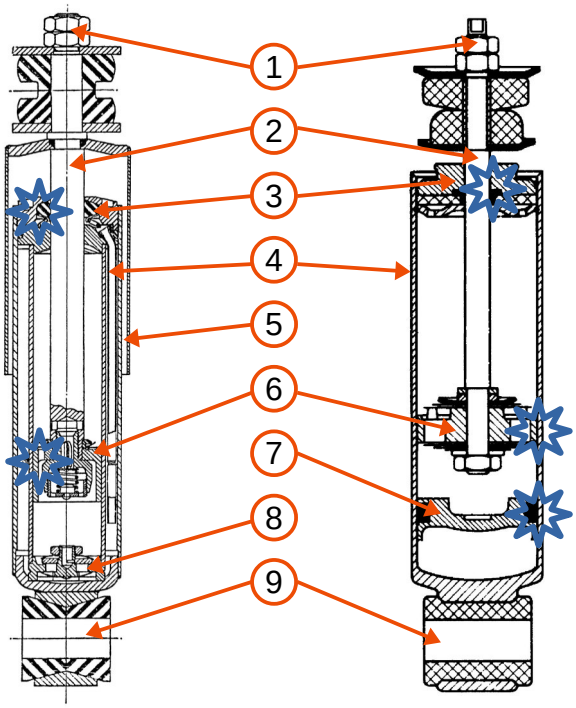

Illustration 1.3: Standard types of direct-acting double tube (left) and mono tube (right) automotive shock absorbers, solid body friction points are marked blue; modified from [2]

The difference between the two types of dampers comes from the different approaches to solve the problem that the rod's volume brought to the tube while stroking has to be compensated. At the double tube damper, this increasing volume while stroking pushes the oil through the base valve (8) into a second tube, the reserve tube (5), mounted around the pressure tube. The reserve tube is only partly (half to two thirds) filled with oil, the rest of its volume is filled with pressurized air at $p<8\,bar$. As additional oil is pushed into the reserve tube, the air is compressed and therefore compensates for the volume of the rod. The static air pressure is necessary to prevent the gas dissolved in the oil from changing back to the gas phase at high damper actuation speeds and with that high oil pressure differences. This would cause cavitation and frothing, resulting in a damping force drop to nearly zero if the gas would pass the piston or base valve. The base valve itself brings its own contribution to the overall damping. Using check valves it is commonly ensured that the double tube's base valve is mainly taking compression damping, while the working piston is taking the rebound part. The reasons are various and are outside the scope of this dissertation.

The mono tube damper compensates the rod's volume contribution in a different way. A floating piston (7), sealed with an O-ring against the tube, separates the pressure tube in an oil-filled upper part and a gas-filled lower part. While compression, the floating piston moves downward according to the volume displaced by the rod. Thus, the gas volume is compressed, leading to the volume compensation, but also to a spring-like push-out force. Because of the rod guide assembly's requirements and design, operating pressure is much higher at $p > 20\,bar$ than in the double tube damper, which increases the shock absorber's gas spring stiffness and must be taken into account by the suspension designer.

Since this dissertation deals with static friction in the automotive shock absorber, it focuses on the solid body friction points. These are the interacting surfaces of the rod with the parts of the rod guide assembly (3) (oil seal, scraper, bearing), of the piston band (6) with the pressure tube and – at the mono tube damper – the floating piston (7) and its O-ring with the pressure tube. This means, all basic friction points of the double tube damper occur in the mono tube damper as well. Thus, this work focuses first and foremost on the mono tube, since it's results are very well transferable to the double tube damper.

1.2 General Problem Description

Modern design cycles are more and more tightly timed, since there is an overall trend to push innovations and enhancements faster to the customer. This decreases the amount of time that is available for the typical design cycle, starting with theoretical design, continuing with prototypes and testing, considering the outcome again in the theoretical design and so on until a finished design is found that can be presented to the customer. That is why, with the help of constantly increasing computing power, these tasks are increasingly parallelized by setting up multiple simulations instead of real prototypes, thus saving time and financial resources. In the best-case scenario the simulation describes the real design sufficiently realistic to only build one final prototype for validation. Therefore, the crux of simulation in the design cycle can be described as follows: The simulation model has to be realistic, reliable and feasible enough to fulfill the designer's needs, but must be simple enough to be faster and easier to setup, and solvable with a smaller amount of computational cost and time than a respective prototype experiment would require.

As mentioned in the introduction, static friction can impair the overall function of hydraulic shock absorbers. As long as static friction is higher than the excitation force, the damper does not start to move, and therefore it deactivates the whole suspension on its specific wheel-body linking. Since this is a fundamental problem, static friction is nowadays usually low enough for this to be mainly a comfort problem. For a "good ride", it is nevertheless crucial, especially on the so called "boulevard drive", which means a comparatively slow ride on a smooth road [2]. Following the general trend to more and more low-noise and low-vibration cars – additionally, if not exclusively propelled by a quasi noise free electric motor – the noise and vibration (commonly summed up as noise and vibration harshness – NVH) generated and transferred by the suspension comes more and more to the foreground of noticeable disturbance for driver and passengers. This and a general expectation of a higher comfort level

leads to constantly increasing friction requirements of the OEMs to the shock absorber supplier.

The above-mentioned increasing friction requirements are obviously different for each OEM, and with that the respective friction definition is different. Equal for all OEM friction specifications is the measurement at very low speeds, since viscous fluid friction can be neglected there (see 1.1), and what is measured can be understood as static friction only. Therefore, the definition of “very low speed” is unique for each case, and the time dependent displacement is either constant or a harmonic oscillation. The typical speeds in the OEM friction specifications are in between $v = 0.4 ... 2.6\, mm/s$ with outliers to even lower (e.g. $v_{reduced} = 0.0083\, mm/s$) but also slightly higher speeds (e.g. $v_{max} = 6.3\, mm/s$), without claim of completeness. An agreed definition of what static friction in a shock absorber represents and determines is not given. [4]

Apart from that, there is a consensus about the critical points to improve – the friction points already marked in 1.3. Since these points are all seal contacts, it is well worth having a deeper look at the mechanisms taking place there. Seal friction is, as mentioned above, a topic of active research since it is relevant for all technical appliances dealing with hydraulics. Nevertheless, it is very complex, since it is dependent on a large amount of parameters and operation conditions as well as boundary conditions, e.g. on the solid body parts, geometry in general, size, shape of seals on macroscopic as well as on microscopic scale, operating speed, temperature and pressure, material properties, surface qualities and so on. Furthermore, seal contacts are more or less lubricated by the hydraulic fluid and / or an additional lubricant, which requires considering all of these properties and conditions for the hydraulic fluid as well as the lubricant(s), respectively. The constantly changing lubrication conditions in the contact zone make seal behavior analysis and prediction even more challenging.

To sum up, there are four core points according to the problem description:

1. Mainly for comfort reasons, static friction in automotive shock absorbers has to be reduced as far as possible, with seal tightness still ensured, according to constantly increasing OEM requirements.
2. Simulations can help to achieve that, but they have to proof that they are less expensive in setup and solution than an equivalent prototype experiment, while still being sufficiently realistic.
3. “Static friction” in automotive shock absorbers is not clearly defined and is treated rather inconsistently.
4. Seal friction is a very complex topic, mainly driven by its dependence on a large amount of solid body and lubricant parameters, additionally impaired by its constantly changing solid and fluid friction contributions.

2 State of the Art

The problem description introduced in Chapter 1.2 shows that multiple research areas are involved for the analysis of friction phenomena in general, and particularly for the appropriate description and simulation of friction behavior in automotive shock absorbers. This chapter introduces the necessary theoretical basics of these research fields. Tribology, the science and technology of interacting surfaces in relative motion, takes the most important and therefore first position in this chapter. To transfer the analyzed friction behavior to a simulation model, appropriate friction modeling is required, which is why the state of the art of friction modeling and friction simulation is presented as the second part of this chapter. Since the friction behavior of bodies rubbing against each other is also significantly influenced by their geometry and material properties, the fundamentals of 3D structural FEM are covered in the third part of this chapter.

2.1 Tribology Basics

2.1.1 Friction Behavior of Rubber / Metal Contacts

Tribology considers the scientific description of friction and wear, covering also lubrication and corresponding interfacial interactions both among solids, and between solids and fluids or gases. The basic tribology setup, a possibly lubricated solid body contact is depicted in 2.1. [5]

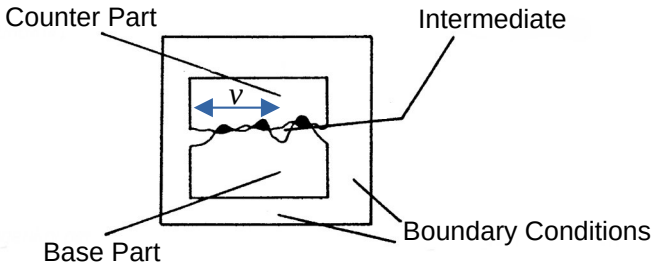

Illustration 2.1: Basic tribological system of two parts interacting along an interface; modified from [5]

As soon as the counter part starts to move relative to the base part, a friction force is generated in the contact zone acting opposed to the relative speed and dependent on the intermediate material and distribution. Tribological analysis of this system leads to the finding of mathematical and / or physical rules to describe the resulting behavior of the friction force. This creates the ability to transfer the gathered knowledge to a similar system, and to predict its (probably time-dependent) friction force behavior as a force response to a displacement excitation, or vice-versa, as a displacement response to a force excitation. Because of the huge variation of base part, counter part, intermediate as well as various boundary conditions, tribology is a

broad field including parts of mathematics, physics, material science and chemistry. For the friction points mentioned in this work (see 1.3) it is possible to narrow this field since they are all lubricated metal versus synthetic material contacts. That type of friction, often also called seal friction is what this section focuses on.

Good and quite comprehensive summaries of the basics of seal friction are provided for example by [6] and [7], on which this section is mainly based. Following the definition given there, all seals of the respective friction points in the automotive shock absorber are reciprocating dynamic seals, because their mating surfaces experience relative motion. All three subgroups mentioned in [6] – rod seals, piston seals and wipers – are represented in this research. The piston band stands out among the other two seals here in that it does not seal an oil filled volume against air and its seal material is PTFE, which is a plastomer contrary to the elastomers of the other seals. For these other seals it can be assumed that friction is lower at rebound stage than at compression stage, where rebound stage means that the rod moves from the oil side to the dry side of its seal. The rod surface is much better lubricated for this movement direction than for the opposite case, the compression stage. It should be noted that the seal's leakage is proportional to the oil film thickness left on the dry side at the rebound stage, thus there is the previously mentioned trade-off between seal tightness and lubrication, which basically means low friction [8].

Plastomers and elastomers, especially the types which are applied in automotive shock absorbers as seals, share some characteristic properties which are driven by the molecular makeup as more or less cross-linked polymers. Typical examples for these characteristic properties are time-dependent strain and non-linear elasticity, both are also excitation frequency and temperature dependent. Time-dependent strain is also called viscoelasticity and represents the reaction of both elastic and viscous stress to strain. While a perfectly elastic material reacts with a stress in phase to an excitation oscillation, a perfectly viscous material (similar to a fluid) strain lags stress by a $90\,°$ phase shift. Viscoelastic materials act somewhere in between, where these properties can be controlled by the main polymer backbone, fillers and additives. These properties also influence other tribology-related properties, e.g. oil retainability, resistance against wear or chemical reactions, fatigue aging and others. [6]

The main reasons for applying plastomers and especially elastomers as seals are consequences from the typical behavior of these materials. They show a low Young's Modulus, which is advantageous for seals because it allows high deformability without generating high contact pressures and easy mounting into housings or grooves. Their resilience enables them to follow irregularities and vibrations, and the high Poisson's ratio (close to $\nu = 0.5$, which means almost incompressible behavior) leads to a direct transfer of applied deformation to contact pressure. Last but not least, plastomers are reasonably inexpensive. The main disadvantages are hard-to-predict friction behavior, contributing directly to the main objective of this work, and their poor resistance to temperature changes and chemical reactions. This is why special caution should be taken to the counter part's material and oil choice as well as to a reasonable operation temperature range. [6]

2.1.2 Friction Mechanisms

Seal friction behavior results from several interfering friction mechanisms which are summarized in 2.2. The contact pressure distribution that determines friction is composed of static seal pretension through mounting defined deflection and seal stiffness, a hydrostatic pressure drop from high-pressure side to low-pressure side, and dynamic pressure build-up due to relative motion. This contact pressure distribution additionally influences the actual contact area of the seal and the counter part and leads to elastic as well as plastic seal deformation in the respective contacts. Counter-part deformation can usually be neglected due to the Young's modulus of the metal body, which is several magnitudes higher the seal's Young's modulus. Interface friction occurs in the actual contact areas, determined by the solid body material and surface quality, sticking lubricant and intermediate reaction layers (see 2.1). [7]

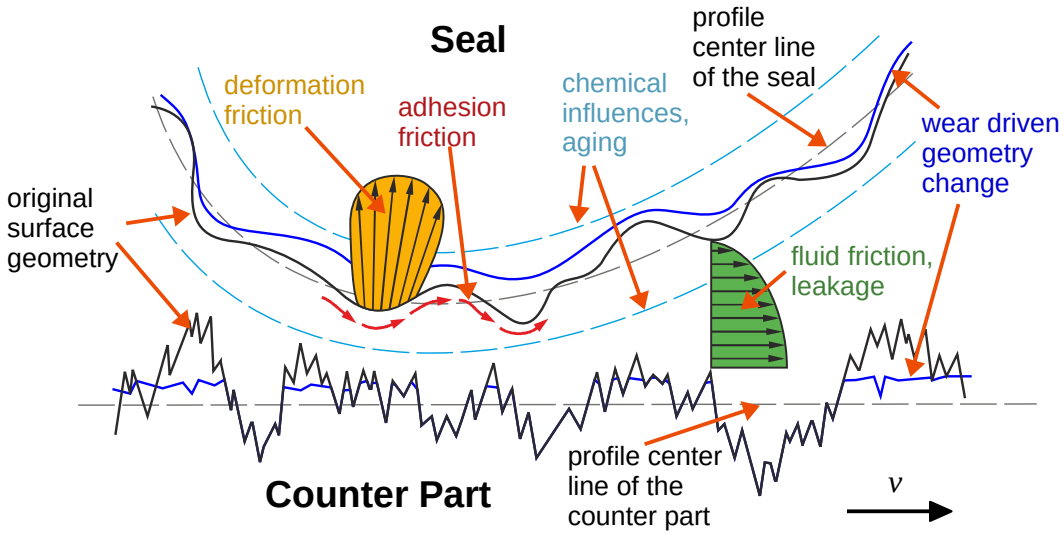

Illustration 2.2: Schematic depiction of the friction mechanisms in a dynamic seal contact; modified from [7]

Deformation Friction

If the comparatively soft seal body is supported by the asperities of the comparatively hard counter part and there is no relative motion, the integral of all superposed local contact pressure is symmetric and equals the overall contact pressing. The viscoelastic seal material creeps into the rough counter part's roughness profile. Thus the actual contact area increases with increasing zero-speed time. A starting relative motion leads to a contact pressure shift to an asymmetric state, and with that to shear stress formation due to the deformation of the seal's surface. Since this shear stress acts against the deformation direction, a force against the relative motion, called deformation friction, is generated. Because of the resulting force speed graph caused by its viscoelastic behavior, deformation friction is also often called hysteresis friction. The increase of overall contact pressure leads to a deeper penetration of the seal's

material into the counter part's roughness profile. Thus, with starting relative motion more material has to be deformed, so that the respective friction coefficient μ (see Chapter 2.2.1) increases slightly with overall contact pressure as depicted in 2.3 [9]. If relative motion speed increases, there is less time per incremental displacement for the viscoelastic back-forming of the seal's material. Back-forming is additionally hindered by the increasing stiffness of the viscoelastic material, since a higher relative speed acts like a higher excitation frequency, which increases stiffness. Those two reasons lead to a decreasing friction coefficient at increasing sliding speeds. [7]

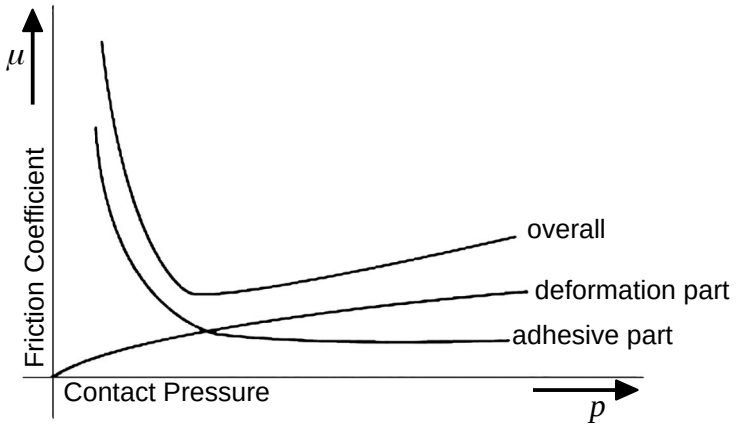

Illustration 2.3: Friction coefficient as a combination of deformation friction and adhesion friction, dependent on normal force for polar friction pairings; modified from [9]

Adhesion Friction

Adhesion friction is determined by formation and destruction of intermolecular bonds between both contacting bodies. These bonds build up at direct contact and get destroyed as soon as the relative displacement due to a relative speed is larger than their respective elongation limit. These bonds are premised on Van der Waals forces and are also linked to the viscoelastic behavior of the material. As the amount of bonds increase with the actual contact area, adhesion friction is more relevant on smooth than on rough surfaces, where large and sharp asperities cause few actual contact points and prevent the formation of interconnected contact areas. The adhesion friction's normal force alias contact pressure dependency is depicted in 2.3 and decreases significantly with increasing contact pressure until a quasi-static plateau is reached [9]. In well-lubricated contacts adhesion friction is usually negligible because of the surface-separating influence of the lubricant. For certain elastomer metal material pairings it is also possible that there is no adhesion force verifiable even at dry contacts [10]. [7]

Viscous Fluid Friction

If a contact is ideally lubricated, there is no direct contact between seal and counter part. The viscous lubricant is bound to the zero-speed conditions on the respective solid body surfaces, thus causing a Couette flow based on relative motion. If there is a static pressure difference between both sides of the seal, this drag flow is superposed by a Hagen Poiseuille flow. Both flow reasons establish the resulting lubricant film thickness and overall flow profile, thus determining the shear rate, resulting in shear stress in the fluid. This is leading to a force opposed to the relative motion direction, called viscous fluid friction [7]. The description of the fluid dynamics in the seal gap is possible with Reynolds-averaged Navier Stokes equations, e.g. developed for Elasto-Hydrodynamic Lubrication (EHL, see Chapter 2.2.3). The resulting film thickness additionally determines the amount of leakage permitted by the seal.

There are also additional long-term effects like wear through material loss in the surface, which causes material loss on the surface, or chemical reactions and cross-link decrease due to high temperatures [6]. All of these effects lead to macro-scale as well as micro-scale geometry and material property changes, directly influencing friction force behavior. Since this dissertation aims to represent and characterize the automotive shock absorber in a new state under the typical friction test conditions at ambient temperatures [4], wear and temperature dependent effects are not considered.

2.1.3 Friction States

The respective contribution of the above-mentioned friction mechanisms is highly dependent on relative speed especially of lubricated contacts. This behavior has first been observed and described by Richard Stribeck [11], who established the classification into the nowadays common five relative-speed-dependent friction states, which are introduced below and which are depicted in 2.4.

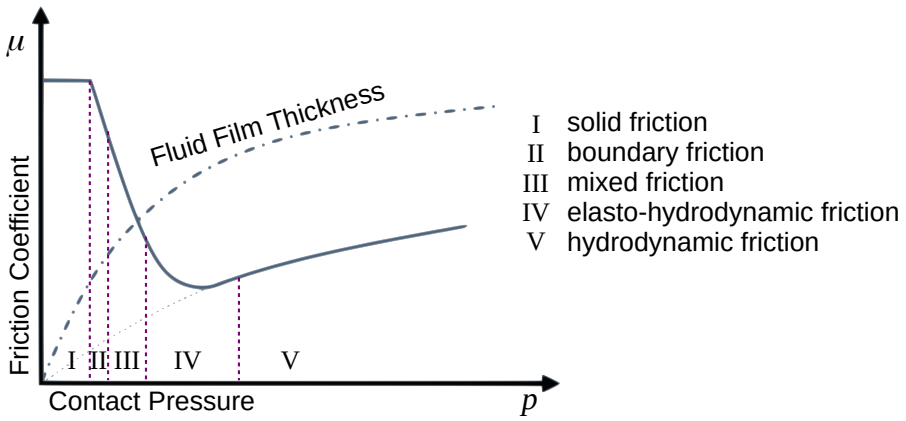

Illustration 2.4: Stribeck curve with associated friction states for lubricated contacts; modified from [12]

Solid Friction

The solid friction state, also called “dry friction” and depicted as friction state (I) in 2.4, is practically not relevant for real applications. It presumes a direct contact of both interacting bodies with no lubricant whatsoever. Since there is always some lubricant in reality – at least dirt, moisture or an intermediate material from chemical contact reactions (see 2.1) – this state is left latest when relative motion occurs. [5] [13]

Boundary Friction

Boundary friction is the typical starting friction state, where the solid bodies are in direct contact, but their non-touching surface parts are wetted with lubricant. As relative motion starts, this lubricant is transported into solid body contact, thus creating friction-lowering reaction layers, depicted as friction state (II) in 2.4. The friction force opposed to the relative motion comes mainly from shearing these reaction layers. Hence, a lower friction coefficient according to solid friction is achieved, but the contact normal force is still transferred only by the touching contact bodies. [5] [13]

Mixed Friction

As relative speed increases, the lubricant brought to the contact zone causes a lift-off of the contacting solid bodies and a fluid film appears. At mixed friction states, the fluid film thickness is still too small to fully separate both surfaces, so that direct contact of the bigger asperities is still happening, but friction decreases significantly, as friction state (III) shows in 2.4. The normal force is transferred both by the fluid film and the still touching asperities. [5] [13]

Elasto-Hydrodynamic Friction

If relative speed is sufficiently high, the fluid film thickness increases to a state greater than the biggest solid body asperities, causing a total lift-off of the two contacting bodies. This state is called elasto-hydrodynamic friction and represents an exceptional state, since the friction coefficient is the lowest achievable for this contact lubricant combination. Friction state (IV) in 2.4 shows this optimum point of non-touching asperities versus lowest possible shear stress in the viscous lubricant. [5] [13]

Hydrodynamic Friction

With further increasing relative speed, the total lift-off of the two contacting bodies is still preserved, but the viscous friction of the lubricant due to shearing inner fluid layers becomes dominant. The result is an almost linear increase of friction force with increasing speed, depicted as friction state (V) in 2.4. This friction state is called hydrodynamic friction or full viscous fluid friction. [5] [12] [13]

The above-described behavior seems to hold true for dry friction as well. The friction decrease with increasing speed (velocity weakening) and the following friction increase (velocity strengthening) are determined then by various process parameters, e.g. adhesion evolution, surface roughness and material parameters. [14]

2.1.4 Transient Friction Effects

Characterizing friction based on the Stribeck curve as depicted in 2.4 leaves out the time-dependent (transient) friction behavior, since the studies underlying the results in [11] have been all steady state investigations. However, friction in general shows highly time-dependent behavior. Furthermore, when studying friction in automotive shock absorbers it is especially important to consider transient friction behavior, since its main influence to the car's comfort behavior occurs in the shock absorber's return points of relative motion (see Chapter 1). Therefore, the appropriate description of transient friction behavior is crucial for the friction simulation to be developed within this work. Accordingly, typical transient friction effects are introduced here.

Pre-Sliding Displacement

As long as there is no relative motion between two contacting bodies, stiction occurs. As soon as a displacement is applied to one of the bodies, a friction force opposed to the displacement direction can be observed. The development of this force at very small displacements, in the so-called pre-sliding range, was investigated by P. R. Dahl in [15]. It showed that the force build-up is similar to the simplified stress strain curve in the elastic deformation range of a solid material, depicted in 2.5 up to the maximum elastic elongation A_{ee}. The main reasons for this behavior are the breaking of adhesive contacts and the force reaction to elastic deformations of the interlocking asperities in the contact zone [14]. The respective contribution is mainly material pairing dependent. As soon as maximum elastic elongation is reached, the pre-sliding range is left and gross sliding occurs.

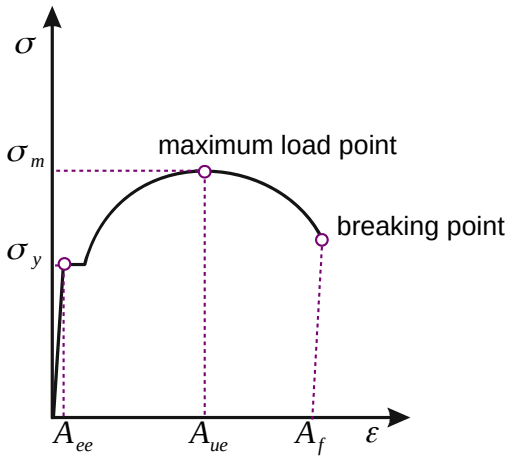

Illustration 2.5: Stress-strain curve of a ductile material with pronounced yield point; with A_{ee} - maximum elastic elongation, A_{ue} - uniform elongation; A_f - fracture; modified from [16]

The behavior in the pre-sliding range is – contrary to most facets of friction behavior – not speed-, but displacement-dependent and fully reversible. This means that if the starting displacement (or force) is released before the pre-sliding range is left, the displaced body returns

to its initial position relative to the contact body. In this state, the force reaction to the displacement points in the same direction as the back-forming displacement, so that the friction coefficient (see Chapter 2.2.1) turns negative. The force-speed graph represents this behavior as a narrow hysteresis around the zero relative velocity, as depicted in 2.6 (a) [17].

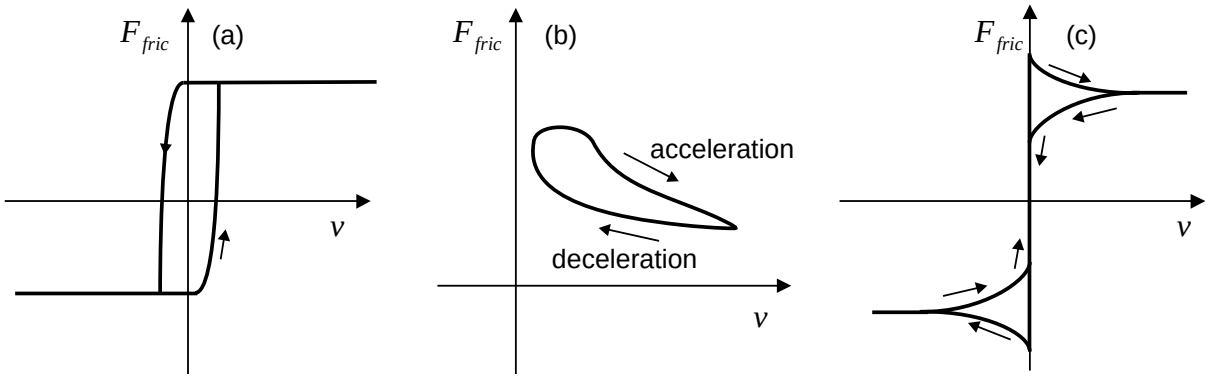

Illustration 2.6: Force-speed graphs of transient friction effects; (a) pre-sliding displacement; (b) frictional lag; (c) non-reversible friction characteristic; modified from [17]

Frictional Lag

As soon as gross sliding is achieved in a lubricated contact, friction decreases with increasing relative speed as depicted in 2.4 at (II) and (III). During transient speed changes in that range it has been observed, that acceleration leads to a higher friction force than deceleration as depicted in 2.6 (b). Similarly, it has been observed that the change of friction is lagging behind the change of speed, best visible in the change of acceleration to deceleration in the same 2.6 (b) [18]. Therefore, this behavior is called frictional lag or friction memory. The physical origin of frictional lag is the time required to modify the lubricant film thickness, which is known as the squeeze effect. In dry contacts it results mainly from the increase of adhesion during contact time [14].

Non-Reversible Friction Characteristic

While the above behavior has been investigated only at speeds which always point in the same direction, it is also observable during regressive (two-way) oscillations with macroscopic sliding. The effect on friction is the same, showing higher friction for acceleration than for deceleration, as depicted in 2.6 (c). It is called the non-reversibility of friction force. [17]

Rising Static Friction (Dwell Time)

The rising static friction effect describes the rise of static friction force with continuing standstill, usually called dwell time. There are several explanations for this behavior, namely, first the time dependency of adhesion, meaning the ongoing build-up of adhesive bonds between the two bodies. Second, it is assumed that the viscoelastic seal material creeps into the counter body’s roughness asperities, pushing out the lubricant, thus further increasing the actual solid

contact surface. This leads to both increased adhesion and deformation friction (see Chapter 2.1.2). [19]

2.2 Modeling Friction

Modeling friction is a common task in engineering with the purpose ranging from a qualitative overview to realistic transient behavior of a part interaction affected by friction. For a realistic model, all relevant friction characteristics from Chapter 2.1 have to be covered, which is possible either by trying to find a well matching mathematical formulation for the friction behavior (heuristic approach, "top-down approach", see Chapters 2.2.1 and 2.2.2), or by finding all relevant friction behavior describing physical parameters and modeling them directly (physical approach, "bottom-up approach", see Chapter 2.2.3) [20]. Since heuristic friction models are usually one-dimensional and mathematically rather simple, their solution process usually needs significantly less computational effort than physics-motivated friction models. Therefore, heuristic friction models are typically used in time- and cost-critical environments like real-time applications (e.g. motion control in general) or early design decisions (e.g. drive train power or frictional resistance estimation) [20] [21] [22] [23].

2.2.1 Static Friction Models

Although Leonardo da Vinci (1452-1519) already started investigating friction as a function of the normal force [24], today's simplest commonly used friction model was defined only in 1821 by Charles Augustin de Coulomb [25]:

$$F_C = sgn(v) \cdot \mu \cdot F_n \tag{1}$$

Where v is the relative speed between both interacting surfaces, μ is the friction coefficient and F_n the normal force acting equally over the contact zone. The spatial depiction is shown in the following 2.7:

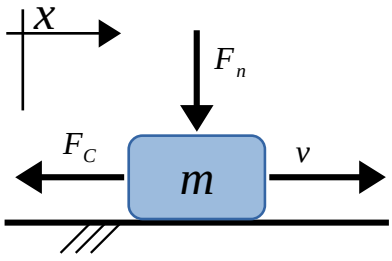

Illustration 2.7: Spatial depiction of relative speed, normal force and friction force used for the Coulomb model

Since this rule is only representative if a static friction state is held, this type of model is called "static friction model". Static in this condition implies no change in operating conditions, resulting in a friction coefficient μ that is constant and independent of speed, contact

time, material, wear, temperature and so on. This leads to a non-changing force-speed behavior without consideration of further friction effects like e.g. stick/slip behavior or pre-sliding displacement. This Coulomb friction behavior is depicted in 2.8 (a) (Level of Coulomb Friction), representing mainly dry static friction.

To represent more of the previously mentioned friction characteristics (see Chapter 2.1), the Coulomb model has been enhanced in various ways: As depicted in 2.8 (b), Morin [26] and Reynolds [27] integrated stick/slip-switching and a linear viscous term, which was later numerically implemented by Karnopp [28]. The Stribeck behavior [11] considering different lubrication states has also been taken into account (see 2.8 (c)) and is nowadays usually modeled by the following equation [19] [29] [30]:

$$F_{Stribeck} = F_C + (F_S - F_C)\, e^{-(v/v_S)^{\alpha}} \tag{2}$$

Where F_C is the Coulomb friction level, F_S is the level of the stiction force, and v_S (Stribeck velocity) and α (Stribeck coefficient) are form factors to describe the speed-dependent friction behavior.

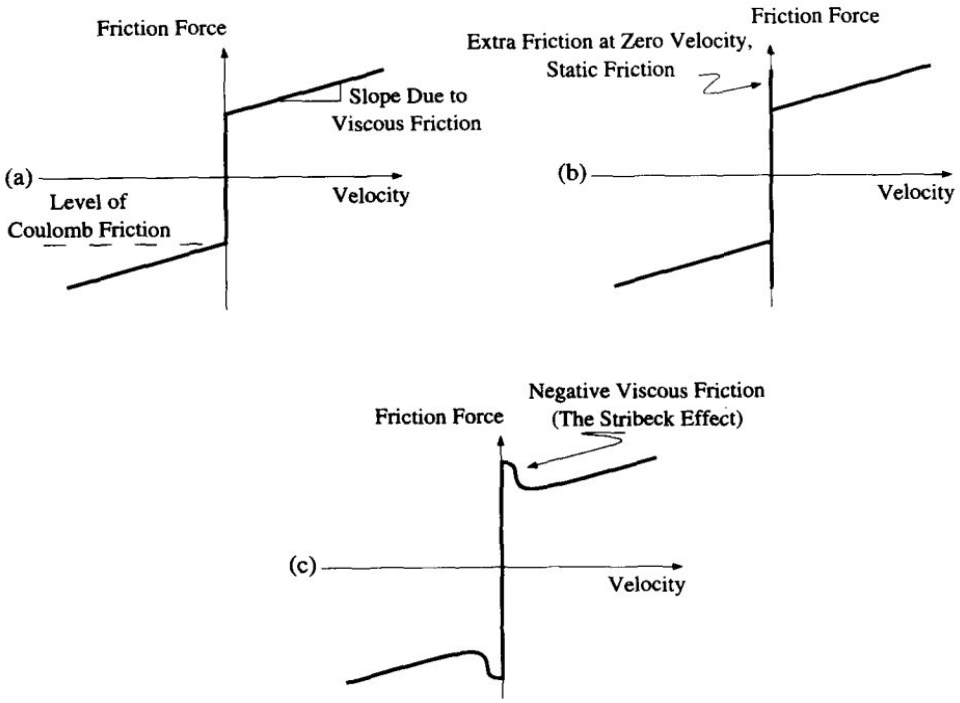

Illustration 2.8: Force-speed graphs of static friction models: (a) Coulomb friction + viscous term; (b) stiction + Coulomb friction + viscous term; (c) Stribeck friction; [19]

All these models share two basic weaknesses. The first is the overall neglection of dynamic (transient) effects (see Chapter 2.1.4), meaning that no significant change of speed in the contact zone is allowed. A consequence is a discontinuity at zero speed, which is not realistic and results in the second weakness, namely the need for model enhancements to overcome numer-

ical solution problems while investigating movement return points. The latter is easily solvable, e.g. by replacing the signum function in equation (1) with a high-slope hyperbolic tangent. To represent the above mentioned transient friction effects, the dynamic friction models were developed.

2.2.2 Dynamic Friction Models

As implied in Chapter 2.1.4, the lubricated frictional behavior can usually be separated in a pre-sliding regime, where the effects of pre-sliding displacement, frictional lag, non-reversible friction characteristic and rising static friction are dominant, and sliding regime, where hydrodynamic effects are dominant. Modeling of the pre-sliding regime and defining the connection to the sliding regime are the main characteristics of dynamic friction models, of which the most common ones are are introduced in this section.

Dahl Model

The first commonly used dynamic friction model was invented by Dahl [15] as a result of the observation of friction behavior of roller bearings at very small displacements. As a consequence of his observations he focused on the mathematical description of the pre-sliding hysteresis while characterizing the gross sliding regime as static speed-independent Coulomb friction. For this purpose, Dahl introduced the so-called bristle approach, which is still the base for some of the following models. This approach assumes that there is at least some lubricant separating the two contacting bodies. Thus, only partial or even no actual contact between the surface's asperities occurs as depicted in 2.9 (a). When relative motion occurs, some of the asperities interlock, causing first elastic deformation of the asperities, which represents pre-sliding behavior. As soon as the relative displacement of the contacting surfaces exceeds the maximum elastic asperity deformation, the asperity contacts break and gross sliding leads to a permanent displacement. The force generated at the maximum elastic deformation is the equivalent to the stiction force in static friction models, while the friction force at constant sliding represents the Coulomb friction force from the static friction models mentioned above.

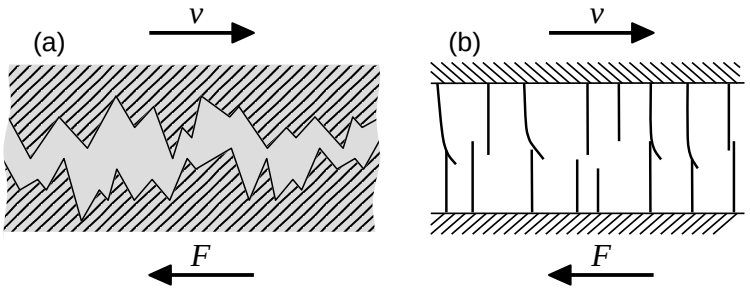

Illustration 2.9: Bristle approach: (a) asperities of the interacting bodies substituted to (b) deformable bristles on one and ideally stiff bristles on the counter surface; modified from [29]

The abstraction of the bristle approach is depicted in 2.9 (b). It simplifies the interaction of the asperities of both surfaces from 2.9 (a) to perfectly rigid bristles on one side (the lower side) of the contact and ideally elastic bristles with the resulting stiffness of both sides on the other side (the upper side) of the contact. By use of the parameters σ_0 (average bristle stiffness), F_C (gross sliding force, Coulomb friction) and F_S (force at maximum elastic bristle deformation, stiction force) the following differential equation (3) is formed to model the system's friction behavior:

$$\frac{dF_S}{dx} = \sigma_0 \left(1 - \frac{F_S}{F_C} \cdot sgn(v) \right) \tag{3}$$

Dahl's enhancements of this formula in his ongoing work (e.g. a material dependent shaping factor) can be reviewed in the respective literature, e.g. [15] [31] [32]. The Dahl model is therefore able to model the above mentioned pre-sliding displacement as depicted in 2.10, but no speed dependent phenomena like Stribeck behavior or frictional lag. Nevertheless it is the basis for many more advanced models.

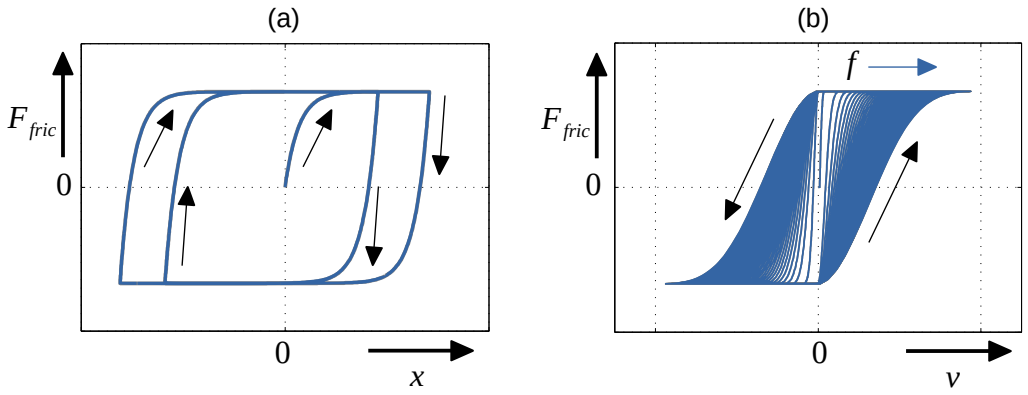

Illustration 2.10: Dynamic behavior of the Dahl model: (a) force displacement graph of the pre-sliding hysteresis; (b) force speed graph of the speed hysteresis with increasing frequency; modified from [29]

LuGre Model

The LuGre model is one of the enhancements of the Dahl model. In [30] Canudas de Wit et al. introduce the ability of the model to consider the deflection of the bristles from the Dahl model. The deflection of all respective bristles is subsequently averaged to one mean bristle deflection z, that is included in the model formulation as an internal state variable. The dynamic average bristle deflection is modeled in the LuGre model as follows:

$$\frac{dz}{dt} = \dot{z} = v - \sigma_0 \cdot \frac{|v|}{g(v)} \cdot z \tag{4}$$

where v is the relative velocity between the two surfaces, σ_0 is the average bristle stiffness from the Dahl model and $g(v)$ is a function to describe gross sliding behavior. The first term gives a deflection that is proportional to the integral of the relative velocity, the second term assumes that the average bristle deflection z approaches the value

$$z_{ss} = \frac{v \cdot g(v)}{|v| \cdot \sigma_0} = g(v) \cdot sgn(v) \cdot \sigma_0^{-1} \tag{5}$$

for steady state motion, i.e. when v is constant. [30] [33]

The function $g(v)$ is therefore responsible for the gross sliding friction behavior and its shape depends on the application. Quite common and exclusively used in this work is the modeling through the Stribeck formulation following equation (2) which leads together with the average bristle stiffness σ_0 from the Dahl model to the following parameterization:

$$g(v) = F_C + (F_S - F_C) e^{-(v/v_S)^{\alpha}} \tag{6}$$

The calculation of the overall friction force F_{fric} is finally modeled as a linear combination of the three friction force contributors elastic bristle deflection, bristle damping and fluid damping, represented in the following formula:

$$F_{fric} = \sigma_0 \cdot z + \sigma_1 \cdot \dot{z} + \sigma_2 \cdot v \tag{7}$$

with σ_1 as bristle damping coefficient and σ_2 as speed-dependency describing viscosity coefficient, where σ_0 and σ_1 can be graphically understood as depicted in 2.11 as a mass-less bristle with attached spring and damper.

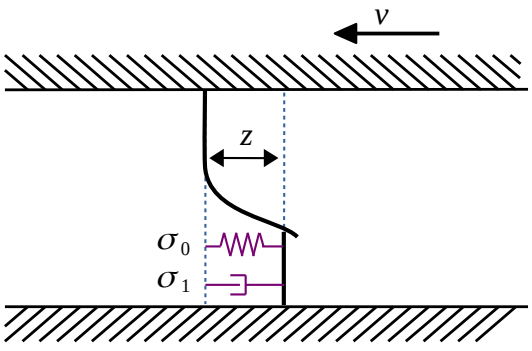

Illustration 2.11: Single bristle with attached spring with stiffness σ_0 and damper with damping coefficient σ_1 as described by the LuGre model

An illustrative parameter study as depicted in 2.12 shows the contribution of each parameter, respectively. The bristle stiffness σ_0 is responsible for width and slope of the pre-sliding hys-

teresis. The bristle damping coefficient σ_1 determines the overshoot peak short after passing the return point, but influences the width and slope of the hysteresis as much as σ_0 .

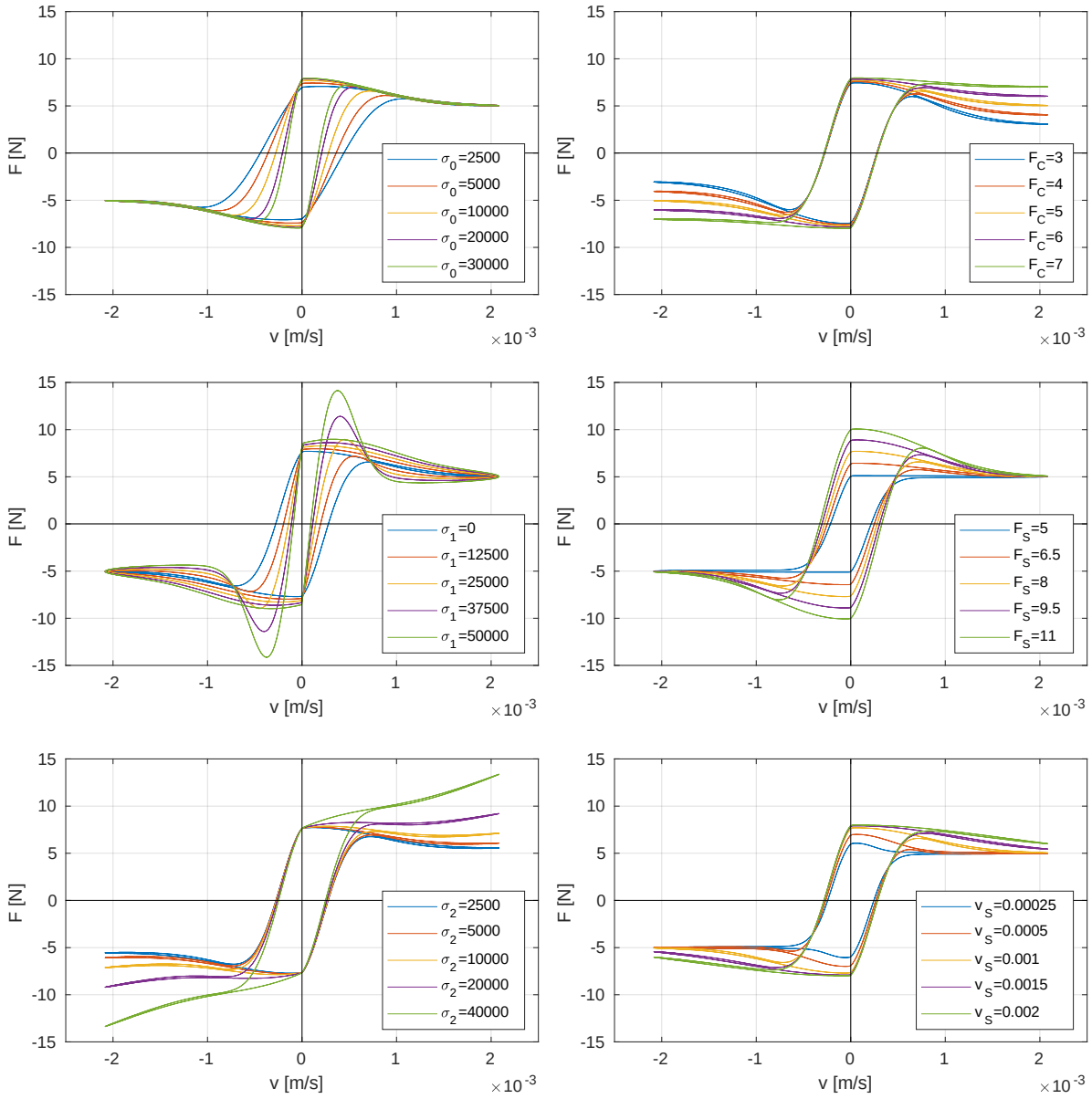

Illustration 2.12: LuGre model parameter study with sine-shaped displacement excitation. One parameter is varied, respectively, while the other parameters are at there default values: $\sigma_0 = 10000\,N/m;\ \sigma_1 = 5000\,Ns/m;\ \sigma_2 = 0.025\,Ns/m;\ F_C = 5\,N;\ F_S = 8\,N;\ v_S = 0.001\,m/s;$

The viscous damping coefficient σ_2 becomes increasingly significant at higher speeds and had to be chosen quite large in this parameter study to make the respective contribution visible. This results in line with its physical equivalent, the viscous damping of the lubricant at high speeds in the states IV and V on the Stribeck curve (see 2.4). The Coulomb friction force F_C determines the level of friction that is asymptotically reached at higher speeds while the

stiction force F_S represents the maximal achievable friction at zero speed. The Stribeck velocity v_S determines the amount of speed change that is necessary to shift from F_S to F_C . The Stribeck coefficient α is not varied here, because it is usually not necessary and commonly kept constant at $\alpha = 2$ to represent a Gaussian decay behavior [29].

The LuGre model enables a smooth transition between the pre-sliding and the gross sliding range, and Stribeck behavior for the high-speed range. Its behavior is frequency-dependent similar to real friction behavior, which is modeled by its speed dependent time constant. This results for example in a wider hysteresis for higher frequencies and constant displacement. Despite its much higher accuracy in comparison with the Dahl model, the LuGre model shows two weaknesses which are related to each other [29]. The first one is the lack of non-local memory modeling, the second is the model's drifting behavior.

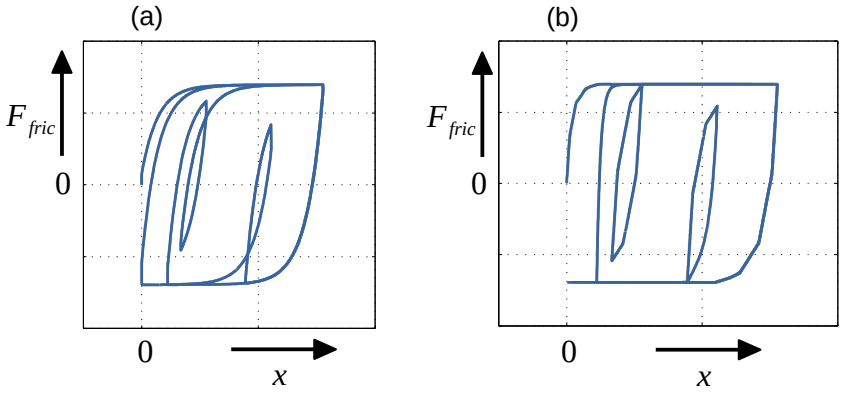

Illustration 2.13: Friction behavior after a displacement direction change inside the pre-sliding hysteresis modeled (a) by the LuGre model (without non-local memory) and (b) the GMS or Leuven model (with non-local memory); modified from [29]

Non-local memory modeling is necessary to appropriately describe the friction behavior occurring at a displacement direction change inside the pre-sliding hysteresis. The LuGre model reacts to such a displacement input with a force output as depicted in 2.13 (a) with non-closing loops and a non-realistic tracing of the outer pre-sliding curve. The Generalize Maxwell Slip (GMS) model (introduced below) in 2.13 (b) shows much more appropriate behavior with directly closing loops on the origin pre-sliding curve. The LuGre model should hence be used with caution if this kind of pre-sliding displacement excitation can appear as an input boundary condition. [29]

The LuGre model's drifting behavior means an ongoing position drift as a reaction to an oscillating force actuation that never exceeds the breakaway force, thus always staying in pre-sliding range. This topic is vividly discussed in various research (e.g. [14] [32] [33] [34] [35]) and resolved in the below-introduced Elasto-Plastic friction model. Because of ambiguous experimental results the real physical appearance of this drifting is so far not finally clarified. For the user it is ultimately mainly important to be cautious if this kind of force input can appear

as an input boundary condition to the model. Given this behavior, it is especially crucial to validate the model's friction behavior against appropriate experiments.

Elasto-Plastic Friction Model

Various enhancements have been developed to overcome the above-mentioned drifting behavior of the LuGre model. One prominent and widely used example is the Elasto-Plastic (EP) model, introduced in [36]. The linear combination of the respective friction contributions, namely bristle displacement-dependent elastic friction, bristle speed-dependent viscous friction and overall speed-dependent viscous friction is kept equal to equation (7) from the LuGre model. The dynamic bristle displacement modeling, however, is varied as follows:

$$\frac{dz}{dt} = \dot{z} = v \cdot \left(1 - \chi(z, v) \cdot \frac{z}{z_{ss}(v)} \right) \tag{8}$$

Equation (9) introduces the function $\chi(z, v)$ for which the authors of [36] suggest the formulation

$$\chi(z, v) = \begin{cases} \left.\begin{array}{cc} 0, & |z| \leq z_{ba} \\ \chi_m(z, z_{ba}, z_{ss}), & z_{ba} < |z| < z_{ss}(v) \\ 1, & |z| \geq z_{ss}(v) \end{array}\right\} & sgn\, v = sgn\, z \\ 0, & sgn\, v \neq sgn\, z \end{cases} \tag{9}$$

with

$$\chi_m(z, z_{ba}, z_{ss}) = \frac{1}{2} \cdot \sin\left(\pi \cdot \frac{z - \frac{z_{ss} + z_{ba}}{2}}{z_{ss} - z_{ba}} \right) + \frac{1}{2} \tag{10}$$

The function $\chi(z, v)$ acts as a switching function between the purely elastic pre-sliding range $(\chi(z, v)) = 0$ and the purely plastic gross sliding range $(\chi(z, v)) = 1$. This case differentiation motivates the name of the Elasto-Plastic model. A new parameter, the attraction factor z_{ba} is introduced, which determines the break-away deflection of the bristles, thus (according to equation (9) and (10)) leading to the beginning of gross sliding if exceeded. [36] [37]

Even if the EP model solves the drifting problem of the LuGre model, it lacks an appropriate description of non-local memory. Moreover, it is more complicated to implement and less stable in application tests for this research compared to the LuGre model, mainly because of the non-linearity of the switching function $\chi(z, v)$. Because of the general similarities of EP and LuGre models, no further analysis of the model behavior is considered necessary here.

Leuven Integrated Friction Model

The Leuven model [38] introduced at the same time as the EP model also enhances the LuGre model by removing drifting behavior, but additionally adds non-local memory to the pre-slid-

ing displacement, thus improving the accuracy of friction prediction at displacement direction changes (velocity reversals) inside the pre-sliding regime. This is achieved by adjusting the linear combination of the respective friction contributions as follows:

$$F_{fric} = F_h(z) \cdot z + \sigma_1 \cdot \dot{z} + \sigma_2 \cdot v \tag{11}$$

with

$$F_h(z) = F_b + F_d(z) \tag{12}$$

where $F_h(z)$ is the hysteresis friction force and F_b and $F_d(z)$ determine the hysteresis function, where F_b represents the beginning force of the hysteresis function and the function $F_d(z)$ represents the current transition curve. To model non-local memory with this hysteresis function, two memory stacks are required, one for the minima of $F_h(z)$, and one for its maxima. At a velocity reversal one value is added to both stacks, which is removed as soon as its corresponding internal hysteresis loop is closed (see 2.13). The stacks reset when the system changes from pre-sliding to sliding, while *z* resets to zero at each velocity direction change and is recalculated at the closing of the internal hysteresis loop. This implementation of non-local memory creates some difficulties and implementation issues. The hysteresis function and especially $F_d(z)$ must be modeled appropriately, resulting in additional parameters, which are often difficult to obtain from experimental parameterization measurements. Additionally, the memory stack size must be chosen sufficiently large to cover the maximum number of velocity reversals, since otherwise a stack overflow occurs. [32] [38]

After facing the above mentioned problems causing a discontinuity of the friction force, the original state equation from [38] was adjusted in [39] as follows:

$$\frac{dz}{dt} = \dot{z} = v \cdot \left(1 - sgn\left(\frac{F_h(z)}{S(v)} \right) \cdot \left| \frac{F_h(z)}{S(v)} \right|^n \right) \tag{13}$$

with

$$S(v) = sgn(v) \cdot \left(F_C + (F_S - F_C) e^{-(|v|/v_S)^\alpha} \right) \tag{14}$$

where $S(v)$ models the Stribeck behavior similar to equation (6), and n is a coefficient determining the transition curve shape. The same article [39] proposed to replace the hysteresis modeling equation (12) by a Maxwell-Slip approach to overcome the above mentioned stack size issues.

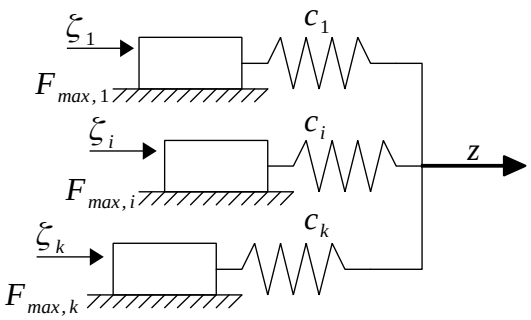

Illustration 2.14: Maxwell slip approach with k mass-less elements; modified from [32]

The Maxwell slip approach is represented by the superposition of *k* elastically sliding elements as depicted in 2.14 with c_i the respective linear spring stiffness, ζ_i the element position and $F_{max,i}$ the respective maximum break-away force. The finite amount of elements is directly related to a disadvantage of this approach that leads to a piece-wise approximation of the hysteresis function, resulting in a compromise of implementation effort versus accuracy. The hysteresis function following this approach is stated as follows:

$$F_h(c)=\sum_{i=1}^{k} F_i \quad \begin{cases} F_i = c_i \cdot (z-\zeta_i) \ , & |z-\zeta_i| < \dfrac{F_{max,i}}{c_i} \\ F_i = sgn(z-\zeta_i)\cdot F_{max,i} \ , & \text{else} \end{cases} \tag{15}$$

2.2.3 Physics Based Friction Models

While dynamic friction models as proposed in Chapter 2.2.2 are built via the analysis of the occurring friction mechanisms, states and transient effects (see Chapter 2.1) and subsequent mathematical emulation, their describing parameters have no physical relevance to real world parameters like roughness, hardness, Young's modulus, viscosity, surface tension, lubrication gap pressure, gap height, and so on. The parameter estimation is therefore a heuristic fitting process, which is why these models are also called heuristic models. Their advantages are mainly the small amount of parameters to determine and the small implementation and calculation effort. The lack of a physical foundation, however, leads to the need of parameterization measurements each time friction related physical parameters are changed. Seeking to overcome this problem, the development of physics based friction models is an important field of modern research. Here, the above mentioned real world parameters can be directly put into the model formulation, which makes these models much more flexible than the heuristic friction models from Chapter 2.2.2.The main downsides are the much higher amount of parameters to be gathered and the much higher computational effort. Because of these advantages, the development of a physics based friction model applicable to the problems described in Chapter 1.2 was the original aim of this dissertation. Extensive theoretical and experimental work has shown that the implementation, parameterization and calculation effort of such a model is not feasible considering the desired compromise of physical correctness and compu-

tational expense (see Chapter 7.1). Therefore, the following introduction to physics based friction models will be rather brief.

Generalized Maxwell Slip Model

The Generalized Maxwell Slip (GMS) model, introduced in [40], acts like a hybrid model that combines both physics based (in the pre-sliding regime) as well as heuristic model properties (in the gross sliding regime). The GMS model is based on the pure physics based model from [41], which has been found to be computationally too expensive for every-day use, since it needs at least 1000 equivalent asperities to be modeled to obtain smooth signals [40]. These asperities are Maxwell elements as depicted in 2.15 which can stick up to a maximum asperity deflection, then switch to pure sliding, but can also completely loose contact as soon as there is no touching counter asperity.

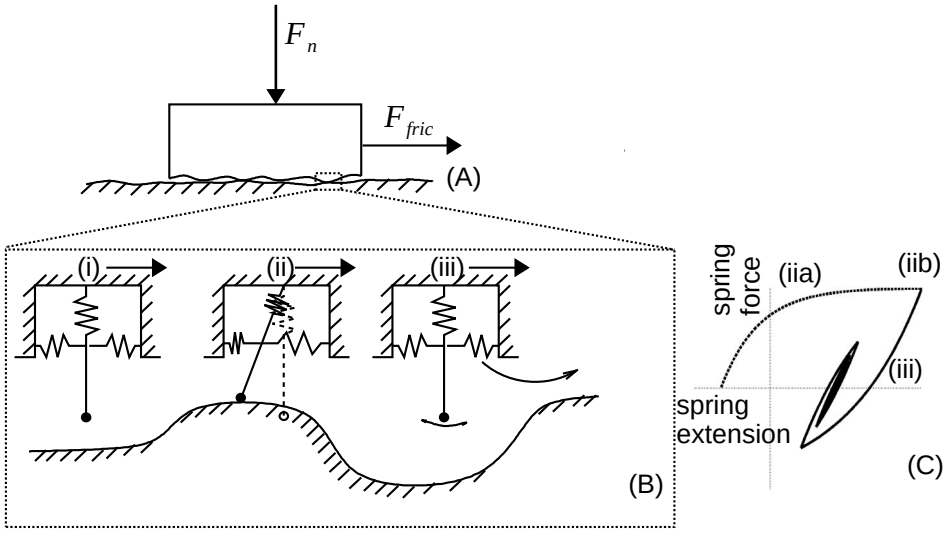

Illustration 2.15: Maxwell-Slip asperity modeling: (A) macroscopic body contact; (B) basic model scenario; (C) spring force behavior during a life cycle of an asperity contact: (iia) sticking, (iib) slipping, (iii) loosing contact; modified from [40]

The general model structure with one non-linear friction equation

$$F_{fric} = f(z, v, x) \tag{16}$$

and one non-linear state equation

$$\dot{z} = \frac{dz}{dt} = g(z, v, x) \tag{17}$$

remains similar to the dynamic friction models from Chapter 2.2.2, while the friction equation in the GMS model is reduced to k elemental state models and one linear viscous term:

$$F_{fric} = \sum_{i=1}^{k} z_i + \sigma_2 \cdot v \tag{18}$$

where the nonlinear dynamic state of each elemental model is stated as follows:

$$\begin{aligned} \frac{dz_i}{dt} &= c_i \cdot v \ , && \text{sticking while } z_i < \phi_i \cdot S(v) \\ \frac{dz_i}{dt} &= sgn(v) \cdot n \cdot \left(\phi_i - \frac{z_i}{S(v)} \right) , && \text{sliding until velocity reversal} \end{aligned} \tag{19}$$

Here, ϕ represents the maximum deflection of the respective elasto-plastic asperity, and n represents an attraction factor that determines the convergence of the friction force to the stationary Stribeck curve $S(v)$ (see 2.4). The GMS model is capable of describing both non-drifting behavior and pre-sliding hysteresis with non-local memory (see 2.13). The model also shows all friction effects mentioned in Chapter 2.1.4, while the modeling of the transition between pre-sliding and gross sliding is stated to be more realistic than with purely heuristic friction models. [29] [40]

Direct and Inverse Elasto-Hydrodynamic Lubrication

Another physical friction modeling approach is pursued in the elasto-hydrodynamic theory, which is usually found in literature under the name Elasto-Hydrodynamic Lubrication (EHL). It uses Reynolds equations to estimate fluid and contact pressure in the lubrication gap and, which are used to determine the lubrication gap height itself. Based on this gap height, fluid flow describing parameters like mass flow and shear stresses in the lubrication gap can be calculated, thus allowing for the estimation of friction and leakage. [7]

The Reynolds equations are special simplifications of the standard Navier Stokes equations, assuming Newtonian fluid behavior (shear stress linearly dependent on shear strain), a lubrication gap much smaller than the geometrical dimensions of the interacting bodies, and ideally laminar flow distribution. This assumes very low Reynolds numbers, which is valid here through equation (20) due to very low speeds (see Chapter 1.2) and a lubrication gap h that has just fractions of a millimeter. Here, $\bar{v}$ is the mean fluid velocity, h is the lubrication gap height, ρ is the fluid density and η is the fluid's dynamic viscosity. [42]

$$Re = \frac{\bar{v} \cdot h \cdot \rho}{\eta} < 1 \tag{20}$$

Additional assumptions simplify the Reynolds equations to their stationary one-dimensional form in equation (21). This form implies constant fluid density and constant dynamic viscosity, neglection of transient lubrication gap height changes and constraint of the flow direction only in the direction of the relative body motion, which neglects crossflows. [43] [44]

$$\frac{\partial}{\partial x}\left(\frac{h^3}{12\eta}\frac{\partial p}{\partial x}\right)=\frac{\partial}{\partial x}\left(\frac{h\cdot(v_a+v_b)}{2}\right)-v_a\frac{\partial h}{\partial x} \tag{21}$$

In equation (21), v_a and v_b represent the respective absolute speed of the contacting bodies in x-direction, h is the lubrication gap height, p the local fluid pressure and η the fluid's dynamic viscosity. Integrating with respect to x leads to

$$\frac{\partial p}{\partial x}=\frac{6\eta(v_a+v_b)}{h^3}(h-h_0) \tag{22}$$

where the integration constant h_0 represents the height of the lubrication gap at the point of maximum pressure. The determination of h_0 and the subsequent calculation of the lubrication gap height distribution are key steps in EHL investigations. [7] [43] [44]

There exist two general approaches to calculate the lubrication gap height distribution based on the simplified Reynolds equations, namely the Inverse Elasto-Hydrodynamic Lubrication (IHL) and the Direct Elasto-Hydrodynamic Lubrication (EHL). Both are based on a preliminary estimated contact pressure distribution over the contact length. This estimation is established either via a Hertzian pressure distribution or by FEM analysis (see Chapter 2.3). While the latter is nowadays used for all kinds of contacts, the former has certain advantages in setup and calculation effort, but lacks accuracy and is only valid for stiff contact pairings with contact partner materials which have similar Young's moduli. That is the case for example in roller bearings or tooth flank friction calculations in gear drives [13] [45]. As soon as one contact partner is comparatively soft – as is the case in the seal contacts considered in this dissertation – the pressure distribution over the contact length is highly material and body geometry dependent and the expected deformations are too large to be estimated accurately with only a Hertzian approach. To separate this large deformation estimation approach from the "classic" EHL for metal-metal contacts, it is often called soft Elasto-Hydrodynamic (sEHD). [7]

IHL, the first of the above mentioned general approaches, based on [46], calculates the gap height indirectly as a result of the hydraulic pressure. Since solid body contact is neglected and the whole seal deformation induced contact pressure is held by the fluid film, the FEM or Hertzian determined contact pressure equals the static hydraulic pressure. The calculation of the hydrodynamic pressure determined by the superposition of the static hydraulic pressure, a pressure flow due to the pressure difference between both sides of the seal, and a drag flow due to contact body motion, is determined by the above mentioned Reynolds equation. These Reynolds equations can be further simplified for rotational symmetric lubrication gaps as they often occur in hydraulic seals. The integration constant h_0 can be calculated analytically. The inverse lubrication gap calculation is widely used in research and engineering because of its simple implementation and numerical stability. Nevertheless it faces some disadvantages, e.g. constraints for the pressure distribution which are unavailable for several seal geometries, leading to an additional need for modifications and assumptions, documented e.g. in [46] and [47]. [7]

EHL, the second above mentioned general approach calculates the gap height directly as a result of the elastic deformations of the contact partners (usually the seal). While the IHL approach neglects the reaction of the fluid pressure to lubrication gap height changes, the EHL considers that influence to the gap height and pressure distribution. The common approach to setup direct EHL is the implementation of the hydrodynamic Reynolds equations to existing structural FEM solvers, extensively documented in [48]. Several other approaches containing e.g. yield matrices or analytical descriptions of the seal gap deformation are introduced in [7]. Direct EHL allows for a higher accuracy than IHL because of the above mentioned fluid pressure consideration, as well as the possibility to implement additional models to describe additional friction-related mechanisms, e.g. temperature effects, structural-viscous intermediates, cavitation or an overlaid solid friction model. The most significant disadvantage compared to IHL is the much higher computational effort that is required to solve the friction setup, mainly because of its numerically expensive coupling of gap height and fluid pressure. [7]

In general, the much higher computational effort of EHL and IHL compared to the dynamic friction models described in Chapter 2.2.2 leads to problems when simulating friction on unit level. In particular, the seal geometry still needs to be simplified to two-dimensional simulation setups, even with the general continuing increase of compute power [7]. Thus it is impossible to consider three-dimensional influences to the seal contacts like tangential seal tension, lateral forces or production-induced non-uniformities. Additionally, even though EHL is theoretically capable to model the reaction of the seal deformation due to fluid pressure distribution changes, this two-way coupling is so far not realized in actual applications because of dramatically increasing computing time. Another disadvantage of the Elasto-Hydrodynamic approach is the assumption of ideal fluid lubrication, thus assuming that the friction state is always elasto-hydrodynamic or purely hydrodynamic (see Chapter 2.1.3). Because of this assumption, appropriate modeling of the motion direction return points requires the implementation of a solid and/or mixed friction model. Possible friction models for this state are introduced in Chapter 2.2.2.

Fluid Structure Interaction

The mechanisms determining the resulting friction behavior in a lubricated solid body contact as depicted in 2.1 and 2.2 are obviously a result of interacting fluid and structural dynamics. Since both fluid dynamics and structural dynamics are considered in the above mentioned EHL and IHL approaches via structural FEM and fluid describing Reynolds equations, they are actually forming a fluid structure interaction analysis. Nevertheless, the common understanding of the term Fluid Structure Interaction (FSI) is an analysis of strongly coupled structural Finite Element Method (FEM) and Computational Fluid Dynamics (CFD), where CFD usually implies the solving of Reynolds Averaged Navier Stokes (RANS) equations with integrated heat and turbulence modeling. [49] [50]

The FSI numerical coupling approach can be categorized by the degree of physical coupling between the fluid and solid solution fields, as depicted in 2.16. Since the lubrication gap height and pressure distributions are strongly coupled and highly significant for the modeling

of friction behavior, at least 2-way implicit or iterative coupling is necessary. This modeling approach is available in several commercial simulation tools, e.g. ANSYS Workbench, DS Simulia or COMSOL Multiphysics. Its application for the desired friction simulation, together with an overlaid solid friction model, would allow to cover virtually all currently known friction-related topics such as roughness, fluid and solid surface energy effects, highly non-linear material stiffness, three-dimensional flows, turbulence, cavitation, material and flow regime changes due to variations of pressure, temperature, shear rate and so on. On the other hand, this FSI approach is numerically extremely expensive, since the already computationally very elaborate structural and fluid simulations now need additional coupling iterations to converge, multiplying the amount of respective inner convergence iterations of both the FEM and the CFD solvers. [51]

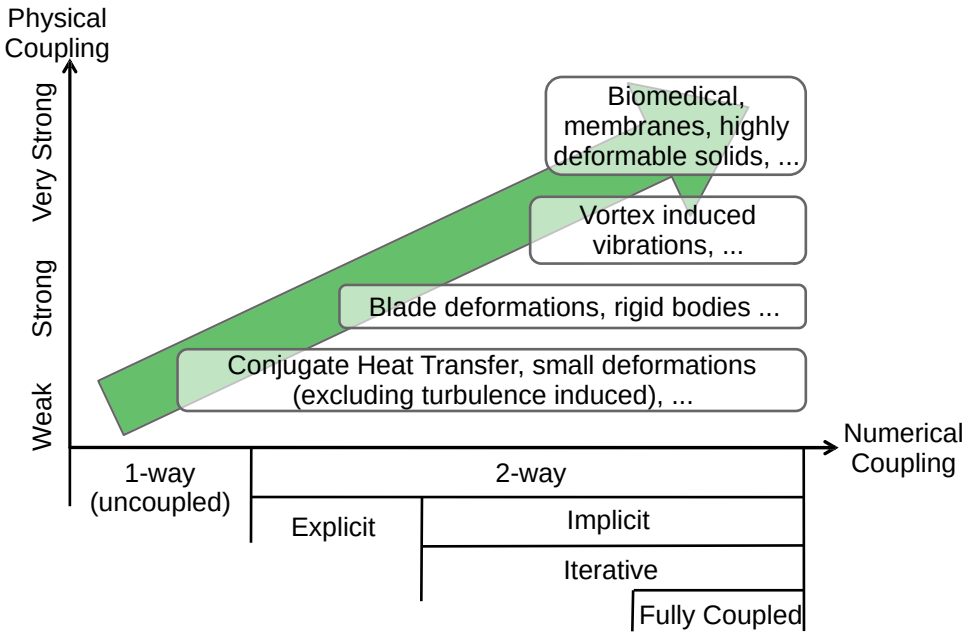

Illustration 2.16: Fluid Structure Interaction Coupling Depth; modified from [51]

As a result, the use of FSI is several orders of magnitude more expensive in setup and simulation time even compared to the already expensive EHL with coupling of gap height and fluid pressure, which is still not in practical use. Thus, its introduction here is only of general and so far rather theoretical interest, and an application is far away from every-day engineering.

2.3 Finite Element Method

2.3.1 Basic Approach

Describing physical situations with mathematical models often leads to multidimensional boundary and initial value problems which are described by systems of differential or integral equations. Most of these problems are proven to be analytically unsolvable, thus, the equations have to be solved numerically in order to predict physical behavior. The most commonly

used modern calculation method for structural mechanics is the Finite Element Method FEM. Since this thesis is particularly concerned with structural mechanics, the FEM will therefore be explained at the example of the elastic deformation of solid bodies. It follows the approach to disassemble the physical body into a limited number of small bodies (element discretization) linked by nodes using the allocation of an element stiffness matrix. This element stiffness matrix contains material data (e.g. Young's moduli) and geometrical properties (in the form of trial or shape functions) of the respective element. The single element stiffness matrices are superposed to an overall stiffness matrix $[K]$, which represents a coefficient matrix for a differential equation system:

$$[K]\cdot\{u\}=\{F\} \tag{23}$$

where $\{u\}$ is the displacement vector, and $\{F\}$ is the load vector, meaning the combination of all forces acting in the domain as experienced by the finite-elements. The overall stiffness matrix represents a coefficient matrix of an equation system. Solving the equation system leads to the unknown values: In case of the Displacement Method, the calculation node displacements $\{u\}$ are unknown, and in case of the Force Value Method, the respective element loads $\{F\}$ are unknown. Since acting forces (boundary forces and volume forces) are usually known with higher accuracy prior to the simulation than resulting displacements, the most common method in engineering application is the Displacement Method. The solving concept aims for the calculation of the unknown displacement vector $\{u\}$ by inverting the element stiffness matrix $[K]$ following the equation

$$\{u\}=[K]^{-1}\cdot\{F\} \tag{24}$$

Result variable of interest, e.g. typically equivalent stresses and force reactions, are subsequently determined by back-calculations (back substitution). [52] [53]

The Rayleigh-Ritz procedure is considered as the base of the FEM and its approach is still valid for modern FEM procedures. It solves (23) for the displacements caused by the load vector. The estimation of stresses and strains or other target values is subsequently done through material property models, which are linear elastic in the most simple cases. The differential equations set up for this purpose are discretized based on polynomial trial functions (shape functions), which are defined according to the geometrical boundary conditions. This approximation method gets less accurate for more complex geometric structures, which requires the increase of the polynomial order of the trial function to retain sufficiently accurate solutions. Since the trial function in the classic Rayleigh-Ritz procedure is used for the whole geometric structure, a very high order polynomial approach may be required. The separation into many elements in the FEM mitigates this issue by using trial functions local to each element. This opens the second approach to increase result accuracy for complex geometric structures, the (local) increase of discretization density. This approach also explains the enormous flexibility of the FEM to model complex geometries as all geometries are broken down into simple small elements. [54]

Unless research in the mathematics of FEM itself is performed, in engineering the subsequent choice of the numerical solving method is usually made automatically by the FEM software, simplifying the user's options to a small set of general method formulations. That is why, further discussion of this topic (e.g. direct versus iterative solvers, matrix integration algorithms, different trial functions etc.) are not within the scope of this introduction and can be obtained in the relevant literature (e.g. [53] [54] [55]) or the respective software documentation (e.g. [56] [57]).

Since structural FEM is a common tool in modern engineering, there are several established tools available (e.g. ANSYS Mechanical or Abaqus) which show user-oriented workflow without the need for programming or deeper understanding on the implemented numerical methods. Nevertheless, the user has to ensure a sufficient understanding for the properties of the chosen FEM, since an inappropriate setup and choice of submodels will lead to faulty simulation results which without proper testing are not always noticeable in the interpretation of results. The overall workflow is similar for all commercial tools and usually divided in pre-processing, solution process and post-processing. Pre-processing starts with adjusting CAD geometry, e.g. simplifications, part merging etc. and subsequent geometry discretization. Discretization or meshing means the disassembly of the geometry into simply describable elements and is a characteristic part of the FEM procedure. Choices in this step include the amount of dimensions, the basic geometric shape and the degrees of freedom for each element, which together determine the general element description and with that the degree of complexity in mathematical modeling. Resulting geometric entities are for example beams, triangles, quadrangles, tetrahedrons, wedges or cuboids. Discretization always requires to find a compromise between result accuracy and computational expense. Appropriate discretization is also crucial for good convergence behavior, since a too small number of elements results in badly shaped elements with unfavorable skewness and aspect ratio. The next step is the definition of contacts, boundary and starting conditions as well as the choice of the material modeling and solution process specifics. The solution process is usually automated, so no further user input is necessary. During post-processing the element stresses, force reactions and other desired values are calculated and refurbished to be displayed to the user. [54]

2.3.2 Contact Modeling and Determination

To be able to model friction in an FEM contact, a contact must first be detected. Without a contact detection method, bodies in FEM setups do not interfere and just pass through each other. Hence, contact definitions are always required if the modeling of impact, sticking or sliding, friction, or interface deformation is desired. Common contact detection algorithms are based on elastic body penetration with the ability to minimize the penetration depth, or based on the insertion of an additional degree of freedom for the contact normal force. Even if still non-linear, the first mentioned penetration based approach is the numerically most stable and therefore the most used approach for contact detection in FEM. [53] [55]

To detect a contact, the solver basically tracks the distance of the two defined contact surfaces at each mesh node. As long as this distance is positive, there is no need for further actions. As

soon as this distance gets negative, a contact is detected. Subsequently, the previously generated contact surface elements determine the contact behavior by the minimization of the negative distance between both surfaces (the body penetration) due to the contact element formulation. In penetration based contact modeling, the contact elements generate a contact reaction force F_N dependent on the penetration depth x_p and the contact normal stiffness c_{normal} as depicted in 2.17 following equation (25). For the Augmented Lagrange approach, an additional term λ is applied, which does not exist for Pure Penalty approaches. This term λ helps to achieve smaller penetrations by adding an artificial contact force. This results in lower sensitivity of the penetration depth to the contact stiffness c_{normal}, which is usually linked to the material stiffness. According to this approach, the Augmented Lagrange approach provides more realistic contact modeling with very low penetration, but requires additional equilibrium iterations for the contact force convergence. [53] [55] [56]

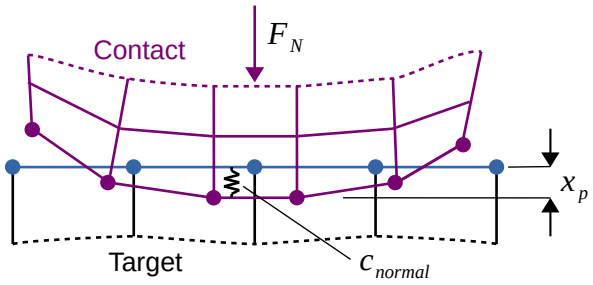

Illustration 2.17: Penetration-based FEM contact modeling; modified from [56]

$$F_N = c_{normal} \cdot x_p + \lambda \tag{25}$$

The contact elements add element stiffness matrices to the overall stiffness matrix and therefore act as mathematical constraints to the respective single body. Advantageous compared to non-penetrating approaches is the faster convergence behavior while facing the disadvantage of increasing calculation time due to the fact that the overall stiffness matrix has to be rebuilt for each contact status change. [53] [55] [56]

3 Definition of Research Targets

Analyzing the state of the art during the previous chapter, and putting this analysis into context with the four four core points of the general problem description from Chapter 1.2 guides to the research approach presented within this chapter. The main research target derived from these core problem points is at the same time the most general target: In order to contribute to the overall improvement of friction force behavior of automotive shock absorbers on unit level, it is necessary to understand the introduced contributing friction mechanisms, and with that to identify all friction-related parameters in the respective contact zones with the aim to predict the friction force behavior based on these parameters in a simulation model. To achieve that, several sub-tasks can be defined:

Friction is generated in the single friction points marked in 1.3. Since these single friction points show differences in geometry, material, operating conditions and lubrication state, it is assumed to be feasible to divide the overall damper behavior in individual friction contributions and summarize their friction behavior in the end. That means in practice that the friction behavior of each single friction point needs to be recorded and analyzed independently of the others. Unfortunately, the required single friction point test rigs are so far not available with the desired precision and flexibility. Thus, these test rigs have to be developed, set up, and validated, so that they record the friction behavior in a way that is representative for the behavior of the specific single friction point in the overall damper.

Seal geometries vary widely, depending on their requirements according to tightness, friction, wear resistance, costs and others. To be able to use the friction prediction model on a wide range of possible geometries, geometry should be taken into account as-is, which requires a 3D simulation tool. The three-dimensional finite element method (FEM) is very useful for this kind of structural mechanics task, commonly validated and easily accessible through commercial software suites. That is why it will be the basis of the simulation model. There, it is also straightforward to take the solid body’s material properties into account, especially the nonlinear and time-dependent behavior of the seal’s materials. To characterize these properties in a sufficiently detailed fashion, while keeping an eye on the practical use, the type of solid material modeling has to be chosen as a compromise between physical correctness, computational expense, and the amount of necessary parameterization measurements.

The friction behavior in the contact zone is dependent on many microscopic parameters and conditions. To model this process with 3D FEM, an unacceptable fine discretization and the modeling of microscopic, often time-dependent effects like adhesion and cohesion, fluid film development, asperity interaction and others, would be necessary. After extensive tests and comparisons to experiments and simulative investigations (see Chapter 7.1), it became evident that an overlaid dynamic friction model in the 3D FEM simulation’s contact zone is much more appropriate considering the desired compromise of physical correctness and computational expense seeking to ensure possible every-day use in engineering. This model has to ac-

curately consider all relevant contributing friction effects, and it has to be parameterized and applied to the simulation.

Summing up the above listed sub-tasks, a general overview over the solution process of this work can be developed, which is visualized in 3.1. Whereas the macro-scale parameters from the three parameter groups geometry, operation conditions and material properties are directly put into the FEM's boundary conditions, their micro-scale parameters are represented by the contact friction model's parameter set which is experimentally obtained. Since the structural FEM model influences the contact friction model's boundary conditions, and the friction generated by the contact friction model influences solid body deflection in the structural FEM model, there is a two-way coupling between these blocks in 3.1. That is also the case for the finally resulting overall friction behavior.

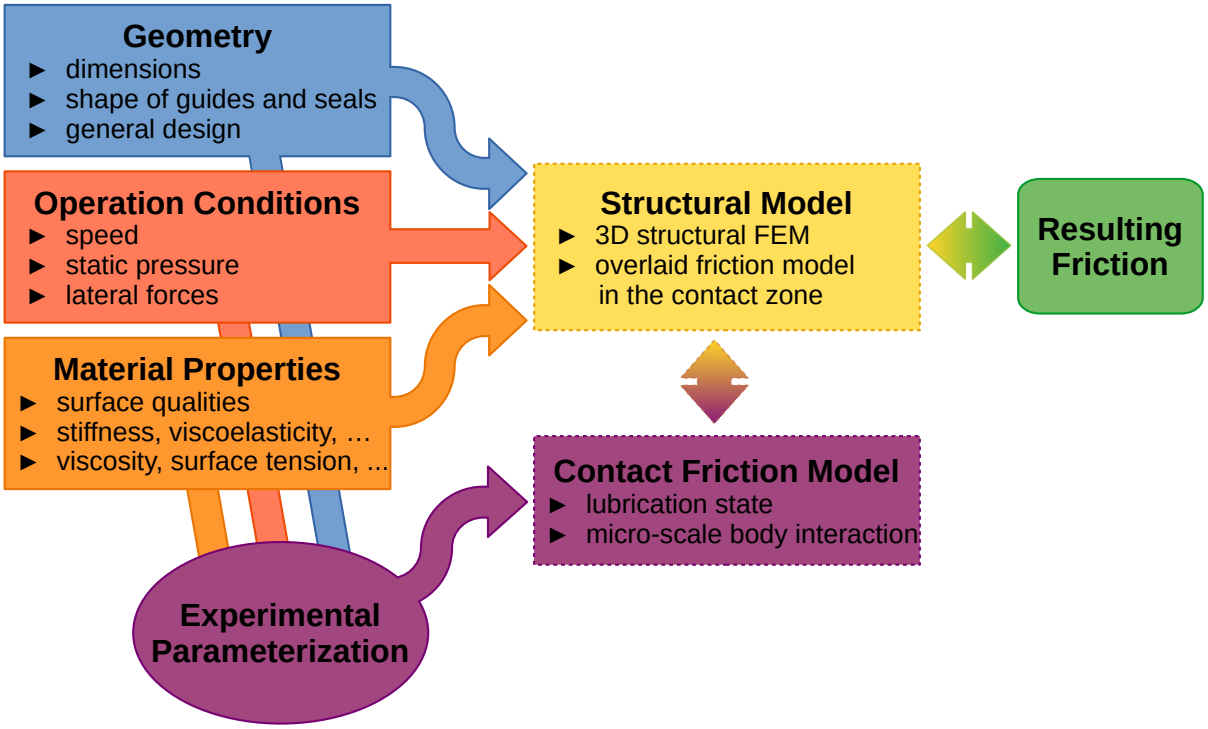

Illustration 3.1: Solution Approach Overview; three main parameter groups are included in the simulation either directly or indirectly via experimental parameterization

As for all simulations, several validations have to ensure the model's overall and specific functioning. It is evident that the simulation is not to be compared only with the parameterization measurements. Especially the transferability of the model to modified geometry and / or adjusted materials is crucial, since that is a common task in product design, and the change of friction force behavior as a response to geometry or material changes is the intended standard application of the outcomes of this work.

4 Experimental Methods

The experimental investigations done within the scope of this thesis aim to fulfill two objectives: On the one hand, they contribute to the general understanding of friction behavior in automotive shock absorbers (dampers) and help explain the occurring friction effects and characteristics. On the other hand, they are intended to be used as the basis for future simulations. The experimental results will define the friction phenomena to be implemented and provide the necessary friction parameters. Finally, the results of the overall simulation will be validated against the experimental results.

4.1 Reference Damper Introduction

Experimental as well as computational investigations in this thesis will be carried out on a representative reference damper. Because of the widespread variations in damper design, e.g. of geometry, parts, materials and so on, it is necessary to determine a reference setup, whose experimental and numerical results can be analyzed and compared to each other. Subsequently, parameters and geometry can be varied and the impact on both experiment and simulation accordingly investigated (see Chapter 8.4). The automotive shock absorber which is used as a reference in this dissertation is a series mono tube damper, applied in rear axle setups of compact cars. Its characterizing dimensions are an $11\,mm$ outer diameter rod and a $36\,mm$ inner diameter tube. The physical reference damper contains all characteristic mono tube parts and friction points as introduced in Chapter 1.1.2 and 1.3 and is available as a take-apart version, allowing for better accessibility of the friction points.

A partially simplified drawing is presented in 4.1. It shows an overview over the reference damper on the left side and magnified depictions of the three single friction points on the right side, namely the rod guide assembly / rod (A), piston / tube (B), and floating piston / tube (C) friction point. As demonstrated in the illustration, the seals penetrate their respective counterparts because this depiction shows the undeformed state representing all geometries before mounting.

The rod guide assembly / rod friction point (A) separates the damper's oil volume from the environment. This happens mainly through the rubber oil seal (6) in contact to the rod (2), which is made from chrome-plated steel. The oil seal is supported by the static seal (7), another rubber part and designed to transmit the damper's inner static pressure to a mainly radial pre-tension force on the oil seal. The bronze-made bearing (3) is located above the oil seal to support the lateral forces to the damper. In this damper design the bearing is carried out as a dry bearing (there is no direct damper oil lubrication due to the below located oil seal) and coated with a friction minimizing PTFE layer. The outer closing is the scraper (1) which prevents dirt from entering the rod guide assembly, and simultaneously ensures the lubrication of the bearing with oil that passed the oil seal or an initial greasing. The scraper is also a rubber part with a pre-tensioning ingrained spring, which is not directly contributing to the scraper / rod friction. All parts of the rod guide assembly are mounted to the aluminum housing (4)

which is closed with a steel closing. The sealing against the tube (12) is ensured by a rubber O-ring (5), the fixation to the tube by a roll closing (series damper) or a screwed cap (take apart damper), both not depicted in 4.1 to maintain clarity.

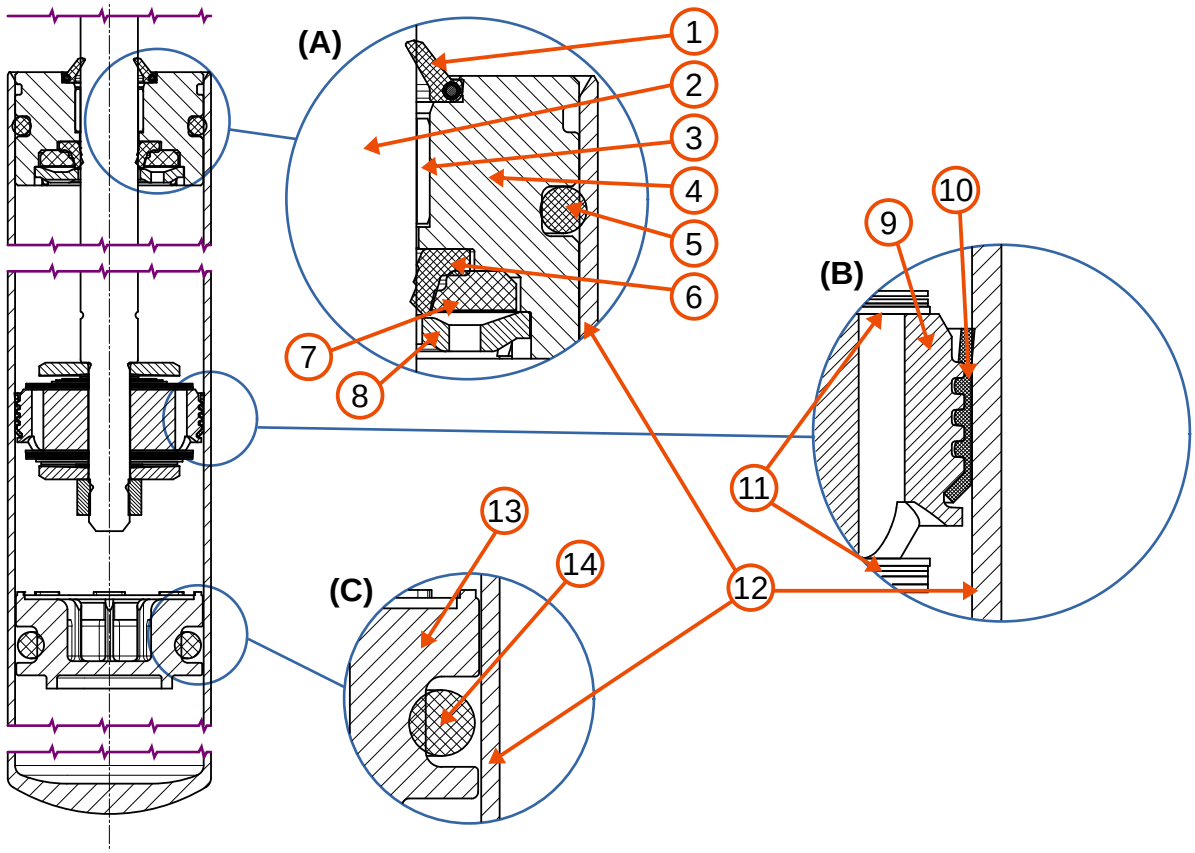

1	Scraper
2	Rod
3	Bearing
4	Housing
5	Rod guide assembly O-Ring
6	Oil seal
7	Static seal

8	Closing
9	Piston
10	Piston band
11	Disc valve package
12	Tube
13	Floating piston
14	Floating piston O-Ring

Illustration 4.1: Reference damper overview with details of the single friction points (A) Rod Guide Assembly / Rod; (B) Piston / Tube; (C) Floating Piston / Tube

The piston / tube friction point (B) prevents the oil from bypassing the piston's bores and valve package (11) to ensure appropriate damping. It also acts as the second support to lateral forces applied to the damper. To achieve both proper tightness and low friction against the tube (12) under lateral forces, the seal is carried out as a PTFE band (10) mounted to the piston (9). Since the piston's bores together with the valve package are generating a hydrody-

namic damping force, which is overlaying the friction measurement, the valve package is generally removed from the piston so that all remaining friction forces are caused purely by friction point (A), (B), and (C), in all reference damper friction measurements within the context of this dissertation.

The floating piston / tube friction point (C) seals the oil volume against the volume compensating gas volume. This is done by a rubber O-ring (14), which is mounted to a glass fiber reinforced plastics floating piston (13) and seals against the tube (12). The gas volume is pressurized with air due to the requirements mentioned in Chapter 1.1.2. This pressure is transferred via the floating piston to the oil volume, thus creating an operating pressure of $25\,bar$ inside the damper.

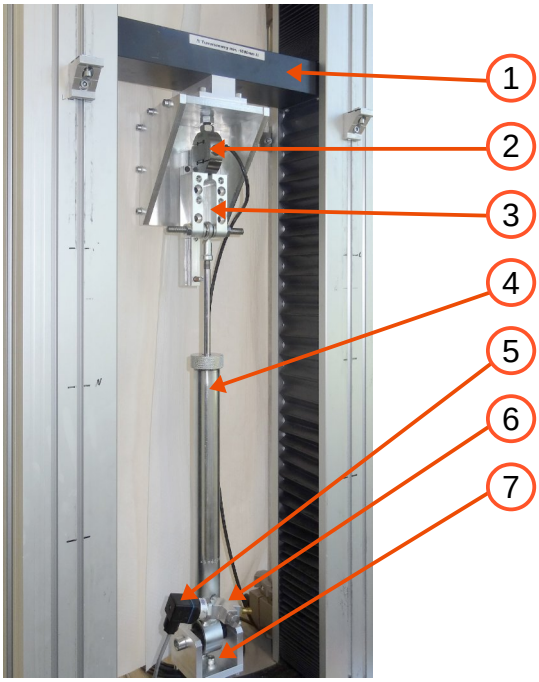

Illustration 4.2: Reference damper friction measurement setup

The test setup to determine the reference damper friction is depicted in 4.2. The basis is a tensile tester of the type Galdabini Quasar 5. It features a maximum force of $\pm 5\,kN$, a maximum speed of $1000\,mm/min$ and the possibility to operate both at constant speed and at sine waves, where the maximum frequency is evidently much smaller than on a comparable servo-hydraulic tester, but high enough for the desired tests with the displacement amplitudes of typical friction tests ($\sim 10\,mm$; [4]). Overall friction is recorded by a single force sensor (2) mounted between the damper (4) and the tensile tester's cross head (1), where an intermediary component (3) prevents the sensor from facing destructive lateral forces which can be applied to the damper (lateral force application setup not depicted). The lower end of the damper is linked to the tensile tester's frame (7). The sensor choice is controlled by the trade-off between the static load to be carried due to operating pressure push out and the measurement precision to be achieved to gather appropriate friction force results. In this setup, the typical

static load is at about $238\,N$ with $25\,bar$ static pressure and a built-in $11\,mm$ rod following equation (26).

$$F_{push\,out} = p_{static} \cdot A_{rod} \approx 238\,N \tag{26}$$

To withstand this force and achieve the required measurement accuracy of fractions of a Newton, an AEP TS-TM strain gauge sensor with a $\pm 500\,N$ measurement range is chosen. 4.2 also shows an adapter (6) to connect both a pressure source to pressurize the damper, and a static pressure sensor (5) which observes this static pressure. This sensor helps notice possible leakages and ensure the correct static pressure before starting measurements.

4.2 Measurement Sequence Definition

As described in Chapter 1.2, the resulting damper friction should be generally as small as possible. The same chapter shows that the quantification of this statement is inconsistent across different dampers due to the various damper friction measurement and analysis definitions to comply with the OEM's requirements. Consequently a proper friction measurement sequence must be defined for this dissertation, which captures and unifies the friction specifications, but also fulfills the requirements for the desired support of the simulation setup (namely friction model choice and parameterization) and validation. To achieve that, two sequences have to be standardized: pre-conditioning and friction force recording. This will take place in the following two sections.

4.2.1 Pre-Conditioning Sequence

Pre-conditioning is necessary for all kinds of tribological measurement setups, since the initial state immediately after mounting is highly uncertain. The aim of pre-conditioning is to ensure similar starting conditions for each setup and each single friction recording with regards to autonomous position correction, wetting, displacement of contamination and run-in. Since each friction cycle modifies the tribological properties of the pairing (e.g. surface property changes due to wear or chemical reactions), a compromise must be found for the pre-conditioning sequence between the above-mentioned similar starting conditions and undesired influence on the state of the friction paring to be investigated. Based on this premise, various pre-conditioning sequences have been defined by OEMs and suppliers in accordance with their respective damper friction definition, starting with very vague descriptions ("three full strokes by hand, or the like") over few full strokes with defined slow speed up to strong run-in sequences with hundreds to one thousand cycles with frequencies greater than $1\,Hz$ [4]. These quite heavy loads on the damper imply a lengthy and necessary cool down phase before friction measurement, which casts doubts on the desired well-defined starting conditions and makes it impossible to test dampers freshly taken from the production line, or single friction points.

In the context of this research project, extensive investigations were undertaken to find an appropriate pre-conditioning sequence for the above-mentioned reference damper. The following sequence has proven to be suitable for reliably reaching similar friction measurement

starting conditions while remaining comparatively short. This guarantees efficient experiments and the possibility to test parts in a very new and unworn state, as it is desired for the common friction requirements [4]. This pre-conditioning sequence is depicted in 4.3 (a) and consists of eleven triangle-shaped strokes with an amplitude of $\hat{A} = 30\,mm$ to ensure conditioned contact surfaces even outside the desired measurement amplitude of $25\,mm$. To be able to switch directly between pre-conditioning and friction recording, the pre-conditioning sequence is carried out on the tensile tester as described above.

4.2.2 Friction Recording Sequence

The definition of the friction recording sequence aims to provide both comparability to the friction specifications [4] and enhanced analysis capabilities for this study. For typical friction tests it is common to use triangle-shaped time-displacement sequences with long-lasting constant speed intervals, although sometimes also sine-shaped sequences with much smoother turn around points are used [4]. The advantage of triangle-shaped measurements is the very constant friction state around midstroke, the typical analysis point of the friction measurement. This ensures reliable and easily analyzable friction measurements with a clear constant friction result at the chosen constant speed, but produces no usable data close to the return points due to the uncertain acceleration behavior of the tensile test benches. Sine measurements on the other hand require more complex test rig motion control, but provide a bigger stroking speed range and appropriate return point description required for dynamic friction model parameterizations. Because dynamic friction behavior and return point behavior is of interest to this study, sine-shaped motion was chosen for the experiments within this dissertation. Triangular measurements have been carried out for reasons of comparability and for secondary tasks, but they are not presented within this dissertation.

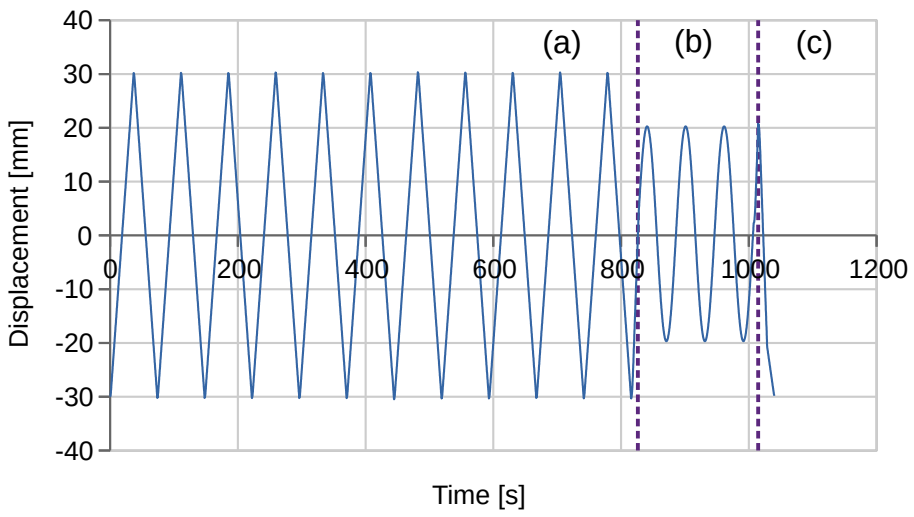

Illustration 4.3: Complete time-displacement progress of pre-conditioning sequence (a), friction recording sequence (b) and return to initial position (c)

The final sequence of both pre-conditioning and friction recording is presented in 4.3. Given that a very low speed is still required to have negligibly small fluid damping, the sine-shaped motion always remains at very low frequencies. The default period for friction recording as depicted in 4.3 (b) is $T = 60\,s$, which equals $f \approx 0.016667\,s^{-1}$ and provides together with an amplitude of $\hat{A} = 20\,mm$ a maximum speed of $v_{max} \approx 2.094\,mm/s$. Three strokes are recorded, whereas only the last one is analyzed, while the previous two strokes show the required repeatability. The presented amplitude of $\hat{A} = 20\,mm$ represents a sliding distance for all friction points, that forces the seal into gross sliding, and no contacting area of the counterpart at minimum displacement is in contact with the seal at the maximum displacement. The achieved maximum speed of $v_{max} \approx 2.094\,mm/s$ is within the range of maximum speeds of common OEM friction measurement specifications [4] and – as discussed in Chapter 5 – constitutes a good compromise of the demand of investigating all relevant friction mechanisms on the one hand, while keeping fluid damping negligible on the other.

4.3 Single Friction Point Test Rigs

To determine the overall friction behavior of the damper, the respective contribution of each single friction point to the overall friction behavior will be determined. To gather realistic data, probes and operating conditions during measurement have to resemble the real damper as closely as possible. Additionally, an easy exchangeability of all friction-related parts is important. Current damper friction measurement methods, as defined e.g. in Tenneco friction specifications [4], do not fulfill these necessary requirements because they focus on the whole damper without possibilities for separating each single friction point's respective friction contribution. As a consequence they are not suitable for the requirements of this work. Therefore new test rigs had to be developed. From the above-mentioned basic requirements, detailed requirements are developed and two test rigs are designed. These two single friction point test rigs allow to measure and characterize the single friction points of the reference damper as introduced in Chapter 4.1, namely the rod guide assembly / rod friction point, the piston / tube friction point and the floating piston / tube friction point.

4.3.1 Single Friction Point Test Rig (1): Piston / Tube and Rod Guide Assembly / Rod

The Single Friction Point Test Rig (1) (SFP1) is designed to enable the analysis of all directly actuated friction points of the reference damper. This test rig contains the working piston / tube friction point and the rod guide assembly / rod friction point (see 4.1). From the above-mentioned global requirements the following detailed requirements are derived:

- Measurement of friction in the respective friction points under standard operation conditions (static operating pressure (typically $25\,bar$), degrees of freedom as in the original reference damper). This ensures the comparability to overall damper friction measurements.
- Measurement of friction at adjustable, stroke-independent pressure. This allows to investigate static pressure-dependent friction behavior.

- No outside influences on the friction related probes. This also ensures comparability to overall damper friction measurements and leads to more realistic results
- Good accessibility / exchangeability of the related probes. This is necessary for appropriate and efficient probe handling.

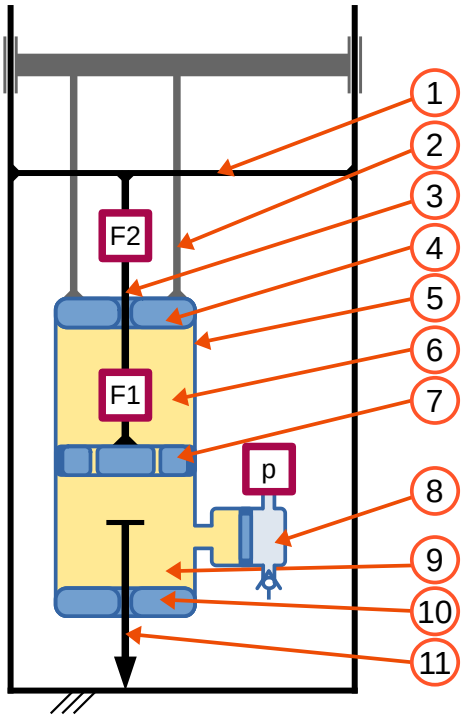

Illustration 4.4: Single Friction Point Test Rig (1): Rod Guide Assembly / Rod and Piston / Tube

The implementation of the above-mentioned requirements results in the principle depicted in 4.4. It shows a single friction point test rig that is mounted to the same tensile tester as introduced for the reference damper measurements in Chapter 4.1. The setup contains four friction related probes, three of which can be transferred directly from the original damper: the rod (3), the rod guide assembly (4), and the piston (7). One, the tube (5), can be transferred with minor modifications. The actuation principle is reversed compared to the original damper, meaning that the rod is fixed to the tensile tester's frame (1), and the tube is actuated by the tensile tester's cross head (2). The resulting displacements stay the same: While stroking, oil flows from the lower part of the tube (9) to the upper part (6), passing the piston's bores on the way. The reversed actuation allows to avoid a compressible air volume for volume compensation of the in- and outgoing rod. Thus, one friction point (floating piston / tube) does not appear in this principle. The corresponding volume compensation is ensured by a secondary rod guide assembly (10) / rod (11) couple which brings the additional advantage of always having constant static pressure on the friction points, even while stroking, following the requirements mentioned above. To apply static operating pressure, a pressure accumulator (8) is added, which does, however, not influence the friction behavior further. The accumulator also

ensures that the secondary rod (11) is always pressed out to the tensile tester's frame (1), which means that no additional fastening is necessary.

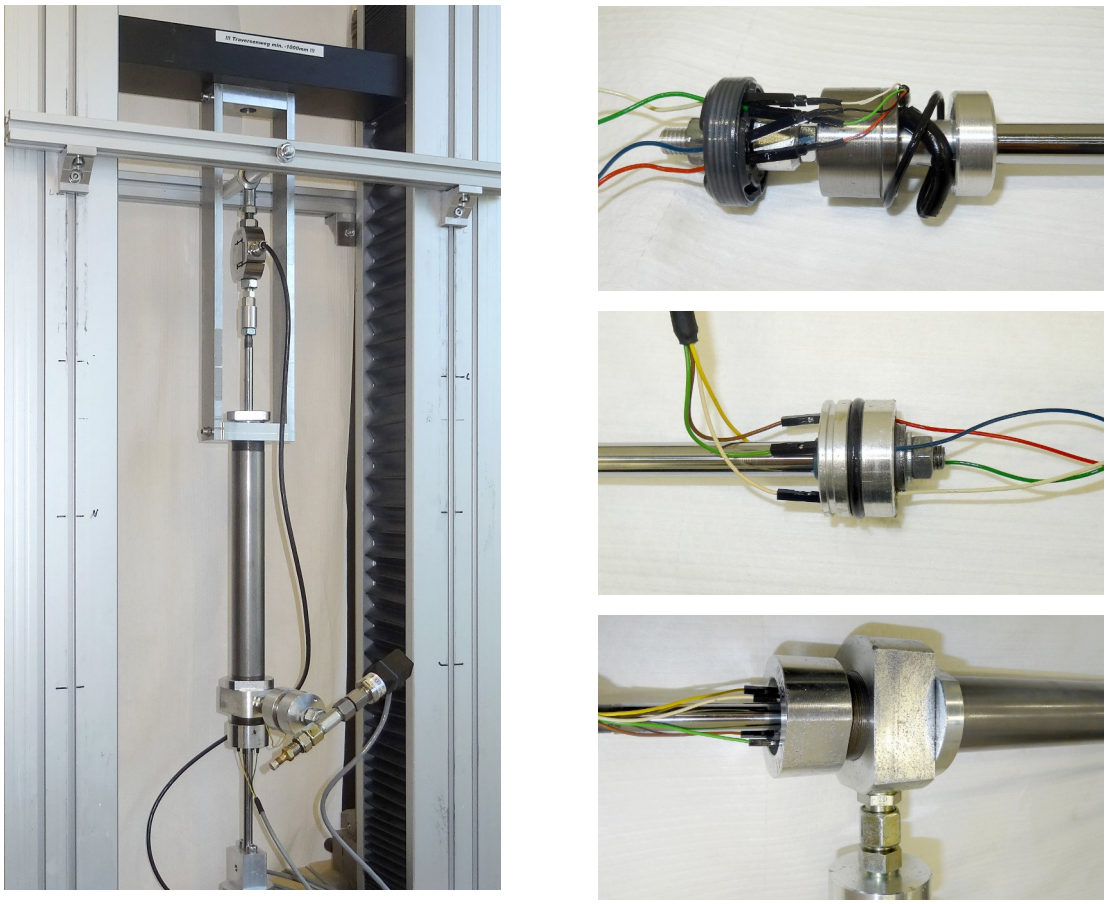

Illustration 4.5: Single Friction Point Test Rig (1) – overall setup (left); Details: Wiring through piston (right top); Wiring through the secondary rod guide assembly (right center); Secondary rod guide assembly and pressure accumulator mounting (right bottom)

There are four sensors included in this test setup, ensuring that the single friction point forces can be measured independently: The first sensor is the displacement sensor between the tensile tester and its cross head. Second, there is a small force sensor (F1) mounted between the rod probe (3) and the piston probe (7), measuring only piston / tube friction. Third, there is a second force sensor (F2) mounted between the rod probe (3) and the tensile tester's frame (1), measuring both rod guide assembly / rod friction and piston tube / friction. By subtracting the measurement of (F1) from the measurement of (F2) and by taring the static (F2) load caused by the rod push-out force because of static pressure from the pressure accumulator (8), the single friction point force at the rod guide assembly / rod contact can be calculated. Because of the high static pressure-induced load on (F2), this force sensor must be dimensioned for higher absolute forces then (F1). The fourth sensor is a static pressure sensor (p), which monitors possible leakages and ensures the correct static pressure before starting measurements. Parts of the design phase and the concept and design evolution were undertaken in the context

of the master theses [58] and [59]. Some final design aspects and special challenges are introduced below. The whole test rig is shown in 4.5 (left).

The choice of the sensor (F1) was made based on the following requirements: The measurement range should not be significantly larger than the expected piston / tube friction to gain a high level of precision. Overall friction on unit level is expected to be lower than $60\,N$. To add a suitable safety margin for mounting and unavoidable lateral force robustness this sensor's measurement range has been defined to $\pm 100\,N$. Strain gauges are most suitable as sensing technology, since piezo-based sensors lack in precision and exhibit a drifting behavior. As a design consequence of mounting inside the tube, the sensor's geometry is restricted to an outer diameter of less than $36\,mm$ including potential wiring. Additionally, the sensor's wiring has to leave the sensor's housing in load direction. All other sensors inquired and available with lateral wiring are problematic either because the allowed bending radius is too small, or the stiff wiring in contact with the tube would induce lateral forces to the sensor. The sensor has to be flooded with damper oil (so called "flushed sensor"), otherwise the difference between the inner atmospheric pressure inside the sensor and the operating pressure in the tube would lead to housing deformations and, concomitant with that, cause measurement errors. Therefore, everything in the sensor has to be oil-proof, especially the strain gauges and the related adhesive. A force sensor that meets all these requirements is the Althen ALF245, which was adapted especially for this research. The choice of the sensor (F2) was much less limited because of similar requirements like in the reference damper test setup introduced above, which is why the choice fell on the same $500\,N$ strain gauge sensor.

In order to enable sensing the resistance change from the strain gauges of the inner force sensor (F1), the wiring of this sensor has to be brought out of the damper tube. In early setups this was done with a non-conductive plastic brace around the tube. Handling problems, particularly the necessity to pass this tube section with the piston, and friction influencing tube deformation by the brace's clamping forces, led to some design changes. The final solution, depicted in 4.5 (right top), is to guide the sensor's wires through the piston's bleed holes, followed by a modification of the secondary rod guide assembly (10) in 4.4. Four bores penetrate the housing and parts of the static seal (see 4.1 (A)). The wires are put through, and each is sealed with epoxy. A photo of the realization of the wiring rod guide assembly is shown in 4.5 (right center). Since the secondary rod guide assembly is not in the flux of force of the two force sensors, its friction is not recorded during measurement. Consequently, the changes of friction behavior of the secondary rod guide assembly due to seal impairment or epoxy influences do not appear in the measurement data.

The mounting of the pressure accumulator to apply static pressure to the test rig was done with a clamped brace as well as a non-conductive wiring brace. Because of same reasons mentioned above, a redesign had to be carried out. The final design is the application of a sealed low-pitch thread on the tube and a large nut with the hydraulic connector of the pressure accumulator, as depicted in 4.5 (right bottom).

4.3.2 Single Friction Point Test Rig (2): Floating Piston / Tube

The third friction point in a typical mono tube damper like the reference damper is the floating piston / tube contact (see 1.3). The main difference to the friction points mentioned in the SFP1 is the indirect actuation of the floating piston. This part's movement is driven by the pressure difference between the tube and the pressure chamber and not directly by the rod. One central requirement to this test rig is to use this indirect actuation as well as the SFP1 to ensure equal movement behavior and consequently to ensure equal friction behavior of the floating piston in reality and in the test rig. The other basic requirements are equal to the requirements to SFP1, as mentioned in Chapter 4.3.1.

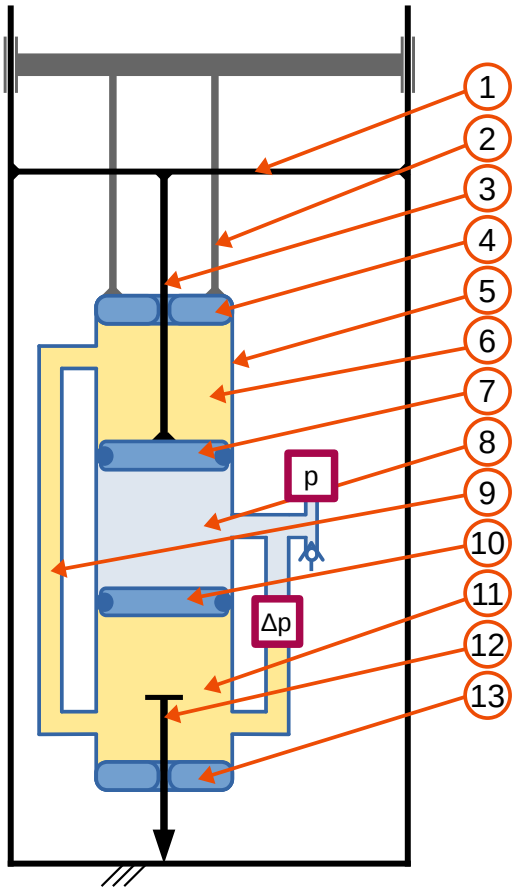

Illustration 4.6: Single Friction Point Test Rig (2): Floating Piston / Tube

The final working principle to meet these requirements is depicted in 4.6. This Single Friction Point Test Rig (2) (SFP2) is mounted to the tensile tester as well as SFP1. The actuation is transferred by the link between the tensile tester's cross head (2) and the tube (5) as well as the actuation of SFP1. However, the actuation principle is not reversing the displacement direction. The description below shows that in this setup the floating piston moves towards the air volume if the test rig's cross head (2) moves downward, similar to the compression stage of the real damper. The counter part to the moving cross head (2) and tube (5) is a rod (3) fixed to the test rig's frame (1). If the cross head moves downward, the displacement piston

(7) linked to the rod (3) decreases the volume of the upper oil chamber (6), which causes the oil to flow through the connection pipe (9) to the lower oil chamber (11). The corresponding rod volume is compensated by the secondary rod (12). Both rods are sealed by standard rod guide assemblies (4, 13). The change of oil volume in both oil chambers forces the probe floating piston (10) to move up (relatively to the tube) together with the pressurized air chamber (8). The friction generated between the floating piston and the tube leads to a pressure difference between the lower oil chamber (11) and the air chamber (8), which is recorded by the pressure difference sensor (Δp). The static pressure sensor (p) is merely observing operation pressure to ensure that the test rig works as intended and without any leakage.

By taking the tube diameter into account (in this case $36\,mm$), the floating piston's friction can be directly calculated from the pressure difference sensor (Δp) with the following equation (27):

$$F_{fric\ FP} = \frac{p_{diff} \cdot \pi\, d^2}{4} \tag{27}$$

That means for the reference damper geometry used in this thesis:

$$1\,mbar \triangleq 0.102\,N \tag{28}$$

Parts of the design phase as well as first setup and benchmark measurements were undertaken in the context of the master thesis [60]. Some final design aspects and special challenges will be introduced below – as previously done for SFP1. The whole test rig setup is depicted in 4.7.

The pressure difference sensor (Δp) has to withstand a difference pressure range equivalent to the typical friction force of a floating piston, and an absolute pressure higher than the typical operating pressure of a damper, in this case $25\,bar$. It has to be considered that on unit level, the friction directly occurring at the floating piston is transferred to the measurable friction force at the rod by a hydraulic transmission driven by the ratio of the rod's and the tube's squared diameter. Hence, with the reference damper's geometry (11 mm rod and 36 mm tube), there is an amplification factor of:

$$amp = \frac{A_{tube}}{A_{rod}} \approx 10.71 \tag{29}$$

Thus, and according to the equations (27) and (28), as the typical overall friction is expected to be lower than $60\,N$, and maximum $25\,\%$ of that at the floating piston, the pressure difference sensor's measurement range should be at least at about $\pm 800\,mbar$. A suitable sensor was found with the model GE UNIK 500 with a measurement range of $\pm 1\,bar$ and a maximum static pressure strength of $60\,bar$.

The connection pipe (9) is mounted to the tube with two clamped braces, where the lower one is also used to connect the oil side of the pressure difference sensor. The pressure difference

sensor’s air side is mounted to the tube with another brace. Because of the air volume inside the tube there is no need for an external pressure accumulator like with SFP1. The problems with clamped braces causing friction influencing tube deformations did not come up on SFP2. Because of the tube length and the much shorter necessary stroke it is possible to always keep enough distance between the floating piston probe and the braces, which will be shown in the next section.

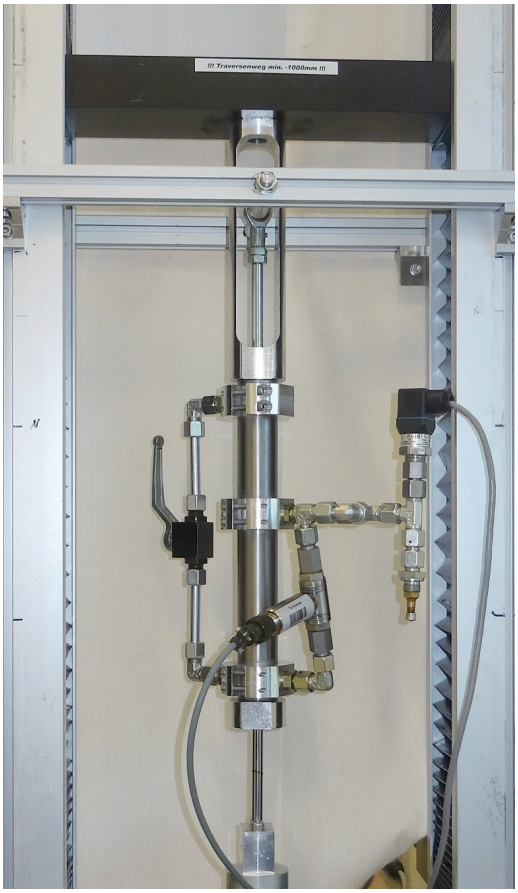

Illustration 4.7: Single Friction Point Test Rig (2) – overall setup

5 Friction Measurement Results

This chapter presents the reference results from the single friction point test rigs introduced above, and with that a characterization of each single friction point. Based on the recorded friction behavior the appearance of the friction effects previously discussed in Chapter 2.1.4 can be investigated. As a consequence, the optimal friction model to describe the measured effects will be chosen based on the friction model discussion in Chapter 2.2, and implemented in the FEM simulation as introduced in Chapter 3.

5.1 Friction Point Piston / Tube

A representative force-displacement graph and force-speed graph of the piston / tube friction point is depicted in 5.1, showing friction results using the above-mentioned friction recording sequence. This data from the friction point piston / tube has been chosen to be presented first because of its simple shape, which qualifies this result for an analysis introduction. The raw measurement data from the inside force sensor (F1) (see 4.4) is only shifted to an average zero force, assuming that pushing and pulling the seal results in equal friction. Even if this assumption is doubtful due to the asymmetric seal design (see 4.1 (B)), it is acceptable for better analysis capabilities and easier friction model parameterization. Additionally, the actual zero-force is unknown, because of uncertain friction states in all single friction points after mounting prior to pre-conditioning. It will be shown later, that the error of this assumption is negligible for simulation results and validation (see Chapter 8.4).

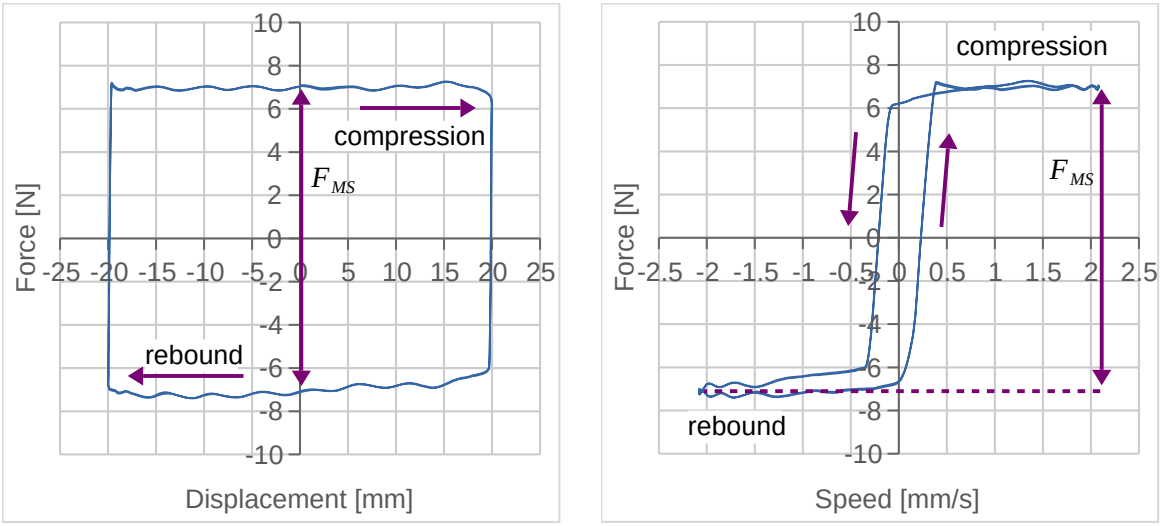

Illustration 5.1: Representative force-displacement graph and force-speed graph of the single friction point piston / tube

The diagrams in 5.1 both contain the second and the third cycle of the friction recording sequence depicted in 4.3 (b), starting at zero with increasing positive displacement. According to the test rig's design, this represents an up-moving tube against the fixed rod, which means

ongoing compression. It can be seen, that no deviation is visible between the two depicted cycles, which demonstrates the reproducibility and constancy of the recording cycle, and the functioning of the pre-conditioning sequence as required. The characterizing friction force definition follows the common definition for damper friction [4] and is defined as the sum of the absolute forces at midstroke, taking into account that the above mentioned uncertainty of the actual zero-friction level makes it impossible to determine the separate friction contribution of compression and rebound movement. The force displacement graph on the left side of 5.1 is shaped nearly rectangular, proving midstroke friction on this single friction point to be representative for a large displacement range. Thus, midstroke friction of this piston tube friction point can be easily determined to $F_{MS}=14.3\,N$. The nearly rectangular shape additionally proves that there are no influences of tube irregularities or clamping-induced diameter changes as mentioned in Chapter 4.3.1.

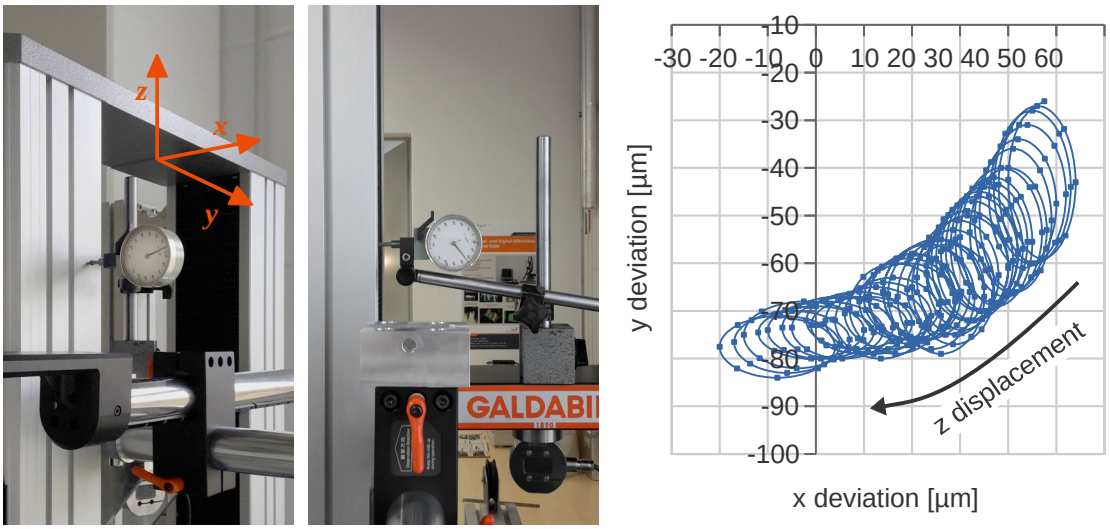

Illustration 5.2: Measurement of the spindle induced oscillation of the tensile tester's cross head with a dial gauge (left side) and the resulting stagger movement in the x-y-plane (z measurement range $-395\,...-195\,mm$, $0.625\,mm$ z-displacement per point); data from [61]

A noticeable phenomenon is the appearance of small waves on the force displacement graph in 5.1. Contrary to initial assumptions this is no friction-induced phenomenon and was first perceived in optical measurements of the piston band with a microscope through a glass-made damper tube [62]. Based on these observations it has been assumed that the test rig's cross head is not perfectly moving in z-direction, but also staggers slightly in the x-y-plane. To proof this assumption, [61] presents the placement of a dial gauge on the cross head and against the tensile tester's frame, for both x and y direction as depicted in 5.2 (left and center) and for the left and the right actuation spindle of the tensile tester, respectively. While the cross head is actuated in z direction, the dial gauge shows the current x or y deviation to the initial zero point according to the respective spindle. It became evident that the cross head's x and y movement versus the frame is reproducible and closely linked to the z-movement. Consequently, the independent measurements of x and y motion can be combined to one x-y dia-

gram. While the x-y movement of the right spindle is comparatively unremarkable, the movement result for the left spindle depicted in 5.2 (right) shows a skew screw-like x-y stagger in a z displacement range that is typical for unit friction measurements as well as single friction point measurements. This graph implies a slightly curved left spindle, which leads to varying lateral forces to the friction points in motion. According to the design of SFP1 introduced in Chapter 4.3.1, this stagger motion causes misalignments and changing contact pressure distributions, thus resulting in varying friction forces. The dial gauge measurements were validated with experiments using a laser line scanner and with experiments using capacitive sensors, both being actuated with a high-precision robot synchronous with the cross head. Since both validation methods proved the behavior introduced above, and produced no further findings while being significantly more complex and costly, the dial gauge measurement method is considered detailed enough [61]. Since the measured deviations of the left spindle are very small and are below the requirements to straightness and concentricity (see [63]), no further actions have been taken to replace or straighten the spindle. The resulting deviations in friction force are also small enough $\left(F_{deviation} \approx \pm 0.2\,N\right)$ that possible attempts to compensate the staggering, like decoupling with magnet or air bearings, have not been implemented.

Because of the better visibility of speed changes and the more detailed depiction of the turnaround points, the force-speed graph on the right side of 5.1 is much more useful than the force-displacement graph to analyze transient friction effects. However, the cross head's speed is no direct output from the tensile tester, thus the speed has to be calculated at each time step. Since the tensile tester's controller lags slightly behind the requested time-displacement progress, the resulting sine wave has a higher period than requested. Thus, speed is an unknown variable at each time step and can not be calculated as the time-derivative of the defined force-displacement function presented in Chapter 4.2.2. Instead, it has to be calculated from the recorded actual time and displacement data in the form of the following equation:

$$\begin{aligned} x &= \hat{A} \cdot \sin\left(2 \cdot \pi \cdot f \cdot (t + \phi)\right) \\ v &= \dot{x} = 2 \cdot \pi \cdot \hat{A} \cdot f \cdot \cos\left(2 \cdot \pi \cdot f \cdot (t + \phi)\right) \end{aligned} \tag{30}$$

where $\hat{A}$, f and ϕ are the determining parameters amplitude, frequency and phase shift. The most straightforward approach of taking the time and displacement differences of each time step to its predecessor is not feasible, because the cross head's displacement sensor resolution is too low to record accurate displacement changes in each time step for the desired recording frequency of $10\,Hz$, resulting in a very jagged speed curve. This is why a displacement function estimation following equation (30) is performed by a Matlab script to determine amplitude, frequency (or associated period) and phase shift, which results in the corresponding speed function. The script searches for zero crossings to determine the frequency and subsequently fits phase and amplitude. Since the tensile tester's controller is not accurately representing the beginning of the first record cycle (see 4.3), some phase shift will appear when fitting equation (30), which is neglected later, since only the second and third measurement cycle is analyzed. This has to be kept in mind, since the force-speed-graph is extremely sensitive to phase shift and period estimation errors as depicted in 5.3. This illustration shows that even

for very small deviations of period and phase shift the graph is either obviously wrong, given that the lines are not matching (5.3, left panel), or the hysteresis width is under- or overestimated (5.3, right panel). This second case is easily overlooked since absolute midstroke friction is not affected. Thus, taking care that the speed function estimation is accurate is crucial for the measurement data reliability.

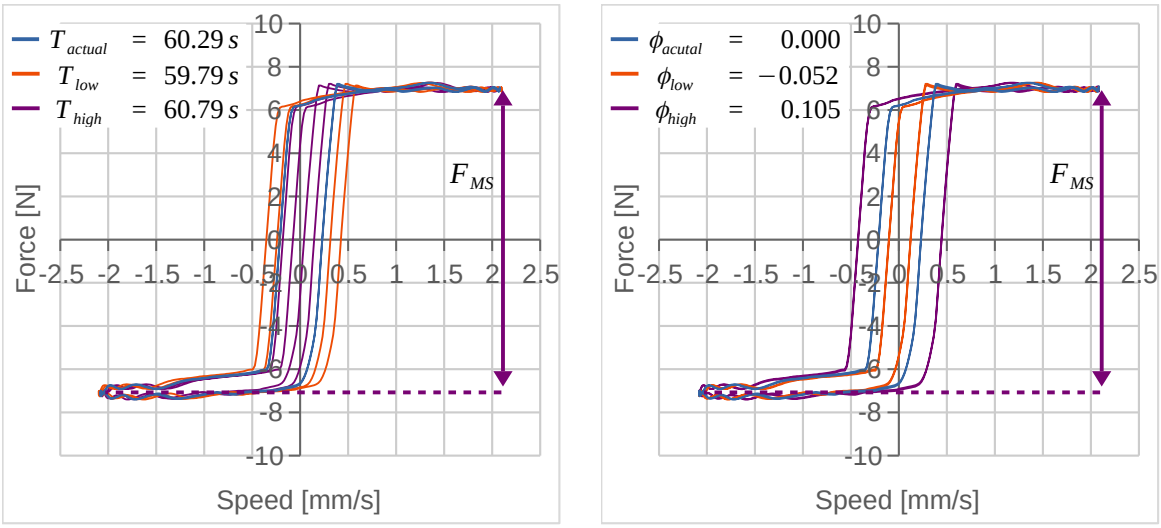

Illustration 5.3: Sensitivity of the force-speed graph of friction measurements to period and phase estimation errors

The above-mentioned spindle-induced force oscillations are still visible in the force-speed graph of the piston tube friction point depicted in 5.1 (right). In general, a nearly point-symmetric behavior can be seen, hence the pass through of the respective friction states is not direction-dependent, even if the seal design is asymmetric (see 4.1). Friction hysteresis is visible, implying presence of pre-sliding displacement. A visible overshoot after passing zero-speed is not observed, nor any visible velocity weakening from the Stribeck effect, implying that there is no significant break-away after motion direction changes. The friction force remaining constant for velocities of $v \approx \pm 0.6\, mm/s$ and higher implies that the necessary speed to make viscous friction the dominant effect is not reached (see Chapters 2.1.3 and 2.1.4). As a consequence it can be stated that the piston tube friction point can be characterized by the absolute midstroke friction and the hysteresis shape, namely slope and width.

5.2 Friction Point Rod Guide Assembly / Rod

The measurement and analysis of the friction point rod guide assembly / rod proceeds similar to the remarks in the previous Chapter 5.1. This concerns the pre-conditioning sequence as well as the friction recording sequence, the shifting of the raw measurement data to an averaged zero force, the record cycles two and three chosen for depiction, and the midstroke friction definition. A representative graph is shown in 5.4. In contrast to the piston / tube friction point, neither is the force displacement graph nearly rectangular, nor is the force speed graph

point-symmetric. It is reasonable to assume that this is caused both by the much bigger design complexity of the friction point (see 4.1 (A)) and the direction-dependent lubrication state. The orange-marked parts of the graph characterize the rod guide assembly / rod friction point qualitatively, but they also define the specific rod guide assembly in their quantitative realization.

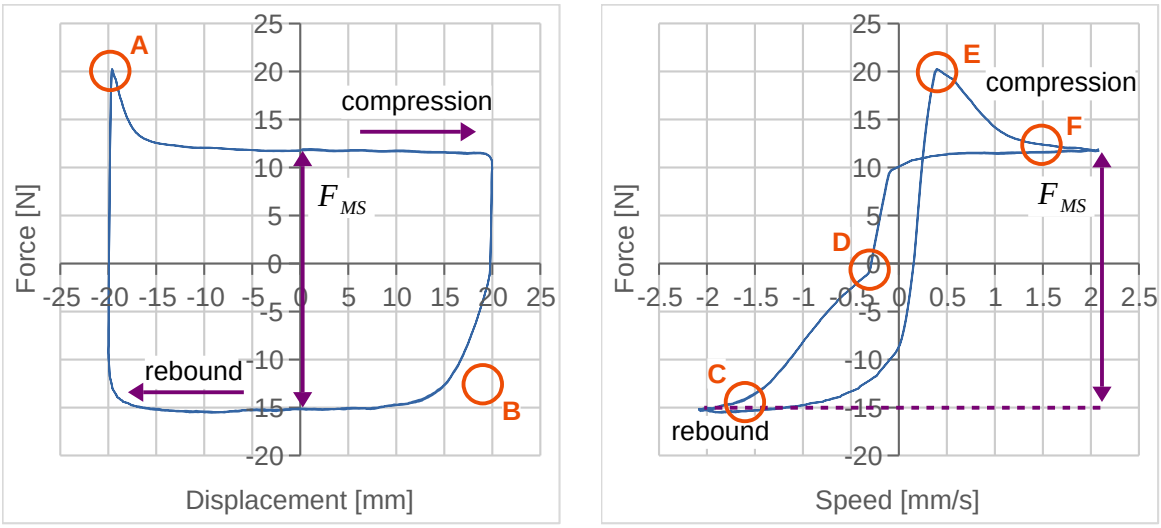

Illustration 5.4: Representative force-displacement graph and force-speed graph of the single friction point rod guide assembly / rod

The force displacement graph in 5.4 shows a significant overshoot at the return point from rebound to compression (A), which is caused by the changes in seal deformation and lubrication state due to the motion reversal. About $10\,mm$ after the motion reversal, a quite constant friction plateau is reached until the next motion direction change is performed. After this direction change, a delayed friction force buildup (B) can be observed, matching roughly the same area that is occupied by the overshoot point (A). Similarly to the compression direction, the rebound direction also shifts to a constant friction plateau after about $10\,mm$ rebound stroke, resulting in easily determinable midstroke friction of $F_{MS}=26.9\,N$. The above-mentioned phenomenon of spindle-induced force oscillations is still detectable, but much less distinct, especially compared to the absolute force values. The force speed graph in 5.4 shows even more clearly than the force displacement graph the completely different friction behavior of the rod guide assembly / rod friction point for both motion directions. The overshoot from (A) is visible once again in point (E), where the speed of return to almost matching compression acceleration and deceleration graphs (F) characterizes the specific rod guide assembly / rod pairing. This overshoot in compression direction indicates significant non-reversible friction characteristics as introduced in Chapter 2.1.4, which is not detectable at all in rebound direction. Further deceleration from the overshoot peak and the subsequent acceleration in rebound direction follows a hysteresis curve, describing pre-sliding displacement. This hysteresis abruptly changes slope and corresponding width from point (D) on, which is usually located very near to the virtual zero-force line. The matching point of rebound acceleration and decel-

eration graphs (C) is characteristic for the specific rod guide assembly / rod pairing, while this matching (C) usually happens at higher speeds than at point (F) during compression. The rebound to compression return range does not experience such a sharp change in hysteresis width and slope compared to point (D) and is quite smooth. In summary, the rod guide assembly / rod friction point can be characterized by the absolute midstroke friction, the hysteresis width and slope individually for the compression-rebound and the rebound-compression turnaround, the overshoot peak height and shape, and the return-to-match behavior individually on compression and rebound.

5.3 Friction Point Floating Piston / Tube

The analysis of the floating piston / tube friction point differs slightly from the analysis of the rod guide assembly / rod and piston /tube friction points due to the different measurement approach and the effects from hydraulic transmission (see Chapter 4.3.2). The pre-conditioning and friction recording sequences are similar to the sequences defined in Chapter 4.2 except for the respective amplitudes, which had to be adjusted to the actually occurring displacements in the real damper. Due to the hydraulic transmission, the actual displacement amplitude of the floating piston during the reference damper friction test according to 4.3 is just $\hat{A}_{FP\,act} \approx 1.85\,mm$. To maintain comparability to the other friction points, two friction recording sequences are presented in this section, one with a comparable amplitude of $\hat{A}_{FP\,comp} = 10 \cdot \hat{A}_{FP\,act} = 18.5\,mm$ and one with an amplitude corresponding to the standard sequence, $\hat{A}_{FP\,act} = 1.85\,mm$. The pre-conditioning sequences were therefore adjusted to an amplitude of $\hat{A}_{FP\,pre} = 20\,mm$ for both measurement amplitudes. The resulting representative force-displacement graphs and force-speed graphs are depicted in 5.5 and 5.6.

The friction force $F_{mes\ comp}$ drawn in blue in these illustrations, is calculated from the recorded difference pressure data according to the equations (27) and (28) and subsequently shifted to an average zero force, as explained in Chapter 5.1. To illustrate the resulting friction contribution of the floating piston / tube friction point to the overall friction at unit level, the orange drawn unit level friction contribution $F_{UL\ comp}$ is included in the diagram, calculated following equation (29). To allow comparisons to the SFP1 results while taking into account that SFP2 is not reversing the actuation direction, the displacement, speed and force values are inverted. That is why rebound and compression tags stay at the same positions in the diagrams. Equally according to Chapter 5.1, all graphs show the second and third cycle of the friction recording sequence, thus proving reliability and reproducibility of the measurement sequence.

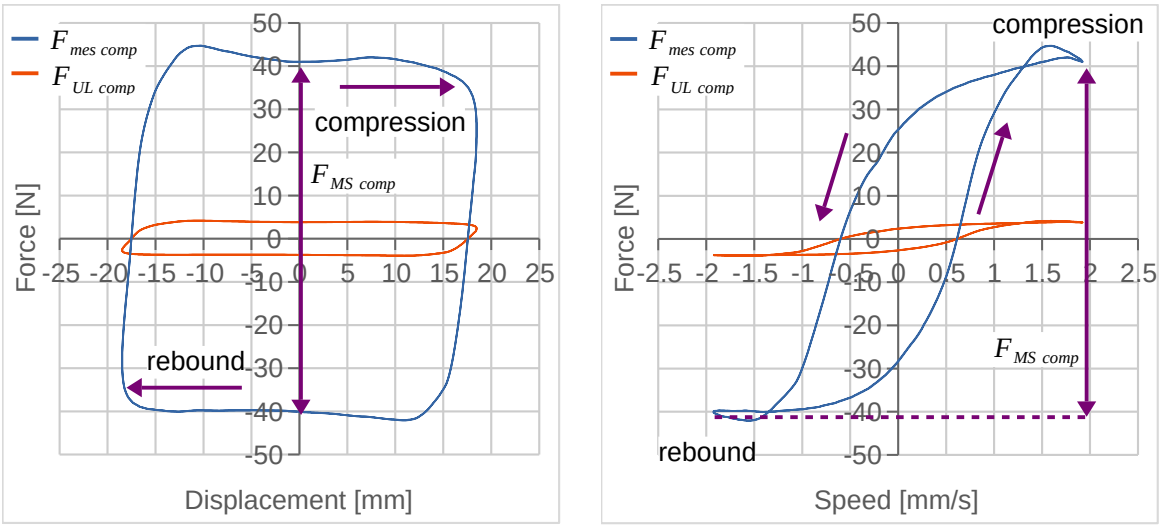

Illustration 5.5: Representative force-displacement graph and force-speed graph of the single friction point floating piston / tube with a displacement amplitude of $\hat{A}_{FP\,comp} = 18.5\,mm$, $F_{mes\ comp}$ *showing measured friction and* $F_{UL\ comp}$ *showing the unit level friction contribution*

The force-displacement graph in 5.5 shows a rounded parallelogram shape with almost constant friction plateaus at midstroke. Thus, midstroke friction can be easily determined following the definition given in Chapter 5.1 to $F_{MS\ comp} = 81.1\,N$, which results in $F_{MS\ UL\ comp} = 7.6\,N$ contributing unit level midstroke friction. Small friction force increases are visible towards both return points, resulting most likely from tube diameter changes. These probable diameter changes could be caused by the clamped braces for the application of the test rig pipes (see 4.7). Since this friction increase is very small and barely noticeable on the graph of the resulting unit level friction contribution, no further design modifications were investigated in that regard. The spindle-induced force oscillations mentioned in Chapter 5.1 and 5.2 do not appear in this measurement, because the test rig's indirect actuation and measurement principle prevents this phenomenon by design (see Chapter 4.3.2).

The force-displacement graph with the lower amplitude of $\hat{A}_{FP\,act} = 1.85\,mm$ depicted in 5.6 shows an even more distinct parallelogram shape than the measurement with $\hat{A}_{FP\,comp}$. This results in the absence of a constant force plateau at midstroke, reducing the usefulness of the midstroke position to measure friction. Given that a constant enough force plateau is reached later in both rebound and compression direction, the characterizing friction $F_{MS\ act}$ is defined as the difference of these two plateaus as depicted in 5.6 and measured to $F_{MS\ act} = 56.9\,N$, which results in $F_{MS\ UL\ act} = 5.3\,N$ contributing unit level midstroke friction. The speed data to create the force-speed graphs was gathered using the same method introduced in Chapter 5.1. The force-speed graph of the friction measurement done with an amplitude of $\hat{A}_{FP\,comp}$ in 5.5 shows a large pre-sliding hysteresis with comparatively smooth transitions from and to the more stable force levels at higher speeds. There, small crossings of the accelerating and decelerating parts of the graph indicate weak non-reversible friction characteristics as introduced in

Chapter 2.1.4, which however are barely recognizable on the graph of the resulting unit level friction contribution. The force-speed graph of the smaller amplitude of $\hat{A}_{FP\,act}$ in 5.6 forms an ellipsoidal shape, in which neither a force plateau nor any matching of acceleration and deceleration graphs is observed. This implies that the pre-sliding range introduced in Chapter 2.1.4 is not properly left and gross sliding is not reached during these measurements.

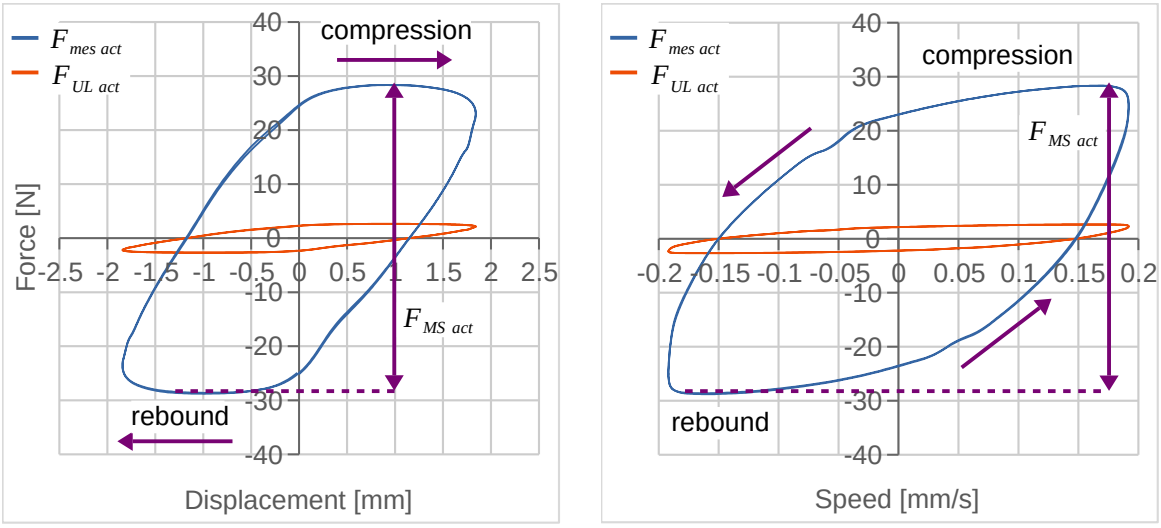

Illustration 5.6: Representative force-displacement graph and force-speed graph of the single friction point floating piston / tube with a displacement amplitude of $\hat{A}_{FP\,act} = 1.85\,mm$, $F_{mes\,act}$ *showing measured friction and* $F_{UL\,act}$ *showing the unit level friction contribution*

Even if this appears at first doubtful given this significant displacement range, certain movement of the O-ring in the floating piston's groove probably causes this behavior as well as the round shape of the force-speed hysteresis in 5.5. The presence of this kind of O-ring motion in the groove was investigated by observing this friction point with a microscope through a glass-made damper tube. An illustrative result is presented in 5.7, showing the O-ring in the floating piston's groove over the course of one friction measurement cycle. It becomes apparent that the O-ring is wandering between both flanks of the groove, depending on the movement direction. It should be noted that the amount of O-ring movement was variable between the investigated O-ring probes, which is probably caused by varying O-ring diameters due to manufacturing tolerances or varying O-ring surface qualities. As a consequence, there were instances where no significant O-ring movement at all was noticed for some measurements on this experimental setup. It should be noted that the friction behavior of the glass tube as the contact partner of the O-ring is obviously different from the steel tube normally used for the damper. Consequently, the transferability of the results of this experiment to real O-ring behavior is questionable and the floating piston's O-ring motion in a real damper remains uncertain. However, the experiments show that the general presence of such movements in the real damper tube is very likely.

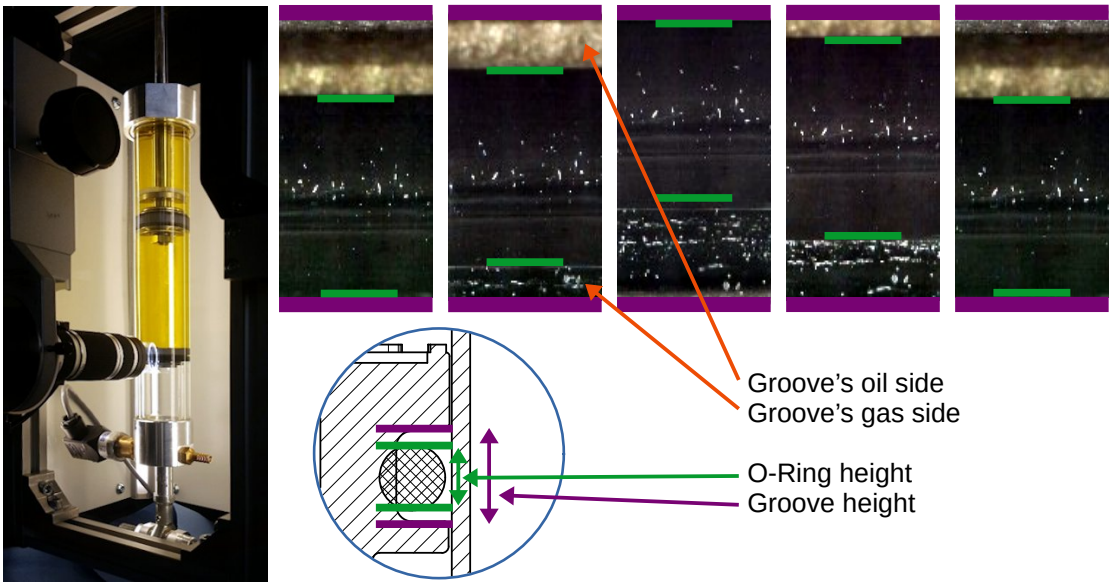

Illustration 5.7: Movement of the O-ring in the floating piston's groove during one friction recording cycle (compression – rebound from left to right), recorded by a camera microscope through a glass-made damper tube

In summary, the characterization of the floating piston / tube friction point based on force-displacement and force-speed graphs is more difficult than for the piston / tube friction point or the rod guide assembly / rod friction point, especially for small amplitudes, which are more likely to occur in real applications. This concerns both the finding of a representative friction value as well as the qualitative description of the graphs. While the first is solved by the use of the alternative midstroke friction definition mentioned above, the latter requires further investigations on the motion behavior of the floating piston's O-ring in its groove, as discussed in the following chapter.

5.4 Measurement Concept Validation

Even if the single friction point test rigs were designed to be comparable to the real reference damper, it has to be proven that their individual measurement results represent the friction behavior of the respective friction points in the damper on unit level. To achieve that, the friction of one set of friction related components, namely one rod guide assembly, one rod, one piston and one floating piston according to the friction points (A), (B) and (C) in 4.1 was measured in two ways. First, all the components were measured together in the take-apart reference damper. Second, all components were inserted into their single friction point test rigs and their individual component friction was measured individually. Afterwards, the friction graphs of the single friction points are super-positioned to evaluate the deviations compared to the unit level measurement. Consequently, only the tube as the last friction related part is not identical between the reference damper and the single friction point test rigs, which is hardly possible, since it has to be severely modified for each of the single friction point test rigs (see Chapter 4.3). The pre-conditioning sequence and the friction recording sequence were performed as

introduced in Chapter 4.2, with a measurement displacement amplitude of $\hat{A} = 1.85\,mm$ for the unit level measurement, the piston / tube measurement and the rod guide assembly / rod measurement, and the corresponding displacement amplitude off $\hat{A} = 1.85\,mm$ or the floating piston / tube measurement. The raw force records of the unit level measurement have to be pressure corrected, since the pressure in the air volume increases during compression due to the rod's volume compensation. Therefore, these gas spring's force displacement graph has been calculated and subsequently validated via still-standing rod push-out force measurements at various displacements. The pressure corrected force displacement progress was then shifted to an average zero force as introduced in Chapter 5.1. This progress was also inverted in displacement, speed and force to make it comparable to the single friction points measurements. All single friction point measurements were performed as described in the chapters above.

The results of all measurements and the superpositioned friction graph are shown in 5.8. This illustration shows that the yellow-colored superposition graph in general matches the blue-colored full reference damper graph quite well. For a more detailed analysis, this section examines the midstroke force F_{MS} and the characteristic points (A), (B), (C) and (D). Changing the movement direction from rebound to compression leads to the typical overshoot peak in point (A), the characteristic of which is weaker in the superposition graph than in the unit level measurement. The peak is caused by the rod guide assembly / rod friction point, then increased by the piston / tube friction graph, but decreased by the slow force response of the floating piston / tube graph to the movement direction change. Since the floating piston / tube graph then slowly approaches a constant state up to midstroke and the piston / tube graph remains constant, the midstroke friction force F_{MS} as the key comparison parameter is matching perfectly. Since all single friction point graphs except the floating piston graph show nearly constant force-displacement behavior around midstroke, this proves that midstroke force testing for the single friction point test rigs is robust and reliable, and the same for the reference damper setup. Additionally, the shape of the floating piston graph is as expected and as already introduced in 5.1. All graphs remain essentially constant towards (B), thus the perfect match of F_{MS} is continued. The following movement direction change from compression to rebound is once again followed by a slow force response of the floating piston / tube graph, causing slightly bigger deviations between the full damper graph and the superpositioned graph of the single friction points in (C). The repeated slow adaption of the floating piston / tube graph to a constant state towards midstroke leads to a matching midstroke friction force F_{MS}, which is continued towards (D) with only minor deviations.

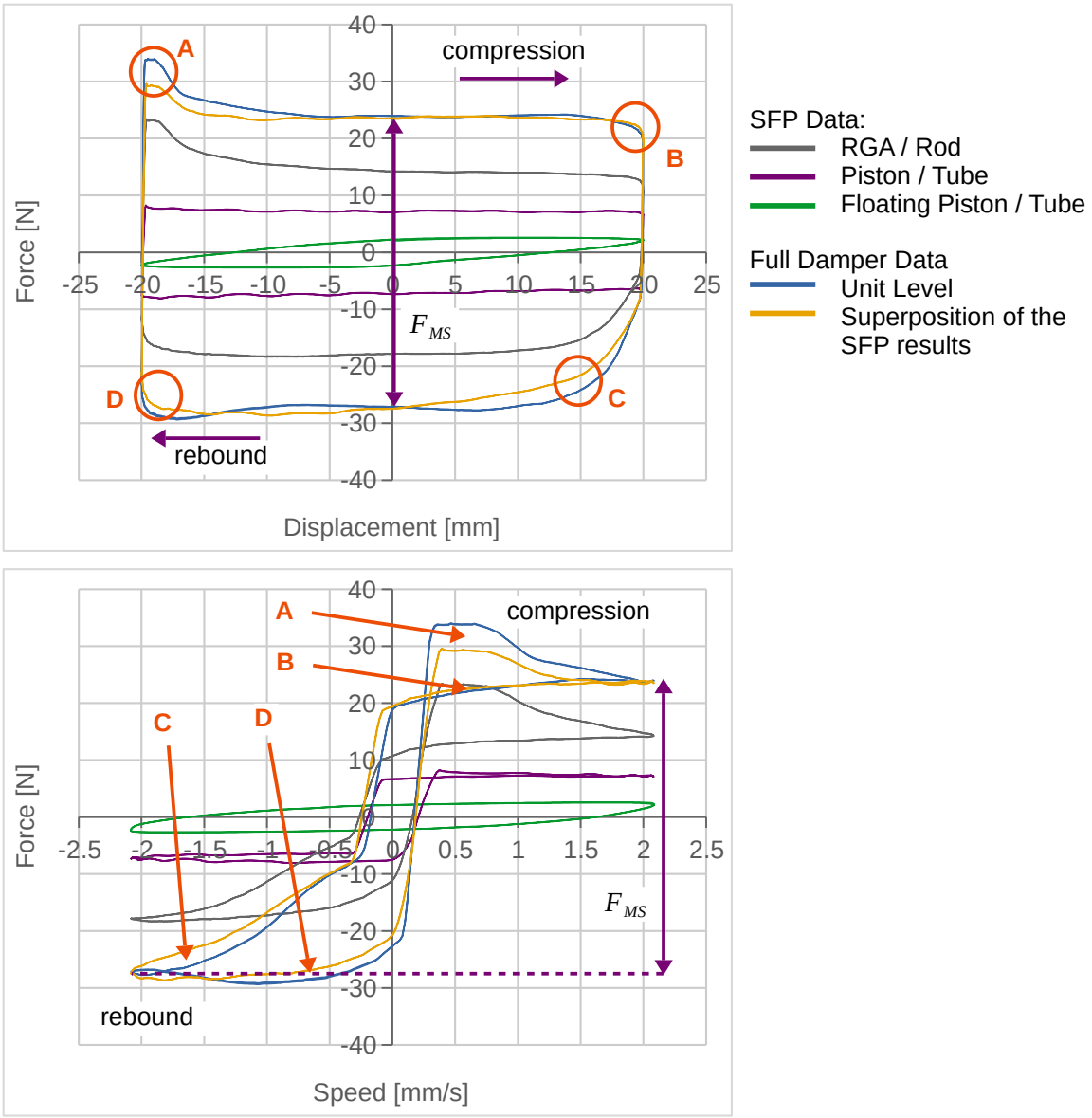

Illustration 5.8: Comparison of the take-apart full damper friction measurement and the superposition of the three SFP measurements rod RGA / Rod, Piston / Tube and Floating Piston / Tube

As a consequence it can be stated that all significant deviations between the super-positioned SFP graphs and the reference full damper graph are caused by the floating piston / tube friction graph. This can be further visualized by replacing this single friction point graph by a fictional idealized floating piston / tube friction graph as shown in 5.9. This floating piston / tube friction is assumed to show perfect Coulomb behavior with only a very steep ramp added at the turnaround points. The resulting super-positioned graph is almost perfectly coincident with the full reference damper graph, even in the above mentioned sections shortly after the turn-around points. The consequences of the non-hysteretic fictional floating piston / tube graph appear in the point (E) and (F) as sharp steps in the super-positioned graph.

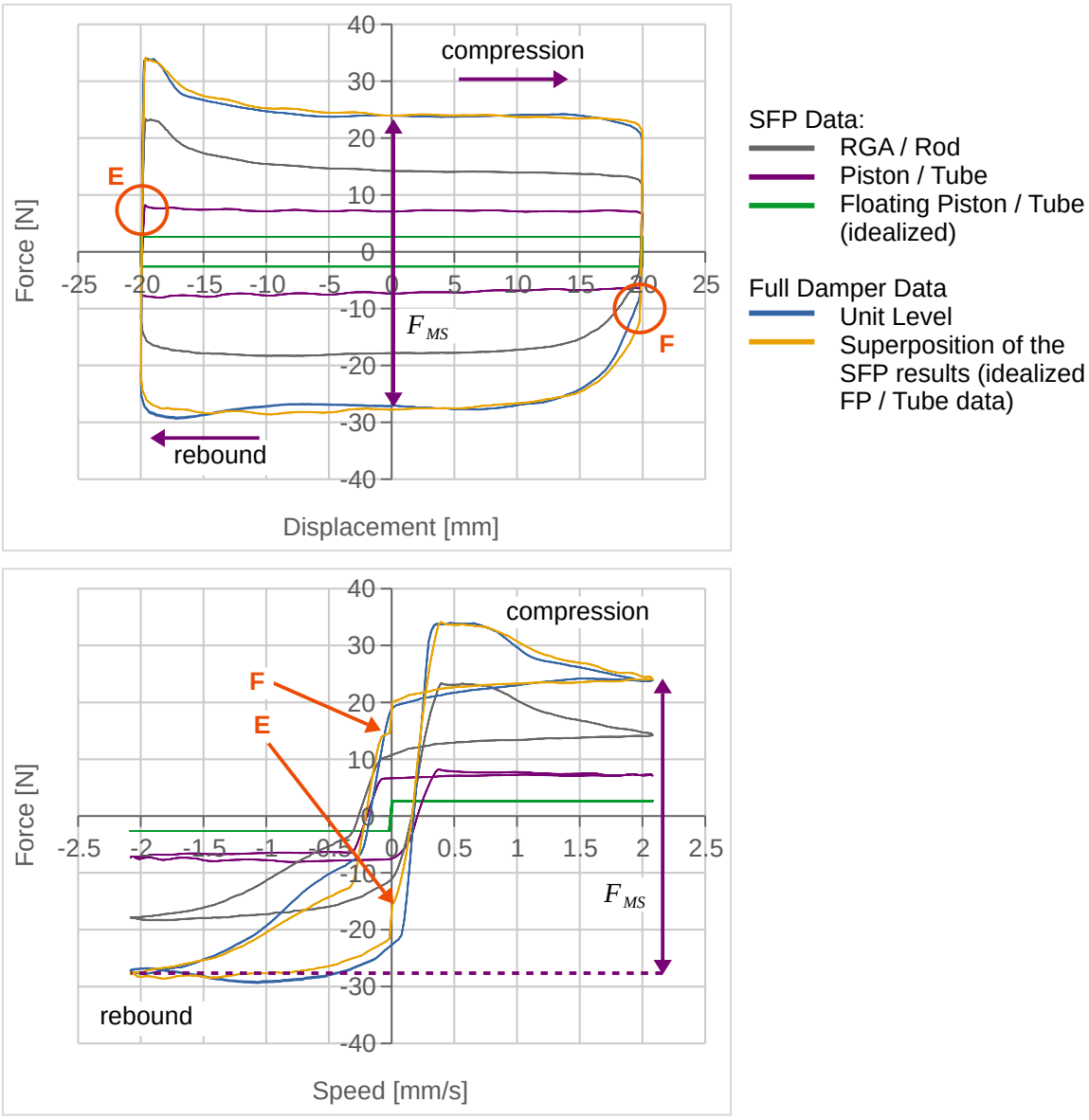

Illustration 5.9: Comparison of the take-apart full damper friction measurement and the superposition of the SFP measurements of RGA / rod and Piston / Tube, and a fictional idealized Floating Piston / Tube graph

The reasons to be found in the design of SFP2 which could distort the real friction behavior of the floating piston / tube contact to the curve presented in 5.8 are discussed below. To record friction as intended, the following two requirements must be met by the test rig's design (see Chapter 4.3.2). First, it has to be ensured that all oil flow and gas flow in the test setup is frictionless and free of any resistance. While this is obviously never the case in reality, [60] showed that the influence on the derived friction force progress should be negligible. The second assumption to ensure validity of the SFP2 setup is the incompressibility of the oil volume, which is necessary for the actuation precision of the floating piston probe and the correctness of the recorded pressure difference. If there is any significant compressibility in the system, this volume inconstancy will act as a delaying energy storage, which prevents the floating pis-

ton to directly follow the relative motion of the displacement piston ((7) in 4.6). This delay can obviously cause the lagged response of the recorded difference pressure signal to the displacement piston actuation. While the solid parts of SFP2 are considered to be stiff enough to prevent significant volume change under varying pressure, possible compressibility can occur in the oil volume. Even though the oil itself can be considered sufficiently incompressible similar to the solid parts, leftover gas bubbles from the filling procedure can cause a significantly compressible oil / gas volume. To solve this issue, the filling procedure is conceived so as to avoid leftover gas as far as possible. Furthermore, the pressurization to operating pressure and the subsequent transition of free gas into the oil should make all leftover gas bubbles disappear [64]. The disappearance of leftover gas bubbles was proven in a glass tube damper in the course of previous investigations, presented e.g. in [62]. As a consequence, leftover gas bubbles in the oil volume can with high probability be excluded as the reason to the recorded friction behavior of SFP2. Another change of the oil volume could be caused by the movement of the seal in the displacement piston while stroking. To minimize this movement, the original O-ring was replaced by an X-ring, as shown in 5.10. While the X-ring can not roll inside the displacement piston's groove because of its X-shape, its ability to move was further minimized by adjusting the displacement piston's groove to the smallest possible size.

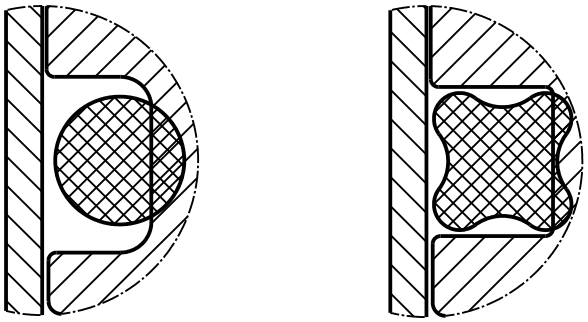

Illustration 5.10: Floating piston's groove and seal design changes to minimize the seal's mobility: O-ring and original groove (left) and X-ring and adjusted groove (right)

Both the application of the X-ring and the groove adjustment improved the accuracy of the SFP2 data to the presented status. However, the characteristic behavior of the floating piston / tube contact (discussed in Chapter 5.3) is still causing the deviations shown in 5.8, even if less pronounced than with the original O-ring in the displacement piston. Nevertheless, the idealized behavior as presented in 5.9, i.e. the total absence of pre-sliding hysteresis, other transient friction phenomena or O-ring rolling in the floating piston's groove, is not realistic either, and will never be fulfilled in practice. It is therefore assumed that the actual friction behavior of the floating piston / tube contact will show at least some of the delaying behavior shown in 5.8, which leaves the question to the causes of the remaining small deviations between the full damper friction curve and the superposition of all single friction point results open to further investigations.

In summary it can be stated that even though the indirect actuation and measurement principle of SFP2 probably causes the above mentioned uncertainties, this principle is indispensable to meet the requirements discussed in Chapter 4.3.2. Particularly the indirect actuation principle is necessary to remain comparability to the overall damper and it leads to the requirement of an indirect measurement principle. Thus, the test rig design's advantages clearly outweigh its uncertainties, especially if the concept-driven weaknesses are minimized as far as discussed. The remaining deviations of the superpositioned graph to the full damper friction graph shown in 5.8 are acceptable, given that most of the graph's sections, especially the mid stroke friction section, show extraordinary coincidence. Thus, all three single friction points can be measured and analyzed as intended with so far unmatched precision and similarity to the full damper behavior.

6 Material Analysis

6.1 Material Properties Introduction

The main research target of this dissertation, the development of a friction simulation model on unit level, is based on FEM analysis and overlaid friction modeling in the contact zone as introduced in Chapter 3. The FEM model is therefore responsible to determine the geometry of the friction points (body deflection and deformation, contact opening and closing, geometric shape of the contact zone) and to determine the contact pressure distribution in the contact zone as an input parameter to the friction models introduced in Chapter 2.2. In order to achieve this goal, appropriate modeling of the material behavior has to be incorporated into the FEM setup. In general, two types of material properties are relevant for this dissertation: The first is material data which is directly influencing the friction behavior, like solid surface properties (e.g. roughness parameters, free surface energy, asperity stiffness and solid material damping) and lubricant properties (e.g. viscosity and surface tension). While this first type only appears implicitly via the parameter set in the chosen friction modeling approach, its friction influencing behavior was investigated and quantified within the context of the overall research project. Nevertheless, since this dissertation specifically focuses on the general approach of a friction simulation through an FEM setup with overlaid dynamic friction model in the contact zone, the influence of directly influencing material parameters as described above is not further discussed here. The second type of material properties is material data which influences friction via the contact pressure or normal force distribution (e.g. stiffness, lateral contraction, creep, relaxation), and is therefore crucial for the FEM simulation.

Part	Material	Young's modulus [N/mm²]
O-ring	NBR70	≈6
static seal	NBR75	≈8
scraper	NBR82	≈16
oil seal	FKM88	≈26
piston band	PTFE	≈680
floating piston	PA6-GF30	≈6200
housing	aluminum	≈70000
piston	steel	>200000
rod	steel	>200000
tube	steel	>200000

Table 6.1: Materials relevant for the friction simulation

The damper's parts relevant to the friction simulation are presented in 6.1 with their material and its approximate stiffnesses. There it can be seen, that the single friction points depicted in 4.1 show typical material pairings of hydraulic seals, where the typical stiffness of the seal material (O-ring, static seal, oil seal, scraper, piston band) is two to four magnitudes lower than the typical stiffness of its respective counterpart (floating piston, housing, rod, tube, piston). The exact material composition of the seal materials is unknown due to proprietary company data of the seal suppliers. That is why the general material class plus their Shore-A hardness (to separate the rubber materials) is used as material description. Hence, NBR70 is a nitrile butadiene rubber with a Shore-A hardness of 70, FKM88 is a fluoroelastomer with a Shore-A hardness of 88, PTFE is a mineral filled polytetrafluoroethylene and PA6-GF30 is a glass-fiber filled polyamide.

The main deformation in the damper's parts can be expected to come from the compensation of the penetrations in the single friction points in 4.1. Because of the large stiffness difference of the respective seal / counterpart material, it can be assumed that no significant deformation will occur in the counterparts. Thus, they can be treated as infinitely stiff. That is why, the material characterization focuses only on the seal materials. Since these seals are all from non-metal elastomer (NBR and FKM) and plastomer materials (PTFE), highly nonlinear and time dependent stress strain behavior is expected [16] [65]. This can be described as a combination of inelastic, elasto-plastic and viscous behavior, as depicted in 6.1. To gather the material parameters in order to characterize these material behaviors describing time dependent stiffness, creep and relaxation, tensile tests and constant stress tests have to be performed. These are documented in the following section.

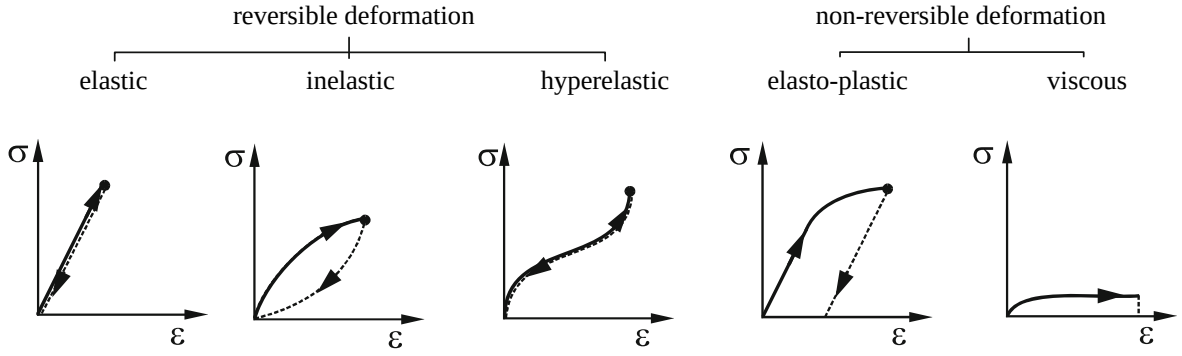

Illustration 6.1: Compilation of reversible and non-reversible deformation processes; modified from [16]

6.2 Material Properties Measurement Method

The test rig used for all of the following material characterization measurements is the same as for all friction measurements, namely a tensile tester of the type Galdabini Quasar 5 together with the $500\,N$ load cell AEP TS-TM 500 as introduced in Chapter 4.2. The strain is recorded during the material tests with a high-precision extensometer type MICRON. Given

that the static seal, the scraper and the oil seal are very small injection-molded parts, additional material probes had to be requested from the seal supplier to allow for appropriate material testing. The material samples provided by the supplier are thin slabs, which do not allow a standardized probe shape for tensile and compression tests (e.g. according to [66]). Therefore individual probe shapes are defined, which are not solid enough for compression tests because of the slab size. This is why only tensile tests are performed, and it is assumed that the material response is similar for tension and compression. This assumption is valid for loads far away from breaking load [65], which is the case here and is shown in the next section. The PTFE probe is made from extruded pre-product for the piston band and is cylinder-shaped. To ensure comparability and efficient testing, only tensile tests were performed for the PTFE probes, too. The material characterization of the O-ring rubber is done on the O-ring itself. Comparative measurements proved that no difference in material behavior is noticeable between a full and a sliced-open O-ring, but the full O-ring probe handling is much easier. Because of the small diameter it is only possible to perform tensile tests here as well.

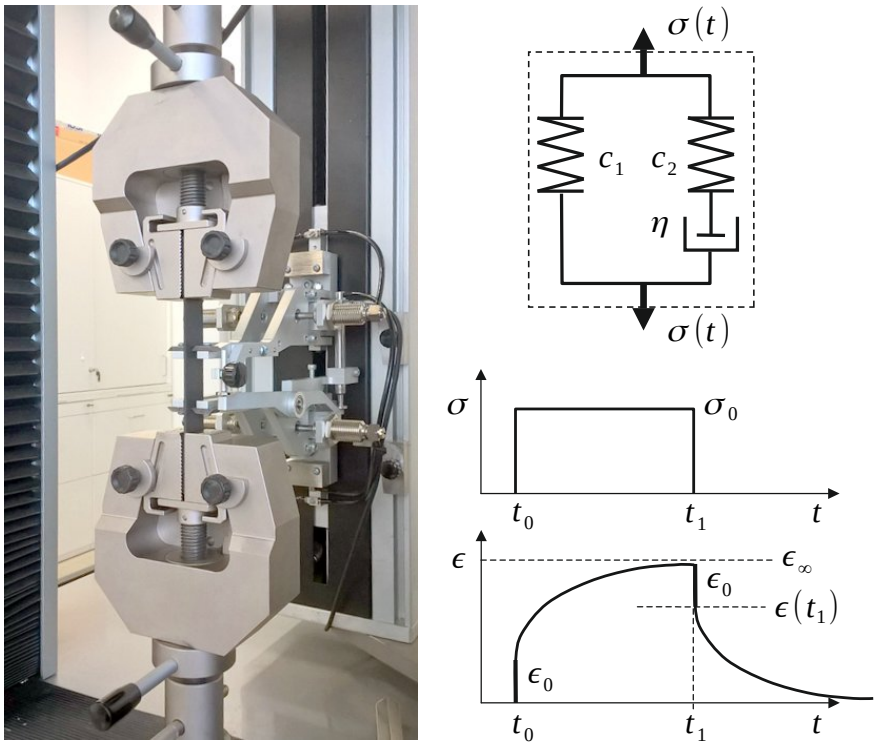

Illustration 6.2: Left panel: Rubber slab constant stress test setup – Right panel: Viscoelastic material model from Poynting-Thomson under constant stress; modified from [65]

The basic measurement method and experimental setup was developed in [67], which also contains most of the performed characterization measurements. First, general tensile tests were performed to determine the respective break load and a rough estimation of the Young's Modulus. Based on that, initial static FEM simulations of the single friction points were performed to estimate what magnitude of equivalent stress could be expected in the seals. This

stress is a result of the seal geometry due to the deformation of the initially penetrated counter parts (see Illustration 4.1). The outcomes show a resulting equivalent stress in the seal that is always below 30 % of the breaking load. Thus, the above-mentioned assumptions regarding the non-necessity of compression tests are valid. Subsequently, various constant-stress tests were performed with stress levels that are in the range of the expected equivalent stress level from the above mentioned FEM pre-investigations. The test setup of a representative slab probe, the qualitative applied stress-time progress and the expected material response due to an idealized Poynting-Thomson model of viscoelastic material behavior are depicted in 6.2. The duration of the loading sequence (t_0 to t_1 in 6.2) and the duration of the following idle sequence are dependent on the actual material behavior and can vary significantly ($0.1 ... 1000\,h$; [65]). Loading and idle time was here set to the following compromise of accuracy versus measurement time: Since the main deformations in the damper's seals happen during its mounting process and no even level of back deformation is carried out, the loading time is much more relevant for the material characterization than the idle time. First measurements showed, that more than 90 % of the viscoelastic deformation and back deformation are usually finished after $30\,min$. To gain a higher accuracy for the loading cycle, its duration is doubled to $60\,min$. Since the tensile tester requires some time to reach the desired load as well as to go back to zero load to follow the back-forming, some load ramping time has to be included. The final sequence is therefore unique for each material, since different loads have to be reached. In the experimental setup a recording of at least $60\,min$ of loading time and $30\,min$ of idle time is ensured.

6.3 Material Characterization

The experimental data to characterize the seal materials is presented in 6.3. There, the strain of the piston band material PTFE is shown on the right axis due to its much smaller strain level compared to the rubber parts. This lower strain level as well as the different absolute strains of the rubber materials result from the different strain states predicted before in the FEM pre-investigations mentioned above. Since the static seal experiences the largest deformations due to mounting and static pressure, its material NBR75 is examined at the highest strain. The low PTFE strain is a result of its comparatively low mounting deformation and its comparatively high stiffness (see 6.1). While loading (t_0 to t_1), it becomes visible that all materials follow the qualitative curve expected in 6.2. After t_1, a varying time is required by the tensile tester to reach the zero load state for the characterization of the back deformation curve. That is why the transition from the falling straight line to the saturating back deformation curve occurs at different time points for the respective seal materials. This back deformation curve remains (differently high) above zero strain. After reaching a stable leftover deformation, this distance to zero strain shows the amount of plastic deformation experienced by the material [65]. Hence, the seal material behavior is proven to be mainly viscoelastic with a varying viscoplastic contribution. While the rubber materials almost reached a steady strain state, the PTFE probe is still creeping significantly for both loading and idle time. However, this has to be considered in the context of the much smaller absolute values. It is proven in

Chapter 7.2.2 that the integrated setup – namely probe selection, investigated strain states and test duration – is suitable for appropriate material modeling for the simulations performed within this dissertation.

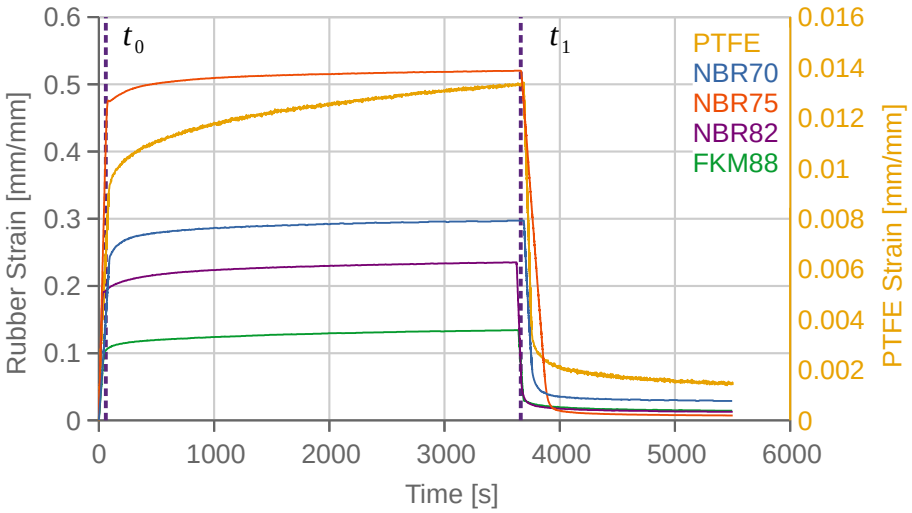

Illustration 6.3: Constant stress test results of the seal materials; t_0 and t_1 corresponding to 6.2

7 Simulative Investigations

7.1 Overall Simulation Approach

Simulating friction is generally not a well-defined task. It requires a variety of decisions, concretizations and delimitations regarding the accuracy of results, parameterization and validation effort, and simulation time. Considering that the outcome of this research is intended to be easily transferable to daily use in an engineering department of a company, the latter two points of this list should be as low as possible, whereas the first – the accuracy of results – has to be as high as required. Practically all friction modeling decisions are based on the best possible compromise of these simple premises. The main objective of this chapter is to present these decisions based on general requirements, which finally describe the overall simulation approach.

Given that friction is highly dependent on the geometry and material properties of the contact surfaces it is necessary to take both of these aspects into account. To facilitate the exchange or modification of the geometry of the friction-related parts the setup should be based on a CAD file. Since body-body interaction between the friction-related and also between the non-friction-related parts are defining the contact generation, contact release and contact deformation, it makes sense to model this behavior in three dimensions. Well-proven FEM software, which usually brings a GUI with it, meets this requirement, and also answers the need for an easy-to-use interface in daily engineering work. While end-user FEM software is usually only capable of treating the solid body part of the friction contact, fluid film formation and behavior in the contact zone is crucial for the description of lubricated friction contacts. To consider this in the overall simulation approach, an additional method must be implemented and coupled to the FEM simulation, since both interact with each other. Possible solutions for this problem start at simply adding a static friction model to the contact zone, continue with dynamic friction models or very simplified fluid calculations (e.g. EHL) and end with fully transient three dimensional CFD, which in combination with the FEM part leads to an FSI problem, which is computationally exceptionally expensive (see Chapter 2.2).

As introduced in Chapter 3, one aim of this research is to understand and identify the friction-relevant parameters in automotive shock absorbers, which implies taking these identified parameters in the friction model setup physically into account. That is not entirely possible with static and dynamic friction models, because they are not fully based on physical parameters, but on heuristically determined mathematical functions. That is why first simulation attempts in this research led to FSI and EHL implementations, which do not suffer from this limitation. However, it became swiftly apparent that both FSI and EHL were not feasible. Namely, the FSI implementation led to an unacceptable compromise of geometry and boundary conditions simplifications versus computational effort (calculation time as well as storage needs). The EHL implementation was designed so as to solve its fluid equations by the internal solver of the FEM software with the aim of keeping the coupling effort as low as possible. However, this attempt failed due to an incomplete documentation of the FE solver’s behavior and treat-

ment of user-defined finite elements. Especially the transfer of the equation system of the fluid-related part in the contact zone to the solver could not be achieved [68]. A first alternative, namely the coupling of an additional external solver to these calculations, would demand significantly more development effort than possible within this research. A commercial example for this approach is the software Tribo-X from Tribo Technologies GmbH [69], which is highly specialized on bearings and gear drives and thus not usable for the lubricated metal versus elastomer and plastomer material contacts in this research. Writing the overall solver code from scratch, as a second alternative, brings with it a lot of disadvantages (e.g. 2D simplifications, complicated setup and user interface, material model assumptions etc., see Chapter 2.2.3), in addition to unacceptable time investment. Finally, EHL does not fit the problem description because of its main application in the elasto-hydrodynamic friction regime. Since actuation speed is very low in damper friction measurements and the turn-around points are of special interest, the relative speed in the contact zone is often near to zero. Thus, the mandatorily applied solid and mixed dynamic friction model to the EHL approach would be most significant during most parts of the simulation. That is why, a dynamic friction model was chosen as the best possible modeling approach. Summarizing, only with the exclusive implementation of a dynamic friction model to the FEM software it is possible:

- To achieve sufficiently low requirements for compute power and storage, and a sufficiently low setup effort to achieve usability in every-day engineering.
- To consider three-dimensional influences, e.g. consideration of tangential seal stress, lateral forces or production non-uniformities.
- To consider all friction states in one friction model.
- To consider friction-induced seal deformation with full coupling to the deformation induced contact pressure and contact area changes.

Consequently, this simulation approach of 3D structural FEM plus overlaid dynamic friction model in the FEM contact zone is chosen for the following investigations on damper friction. 7.1 shows a basic depiction of that approach according to the single bristle approach from 2.11. In 7.1, the friction model is only applied as soon as the respective purple finite element contact is detected. With subsequent superposition of the friction force contribution of each purple contact element, it is possible to take all the above-mentioned points into account. The choice of the 3D FEM software was made based on availability and features. Namely, for the following analysis the simulation software suite Ansys Workbench was selected. It features the most important requirements of the introduced simulation approach, namely a highly customizable FE solver and the possibility to apply self-written code to the solution process, which is crucial for the implementation of a dynamic friction model. The Ansys Workbench also contains convenient pre- and post-processing tools and an efficient graphical user interface, and is therefore widely used in commercial and academic environments. Consequently, the Ansys Workbench meets all requirements of the chosen simulation approach and is used as the basis for the friction simulations performed in the context of this dissertation, corresponding to its documentation [56] [57].

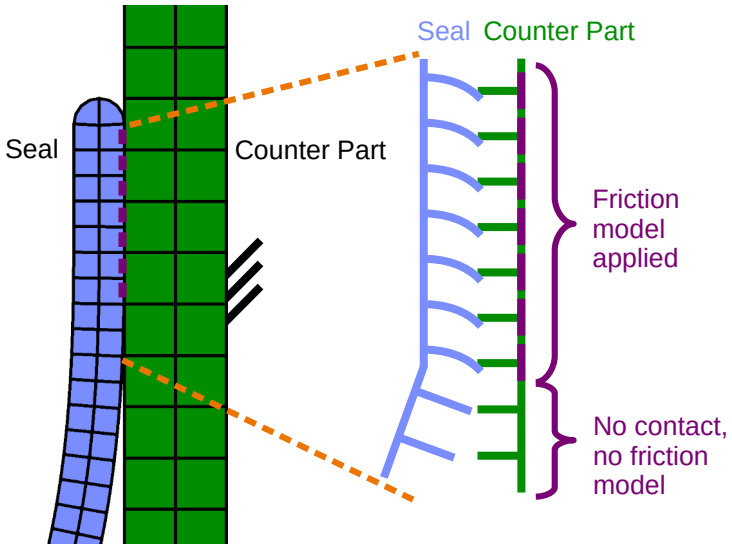

Illustration 7.1: Basic friction model application principle to the FEM model according to the single bristle approach from 2.11

Next, an appropriate dynamic friction model has to be chosen. According to Chapter 2.2.2, the LuGre model, the EP model and the Leuven / GMS model come into consideration. Among these, the LuGre model presents the easiest handling and lowest parameterization requirements, whereas the EP and Leuven / GMS approaches have the capability to model more friction effects, and provide thus more realistic behavior under certain circumstances. However, the distinguishing capabilities of the EP and Leuven / GMS models versus the LuGre model are not relevant among the boundary conditions of this dissertation. Since the simulation's main target is to resemble the friction testing conditions [4], some limitations can be presumed, for example a limit to the necessity to model proper non-drifting behavior or non-local memory. As Chapter 4.2 shows, the friction behavior of the damper is always a force response to a displacement actuation. Since this implies an always known and defined displacement, drifting behavior as a consequence of fluctuating force actuation never occurs. Since the EP model's main enhancement over the LuGre model is the prevention of the mentioned drifting behavior, its application is likely unprofitable due to its higher implementation and parameterization effort. The lack of appropriate non-local memory modeling within the LuGre model is also uncritical, since the intended actuation procedures according to Chapter 4.2 do not contain sequences where the displacement direction is changed within the pre-sliding hysteresis without passing the zero-displacement (and thus also without passing the zero elastic bristle deflection state, too). Instead, the displacement is always reset to zero after each direction change. The additional advantage of more realistic modeling of the pre-sliding regime of the GMS model as well as of the Leuven model with the Maxwell slip approach is also not needed in the above introduced approach: The better resolution of the pre-sliding regime in GMS and Leuven model comes from the modeling of multiple bristles via Maxwell elements, what is also obtained within the approach of this dissertation. As 7.1 shows, this is implemented by repeatedly calling the LuGre model in multiple FEM contact elements, taking into

account changing contact geometry due to body deformations, material properties, displacement actuation or tangential stress due to the friction model itself.

The above-mentioned material modeling has to be suitable to appropriately transfer the real material's behavior characterized in Chapter 6.3 to the FEM setup. Therefore, the element's stiffness, its transverse deformation behavior and its density have to be defined as well as the material's time-dependent stress decrease due to viscoelastic and viscoplastic behavior.

7.2 FEM Pre-Process

The FEM pre-process contains all steps and measures to be taken to prepare the simulation setup properly. It therefore represents the transfer from reality to the mathematical model, which is subsequently solved by the FEM software. The pre-process for the simulations investigated within this dissertation consists of the geometry abstraction, the modeling of material behavior, contact behavior and friction behavior, the spatial and temporal discretization of the calculation domain as well as the definition of initial and boundary conditions, all of which are documented in the following section.

7.2.1 Geometry Abstraction

To investigate the influence of different geometries and geometry changes on the friction behavior, the geometry has to be transferred from the real damper part to an abstraction for the simulation model. The level of detail as well as the overall size of this abstracted geometry strongly impacts the computational requirements, which always requires a compromise balancing realistic behavior description and calculation effort. To keep the transfer process affordable, the easiest approach for the application engineer is to directly load the existing CAD geometry into the FEM software without further intervention. However, especially in seal design, the actual part shape often deviates quite significantly from the underlying CAD geometry. As an example, the CAD geometry of the piston band is shown in comparison to two cross cuts from real piston bands in 7.2. It is shown that the CAD geometry is heavily simplified in comparison to the real geometry. Where the CAD geometry shows sharp edges on almost all transitions, the real geometry is much rounder with differently sized radii instead of the sharp CAD edges. Another obvious difference between CAD data and real geometry is the material distribution of the piston band. While the left real piston band example in 7.2 shows incomplete filling of the piston's grooves and a thin end lip, the right real piston band shows complete filling of the piston's grooves and a bulky end lip. In comparison, the corresponding groove filling of the CAD geometry represents more or less an intermediate compromise, while its end lip is even thinner than the end lip of the left real geometry example. It should also be noted that these cross cuts only show one cross-cutting position and that the geometry is very likely to deviate around the perimeter. Similar observations were performed on the other seals, namely on the scraper, oil seal, static seal and on the floating piston's O-ring (see 4.1). As a summary it can be stated that differences between the real geometry and the CAD geometry as well as geometry differences from manufacturing tolerances bring uncertainties to the model, which can not be completely eliminated. Even if this dissertation's simulation

approach is capable to investigate the influence of those geometry uncertainties on the friction behavior, they are usually not controllable by the responsible CAE engineer. That is why, and for the definition of a reference case, the CAD cross cut geometry is here transferred to the simulation setup almost unmodified. The only changes applied are the addition of small radii where the CAD geometry shows sharp edges, and the elimination of the infused spring of the scraper. The sizes of the radii were chosen based on microscopic measurements performed on the 3D laser scanning microscope Keyence VK-X 150 of the automotive engineering group.

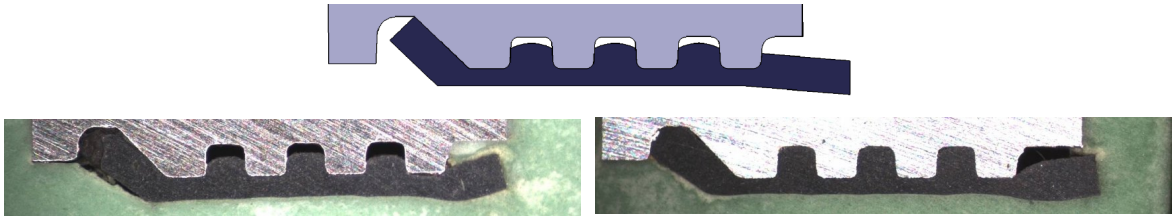

Illustration 7.2: Comparison of CAD geometry of the piston band (center top) and cross cuts of two examples of corresponding real parts (left bottom and right bottom)

Another point to mention when abstracting the geometry for the FEM setup is to decide which features are considered necessary to be modeled within the simulation. Since finite element setups for the application of an EHL friction model should be as simple as possible, and tangential flow is neglected as usual (see Chapter 2.2.3), two-dimensional geometry, i.e. the seal's and counter part's cross section is commonly assumed to be sufficient and is therefore chosen. Thus, a perfectly rotational symmetric geometry would be assumed for an EHL setup and further transferred to a linear periodic geometry. This approach lacks the possibility to model three-dimensional effects like tangential seal tension, lateral forces or production-induced non-uniformities. The next and slightly more complex possibility to reduce the geometry complexity is to use rotational symmetric boundary conditions, what basically means to set up only one wedge of the whole perimeter of the geometry. This approach assumes perfect rotational symmetry, similar to the two-dimensional approach. As a consequence, the rotational symmetric wedge approach enables the FEM setup to model tangential seal stresses, but makes the approach unable to model effects which would violate rotational symmetry, such as the influence of lateral forces or manufacturing deviations. If the modeling of the latter effects is required, an at least area-symmetrical geometry has to be chosen, which basically means virtually cutting the damper vertically into two halves.

The necessity of modeling at least tangential seal tensions for friction simulations becomes evident through the comparison of two model approaches of the floating piston / tube contact as depicted in 7.3. There, on the left side, the model is set up from a $4°$ wedge of the original CAD geometry (similar to the setup presented in the right panel of 7.4), while the right side model is set up as a 2.5 D model of the original CAD geometry, where 2.5 D means a flat FEM setup with a mesh consisting of only one element layer. Both sides of 7.3 show a steady state which fulfills the contacts modeled according to Chapter 7.2.3 and which shows the equivalent stress distribution after $30\,min$ still-standing time for appropriate O-ring material

relaxation (see Chapter 7.2.2). The illustration demonstrates that the stress distribution of the 2.5 D setup is axisymmetric according to the vertical center line of the O-ring, while the stress distribution of the 4 ° wedge setup is visibly asymmetric. This asymmetry is caused by the general widening of the O-ring's diameter due to it's initial shape, which is depicted in 4.1 (C). In this Illustration, the O-ring penetrates the floating piston, but not the tube, which causes the mentioned diameter widening while fulfilling the contact definition. This is not considered in the 2.5 D setup, where the O-ring slice has no relation or connection to its perimeter. The consequence of the general widening are tangential seal tensions, which cause a much higher overall equivalent stress level in the 4 ° wedge setup with a much smaller stress maximum, as compared to the 2.5 D setup. Since the general widening of the O-ring also occurs in reality during the mounting process, the 4 ° wedge results are considered much more realistic than the 2.5 D results.

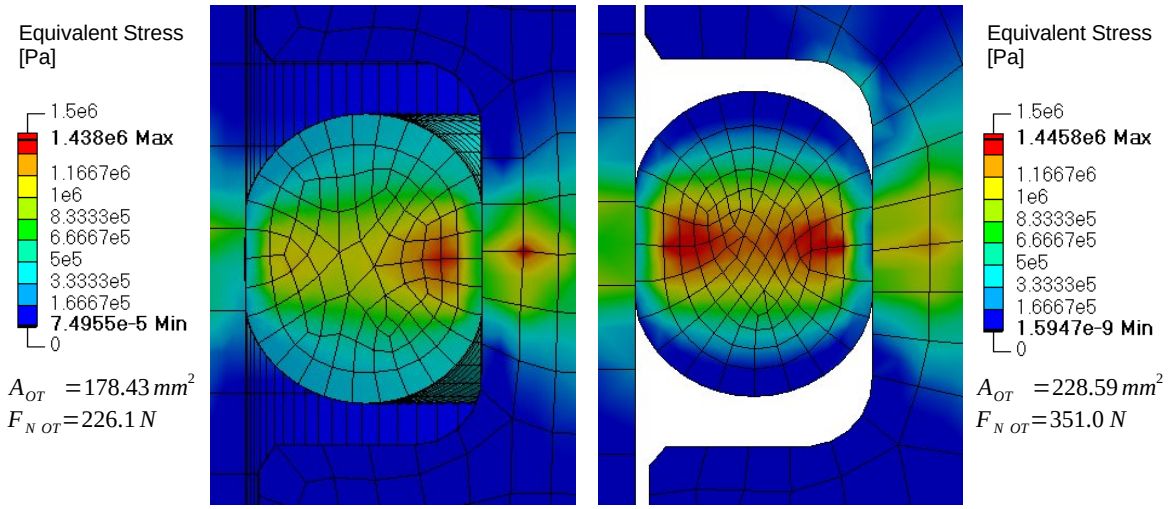

Illustration 7.3: Comparison of the equivalent stress distribution in a rotational symmetric FEM setup (left) and a flat 2.5 D FEM setup (right) with the resulting contact area A_{OT} and circumferential O-ring / tube contact normal force $F_{N\,OT}$

Even if the internal stress distribution is not directly affecting the friction behavior in the contact zone, it affects the contact area and contact normal force that are created between the O-ring and its counterparts. The related FEM calculation results of the contact area A_{OT} and the circumferential contact normal force $F_{N\,OT}$ are also shown in 7.3, where A_{OT} and $F_{N\,OT}$ are projected to the full perimeter of each setup. The resulting contact area between O-ring and tube A_{OT} of the 2.5 D setup is 28.1 % too large compared to the 4 ° wedge setup, which is caused by the lower lateral forces due to the above mentioned general diameter widening. In this too large contact area, an also significantly too large contact normal force is reached (+55.2 % compared to the 4 ° wedge setup). The friction force is calculated within this dissertation from the tangential shear stress derived from a friction coefficient dependent on several parameters, contact pressure and contact surface according to equation (31) (see Chapter

7.2.4). As a consequence, the friction force of the 2.5 D setup would be significantly overestimated.

$$F_{fric} = \tau_{fric} \cdot A_{OT} = \mu(\cdot) \cdot p_{OT} \cdot A_{OT} = \mu(\cdot) \cdot F_N \tag{31}$$

Whereas the modeling of tangential seal stresses is – as already discussed – always required to determine the contact pressure with sufficient accuracy, the modeling of non-rotational symmetric effects is possible with full-perimeter approaches. To achieve a commonly usable reference friction simulation model at unit level with the lowest possible computational requirements for fast application and solving, the rotational symmetric wedge approach has been chosen for this dissertation. This wedge approach provides sufficiently low computational effort, but considers three-dimensional effects to the desired extent. Additionally, the enhancement of the rotational symmetric approach to an area-symmetric half-model is very simple and straightforward and was successfully implemented in a follow-up project seeking to investigate the influence of external lateral forces to the friction behavior.

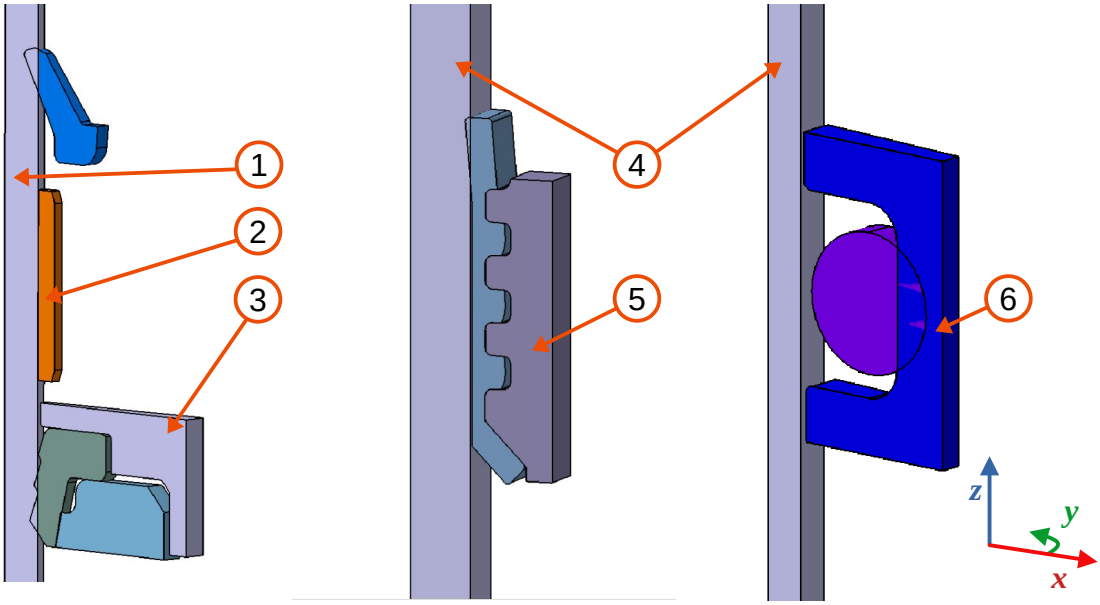

Illustration 7.4: Geometry abstraction for the FEM simulation; left: 4° wedge of the rod guide assembly / rod friction point; center: 4° wedge of the piston / tube friction point; right: 4° wedge of the floating piston / tube friction point

The final geometry abstraction is depicted for each friction point in 7.4. As shown in this illustration, additional simplifications are applied to all parts of the depicted single friction points that are no seals, namely the rod (1), the bearing (2), the housing (3) of the rod guide assembly, the tube (4), the piston (5), and the floating piston (6) (see 4.1. for comparison). Since the stiffnesses of the rod and of the housing are several magnitudes higher than the stiffnesses of the seals (see 6.1), no significant deformation of either of them is expected. Thus, to minimize the FEM setup geometry as far as possible, the rod is assumed to be hollow and the

housing is reduced to the state where only the contact geometry to the oil seal and to the static seal is preserved from the real geometry. Since the scraper is in reality not able to move relatively to the housing and the housing does not move relatively to the ground, the respective contact faces of the scraper to the housing are treated as fixed to the ground later in the setup process. This boundary condition brings the possibility to reduce the housing geometry (3) to the state shown in 7.4 (left). The bearing (2) is never in contact with the rod in this wedge approach since lateral forces, which would cause a violation of the perfect rotational symmetry condition, are not applicable here. The bearing is nevertheless included into the FEM model as a preparation for upcoming investigations. The assumption of significant deformation is also valid for the piston. Furthermore, since no oil volume is directly modeled in this setup, all oil flow-related geometry (valve package, bores, etc.) can be neglected. As 7.4 (center) shows, the piston is simplified to a hollow ring (5) only keeping the realistic geometry that is in contact to the piston band. Given that the shape of the floating piston is – except of its groove shape – also not influencing the friction in the floating piston / tube friction point, only the floating piston's groove dimensions are preserved for the simulation, resulting in the geometry (6) shown in 7.4 (right).

7.2.2 Material Modeling

As explained in Chapter 6, all counter parts of the seals, namely the rod, the housing, the piston, the floating piston and the tube could be modeled infinitely stiff since no significant deformations are expected for them. Given that FEM simulations with penetration-based contact detection converge better if some stiffness is set, in this dissertation all of these parts are treated as a high-stiffness structural steel with a Young's modulus of $E_{Steel} = 2 \cdot 10^5 \, MPa$, the standard material in Ansys Workbench. The material's density, which is equally required by the FEM solver, is also kept on the standard structural steel model value of $\rho_{Steel} = 7850 \, kg/m^3$. The densities of the seal materials are determined by the use of a hydrostatic scale and are listed in the following 7.1:

Material	**NBR70**	**NBR75**	**NBR82**	**FKM88**	**PTFE**
Density [kg/m³]	1214	1275	1448	2010	2300

Table 7.1: Density of the seal materials measured with a hydrostatic scale

Since the seals show significant time-dependent stress-strain behavior, this behavior has to be covered within the seal's material models. To maintain ease of use, a modeling approach should be used, the parameterization of which is already prepared in the simulation software. In [70] three of those modeling approaches considered to be suitable have been investigated: the Prony Shear Relaxation model, the Modified Time Hardening (MTH) model and the Bergström-Boyce model [57]. While the Prony model is only capable to model linear viscoelastic behavior, the MTH model and the Bergström-Boyce model can model both viscoelastic and viscoplastic behavior, even for nonlinear material behavior. Simultaneously,

compared to the relatively simple Prony model, the required amount of stress states to be recorded in experiments and the subsequent parameterization effort based on these experiments is significantly higher for the MTH model and even more for the Bergström-Boyce model. As shown later in this section, the Prony model is sufficiently equipped to appropriately describe the seal's material behavior as introduced in Chapter 6.3. Therefore a deeper introduction of the MTH model and the Bergström-Boyce model is not necessary here, but can be found in [70].

The Prony Shear Relaxation model adds linear viscoelastic behavior to a base elastic material model. The base elastic material models in this dissertation are determined by the material's initial shear modulus G_0 and density ρ, where the initial shear modulus G_0 is composed of the initial Young's modulus E_0 and the Poisson's ratio ν as follows

$$G_0 = \frac{E_0}{2 \cdot (1+\nu)} \tag{32}$$

where a Poisson's ration of $\nu = 0.5$ describes an ideally incompressible material. For elastomers and plastomers under a load far from their breaking load as they appear in this dissertation, almost incompressible behavior can be assumed, which leads to the determination of constantly $\nu = 0.49$ for all seal materials [65] [70].

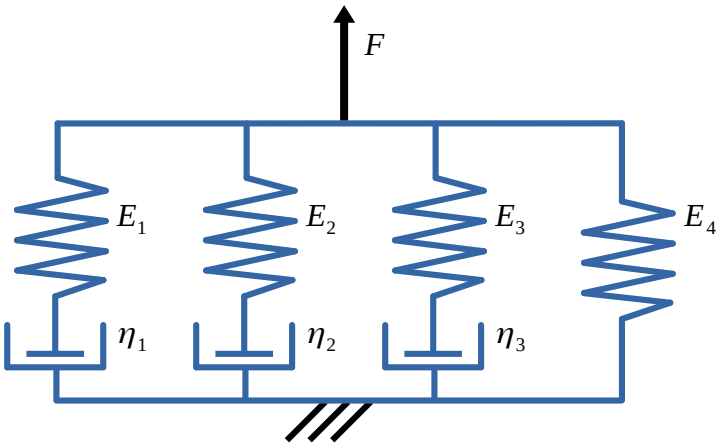

Illustration 7.5: Prony Shear Relaxation material modeling approach with three Prony terms; modified from [57]

The viscoelastic behavior is subsequently modeled with a Prony series as a time-dependent decreasing shear modulus with the following form:

$$G(t) = G_0 \cdot \left(\frac{G_\infty}{G_0} + \sum_{i=1}^{k_G} \alpha_i^G \cdot e^{-\frac{t}{\tau_i^G}} \right) \tag{33}$$

where t is the time, $G(t)$ is the time dependent shear modulus, and G_0 and G_∞ are the initial shear modulus at $t=0$ and the equilibrium shear modulus at $t=\infty$. Following the assumption of a constant Poisson's ratio and equation (32) as mentioned above, the shear modulus is only dependent on the Young's modulus. Thus, the Prony model can be understood as a time dependent Young's modulus, modeled as a parallel combination of in-line springs and dampers as depicted in 7.5. In this illustration, the number of spring damper groups represents the number of Prony terms, namely k_G in equation (33). The qualitative shape of the relaxation curve is determined by the relative moduli α_i^G and the relaxation time τ_i^G. [57]

By importing the constant stress records from Chapter 6, the internal curve fitting tool of the Ansys Workbench material modeling section is able to determine the parameters α_i^G and τ_i^G for the previously defined number of Prony terms. It turns out, that the best matching results are achieved with three Prony terms for all seal materials except for the piston band, which can be best approximated with two Prony terms. Since the Prony model describes only the qualitative relaxation behavior, the absolute strain response to a stress application is determined by the initial Young's modulus. Because of the nonlinear behavior, the respective initial Young's modulus of the seals can not be calculated from the slope of the linear stress strain curve, as is valid for most metals. That is why, the Young's modulus for plastics is commonly determined as the slope of the tangent or secant at the beginning of the stress strain curve, e.g. between $t=0$ and $t=t_0$ in 6.3. However, the definition of this time span as well as the definition of the tensile test's displacement speed is not consistent, and is indeed commonly unique for each type of material [65] [71]. As a consequence, a roughly estimated Young's modulus is taken here, which is subsequently fine-tuned in FEM simulations. Those simulations are set up to replicate the previously performed constant stress tests one-to-one in probe geometry and boundary conditions, as described in Chapter 6.2.

A comparison of the material models with curve-fitted Prony Shear Relaxation parameters and fine-tuned Young's moduli via constant stress FEM simulations versus the real test data is presented in 7.6. As shown there, the simulation curves match the measured curves with higher than sufficient accuracy for the time period where the probe is loaded with constant stress $(t<3600\,s)$. When the probes are unloaded, the quality of the match is mainly dependent on the amount of plastic deformation experienced by the real probe. Since the Prony model is only capable of modeling linear viscoelasticity, the plastic deformation experienced by the real probes while held under constant stress is recognized as viscoelastic in the curve fitting process. While this leads to the good strain match in the loading sequence of the simulation, all strain is considered to run towards zero for the idle section $(t>3600\,s)$, in consequence of which the plastic deformation is neglected by the material model. This leads in the idle section to noticeable deviations for the materials NBR70 and FKM88, and to barely visible deviations for the materials NBR82 and NBR75. For the PTFE model, bigger deviations are expected later in the idle progress because of the significantly negative slope of the simulation curve at the simulation end time. However, the back forming behavior of the materials is less important for the simulations within this dissertation, because the most significant de-

formations of the seals happen while mounting. While the mounting process is considered prior to the friction simulation, any dismounting process after the friction simulation is obviously not relevant for the friction behavior. The deformations while stroking due to frictional stress in the contact zones are expected to be both very small and fully reset each time a return point is passed while stroking. Hence, significant plastic deformations due to the stroking process are not expected. That is why the occurring deviations in the idle section of the material model tuning and validation simulations are negligible for the overall simulation model. The Prony Shear Relaxation model proves therefore to be the most suitable for the simulations performed in the context of this dissertation.

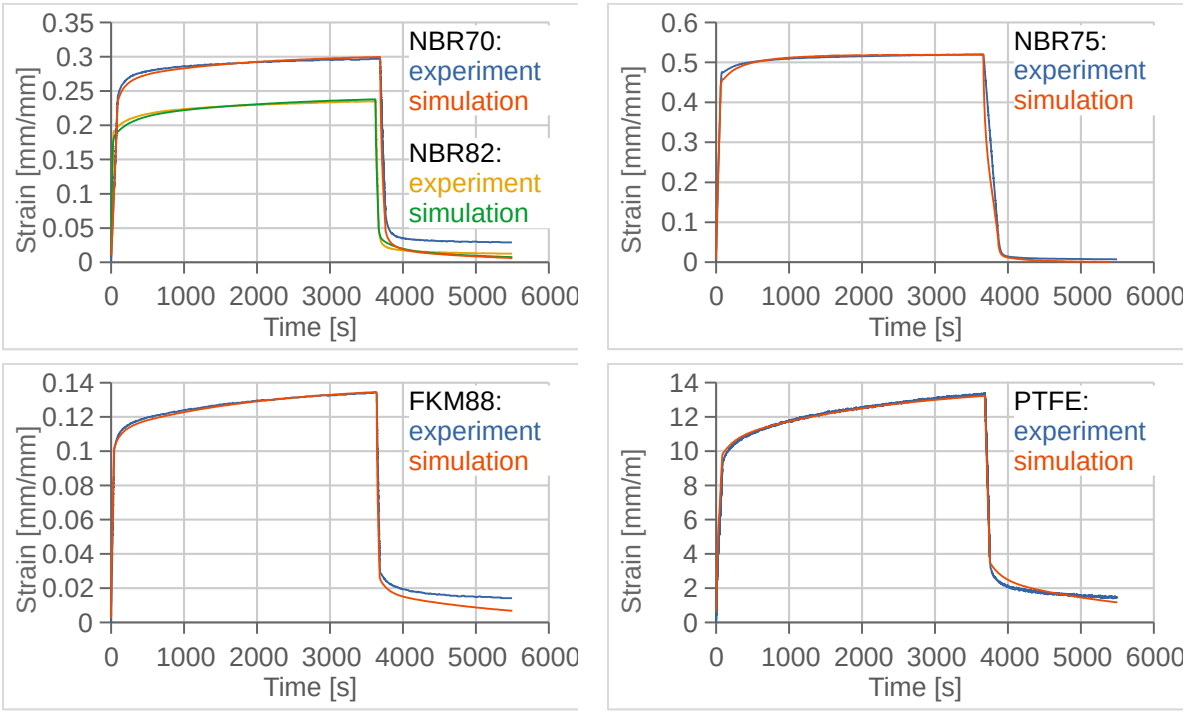

Illustration 7.6: Comparison of the constant stress test results from 6.3 versus constant stress FEM simulations for each seal material modeled with the Prony Shear Relaxation material model

7.2.3 Contact Modeling

To fulfill the requirements of this dissertation, the contacts have to be detected and treated in a way that a dynamic friction model can be applied. This requires the generation of the necessary input parameters of the friction model, e.g. the contact normal force, the contact area, the sliding distance and its derivatives. Additionally, the contact model has to show a fast and stable convergence behavior, even for large stiffness differences and large deformations of the contacting bodies, as is expected from the material modeling from Chapter 7.2.2. To achieve these requirements, the following contact model was applied to all eligible part faces. The general contact formulation is the Augmented Lagrange contact model, already introduced in Chapter 2.3.2. It is a penetration-based contact model with decreased absolute penetration due

to equation (25), which additionally decreases the contact's sensitivity to the contact normal stiffness [56]. The contacts are treated asymmetrically, which means that one contact surface and one target surface is defined, where only the contact surface can penetrate the target surface. This is much more efficient than modeling symmetric contacts, where both participating surfaces can penetrate each other. According to the determination guidelines from [57], the seal surfaces are always defined as the contact side, and the counterparts (namely rod, piston, tube and floating piston) are always the target side due to the material stiffnesses, convex seal shapes and finer seal meshes (see Chapter 7.2.5). The contact is detected and a contact element is created as soon as a contact surface's Gauss point (i.e. one integration point of an element) penetrates the target surface. Attempts to use the element's nodal points for contact detection (nodal-normal to target contact detection; [57]) leads to faster contact convergence, but leads to wrong estimates for the normal force and sliding speed, resulting in a wrong dynamic friction model behavior. Consequently, the nodal-normal contact detection approach is only suitable for contacts without the implementation of a dynamic friction model (e.g. the oil seal / static seal contact). To maintain uniformity between models and since the simulation speed-up is not significant due to the few application possibilities, the nodal-normal to target approach was discarded here. The contact element itself is three-dimensional on three-dimensional underlying geometry, but has no height (and accordingly no volume). It follows the shape of the underlying 3D element. Thus, it uses an internal two-dimensional coordinate system to appropriately determine sliding distance and direction (also called slip increment) and spatial contact stress distribution, as is generated by the friction model. [57]

The contact stiffness is automatically determined and adjusted by the FE solver to achieve a fast converging iteration process until the maximum allowed contact penetration is satisfied. The contact stiffness determination is affected by the defined material properties, the element size and the penetration tolerance [57]. As it became evident, that the smoothness of the friction progress calculated by the dynamic friction model is affected by the contact penetration, therefore the penetration tolerance was decreased to 0.025 from its default value 0.1. This means only a maximum contact penetration of $2.5\,\%$ instead of $10\,\%$ of the corresponding seal element height is acceptable. This stricter requirement is achieved by increasing the continually adjusted contact stiffness by the solver and performing more contact iterations, which results in a small increase in simulation time [57]. In addition to the normal stiffness, the tangential stiffness has to be defined for the contact element, since the tangential stiffness is part of the friction-determining parameters (see Chapter 2.2.2). Given that the friction model between the respective seal and the moving counterpart (namely the rod or the tube) is implemented externally, the respective contact has to be defined frictionless in the FEM program. All rod guide assembly contacts which are expected to show no significant sliding, namely the oil seal / housing contact, the static seal / housing contact and the oil seal / static seal contact are set to a standard Coulomb friction coefficient of $\mu = 0.4$, which is arbitrary, but within a reasonable range and found to be suitable to stabilize the setup by preventing flicking and gross sliding among these contacts. The piston band / piston contact is defined as bonded, which is realistic due to the manufacturing process [64].

The contact setup of the floating piston's single friction point has been determined based on the objective to achieve a stable simulation process. At this single friction point, the spatial position of the O-ring relative to the floating piston's groove end stops is determined only by forces. Since the pre-sliding displacement behavior implemented in the LuGre model shows near-zero force response to very small displacements, the O-ring position is very unstable and therefore highly uncertain. This instability is increased by the use of a steady-state solver, which is necessary to achieve suitable simulation time. In this solver the neglection of all time-dependent terms prevents motion damping due to the neglection of inertia [53] [54] [56]. As a result, it was not possible to get a converging simulation setup with an O-ring that is not further stabilized in its position. A first step to stabilize the solution was to define the contact of the O-Ring to the floating piston as a Coulomb contact with a friction coefficient of $\mu = 0.4$, as for the above mentioned contacts without a dynamic friction model of the rod guide assembly. As discussed above, this value is completely arbitrary. However, it is impossible to perform an appropriate parameter estimation process here as for the gross sliding friction points by using the single friction point test rigs, while preserving the pressure actuation of SFP2 with its indirect friction measurement via a difference pressure (see Chapters 4.3 and 7.3). Since the main target of this friction definition is the stabilization of the O-Ring, the absolute value of the friction coefficient is not actually that important. Instead, the amount of elastic slip tolerance added to the ideal Coulomb model by the Ansys Mechanical friction definition is decisive. A distinction is made in this model between sticking and sliding, where sticking is active as long as the applied frictional stress is below a defined limiting stress $\tau_{\lim}$ which the sticking contact is able to carry according to equation (34):

$$\sqrt{\tau_1^2 + \tau_2^2} \leqslant \tau_{\lim} = \mu \cdot p + b \tag{34}$$

where p is the contact pressure and b is the defined contact cohesion [57]. According to this equation, the maximum equivalent stress generated in the friction contact, composed by the stress contributions per direction τ_1 and τ_2, is capped to $\tau_{\lim}$. Even though applying a Coulomb friction coefficient of $\mu = 0.4$ prevents the O-ring from gross sliding in its groove while ensuring the ability to transfer frictional stress, this measure is not sufficient in it self to stabilize the floating piston / tube FEM setup. That is why additional stabilization is required here, applied as boundary conditions (see Chapter 7.2.6).

7.2.4 Friction Modeling

As described in Chapter 7.1, a dynamic friction model, namely the LuGre model is applied to each contact element generated between each seal and counterpart according to Chapter 7.2.3. The chosen FEM simulation environment Ansys Mechanical provides an interface to implement self-written friction models to detected contacts, a function which is called USERFRIC. The preferred programming languages for this task is Fortran and the closely Fortran-related Ansys Parametric Design Language APDL, because the core FEM solver code of Ansys Mechanical is also written in Fortran. The overall implementation of the LuGre model is separated into two subroutines developed within this dissertation. The first, namely the *userfric*

subroutine, acts as an interface between the FEM setup and the actual friction model. The program flow chart of this *userfric* subroutine is depicted in 7.7. This subroutine hands over information from the FE solver that is required to solve the friction model, e.g. the current time step size and parameters which describe the contact status like contact pressure and slip increments per direction. It also initializes or gathers stored data from the previous FEM time step, namely the previous slip increments and the bristle deflection z . Subsequently to the initialization and gathering, the current motion state is determined by the time-derivative of the slip increments in both directions of the contact element. With this data, the friction model is well defined and it is now called once per direction of the contact element. Separating the properties describing the element motion like slip increment and sliding speed is necessary, since the cell orientation as well as the sliding direction is usually unknown and can also change during the simulation progress. If the FEM solver converges on a solution for the current time step, the state variables z and v are updated. If the time step does not converge, the solver usually tries a bisection, which means a solution attempt with smaller time step size. For this case, the previous state variables are preserved to ensure appropriate initial conditions for the new time step. Subsequently, the frictional stress is calculated for the contact element, resulting in the determination of the slip distance and direction and the stored elastic energy of the contact element. Afterwards, the tangent matrix is updated and with that the friction contribution to the overall stress and deformation properties of the FEM setup is applied. The basic approach of linking the dynamic friction model and the FEM solver by use of the *userfric* subroutine was developed in [68], on the basis of which [72] contributed significant corrections and optimizations.

The second of the above-mentioned subroutines is the *LuGre* subroutine, which contains the dynamic friction model itself. The corresponding program flow chart is depicted in 7.8. The *LuGre* subroutine starts with parameter initialization or gathering from the previous time step handed over by the *userfric* subroutine. The LuGre parameters themselves are either hard coded to the subroutine or defined as a user input in Ansys Mechanical and handed over to the *LuGre* subroutine as a user-defined material property (*uprop* , see [57]). Next, it is determined whether the FEM simulation is still in the mounting phase (described in Chapter 7.2.6), where all related contacts are defined as frictionless, since this leads to a faster solution process. If the FEM simulation is in the friction recording phase, the LuGre differential equation is solved numerically by a fourth order Runge Kutta algorithm. This integration algorithm uses a time step size which is ten times smaller than the current FEM time step size, which proved to be a good compromise of numerical stability versus calculation time.

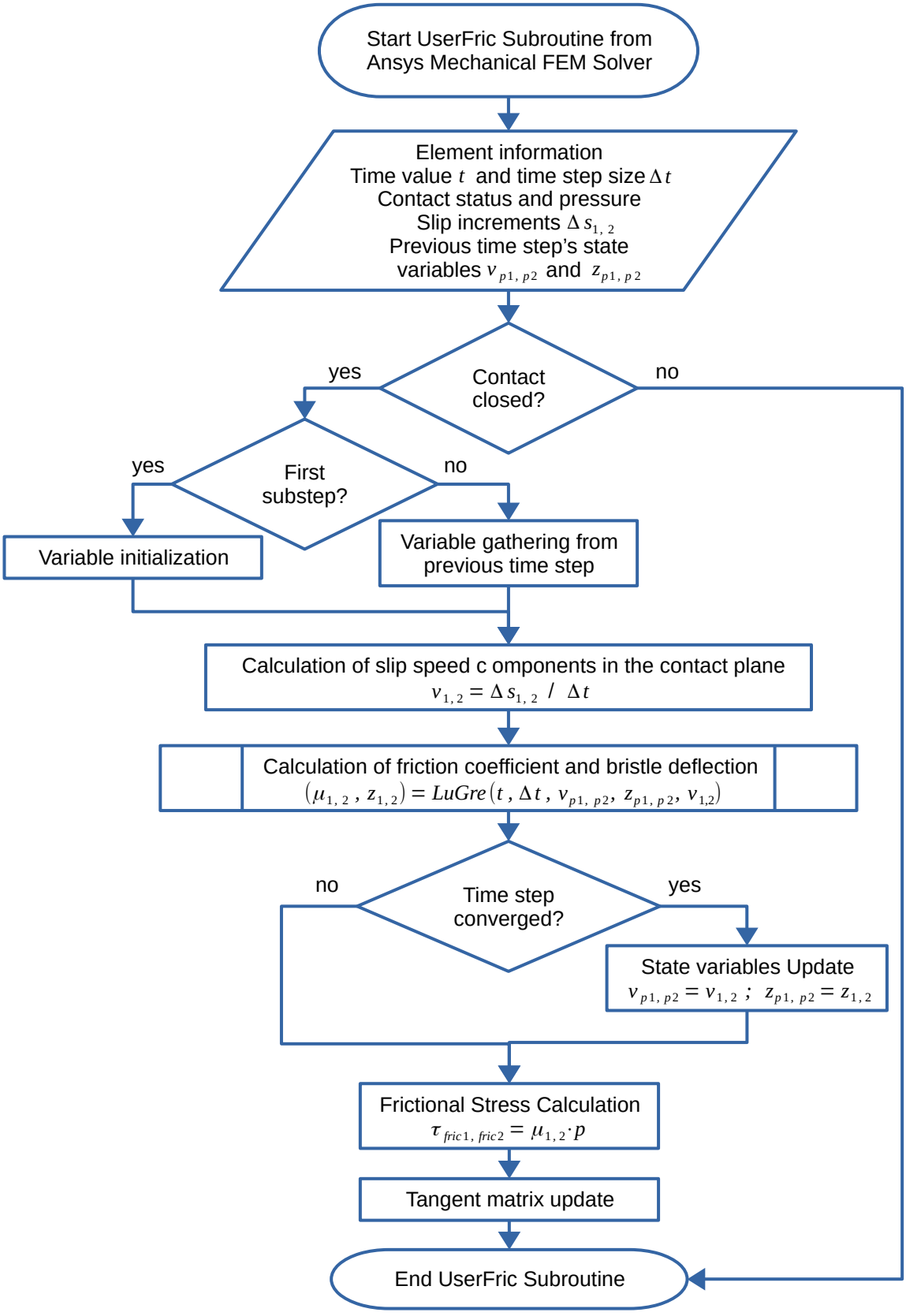

Illustration 7.7: Program flow chart of the userfric subroutine

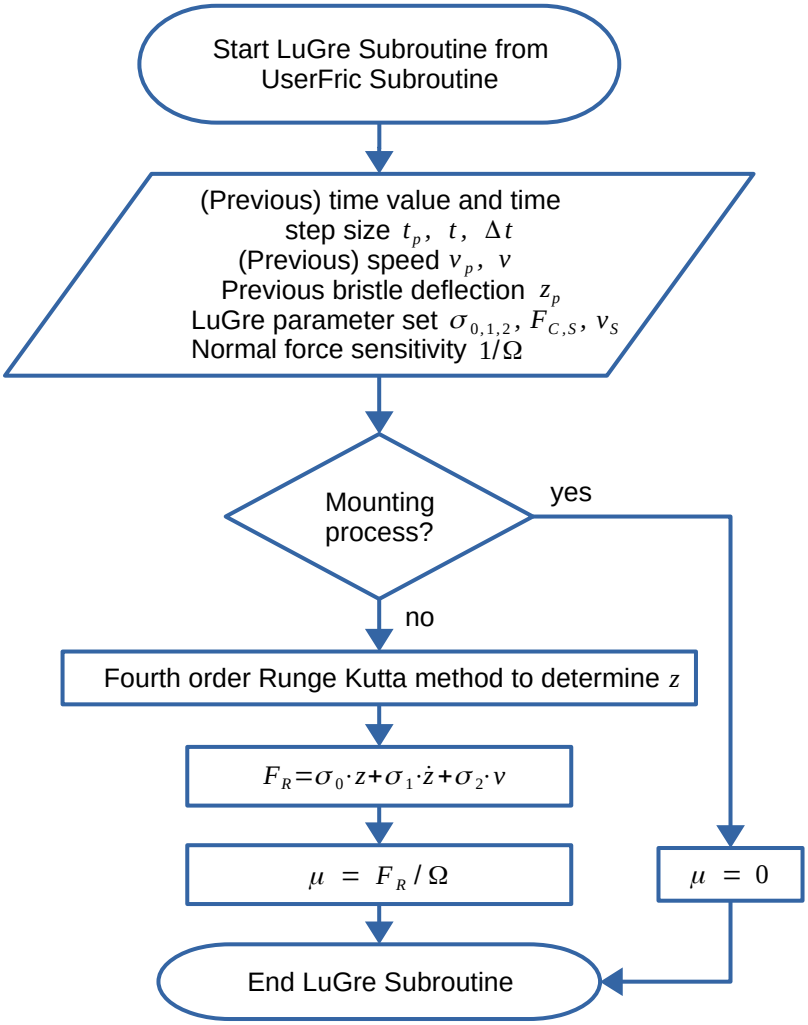

Illustration 7.8: Program flow chart of the LuGre subroutine

Since the output of the LuGre model is a friction force, which is so far not influenced by the contact normal force within the implementation introduced above, the friction force F_R within the *LuGre* subroutine is converted to the friction coefficient μ by the application of the additional parameter Ω following equation (35):

$$\mu = \frac{F_R}{\Omega} \tag{35}$$

This parameter Ω represents the inverse normal force sensitivity of the friction contact and has the unit Newton to fulfill the convention of a friction coefficient with the unit $[1]$. It has to be tuned to an appropriate value subsequent to the FEM simulation as discussed in Chapter 8.1, where $\Omega = 100\,N$ proved to be a good starting value. As a result of the introduction of Ω, the friction coefficient μ can be used for the tangential stress determination in the FEM setup as described above.

7.2.5 Spatial Discretization

Discretization describes in general the transfer of continuous entities into discrete counterparts. Regarding the FEM pre-process, discretization describes the transfer of the real geometry into a finite amount of elements (spatial discretization) and the transfer of the continuous time progress into a finite amount of time steps (temporal discretization). Since the latter is directly connected to the choice and temporal appearance of boundary conditions, the temporal discretization of the FEM setup of this dissertation is presented in Chapter 7.2.6. Most of the necessary spatial discretization steps (e.g. choosing the element type and element formulation, local element size and element size transition, geometry simplification, mesh smoothing etc.), are commonly performed automatically by a meshing software based on general user settings. That is why this section focuses on general properties of the resulting mesh. The meshing software used for this dissertation is the program “Ansys Meshing” which is part of the Ansys Workbench. Further information considering discretization theory in general, the meshing strategy, and the meshing process performed by Ansys Meshing can be found in the respective literature [53] [54] [73].

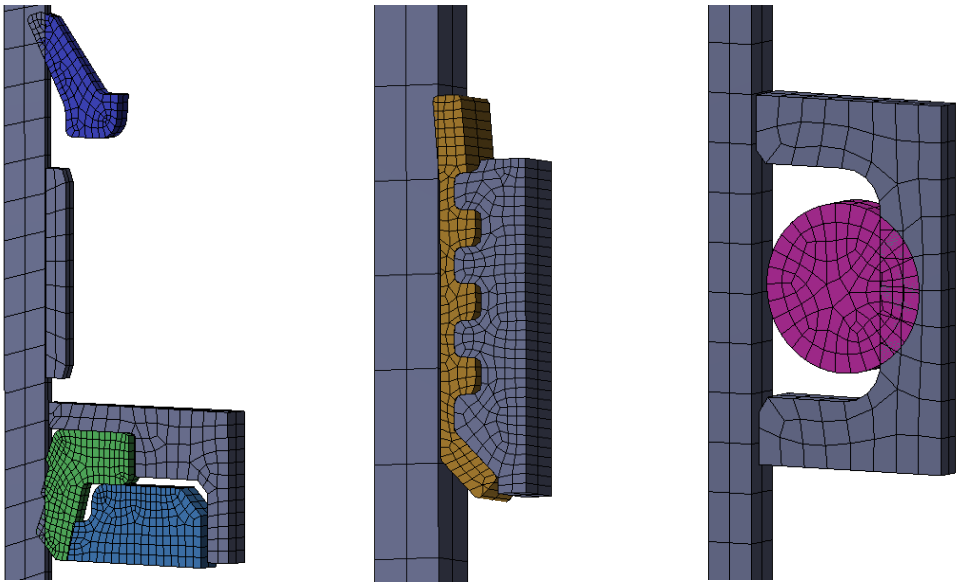

Illustration 7.9: FEM meshes of the single friction points based on the undeformed geometry from 7.4: rod guide assembly / rod (left); piston / tube (center); floating piston / tube (right)

The main aim for the user in the meshing process is to achieve a mesh that is computationally reasonably simple, but still covers the abstracted geometry sufficiently and leads to a stable and converging solving process. The resulting meshes for this dissertation based on such a compromise of computational effort versus model and geometry accuracy are depicted in 7.9. As introduced in Chapter 7.2.1, the underlying geometry is a 4 ° wedge of the original CAD data which is simplified to the necessary parts. Thus, rotational symmetry is assumed. As a consequence, the 2D mesh of the half virtual cutting area can be swept around a 4 ° arc of the full perimeter, which leads to a rotational symmetric, thus structured and computationally

very favorable mesh containing only wedge and hexahedral elements. Because of the rotational symmetry assumption, two sweep divisions are sufficient to achieve a stable mesh while preserving a very low element count. As a consequence, each sweep division and with that each element covers 2° of the perimeter. Because of the significant stiffness differences between the seals and their counter-parts, and the therefore expected very small deformations, all non-seal parts can be meshed quite coarsely as shown in 7.9. The seal meshes are mainly determined by the finding of a stable convergence behavior, for which the element size can be both too large and too small. Critical points are especially the locations with the highest expected strains and stresses. These are the parts of the geometry where a contact is detected first, namely the lip tip of the scraper, the three lips of the oil seal and the end lip of the piston band. The meshing of the floating piston's O-ring is mainly determined by the element quality (skewness and aspect ratio) of the outermost elements which experience the biggest deformation while fulfilling the contact definition.

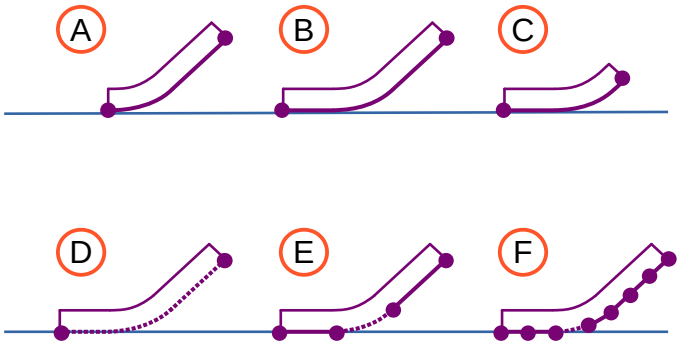

Illustration 7.10: Discretization influences to the estimated overlapping of a detected contact element only partially in contact

Special caution is required for the meshes in the contact zones where the friction model is applied. The friction model, which is called for each contact element, uses the contact pressure for the friction calculation, as introduced in Chapter 7.2.4. Assuming a flat and evenly loaded contact, the contact pressure and with it the contact normal force is evenly distributed over the contact element. Consequently, the friction calculation in its present application is mesh-independent for this flat contact case, since an increase of the number of contact elements results in a corresponding decrease of contact normal force per contact element. However, if the contact is non-flat in any way, or the number of elements that are actually in contact is changing over time, the contact mesh becomes relevant for the calculated friction force results. Both the non-flat contacts and the changing number of elements in contact over time occur within the simulations presented within this dissertation. The influence of the spatial discretization to a non-flat or changing contact is shown in principle in 7.10. If one two-node element is only in partial contact to its target surface as shown in 7.10 (upper line), the contact is detected only at the left node, while the right node is not yet in contact. Thus, as soon as one contact element is not fully in contact, its merely partial contribution to the support of the contact normal force of the full contact leads to miscalculations of its actual friction contribution according to

the frictional stress calculation in 7.7. As a consequence in 7.10 (upper line), only the left node is carrying parts of the contact load. The amount of contact normal force carried by the left node is the same for the examples (A), (B) and (C), if there is no further adjustment in the element formulation. Thus, the amount of load is overestimated for (A), where in reality only a small load-carrying contact area is present. The amount of supported contact normal force is estimated just correctly for (B), where half of the nodes (one) represents one half of the element in contact. Finally, the amount of load is underestimated for (C), where the element is almost fully in contact. This friction force calculation error becomes all the more significant, the more contact elements are in partial contact per friction point, which directly correlates with the absolute size of the contact area. This error can be minimized by increasing the mesh resolution in such a contact area, as depicted in 7.10 (bottom line). The partial contact element (the dotted line) in (D) covers the full length of the potential contact. Consequently, changes in the contact length due to rolling or element deformation have erroneously no influence to the calculated contact normal force and with that erroneously no influence on the determined friction. In (E), the potential contact length is divided into three contact elements, which results in the earlier recognition of larger actual contact length changes as soon as the right node of the dotted partial contact element gets into contact, or the left node of the dotted partial contact element lifts off. (F) shows an even smaller influence of the dotted partial contact element on the overall friction result because of a further increased mesh resolution. [72] performed extensive studies regarding this partial contact element behavior. It is shown that a change in the number of nodes in contact leads to a jump in the friction force which can be deduced from the above-described behavior and which can by decreased by increasing the amount of contact elements in a certain contact zone. However, this partial contact influence to the friction result is not fully avoidable by advanced increase of the mesh resolution, since its root cause can not be eliminated. Nevertheless, the partial contact influence to the friction result is further mitigated by the use of contact element types with multiple nodes per element (e.g. CONTA174 with additional nodes and integration points halfway between the corner nodes, see [57]) and by the use of area-considering weighting functions during contact detection, which are not further documented in [56].

The final meshes of the single friction points as depicted in 7.9 show therefore a compromise of lowest possible computational effort, sufficiently discretized contact zones, and stable overall convergence. The influence of partial contact elements on the friction result as described above could be minimized during a mesh study to an acceptable uncertainty of the absolute friction force. To give an example, a mesh study of the oil seal / rod contact is depicted in 7.11. While the green oil seal’s mesh on the left side is visibly finer than the original mesh on the right side, the gray rod’s mesh was not altered since its contact contribution as the target side is mesh independent (see Chapter 7.2.3). The finer left-side mesh achieves a higher number of elements in contact k_{Con} while resolving the contact definition.

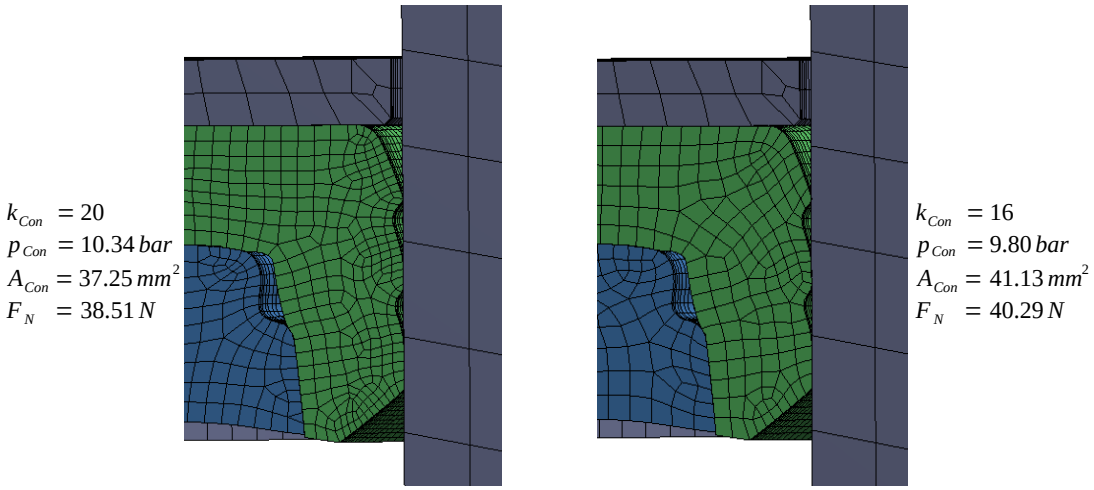

Illustration 7.11: Characteristic mesh study of the oil seal / rod contact to estimate spatial discretization influences on characteristic contact parameters

The resulting average contact pressure p_{Con} and contact area A_{Con} differs due to the above-mentioned influence of elements partially in contact. However, the absolute deviation of these parameters is acceptably small. Since the determined contact area and contact pressure can be both overestimated and underestimated, the deviation to the average value is used for comparison, where both sides show only $\pm 2.7\,\%$ pressure deviation and $\pm 5.0\,\%$ area deviation, which results in a deviation of the friction-relevant circumferential normal force F_N of only $\pm 2.3\,\%$. The overall element and node count of the final meshes is very low due to the mesh optimization and the thin 4° wedge with only two sweep divisions, resulting in 1382 elements / 9151 nodes for the rod guide assembly / rod friction point, 852 elements / 5877 nodes for the piston / tube friction point, and 488 elements / 3323 nodes for the floating piston / tube friction point.

7.2.6 Boundary Conditions and Initial Conditions

Boundary conditions in general delimit the area of calculation at the boundaries of a mathematical simulation setup. Typical boundary condition types for mechanical FEM simulations are spatial restrictions and definitions (e.g. supports, end stops, displacements, velocities, accelerations) or forces (e.g. applied forces, torques, gravitation, pressures). Initial conditions are conditions of the same types, which are only valid at the beginning of the calculation, and which define the initial state of the setup at every location. The scope of this section is a documentation of the boundary conditions and initial conditions applied to the above introduced FEM model. The emergence and evolution of the boundary conditions is directly linked to the temporal discretization, and is consequently included in this section. All three simulation setups are divided into three main phases.

The first phase is called “mounting phase”. Its purpose is the arrangement of all bodies and the application and evolution of all boundary conditions to a state that resembles a newly constructed shock absorber, just recently mounted and pressurized. During simulation of this

phase, the contact definitions of all corresponding damper parts are resolved in order to replace the initial penetration of the seals and counterparts (see 7.4) by the respective deformation and deformation-induced stress. Subsequently, static pressure is applied to the parts which face a significant pressure drop in reality, namely the oil seal and the static seal. This is crucial since the correct contact pressure of the oil seal against the rod is additionally determined by the static pressure in the damper, whereas the contact pressure of the other seal contacts (scraper, piston band, floating piston's O-ring) is only determined by the seal's deformation due to the contact definition. Since the amount of deformation that is experienced by the seals during this phase is very high compared to the rest of the simulation, comparatively small time steps of $\Delta t = 0.001 ... 0.1\, s$ are necessary to achieve a stable convergence behavior. The actual time step size is therefore chosen by the solver itself, which increases the time step size if less than a certain number of equilibrium iterations is required in the previous time step, and decreases the time step size in case of non-convergence, following the bisection method [57].

The second phase is called "relaxation phase" and represents the period of time that is needed by the viscoelastic material model to reach a nearly steady state (see Chapters 6.3 and 7.2.2). This phase is comparable to the storage time that is passed in reality between damper mounting and measuring. After this phase a state is reached which resembles the initial state of the friction recording phase of the single friction point measurements. Analysis of the simulation of the relaxation phase showed that a relaxation time of half an hour is sufficient to achieve this desired steady state, which is easily verifiable, given that the ongoing relaxation during the following friction recording phase would result in a decreasing contact pressure, which would result in constantly decreasing friction during stroking. Further influence of the material modeling on the friction result is discussed in Chapter 8.3. Since all boundaries of the FEM setups stand still during this phase and the only influencing factor is the slow relaxation behavior of the viscoelastic materials, comparatively large time steps of $\Delta t = 10 ... 120\, s$ are possible for this phase.

The third phase resembles the friction recording itself and is therefore called "friction recording phase". The relative motion is caused by displacement definitions of the moving rod against the rod guide assembly fixed to the ground (rod guide assembly / rod friction point), the moving piston against the tube fixed to the ground (piston / tube friction point), and the moving tube against the floating piston fixed to the ground (floating piston / tube friction point, see explanation below). To remain comparable to the single friction point test rig measurements, the same actuation function is chosen for these displacement boundary conditions as introduced in Chapter 4.2.2. Since the friction simulation setup considers neither oil flow or wetting in its FEM part nor wear or dirt, and since viscoelastic relaxation is already covered in the relaxation phase, no pre-conditioning similar to the real setup is required as discussed in Chapter 4.2.1. The choice of the time step size for the friction recording phase is determined less by convergence behavior than by a sufficiently resolved friction behavior, which is why a steady time step size of $\Delta t = 0.25\, s$ is defined.

While the rod guide assembly / rod friction point and the piston / tube friction point FEM set-ups achieve stable convergence with standard and realistic boundary conditions, additional measures had to be implemented to stabilize the floating piston / tube friction point. The decisive difference of the latter friction point is that – unlike all other parts of the damper – the O-ring's position according to the floating piston's groove end stops is determined only by forces instead of displacements. This results in a highly uncertain location of the O-ring during simulation because of the near-zero friction force of the LuGre model at very low speeds and the use of a steady-state solver, as already introduced above. As it became evident that the prevention of gross sliding of the O-ring according to the floating piston using a Coulomb model with high elastic slip tolerance is still insufficient to stabilize the setup, overall sliding of the O-ring in its groove has to be additionally restricted. The O-ring's displacement degree of freedom is accordingly locked in actuation direction (z direction) via a remote point boundary condition (see [56]). As shown in 7.12, this remote point is located in the center of the O-ring wedge (black cross), thus still allowing the O-ring to rotate around its center line (orange arrow). Consequently, this measure enables the O-ring to preserve its real movement behavior towards the tube, but restricts it towards the floating piston. Since the O-ring is locked in actuation direction, the actuation principle has to be reversed (i.e. the tube is actuated and the floating piston is fixed to the ground) to perform the actuation sequence introduced above.

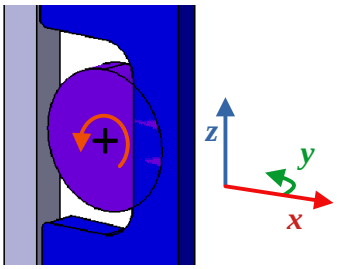

Illustration 7.12: Stabilization of the O-ring in the floating piston's groove via remote point

While these measures sufficiently stabilize the FEM setup, they additionally require to simplify the parameterization of the LuGre friction model for the floating piston / tube friction point to one parameter set, which is describing both the floating piston / O-ring friction behavior and the O-ring / tube friction behavior. This necessity to simplify the friction model's parameterization is actually helpful, since only the overall friction response to the test rig's displacement is recorded in experiments on SFP2. Consequently, the respective contribution to the friction behavior of the O-ring rolling and the O-ring sliding, both according to the tube and according to the floating piston, can not be easily separated in experiments. Eliminating the O-ring / floating piston friction contribution in the FEM setup results therefore in both the requirement and the possibility to cover the tube friction contribution as well as the floating piston friction contribution in one single friction model parameter set. The determination of the related friction model parameter sets is described in the following Chapter.

7.3 Parameterization of the Friction Model

The LuGre model, which is the dynamic friction model applied to each contact element in the relevant seal / counterpart contacts, is determined by its mathematical formulation and its parameter set consisting of the six parameters σ_0, σ_1, σ_2, F_C, F_S and v_S (see Chapter 2.2.2). In order to efficiently determine such a parameter set for each single friction point simulation, a method has been developed to determine the values of these six parameters based on the single friction point measurements discussed in Chapter 5. The common parameterization approach implies as a first step the determination of the static parameters, namely F_C, F_S, v_S and σ_2. These static friction parameters are easily obtainable from steady state friction experiments, i.e. experiments with various constant sliding speeds. Subsequently, the parameters which characterize the turn-around points, σ_0 and σ_1 are determined during experiments with changing speed [30] [33]. This common approach requires many experiments, which creates an inefficient parameterization process. This is why, all parameterizations within this dissertation are performed using a Matlab script which determines the parameters based on the *lsqcurvefit* function from the Matlab Optimization Toolbox. The *lsqcurvefit* function solves nonlinear cure-fitting problems in the least-squares sense. In particular, it finds coefficients *x* that solve the following problem:

$$\min_x \| F(x, xdata) - ydata \|_2^2 = \min_x \sum_i \left(F(x, xdata_i) - ydata_i \right)^2 \tag{36}$$

with *xdata* being a vector or matrix of input data, and *ydata* being a vector or matrix of observed output data, where $F(x, xdata)$ is a vector-valued or matrix-valued function of the same size as *ydata* [74]. When applied to the single friction point's friction behavior, $F(x, xdata)$ is the LuGre formulation according to Chapter 2.2.2, numerically solved by a fourth order Runge Kutta algorithm similar to the one introduced in Chapter 7.2.4, *xdata* is the speed derived from the experimental displacement data (see Chapter 5.1), and *ydata* is the experimental friction force. Three additional vectors have to be provided to the *lsqcurvefit* function prior to its execution, namely a vector which provides an initial guess for the LuGre parameters, and two vectors to define lower and upper bounds for the resulting parameter vector during the optimization process. The parameterization process itself is performed within only a few seconds on standard PC hardware and is mainly driven by the appropriate choice of the introduced additional vectors, which presumes a rough idea of the expected values of the LuGre parameters. The general concept of the described parameterization process has been developed in [75]. The resulting parameters derived from the single friction point measurements as well as specifics of the parameterization process of the single friction points are presented in the following sections.

7.3.1 Parameterizing the Piston / Tube Friction Point

Parameterizing the piston / tube contact is quite straightforward due to the comparatively simple shape of the force-speed graph, which almost perfectly mimics typical LuGre behavior.

Consequently, the recorded graph from the experiment and the optimized solution of the LuGre function in Matlab match almost perfectly as depicted in 7.13 (left), with the corresponding LuGre parameter set shown on the right side. While the width and the slope of the pre-sliding hysteresis as well as the absolute amount of friction match very well, the only small qualitative deviation of the LuGre graph versus the experimental friction record is the slightly slower transition of the LuGre force changing from the pre-sliding hysteresis to the almost stable force level at higher speeds.

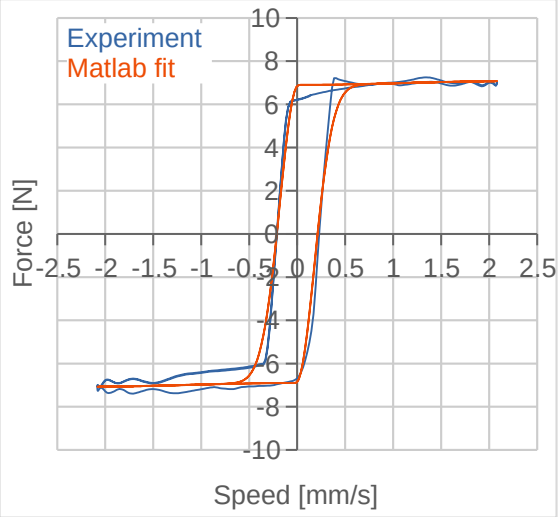

σ_0	=	20.643E+03	N/m
σ_1	=	10.010E-06	Ns/m
σ_2	=	10.004E-06	Ns/m
F_C	=	7.100E+00	N
F_S	=	6.893E+00	N
v_S	=	1.432E-03	m/s

Illustration 7.13: Comparison of the SFP1 piston / tube friction graph with a LuGre friction graph determined by the parameter set optimized on the base of this experimental piston / tube friction data

As already introduced in Chapter 5.1, the friction behavior of the piston / tube friction point can be characterized by the absolute midstroke friction and the hysteresis slope and width. Accordingly, the resulting parameter set in 7.13 is generated as expected with almost equal F_C and F_S and almost zero σ_1 and σ_2. While the almost equal F_C and F_S and the near-zero σ_2 show that there is neither significant Stribeck behavior nor high-speed damping, the near-zero σ_1 describes the non-appearance of an overshoot caused by non-reversible friction characteristic. The absolute value of v_S is very insignificant to the LuGre graph in this case because of the similarity of F_C and F_S.

7.3.2 Parameterizing the Rod Guide Assembly / Rod Friction Point

The parameterization process for the rod guide assembly / rod friction point is more complex than the previously described parameterization of the piston / tube friction point. This increased complexity is caused by the asymmetric friction force behavior of this friction point, as already discussed in Chapter 5.2, and the special feature of having two different contact zones in this single friction point, namely the scraper / rod contact and the oil seal / rod contact. Since both of these contact zones likely differ significantly in their friction behavior, at

the very least because of their differing lubrication conditions, it is obvious to apply different LuGre parameter sets on both contact zones. To determine different LuGre parameter sets, the respective friction contribution of each contact zone has to be investigated. A straightforward approach to investigate those respective friction contributions would be to measure the overall rod guide assembly / rod friction in SFP1 as documented in Chapter 4. Subsequently, the scraper would be removed, and the therefore modified rod guide assembly friction would be measured on SFP1 as well. By assuming zero bearing friction at zero lateral load, the difference between those two measurements would be the scraper friction. In reality, both seal's friction behaviors interfere with each other. While a scraper-only application is obviously not feasible, the rod guide assembly friction behavior with only the oil seal against the rod shows different results than expected, since friction measurements without scraper often show equal or higher friction than with scraper. This behavior is probably caused by the oil retention capabilities of the scraper, which is therefore not only preventing dirt from entering the rod guide assembly. Instead, the scraper is additionally preserving some of the lubricant film that passed the oil seal during rebound, resulting in significantly better lubrication on the oil seal during compression. Consequently, it is difficult to separate the actual friction contribution of the scraper / rod contact and the oil seal / rod contact to the overall rod guide assembly / rod friction point, which is why this separation is not performed within this dissertation. To keep both the measurement sequence and the parameterization as straightforward as possible, the treatment of both the oil seal / rod contact and the scraper / rod contact with only one LuGre parameter set has been chosen.

The above-mentioned asymmetry of the force-speed friction behavior leads to the need of a separation of at least some of the LuGre parameters for each movement direction. Extensive studies in the context of this dissertation have shown that the separation of σ_1 and F_C in a positive-speed σ_{1+} and F_{C+} and a negative-speed σ_{1-} and F_{C-} is both sufficient for a well-matching LuGre graph and leads to stable convergence in the subsequent FEM implementation. The above-introduced Matlab script is enhanced by the larger parameter vector due to the separation of σ_1 and F_C, and a blending function following equation (37), where *v* is the sliding speed. For the blending of F_C, $\sigma_{[...]}$ has to be replaced by the corresponding $F_{[...]}$, respectively. The amplification factor *amp* determines the slope of the tanh function near zero speed, and therefore has to be tuned to a sufficient compromise of smooth blending and accurate near-zero friction description determined by the respective plus-side or minus-side parameter of σ_1 and F_C.

$$\sigma_1 = \frac{\sigma_{1+} + \sigma_{1-}}{2} + \left(\sigma_{1+} - \frac{\sigma_{1+} + \sigma_{1-}}{2} \right) \cdot \tanh(v \cdot amp) \tag{37}$$

The resulting LuGre graph is depicted in 7.14, in comparison to the rod guide assembly / rod friction measurement graph already discussed in Chapter 5.2. To implement the parameter separation to the friction model called for each FEM contact element, equation (37) has to be implemented to the *lugre* function. Since the blending with equation (37) has to be performed

within the FEM model in any case so as to achieve a smooth transition between the positive-speed parameters and the negative-speed parameters, additional blending in the Matlab script would falsify the LuGre parameters. This is why, the optimized parameter set shown in 7.14 is achieved through a very high tanh amplification factor of $amp = 10^6$.

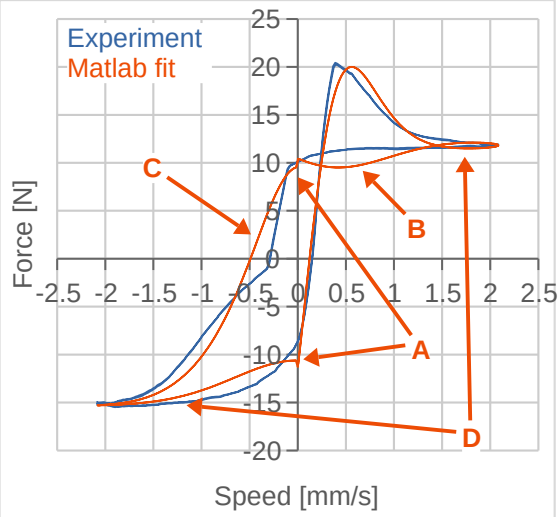

σ_0	=	5.577E+03	N/m
σ_{1-}	=	3.107E+00	Ns/m
σ_{1+}	=	40.670E+03	Ns/m
σ_2	=	10.000E-06	Ns/m
F_{C-}	=	15.354E+00	N
F_{C+}	=	11.862E+00	N
F_S	=	8.716E+00	N
v_S	=	976.013E-06	m/s

Illustration 7.14: Comparison of the SFP1 rod guide assembly / rod friction graph with a LuGre friction graph determined by the parameter set optimized on the base of this experimental rod guide assembly / rod friction data

This value for *amp* results in sharp steps in the LuGre graph at zero speed due to the sharp transition between the negative-speed parameter set and the positive-speed parameter set and vice-versa (A). Maintaining only one σ_0 and F_S for both speed directions ensures nevertheless a zero-speed transition without too large steps in the friction graph, since both of these parameters are co-responsible for the near-zero friction behavior (see 2.12). The absolute value of σ_0 is significantly lower than the σ_0 value of the piston / tube friction point (see 7.13), which leads to the wider part of the pre-sliding displacement hysteresis at low negative speeds in 7.14. The narrower hysteresis width on the low positive-speed side is caused by the very high value of σ_{1+}, which is also necessary to simulate the large overshoot peak at increasing positive speeds. Apart from the well-matching description of this overshoot peak, the high value of σ_{1+} also causes a significantly too low friction at (B), which represents one of the larger qualitative deviations of the LuGre function compared to the experimental data. Given that the above-mentioned overshoot peak does not occur on the negative-speed side, the corresponding value of σ_{1-} is virtually zero. The second larger qualitative deviation concerns the range of increasing low negative speeds (C), where the LuGre graph shows constant widening of the pre-sliding hysteresis, while the experimental data shows abrupt slope changing near the zero friction level. Both graphs in 7.14 match well at higher speeds with only minor deviations, whereas the parts of the Matlab fitted LuGre graph with equal but increasing or decreasing speed are always closer to each other than the corresponding parts of the experimental

graph (D). The separation of F_C into F_{C+} and F_{C-} allows matching of the different maximum-speed friction forces. The Stribeck behavior, which is commonly described by the difference of F_C and F_S does not occur here, which is why the Stribeck velocity v_s is virtually zero just as the parameter σ_2, which describes the high-speed viscous fluid damping.

7.3.3 Parameterizing the Floating Piston / Tube Friction Point

The force-speed friction behavior of the floating piston / tube friction point is sufficiently point-symmetric to use one parameter set for all sections of the force-speed graph, similar to the piston / tube friction point in Chapter 7.3.1. However, parameterizing the floating piston / tube friction point is not as straightforward as parameterizing the piston / tube friction point, since its friction behavior differs significantly from typical LuGre behavior. This difference is most probably caused by the superposition of sliding friction and O-ring rolling in the floating piston's groove, as already discussed in Chapter 5.3. However, in order to use the same friction modeling approach as for the other two single friction points, a LuGre parameter set that sufficiently characterizes the floating piston / tube friction point is still obtained.

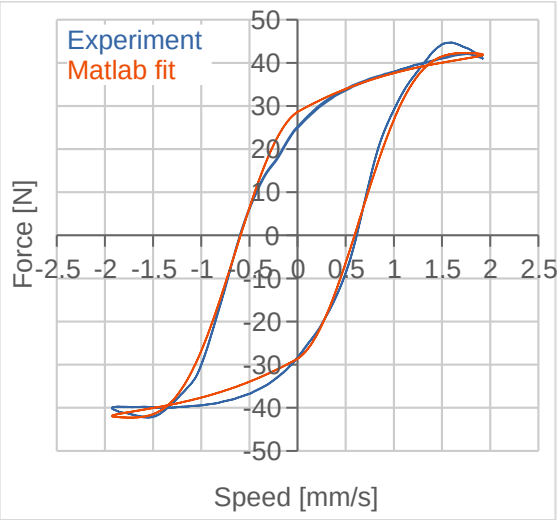

σ_0	=	7.414E+03	N/m
σ_1	=	10.005E-06	Ns/m
σ_2	=	12.385E+03	Ns/m
F_C	=	10.010E-03	N
F_S	=	31.748E+00	N
v_S	=	2.552E-03	m/s

Illustration 7.15: Comparison of the SFP2 floating piston / tube friction graph with a LuGre friction graph determined by the parameter set optimized on the base of this experimental floating piston / tube friction data

Two reference measurements are available as a basis for the parameterization, as already discussed in Chapter 5.3. $\hat{A}_{FP\,act} = 1.85\,mm$ represents the actually occurring amplitude during reference damper measurements and $\hat{A}_{FP\,comp} = 18.5\,mm$ enables to perform one-on-one comparisons to the other single friction point measurement results. First parameterization attempts used the actually occurring $\hat{A}_{FP\,act}$. Though, some of the LuGre parameters are mainly determining the high-speed friction behavior (e.g. σ_2 and v_S). This high-speed range is not achieved during the $\hat{A}_{FP\,act}$ measurements, since its friction graph is not properly leaving the

pre-sliding displacement range as shown in 5.6. Consequently, the measurement data basis for the fitting of high-speed LuGre parameters is not sufficient. Nevertheless, the $\hat{A}_{FP\,act}$ fitting results show that the very round shape of the graph is qualitatively parameterizable sufficiently well. However, the resulting parameter set is neither physically explainable, nor transferable to simulations with higher maximum speeds as observed with $\hat{A}_{FP\,comp}$ because of the insufficiently high speeds of the $\hat{A}_{FP\,act}$ measurement data. Because of this limitation, the experimental results with $\hat{A}_{FP\,comp}$ are used for the floating piston / tube parameterizations for this dissertation, which are also parameterizable sufficiently well, but with results that are also transferable to low-speed or low-amplitude simulations (see parameter set discussion below). The resulting force-speed graph of the optimized LuGre Matlab fit compared to the experimental $\hat{A}_{FP\,comp}$ data is depicted in 7.15.

The absolute value of σ_0 lies within the same range as the σ_0 values of the other single friction point parameter sets, which is reasonable since the pre-sliding hysteresis width is of comparable width. Even if the experimental graph is showing a small crossing which could be interpreted as overshoot peaks from non-reversible friction characteristics (see Chapter 5.3), the responsible LuGre parameter σ_1 is near zero. The appearance of a corresponding graph crossing at higher speeds in the Matlab fit of 7.15 implies that its cause lies in the choice of the other parameters. The parameter σ_2 has a very high value compared to the other single friction point parameter sets. Its typical physical interpretation is very unlikely in this case, since σ_2 characterizes the fluid damping that is caused by the viscosity of the lubricant, which is the same damper oil for all single friction points. However, it should be noted that the main goal of this parameterization process is the determination of the best-matching LuGre curve against the background of the combined rolling / sliding behavior of the O-ring towards the tube and the floating piston. This is sufficiently achieved through the property of σ_2 to linearly increase the sliding friction force and the “tilting” of the pre-sliding hysteresis, both with increasing speed (see 2.12). While F_S characterizes the zero-speed friction force, F_C is almost zero, which limits the force increase with increasing speed, caused by the very high σ_2, the influence of which also increases with speed. The value of v_S is significant for this parameter set, since it ensures the matching of the curves due to the absolute values of F_C, F_S and v_S. The achieved LuGre parameter set therefore results in a well-matching graph, although the use of the parameters within this parameter set is not fully consistent with their physical meaning (see Chapter 2.2.2). Therefore, the transfer of this parameter set to tribological systems with different geometry, material behavior and boundary conditions should be performed with caution. Nevertheless, the goal is achieved of one parameter set which covers the combination of O-ring sliding behavior and O-ring rolling both according to the tube and to the floating piston, which is a requirement from Chapter 7.2.6 to stabilize the floating piston / tube’s FEM setup.

Extensive investigations on the floating piston / tube friction point parameterization were also performed by [76]. It was proven there that the LuGre parameters – albeit dependent on the

displacement and speed frequency – are not depending on the achieved maximum speed. These findings created important insights regarding the transferability of parameter sets to different experimental and simulation setups. Consequently, the LuGre parameter set, which was determined based on experimental data with $\hat{A}_{FP\,comp}$, is assumed to be transferable to setups with $\hat{A}_{FP\,act}$, which is the floating piston's displacement amplitude actually occurring in the reference damper. This amplitude $\hat{A}_{FP\,act}$, is therefore modeled in the FEM setup of the floating piston / tube single friction point. The validity of this assumption is shown in Chapter 8.3.3.

7.4 Process

Since the process, i.e. solving of nonlinear equation system consisting of the overall stiffness matrix, the displacement matrix and the external loads is performed by the Ansys Mechanical APDL solver almost automatically, only non-default solver settings are documented here that had to be applied so as to efficiently achieve reliable and converging results. The equation solver type used for all simulations is the Sparse Direct Equation Solver of Ansys Mechanical APDL. This solver is highly specialized to the solving of equations systems based on sparse and asymmetric matrices as they are typical for FEM setups. It is chosen over the alternative Preconditioned Conjugate Gradient Iterative Equation solver due to the decision guidelines of [57] which recommend the Sparse Direct Equation Solver for models with big differences in material properties and weak displacement boundary constraints, as occurring in frictional contacts. The Sparse Direct Equation Solver is more robust than the PCG solver and also showed significantly better convergence behavior in this dissertation's simulations than the PCG solver, while its disadvantage of increased memory and disk space requirements was not a limitation due to the available high-performance compute servers in the university's compute center.

The chosen Sparse Direct Equation solver is further configurable to sufficiently match the requirements of the specific FEM setup. All the special settings documented here are required to mitigate difficulties of the FEM model due to the high non-linearity and asymmetry of the setup. An equation system and an FEM model in particular is considered non-linear as soon as a non-linear response to a given excitation occurs. In the FEM setups of this dissertation, non-linear behavior is caused by the non-linear material models (see Chapter 7.2.2), the expected large deflections of the seals (see Chapter 7.2.1) and the significant influence of the various frictional contact definitions to the overall model behavior, whereas the contact definitions cause a non-equilibrium state even in the undeformed state. Following these model properties, the activation of the solver option "large deflections" is crucial to achieve accurate results. The activation of large deflections results in the consideration of large strains (implying stress stiffening) and large (partial) body movement by reusing the last time step's strain state for the current time step instead of applying the initial geometry for the current time step [55] [56] [57]. The use of this solver option is quite common in modern FEM solving since the required additional compute power is usually available.

For the determination of the minimum of the potential energy of the FEM setup, a fully asymmetric Newton-Raphson method is used. This method searches implicitly for the root of the derivative of the potential energy of the system by iterative tangential approximation, until an acceptably low residual (characterized by force and displacement residuals) is achieved. Because of the above-mentioned non-linearity of the system, the initial guess of the Newton-Raphson method per time step has to be close to the actual root, since otherwise non-convergence is likely to occur. A close initial guess can be achieved by choosing very small time steps, which linearizes the system's stiffness in this time range, but results in an increase in simulation time. This limitation can be mitigated by the use of line search algorithms, allowing to choose larger time steps. Line search algorithms act as a convergence enhancement tool, where the calculated displacement increment of an iteration is multiplied by a program-calculated scale factor of the range $0 \ldots 1$ whenever a stiffening response is detected. The following equilibrium iteration is therefore provided with a smoothed initial guess for the displacement, which leads to a much faster convergence of the time step with abruptly stiffening system behavior [55] [57]. Since the closing of a contact represents a sharp increase in stiffness, the simulation of contact problems is a typical application of line search algorithms, which is why the use of line search is enforced for all simulations within this dissertation.

One requirement for the FEM setups of this dissertation is the solution in a reasonable time span to ensure usability in common engineering. The actual overall solving time of the FEM setups of the three single friction points introduced in the sections above is dependent on the available hardware, e.g. the type and number of CPU cores, the size and speed of the RAM and the speed of the file system, which is why only rough information about the solving time can be provided here. The used hardware consists of the common compute nodes of the TU Ilmenau compute center with AMD first generation Epyc CPUs and Intel fifth generation Xeon E5 CPUs. Because of the poor scaling of the sparse matrices solving process and the amount of elements per setup, usually only eight cores were used, which results in a RAM usage and simulation time of $\sim 8.0\,GB$ and $\sim 1{:}15\,h$ (rod guide assembly / rod), $\sim 5.3\,GB$ and $\sim 0{:}50\,h$ (floating piston / tube), and $\sim 3.0\,GB$ and $\sim 0{:}20\,h$ (piston / tube) per simulation run.

8 Analysis of the Parameterized Simulations

8.1 Post-Processing Preparation

In order to analyze the FEM simulation results, some refactoring of the raw result data is necessary. While some per-element values are already back-substituted by the FEM software (e.g. element stresses and element force reactions), additional user input is required to gather the force reaction data that represents the friction point's friction behavior. However, the values back-substituted by default are sufficient to check the overall plausibility of the results of the three single friction point FEM setups, which is a standard procedure in CAE prior to deeper result analysis to eliminate user input and modeling mistakes [53]. Some aspects of the plausibility checks of the simulations performed in the context of this dissertation are discussed in Chapter 8.2. The force reaction to the displacement excitation in each FEM setup can be obtained either directly at the defined contact surfaces, for which usually the force reactions of the elements directly underneath the contact elements are summed up, or this force reaction can be obtained at the exciting boundary condition, i.e. the displacement boundary condition of the rod, the piston, or the tube. The latter approach of analyzing the force reaction of the exciting boundary condition is advantageous as compared to the first approach because of two reasons: First, the use of the contact force reaction may be misleading because of additional force-influencing boundary conditions, which share topology with the contact surface. This topology sharing is the case at the rod guide assembly's oil seal, where the potential contact surface to the rod is additionally used as an application surface for the static operating pressure of the damper. Since this pressure boundary condition contributes to the underlying element's internal force balance, it is likely that this condition falsifies the extraction of the tangential force reaction in the contact, which is friction [56]. Second, the latter approach implies the necessity of the manual superposition of the force reactions of all contributing contact regions of the single friction point, if there is more than one contact region. This also affects in particular the rod guide assembly / rod friction point, where the single friction point friction is a combination of oil seal friction and scraper friction (and bearing friction in the case of lateral forces). Consequently, the use of the force reaction obtained at the exciting boundary conditions is chosen here to analyze the single friction point's friction behavior.

The usage of rotational symmetric boundary conditions as introduced in Chapter 7.2.1 is not only significantly reducing the computational effort of the FEM setup solution. The program Ansys Mechanical is also capable of projecting the result data of the $4°$ wedges to the full perimeter. This leads to easy and straightforward post-processing, since all perimeter-associated parameters are automatically calculated regarding their contribution to the full damper, such as the above-mentioned force reaction to the exciting displacement boundary condition, which is friction. The automatic projection to the full perimeter also allows the visualization of the full single friction point geometry, which helps to make the analysis of stress distribution, part deformation or other spatially distributed values easier to understand. As a conse-

quence, the following illustrations generated from the FEM result data always show the whole perimeter, if necessary sliced open to visualize inner value distributions.

As described in Chapter 7.2.4, the additional parameter Ω has been introduced to implement the desired contact normal force sensitivity of friction according to equation (35). Since the contact normal force is a result of the FEM simulation based on material data, geometry and contact definition, this parameter Ω can not be fitted to comply with reality directly and only based on the single friction point measurement data, as has been performed for the LuGre parameters in Chapter 7.3. It is therefore necessary to perform the Ω tuning subsequent to the FEM friction simulation. Because Ω does not determine the qualitative shape of the friction behavior, but acts only as a scaling factor for the friction result, the actual fitting can be done simply by comparing the absolute friction force values of the experimental data and the friction simulation data, which results in an adjustment factor to be applied to Ω . Since the qualitative shapes of the LuGre-determined simulations and the friction measurements show different deviations at different speeds or displacements (e.g. see 7.14), this comparison between measurement data and simulation data can either be performed averaged over the whole speed / displacement range, or specific speeds / displacements of particular interest are chosen for the determination of Ω . Seeing that friction is usually evaluated on midstroke results (see Chapter 4.2), midstroke friction (i.e. friction at zero displacement and maximum speed) was chosen here as the key comparison point for the Ω fitting.

8.2 Simulation Results Overview

This section provides an overview of the general properties of the FEM simulation results. The analysis of the stress distribution, the contact resolution, and solid body motion and deformation acts as a plausibility check for the overall setup and provides insights into the general behavior of the respective single friction point under the defined loads, apart from the friction behavior. Similar to the previous chapters, the first friction point to be analyzed within this section is the piston / tube friction point, the equivalent stress distribution of which is depicted in 8.1. In this illustration, the left panel shows the equivalent stress distribution just after mounting, whereas the right panel shows the equivalent stress distribution after additional $30\,min$ of standstill. This state of the right panel represents the state of the simulation setup just prior to the friction recording sequence, where the setup is mounted, pressurized to operating pressure, and at least half an hour has passed at standstill so as to achieve proper material relaxation (see Chapters 6.3 and 7.2.2).

In both panels of 8.1, both the piston / piston band contact and the piston band / tube contact are properly resolved, hence both contacts are closed, but the body penetration is reduced to a barely visible state. At the piston / piston band contact, zero penetration is consistent with the definition for a bonded contact [57]. In contrast, near-zero penetration at the piston band / tube contact shows convergence for the friction-related contact, which is determined by a penetration-based contact formulation (see Chapter 7.2.3). The piston band / tube contact is not closed over the full height of the piston band, but only between the piston band's end lip and the tube. Between most of the height of the piston band and the tube, there is a gap in the ge-

ometry, which is impossible to be closed because of two restrictions: First, the piston band can not detach itself from the piston due to the bonded contact definition. Second, the rotational symmetry boundary condition that is applied to the model to decrease the FEM setup size restricts the whole model to remain perfectly rotationally symmetric. This boundary condition prevents any piston or piston band tilting relative to the tube, which could cause a larger or smaller contact area between the piston band and the tube. Since it has been proven that the geometric tolerances of the piston band are quite large, and that much thicker and smaller piston bands are possible (see Chapter 7.2.1), the influences on the friction behavior of different piston band geometries and smaller or larger piston band / tube contact areas have to be investigated in future analyses. However, since extensive piston band geometry investigations are required to determine the piston band geometry range, the geometry abstraction process would become much more complex compared to the almost direct CAD data import, which was chosen for this dissertation. For the friction modeling, the contact status that is shown in 8.1 results in friction generation only on the contacting end lip of the seal. This is acceptable, because the contact normal forces on the whole length are expected to be very low for most of the possible piston band geometries, without the existence of lateral forces or lateral force inducing misalignments [64].

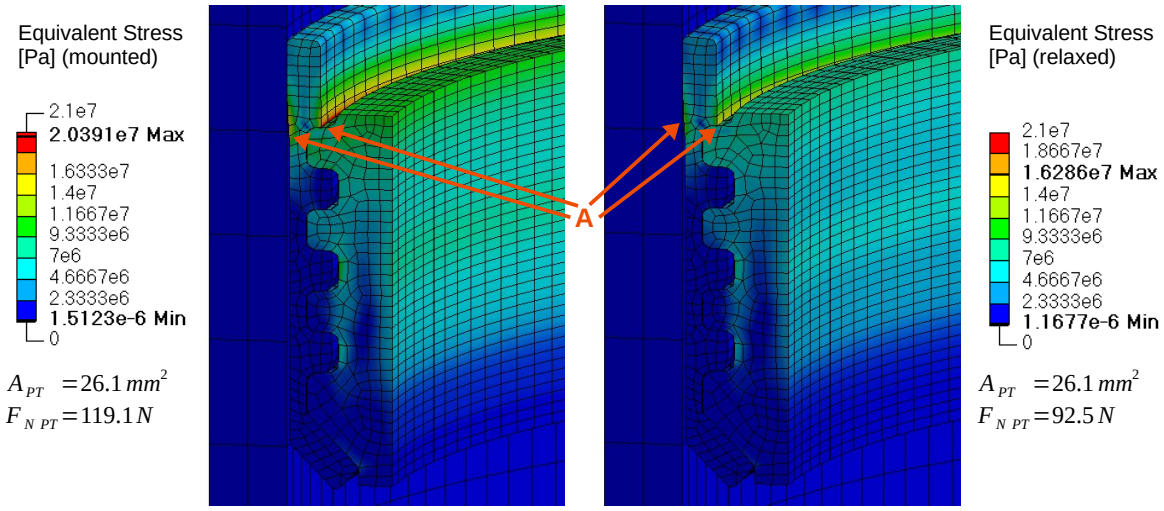

Illustration 8.1: Comparison of the equivalent stress distribution of the piston / tube FEM setup before (left) and after (right) material relaxation time with the resulting contact area A_{PT} and the circumferential piston band / tube contact normal force $F_{N\,PT}$

The stress distribution in both panels of 8.1 is plausible and quantitatively within a reasonable range, and follows qualitatively the deformation distribution. Thus, the average equivalent stress level of the piston band is higher especially at the transition to the end lip and almost zero in the rest of this part, since only the end lip is significantly deformed due to the contact resolution. The highest equivalent stress is reached at the upper end of the piston / piston band contact (A), which is caused by the combination of comparatively large deformations due to the deformation of the seal lip, and the bonded contact definition between the piston band and

the piston, which prevents any relative movement there. This is likely to be different in reality, where at least small relative contact movement should be possible, even if the mounting process ensures a reasonably solid connection [64]. This high stress however only appears for the adjacent node, and is therefore unlikely to falsify the friction result. The comparison of the left panel and right panel of 8.1 shows the overall decrease of the equivalent stress during a phase of $30\,min$ standstill, best visible near (A). This decrease is expected, since the PTFE material model shows significant relaxation behavior, and the deformation-determining boundary conditions are constant. For the contact state, the relaxation phase results in an insignificant increase of contact area $(+0.02\,\%)$, but a significant decrease of circumferential contact normal force $(-22.3\,\%)$, which is directly influencing the friction model, as discussed below.

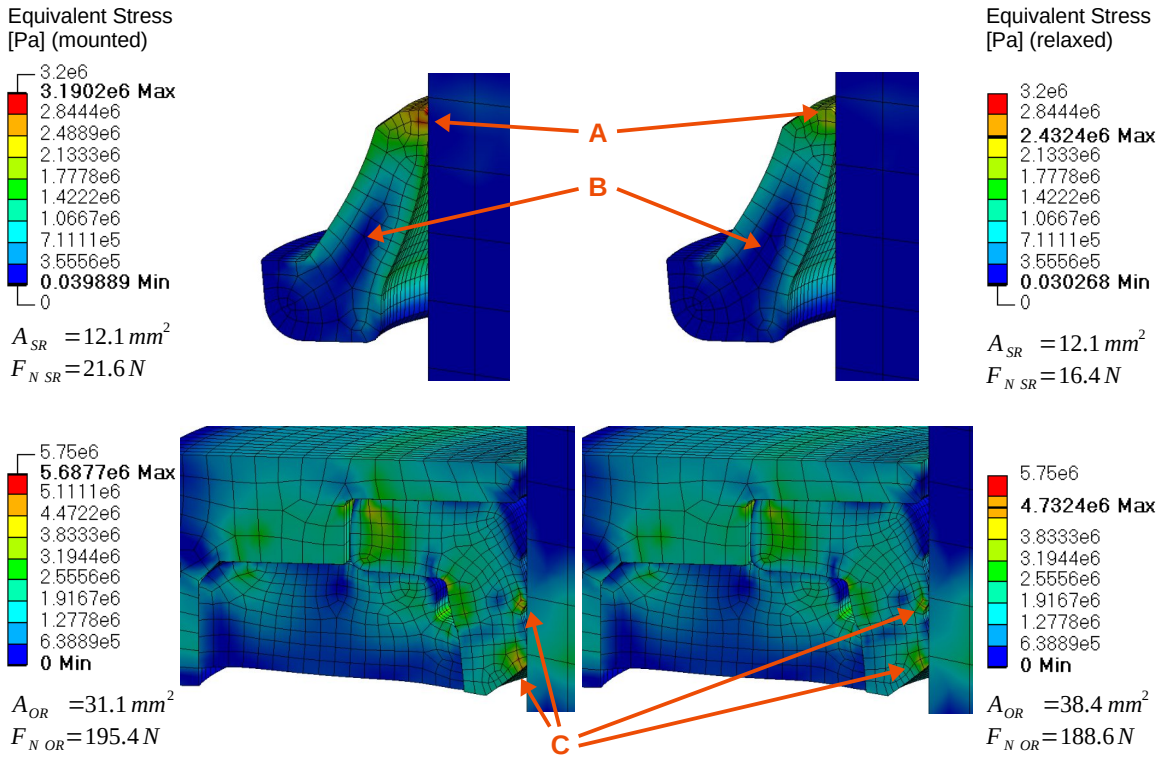

Illustration 8.2: Comparison of the equivalent stress distribution of the rod guide assembly / rod FEM setup, divided into the scraper / rod contact (top) and the oil seal / rod contact (bottom) before (left) and after (right) material relaxation time, with the resulting contact areas A_{SR} and A_{OR}, and the circumferential scraper / rod and oil seal / rod contact normal forces $F_{N\,SR}$ and $F_{N\,OR}$

The equivalent stress distribution of the rod guide assembly / rod friction point is depicted in 8.2, where the left panel shows the equivalent stress distribution just after mounting, and the right panel shows the equivalent stress distribution after additional $30\,min$ of standstill to ensure proper material relaxation, as explained above. The related overall equivalent stress decrease of the scraper / rod pairing is best visible near the contact zone (A) and by the enlarged blue area within the scraper's body (B). The scraper / rod contact shows no unexpected behav-

ior, since no further parts or boundary conditions are involved. The contact resolution shows good convergence represented by barely visible body penetration, and the qualitative equivalent stress distribution is reasonable considering the boundary conditions and the deformation distribution. Because of the much softer seal material as compared to the piston band, the quantitative stress range is one magnitude smaller than the stress range of the piston / tube friction point mentioned above. Because of the much smaller contact area and the much softer seal material, the resulting contact normal force is much smaller than within the piston / tube friction point, even if the deformation of the scraper is larger than the deformation of the piston band. Because of the simple setup without further influences on the bodies, the contact area change resulting from the material relaxation phase is insignificant $(+0.05\,\%)$, while the change of the contact normal force is significant $(-24.0\,\%)$, but reasonable following the material formulation from Chapter 7.2.2.

The oil seal / rod contact behavior is significantly different from that of all other seal / counterpart contacts because of the additional impact from the static pressure-loaded static seal. This part is transmitting the damper's static operating pressure to the oil seal / rod contact due to its geometric and material properties. The therefore increased oil seal / rod contact pressure ensures the tightness of the oil seal, especially in high-speed scenarios. The consequence of the combination of oil seal, static seal and static pressure is a significantly increased average stress level in both the oil seal and the static seal, as compared to the scraper. This equivalent stress level is decreasing during the relaxation phase, as expected, which is best visible at the contact zones (C), but as well through the more pronounced blue shading within the less deformed parts of the seals. Simultaneously, the oil seal / rod contact area increases much more significantly than at the scraper / rod contact or at the piston band / tube contact $(+23.4\,\%)$. This increase is caused by the ongoing deformation of the relaxing static seal, leading to even further increased pressure on the oil seal. As a consequence, this influence of the static seal on the oil seal leads to an only slightly decreasing circumferential contact normal force in the oil seal / rod contact during the relaxation phase $(-3.4\,\%)$.

The equivalent stress distribution of the floating piston / tube friction point is shown in 8.3. The depiction convention resembles that of the illustrations above: The left panel shows the equivalent stress distribution just after mounting, and the right panel shows the equivalent stress distribution after additional $30\,min$ of standstill to ensure proper material relaxation. Both the O-ring / tube and the O-ring / floating piston contacts are resolved well and determine the O-ring's deformation. The equivalent stress distribution is visibly asymmetric due to the tangential seal stresses which are generated by the overall diameter widening of the O-ring (see Chapter 7.2.1). The equivalent stress distribution is therefore plausible following the deformations experienced by the O-ring. The quantitative stress level of the floating piston's O-ring is lower than the overall stress level in the other seals due to the moderate deformation and the softest material (see Chapter 7.2.2). During the relaxation phase, the O-ring's overall stress level decreases according to the material modeling, which is visible by the virtually complete disappearance of red shadings in the right panel of 8.3. This distinct decrease of equivalent stress leads to an insignificant contact area increase $(+0.08\,\%)$ and a significant

circumferential contact normal force decrease $(-15.9\,\%)$, which is in the same range of the other seal / counterpart contacts, with the exception of the oil seal.

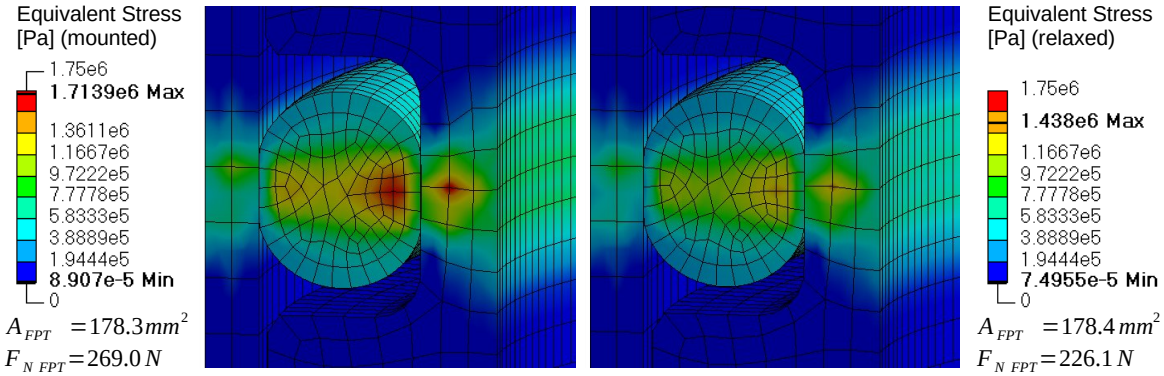

Illustration 8.3: Comparison of the equivalent stress distribution of the floating piston / tube FEM setup before (left) and after (right) material relaxation time with the resulting contact area A_{FPT}, and the circumferential O-ring / tube contact normal force $F_{N\,FPT}$

All resulting contact normal force changes of the seal / counterpart contacts during the material relaxation phase are plotted together in 8.4. The contact normal force F_N is directly influencing the friction force generated in the FEM contact by the friction model, as introduced in Chapter 7.2, and is therefore a very important parameter with regard to the overall friction simulation behavior. However, it should not be investigated without consideration of the contact geometry and contact discretization, since both influence the derived contact area, as discussed in Chapter 8.4.2. Notwithstanding these considerations, the qualitative F_N change during the relaxation phase represents the qualitative change in expected friction generation, and is therefore worth being investigated.

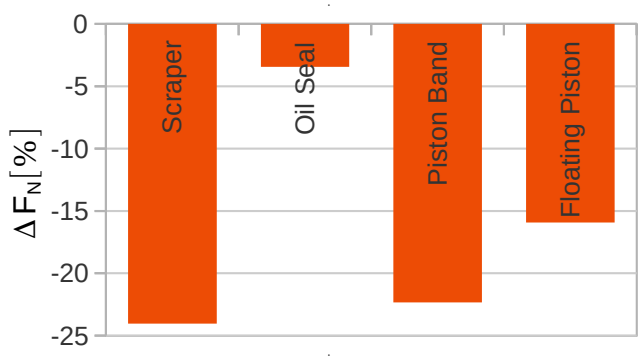

Illustration 8.4: Contact normal force change (in percentage) during the material relaxation phase, depicted for each seal / counterpart FEM contact

The general expectation for the development of F_N during the relaxation phase is a significant decrease, as is experienced by the scraper / rod contact, the piston / tube contact and the float-

ing piston / tube contact in 8.4. However, in certain setups with additional influences through third bodies or external boundary conditions, a less significant contact normal force decrease or even a contact normal force increase during the relaxation phase is possible, as experienced by the oil seal / rod contact. Consequently, it is not clear if the circumferential contact normal force F_N is increasing or decreasing, or if the amount of F_N change estimable with acceptable accuracy prior to a friction simulation, if viscoelastic material behavior occurs similar to the simulations setups of this dissertation. This is why appropriate material modeling, as performed in Chapter 7.2.2, is crucial for the accuracy of seal / counterpart friction simulations.

8.3 Analysis of the Simulated Friction Force Behavior

This chapter presents the results of the overall friction simulation, i.e. the friction simulation results achieved by the application of the solution approach introduced in Chapter 3, and documented in detail in Chapter 7. As shown in 3.1, geometry data, operation conditions and material properties are implemented into a structural FEM model with overlaid friction model in the detected contact zones. The friction results can only be analyzed after the inverse contact normal force sensitivity Ω is tuned to match the midstroke friction force of FEM simulation data and SFP measurement data (see Chapter 8.1). Since the quantitative deviations between SFP measurements and FEM simulations are therefore already minimized, the analysis of the simulation results focuses less on quantitative deviations and is more focused on qualitative effects.

8.3.1 Analysis of the Piston / Tube Friction Simulation

Given that the friction behavior of the piston / tube friction point has already been proven to mimic typical LuGre behavior almost perfectly, influences on the friction behavior which are caused by the FEM implementation can be clearly isolated from further external effects. To achieve the above-mentioned quantitative match of midstroke friction, the inverse contact normal force sensitivity of the piston tube contact is determined to $\Omega_{PT} = 92.8\,N$. Since the qualitative force-displacement and force-speed friction behaviors are already covered accurately by the applied LuGre parameter set (see Chapter 7.3.1), the FEM model is expected to accurately match the graphs of this single friction point as well. This expectation is fulfilled, as presented in 8.5, in which the FEM force reaction to the displacement boundary condition at the piston is compared to SFP measurement results. Both the FEM force-displacement graph and the FEM force-speed graph match well with their SFP measurement counterparts. It has been shown that the small force oscillations visible in the experiment's force-displacement graph are induced by the test rig (see Chapter 5.1), which is confirmed here as they are not occurring in the simulated friction behavior.

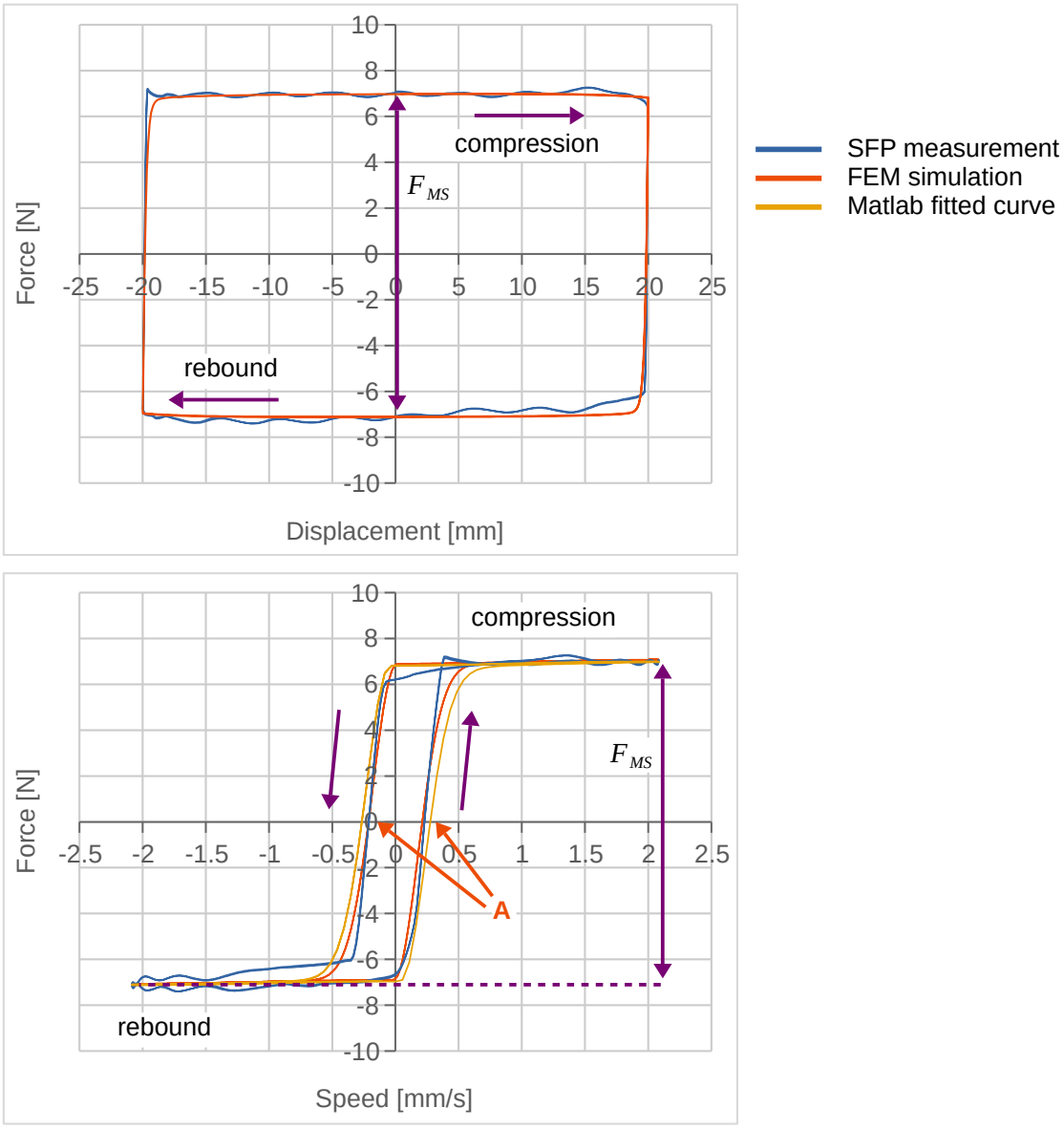

Illustration 8.5: Comparison of the FEM simulation and SFP measurement of the friction behavior of the single friction point piston / tube

The only change in shape between the FEM model and the resulting force-speed graph is the slight widening of the pre-sliding hysteresis compared to both the measurement data and the Matlab fit. The width of the pre-sliding hysteresis is mainly determined by σ_0 and σ_1 from the LuGre model formulation. The parameter estimation routine performed as documented in Chapter 7.3 tunes these parameters to qualitatively fit the measurement data. As shown in 8.5 (bottom), the Matlab parameter determination results in a curve that is perfectly matching the SFP measurement graph at the zero crossing (A), as already discussed in Chapter 7.3.1. This zero-crossing match with the SFP measurement data is not valid for the force-speed graph of the FEM simulation, where the pre-sliding hysteresis of the FEM simulation is slightly wider than the pre-sliding hysteresis of the SFP measurement and the Matlab fit. The reason for this

behavior is to be found in the deformation behavior of the seal lip in the FEM simulation due to the applied friction force. The seal lip acts as an additional spring-damper combination, which changes its deflection during speed changes and displacement reversals. This deflection behavior is visualized in 8.6 by the comparison of the displacement boundary condition (orange) applied to the piston and the axial distance (blue) between the end lip of the piston band (A) and the displacement application face of the piston (B) during the friction recording phase. As shown in 8.6, the axial distance between (A) and (B) is decreased during rebound (the spring-damper combination is compressed) and is increased during stroke (the spring-damper combination is stretched). The shape of this deflection therefore explains the small deviations in qualitative friction behavior.

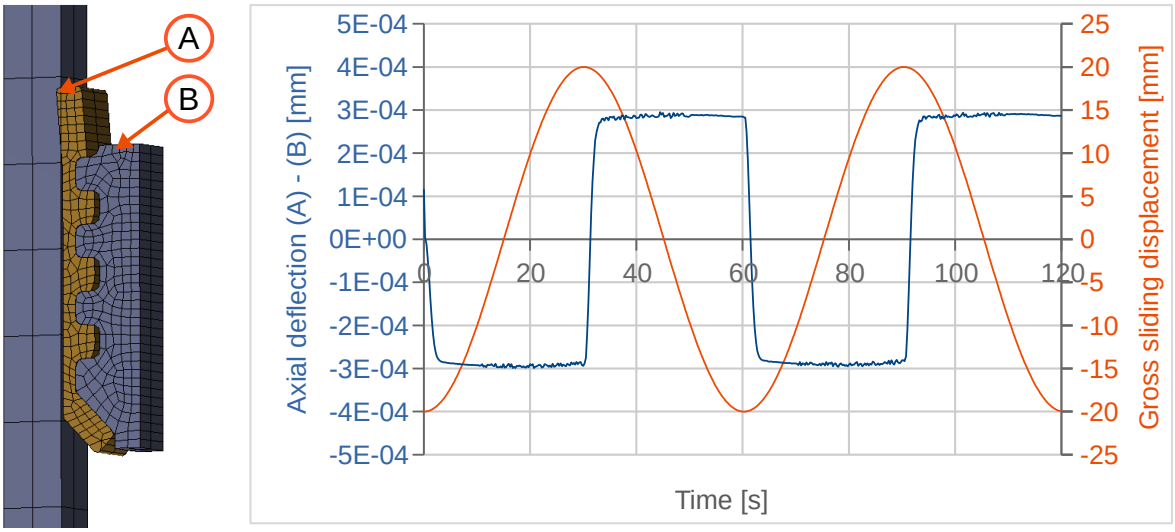

Illustration 8.6: Left panel: FEM model of the piston / tube friction point including the end lip of the piston band (A) and the displacement application face of the piston (B). Right panel: Comparison of the displacement boundary condition applied to the piston (orange) and the distance between (A) and (B) (blue) during the friction recording phase

The axial (A) – (B) distance change (the spring-damper deflection) is maximum $\pm 0.0003\,mm$ in this case. Despite this very low value, it is influencing the friction behavior: The amount of spring-damper deflection visualized in 8.6 is dependent on the viscoelastic material data of the piston band (see Chapter 7.2.2), and on the friction force generated in the piston band / tube contact. The amount of friction in the piston band / tube contact is also dependent on the material data, given that the material data determines the contact normal force due to the lateral deformation of the seal. The amount of friction in the piston band / tube contact is further dependent on the amount and rate of the displacement boundary condition of the piston, of the seal lip's axial spring-damper deflection, the contact normal force sensitivity and the LuGre parameter set. As a consequence of the dependency on these various parameters, the individual contribution of the additional spring-damper combination behavior of the seal lip to the friction behavior can not be easily determined or corrected. The SFP measurement data represents merely the friction force versus displacement and speed between the actuated piston and

the tube. All occurring lip seal deflection, which contributes to the pre-sliding hysteresis of the recorded friction behavior, is already covered in the LuGre parameter set through the Matlab fit, and therefore covered twice in the overall FEM friction simulation model: The seal lip deflection occurring in the FEM simulation is added to the LuGre pre-sliding deflection in the contact zone. Since the additional spring and damper of the seal lip are linked in parallel to each other, but in series to the spring and damper modeling of the LuGre model, their contribution to the overall deformation and stress level results in a decrease of spring stiffness and damper rate. According to the LuGre modeling, this decrease of spring stiffness and damper rate can be understood as a decreasing σ_0 and σ_1 , and therefore leads to an underestimation of tangential contact stiffness and tangential contact damping. Consequently, a widening of the pre-sliding hysteresis of the FEM simulation according to the SFP measurement data and the Matlab fit has to occur, as outlined in Chapter 2.2.2. As a result, the FEM friction graph in 8.5 (bottom) behaves as expected.

Despite these expected difficulties, the width difference of the pre-sliding hysteresis of the FEM model compared to the SFP friction measurement in 8.5 (bottom) is very small, which implies only a weak link between microscopic and macroscopic material behavior. This is crucial and has to be ensured for all friction points, because the simulation methodology developed and applied within this dissertation strictly separates macroscopic material behavior as input parameters for the structural FEM setup, and microscopic material behavior as input parameters for the dynamic friction model. To ensure the separability of macroscopic and microscopic material behavior in general, [70] investigated the influence of the change of the Prony parameters on the friction result in a very straightforward and thus tightly controlled simulation setup. It was shown that the Prony parameters do not significantly influence the qualitative shape of the friction simulation results. Nevertheless, the quantitative amount of friction is influenced by the Prony parameters, because the friction force is determined by the contact normal force generated by the seal deformation. Thus, the contact normal force (and with that the quantitative amount of friction) is material-side dependent on the material's initial stiffness, the material's relaxation modeling and the amount of time passing prior to the friction recording phase, as considered during the choice of the material modeling for the simulation setup.

In summary, the simulation result of the piston / tube friction point resembles the SFP measurement with high accuracy, proving the general applicability of the friction simulation methodology of this dissertation. The slightly underestimated tangential contact stiffness and contact damping, resulting in a slightly overestimated pre-sliding hysteresis width, is model-immanent, but (at least for this friction point) not significant. However, the influence of the macroscopic material behavior on the qualitative shape of the force-displacement and force-speed graphs should be considered when analyzing similar simulation results.

8.3.2 Analysis of the Rod Guide Assembly / Rod Friction Simulation

As depicted in 8.7, the FEM friction simulation curve of the rod guide assembly / rod friction point matches the SFP measurement curve with an accuracy that is expected from the LuGre parameter estimation in Chapter 7.3.2. The quantitative fit is achieved by the determination of the inverse contact normal force sensitivity of the rod guide assembly / rod contact to $\Omega_{RGA\,R}=187.1\,N$, as introduced in Chapter 8.2. This value of $\Omega_{RGA\,R}$ is significantly higher than the inverse normal force sensitivity of the floating piston / tube contact $\Omega_{P\,T}$ $(+126.0\,\%)$. Consequently, when applying the same contact normal force, less than half of the friction of the rod guide assembly / rod friction point is generated per applied normal force in the piston / tube friction point, or the same contact normal force in the piston / tube friction point results in less than half of the friction compared to the rod guide assembly / rod friction point, assuming equal LuGre parameters sets for both contacts. This implies a significantly better lubrication state at the piston / tube friction point, since hydrodynamic friction is usually less affected by increasing normal force than dry or mixed friction (see Chapter 2.1). This implication is reasonable, given that the piston band / tube contact is facing damper oil from both sides, whereas the oil seal / rod friction point is only facing oil from the lower side, and the scraper / rod contact is experiencing lubrication only by leftover oil or additional grease on the rod.

Similar to the analysis of the piston / tube friction point, some qualitative deviations occur between the FEM simulation curve and the Matlab fit. The most significant deviations are the reduced height and width of the force overshoot after the motion direction turnaround from rebound to compression (A), the pre-sliding hysteresis, which is slightly shifted, but not significantly width-altered (B), and the slightly too-low force level of the FEM simulation over the whole decreasing-speed part from compression to rebound (C) of the friction recording phase. The blending function, which ensures smooth transition between the positive-speed and negative-speed LuGre parameter sets is also shown in 8.7 (ten times magnified for better visibility). By visualizing this function it is easily assessable, at which displacement or speed the respective parts of the parameter set are contributing to the description of the friction behavior. The depicted tanh function is achieved by the application of an amplification factor $amp=6000$ into equation (37) within the *lugre* subroutine. This value for *amp* has proven to be a good compromise of effectively smoothing out the step-like transition areas of the Matlab fit, while preserving the characteristics of the positive-speed side and the negative-speed side of the friction graph.

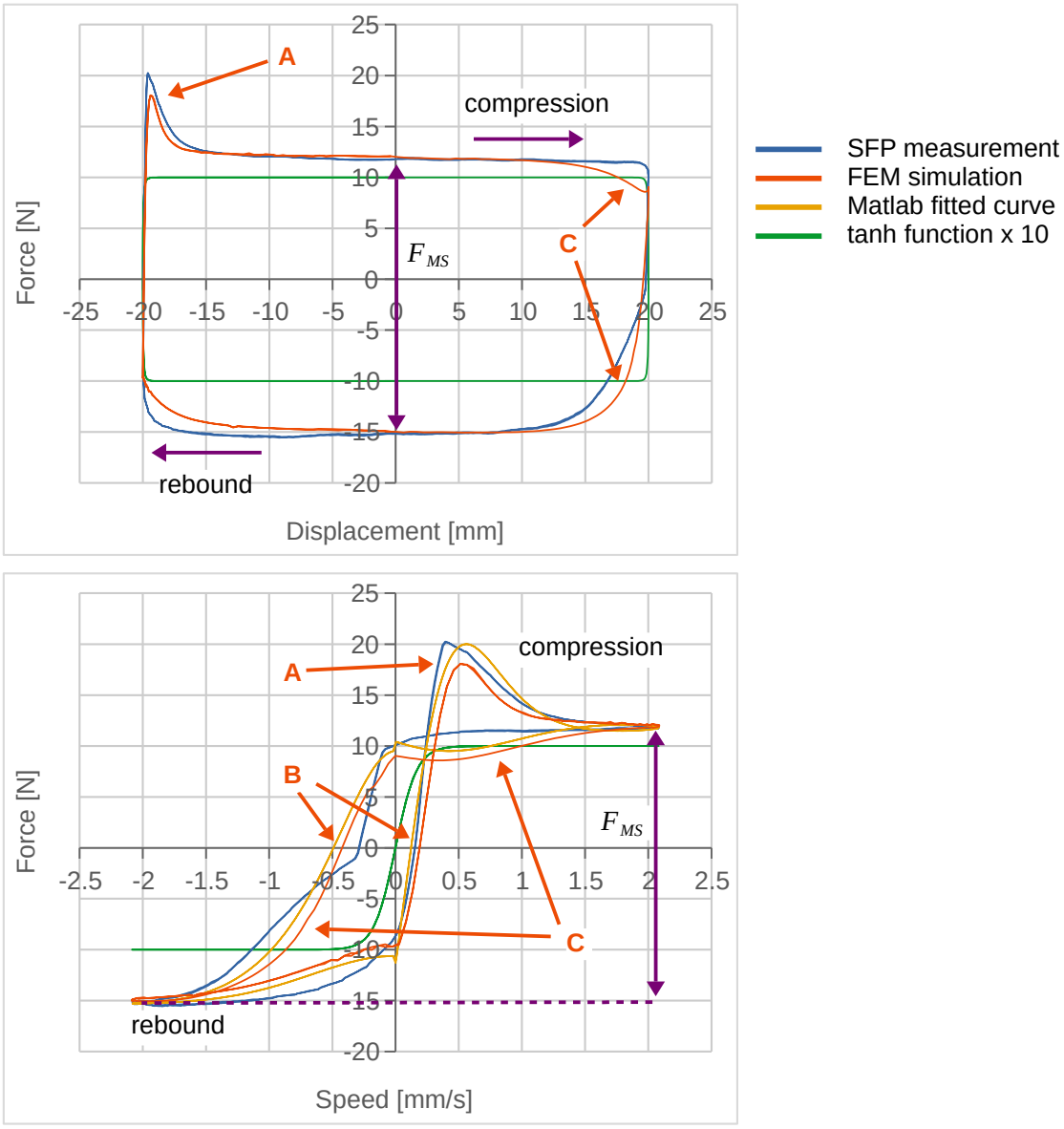

Illustration 8.7: Comparison of the FEM simulation and SFP measurement of the friction behavior of the rod guide assembly / rod single friction point

The reason for the above-mentioned qualitative differences in friction behavior between measurement and simulation, mainly on the positive-speed side, is most likely the same reason as for the qualitative friction graph deviations at the piston / tube friction point: Since the seals respond with axial deformation to the friction force generated in the respective contact zones while stroking, additional spring and damper elements are added to the friction simulation system. Given that the determining material stiffness and viscoelasticity are already covered by the corresponding LuGre parameter set, the friction describing contact damping and contact stiffness is underestimated. A more detailed discussion of this behavior and its influence on the friction behavior can be found in Chapter 8.3.1. Following these investigations, the deflection of the seals of the rod guide assembly / rod friction point, namely the scraper and the oil seal, is visualized in 8.8. For the rod guide assembly / rod single friction point, it is suffi-

cient to consider the axial deflection of the respective seal's contact zone. This simplification is possible, since both seals do not gross slide together with the part where the exciting displacement boundary condition is applied, as is the case for the piston band connected to the piston. Since the simulated friction in the contact zone acts as the exciting force to the seal deflection, the amount of deflection represents the amount of contact friction adequately and is therefore additionally worth to be investigated. The analysis of the contact force reaction in the underlying finite elements is not feasible here due to the shared topology of the oil seal / rod contact and the static pressure boundary condition on the oil seal, as already introduced in Chapter 8.1.

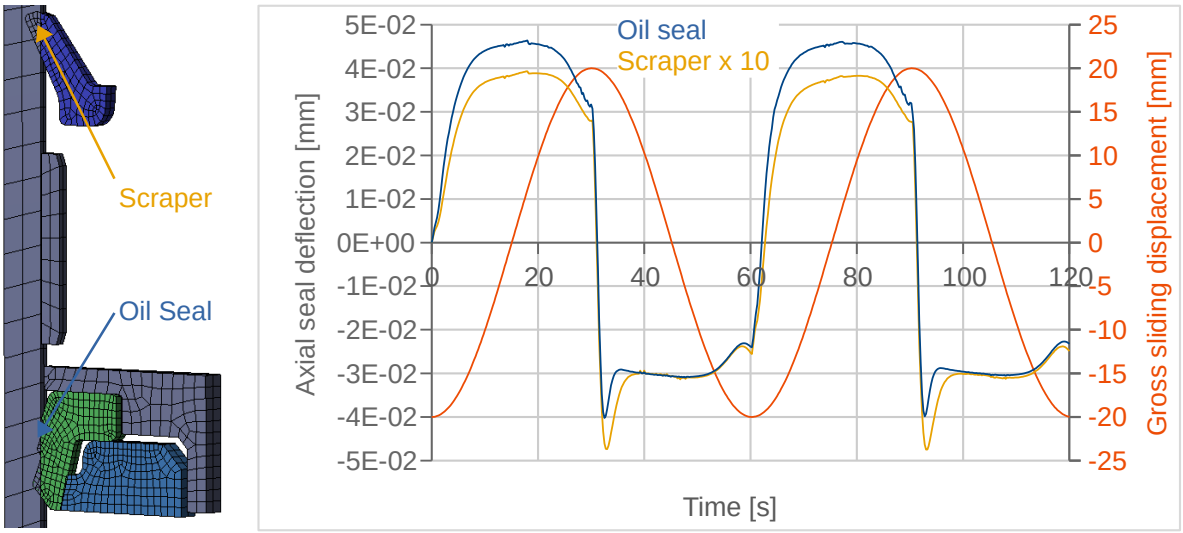

Illustration 8.8: Comparison of the axial contact zone deflection of the scraper and the oil seal inside the rod guide assembly / rod friction point against the displacement boundary condition of the rod during the friction recording phase

It should be noted that the actual friction contributions of the oil seal and the scraper are not separately investigated within the simulation setup, as already discussed in Chapter 7.3.2. The analysis therefore examines if the simulated friction contribution of both the oil seal and the scraper is reasonable, which is important to achieve realistic seal deformations within the FEM simulation. Comparing to the deflection of the piston band lip in 8.6, it becomes apparent that the scraper's deflection is one magnitude higher and the oil seal's deflection is two magnitudes higher as compared to the piston band's deflection. This difference in simulated deflection magnitude can be expected both due to the material stiffness differences, and due to the differences in contact normal force and contact area. While the piston band's stiffness is more than 20 times higher than the stiffness of both the scraper and the oil seal, the scraper's stiffness is still significantly higher than the oil seal's stiffness (see 6.1). Assuming the same amount of generated friction in the contact zone, a lower deflection would occur at the stiffer part, which is valid for the scraper and the oil seal, as demonstrated in 8.8. The mentioned contact normal force and contact area differences directly influence the friction between both seals of the rod guide assembly, following equation (31). While the resulting contact normal

forces of the piston band / tube contact and the oil seal / rod contact are of the same order of magnitude due to the contact pressure-increasing static seal (see Chapter 8.2), the contact normal force of the scraper / rod contact is one order of magnitude lower. The expectation is a friction force difference of one order of magnitude between the oil seal / rod contact and the scraper / rod contact, assuming equal contact normal force sensitivities for both contacts. While the actual contact normal force sensitivity for each contact zone can not be determined easily, given that the respective friction contribution would have to be determined as discussed above, the magnitude of the simulated friction contribution of oil seal friction and scraper friction are reasonable according to the discussed properties of the contact zones.

Seal deflections in an FEM friction contact as described in this dissertation cause qualitative changes of the friction behavior compared to the LuGre friction behavior, as already discussed in Chapter 8.3.1. Their most significant effect on the oil seal / rod friction zone is the distinct decrease of the overshoot peak compared to the scraper, as shown in 8.7 (A) and in 8.8. Since the above discussed seal deflection acts as a reduction of contact stiffness and contact damping to the overall friction behavior, and therefore as a reduction of the LuGre parameters σ_0 and σ_1, the decreased overshoot peak after passing the rebound-compression turn-around point is expected according to 2.12. The related decrease of the pre-sliding hysteresis width is not observed in 8.7 (B), a result which is most likely caused by the respective scraper and oil seal geometry, and by their opposed application within the rod guide assembly. Both the seal geometry and the opposed application push the oil seal and pull the scraper at rebound and vice versa.

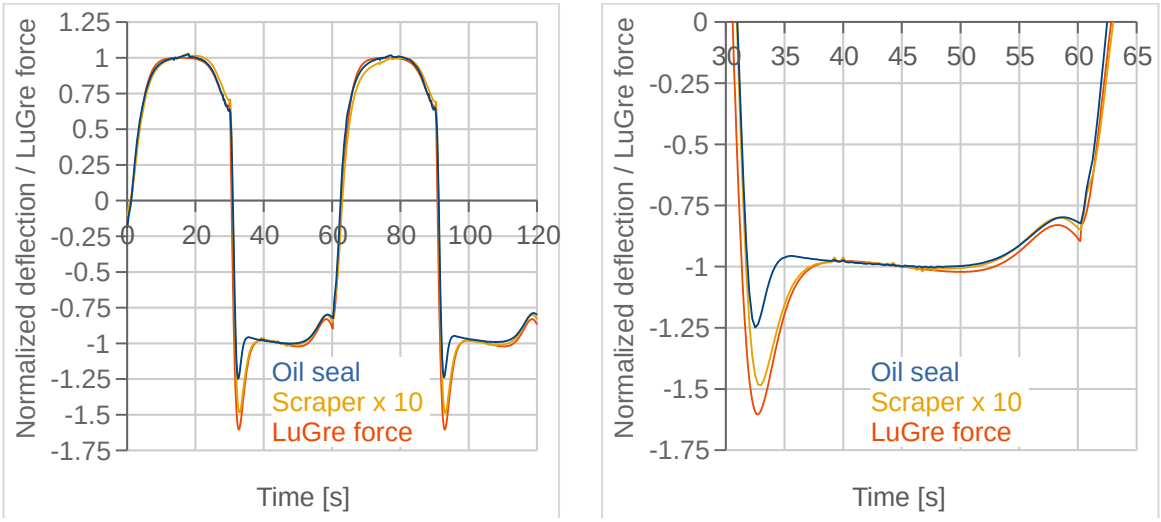

Illustration 8.9: Normalized oil seal and scraper deflection compared to the normalized LuGre force during friction recording phase (left); magnified between 30 *s and* 65 *s (right)*

To illustrate the contribution of both the scraper and the seal lip to the qualitative change in friction behavior as compared to the expected friction behavior from the LuGre parameter set, the scraper's and the oil seal's axial deflection representing their friction behavior, and the Lu-

Gre friction force are depicted in 8.9, all of them normalized to their respective midstroke value. Here, especially on the right panel of 8.9, which shows a magnified part of the left panel, the relative contribution to the decrease of the overshoot peak is visible: While the scraper shows only a small relative decrease, the oil seal's decrease of the overshoot peak is significant. Transferred to the quantitative results, in which the friction contribution of the oil seal is one order of magnitude larger than the contribution of the scraper, this shows a clear responsibility of the oil seal for this qualitative deviation. Another significant observation in 8.9 is the shift of the overshoot peak towards lower speeds (oil seal) and towards higher speeds (scraper). This contrasting behavior is also most likely caused by the geometry and opposed application of the seals within the rod guide assembly, as already mentioned above. This peak-shifting behavior explains the shifted but not significantly width-altered pre-sliding hysteresis in 8.7 (B).

In summary, the friction results of the FEM simulation of the rod guide assembly / rod friction point still resemble the related SFP measurements with high accuracy. The reasons for the qualitative deviations towards the Matlab fitted LuGre curve are both the slightly underestimated tangential contact stiffness and the contact damping. Even if the force overshoot peak after the rebound-compression turn-around is model-immanently underestimated ($-9.5\,pps$ force peak deviation compared to the SFP measurement), all other qualitative characteristics, especially the pre-sliding hysteresis width, are sufficiently recovered. The deviations are most likely caused by the counteracting seal geometries and seal applications within the rod guide assembly. Altogether, the influence of the macroscopic material behavior on the qualitative shape of the force-displacement and force-speed graphs is noticeable, but predictable in its tendency and still acceptably small.

8.3.3 Analysis of the Floating Piston / Tube Friction Simulation

The force-displacement and the force-speed results from the FEM friction simulation compared to the SFP measurement of the floating piston / tube friction point with a displacement amplitude of $\hat{A}_{FP\,comp} = 18.5\,mm$ are shown in 8.10. The quantitative fit of the midstroke friction $F_{MS\,comp}$ is achieved by the use of the inverse normal force sensitivity of the floating piston / tube friction point $\Omega_{FP\,T} = 225.2\,N$, as introduced in Chapter 8.2. This $\Omega_{FP\,T}$ is 172.0 % higher than $\Omega_{P\,T}$ and 20.4 % higher than $\Omega_{RGA\,R}$, implying an overall even less lubricated state than in the rod guide assembly / rod friction point. This interpretation is reasonable for the same reasons discussed in the section above, given that one side of the floating piston's O-ring is only lubricated with almost non-existent leftover oil on the tube due to near zero leakage. The qualitative match of the measurement and simulation graphs in 8.10 is very accurate, and in that respect comparable to the eminently well matching piston / tube friction graphs in 8.5. Even with this very accurate match, especially towards the related Matlab fit, the axial seal deflections during motion deserve to be discussed, just as in the previous two sections. Since the axial movement of the O-ring is locked via a remote point (see Chapter 7.2.6) only the axial deflection in the contact zone that is related to an O-ring rotation around its cross section is possible.

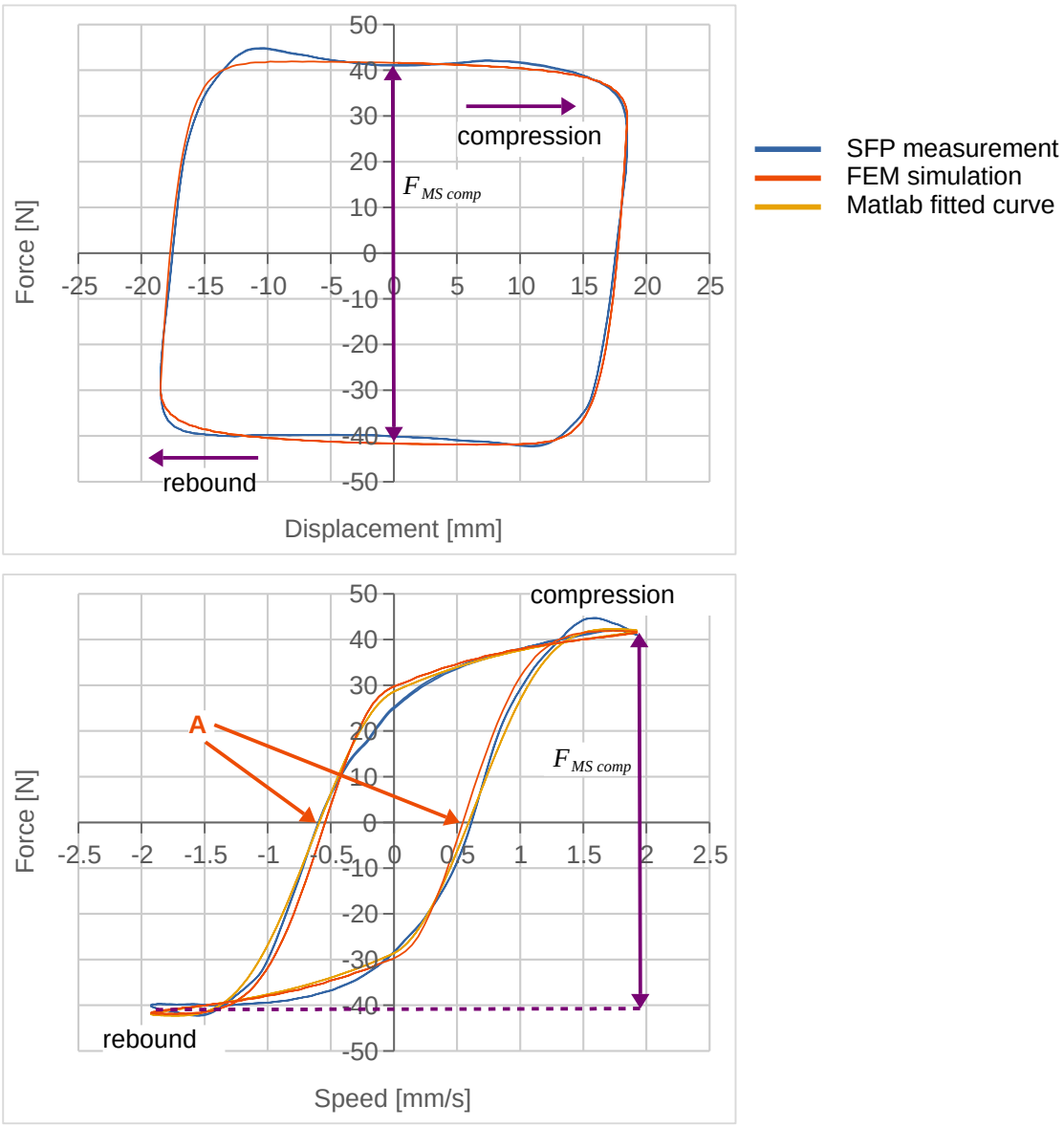

Illustration 8.10: Comparison of the FEM simulation and the SFP measurement of the friction behavior of the single friction point floating piston / tube with a displacement amplitude of $\hat{A}_{FP\ comp} = 18.5\,mm$

As shown in 8.11, the amount of this axial seal deflection is of a similar magnitude as the axial seal deflection of the rod guide assembly / rod friction point (see 8.8). Since the material data of the seals of both friction points are equally comparable, similar influences on the friction behavior could be expected due to the systematically underestimated tangential contact stiffness and damping, as already discussed in the sections above. However, the width change of the pre-sliding hysteresis in 8.10 (A), which is driven by σ_0 , is barely visible and furthermore in the opposite direction: The width of the pre-sliding hysteresis of the FEM friction simulation is slightly smaller than the pre-sliding hysteresis width of the Matlab fit. Since σ_1

is already near zero in this simulation (see 7.15), a further decrease of the tangential contact damping causes no visible effect in the simulation. Possible reasons for the counter-intuitive behavior of the FEM simulation compared to the Matlab fit are differences between solving the friction model in the contact zone and the LuGre model in the Matlab script, or influences on the friction behavior by the artificial stabilization by help of the remote point to achieve convergence in the FEM model. Since the FEM friction graph and the Matlab fit graph match nearly perfectly, further investigations into these reasons have not been performed.

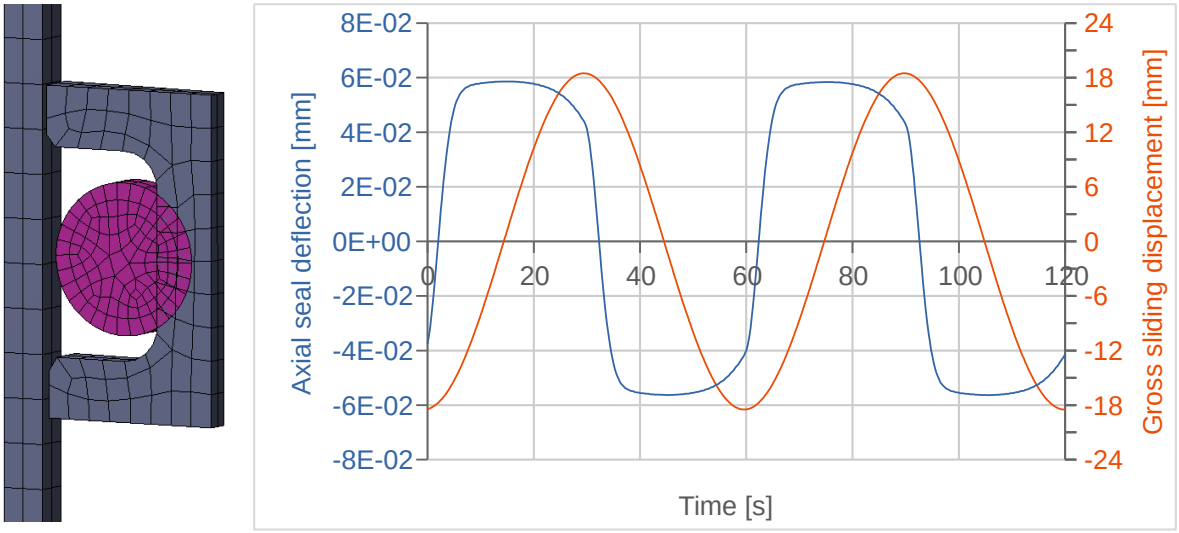

Illustration 8.11: Comparison of the axial contact zone deflection of the floating piston's O-ring against the displacement boundary condition of the rod during the friction recording phase with a displacement amplitude of $\hat{A}_{FP\,comp} = 18.5\,mm$

Following equation (29), the actually occurring motion sequence of the floating piston during the reference friction measurement sequence has an amplitude of $\hat{A}_{FP\,act} = 1.85\,mm$, with a period of $T = 60\,s$, as introduced in Chapter 5.3. Since the parameterization of the related friction measurements with $\hat{A}_{FP\,act}$ emerged not to be useful for the FEM friction simulation (as already discussed in Chapter 7.3.3), the parameter set of $\hat{A}_{FP\,comp}$ including the above-mentioned value for $\Omega_{FP\,T} = 225.2\,N$, is transferred to the $\hat{A}_{FP\,act}$ investigations. The friction model parameters are transferable, since they describe the friction behavior in the microscopic contact zone, the properties of which should not change with differing displacement boundary conditions. The presented results of the $\hat{A}_{FP\,act}$ FEM friction simulation while using the $\hat{A}_{FP\,comp}$ parameter set is therefore additionally an investigation of the transferability of parameter sets.

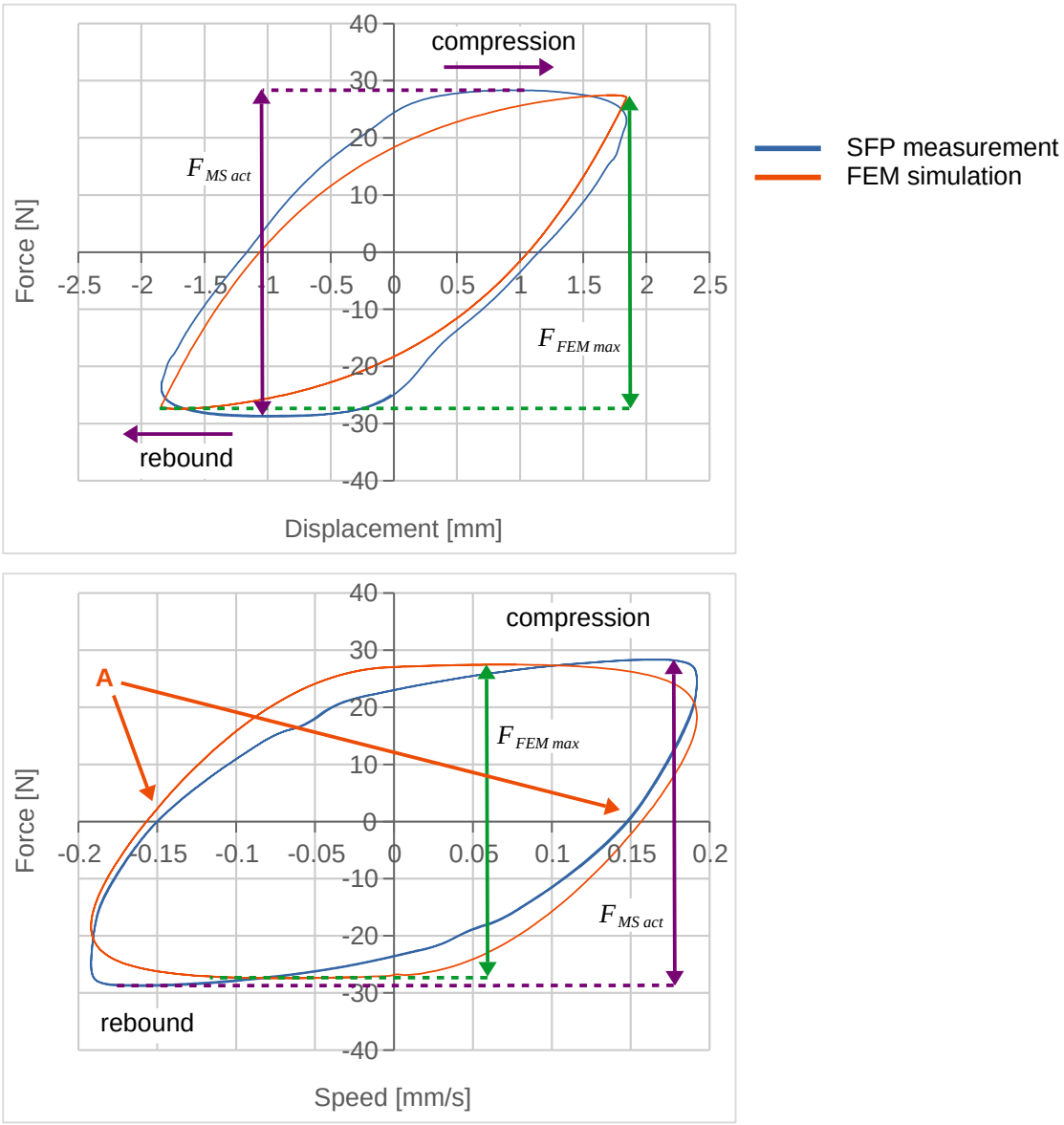

Illustration 8.12: Comparison of the FEM simulation and SFP measurement of the friction behavior of the single friction point floating piston / tube with a displacement amplitude of $\hat{A}_{FP\ act} = 1.85\,mm$

The mentioned friction simulation results are depicted in 8.12. Usually midstroke friction is used to characterize the quantitative damper friction, which is difficult for both the $\hat{A}_{FP\ act}$ measurements and simulations, since no constant friction plateau is reached at midstroke. That is why, the characterizing $F_{MS\ act}$ was defined as the difference of the two friction force plateaus which are reached at compression and rebound displacement (see Chapter 5.3). This definition is not useful for the analysis of the $\hat{A}_{FP\ act}$ FEM friction simulation, since a constant friction plateau is reached neither at midstroke, nor later in the force-displacement graph of 8.12. Given that the midstroke friction $F_{MS\ act}$ is characterized by the maximum friction in the floating piston / tube friction point, also the maximum friction $F_{FEM\ max}$ of the FEM simulation

is used for comparison here. This course of action is especially sensible, since the force speed graph in 8.12 (bottom) shows almost constant maximum friction over the speed range where $F_{FEM\ max}$ is obtained.

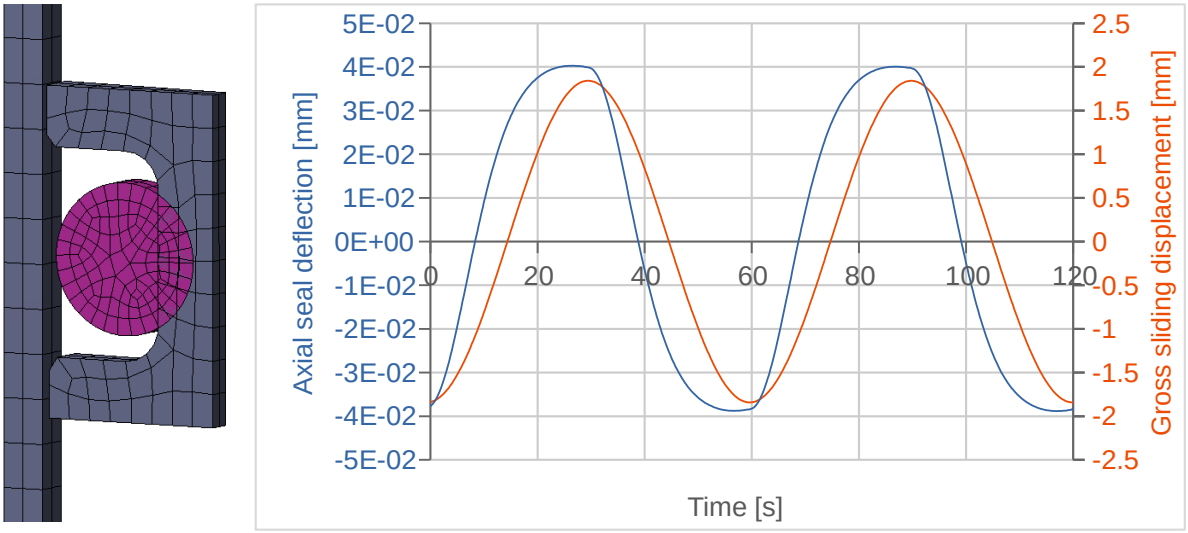

Illustration 8.13: Comparison of the axial contact zone deflection of the floating piston's O-ring against the displacement boundary condition of the rod during the friction recording phase with a displacement amplitude of $\hat{A}_{FP\ act} = 1.85\,mm$

Both panels of 8.12 show that the deviation between $F_{FEM\ max}$ and $F_{MS\ act}$ is acceptably low ($-3.9\,\%$ for $F_{FEM\ max}$), which proves the transferability of the inverse normal force sensitivity $\Omega_{FP\ T}$. The quantitative deviation between the FEM simulation graph and the SFP measurement graph is significantly larger for $\hat{A}_{FP\ act}$ as compared to $\hat{A}_{FP\ comp}$ (see 8.10). However, the qualitative shape is still similar, which proves the transferability of the LuGre parameter set to different motion cases. While counter-intuitively narrower in the $\hat{A}_{FP\ comp}$ simulation, the hysteresis width of the $\hat{A}_{FP\ act}$ simulation is now wider than the hysteresis width of the SFP measurement (8.12 (A)). Consequently, the tangential contact stiffness altering seal deflections in the contact zone are investigated in 8.13. As demonstrated there, the magnitude of simulated seal deflection is obviously smaller according to the lower friction level compared to the $\hat{A}_{FP\ comp}$ simulations. However, since the contribution of the seal deflections of the $\hat{A}_{FP\ comp}$ simulation is considered not to be significant, as mentioned above, it is considered even less significant for the $\hat{A}_{FP\ act}$ simulation. As a consequence, the reasons for the qualitative deviations of both graphs of 8.12 are most likely to be found in the very-low displacement amplitude and the artificial axial locking of the O-ring aiming to achieve convergence in the FEM model. While the latter is obviously changing the system's friction behavior, the very low displacement amplitude of the $\hat{A}_{FP\ act}$ results in a friction behavior which is – according to the LuGre parameter set – never leaving the pre-sliding range. This is unique for all investigated friction points, and not the optimal application for the LuGre model (see Chapter 2.2.2).

However, the qualitative deviations between the $\hat{A}_{FP\,act}$ FEM simulation and the SFP measurement are still sufficiently small, especially when considering the number of necessary, but friction behavior influencing actions mentioned above. Together with the very low quantitative deviation of only $-3.9\%\ F_{FEM\,max}$, it is therefore shown that the floating piston / tube friction point is described in its friction behavior with sufficient accuracy by the introduced friction modeling approach.

8.4 Validation

In the previous chapter it is shown at the example of the floating piston / tube friction point that the friction modeling approach of this dissertation allows to transfer friction model parameter sets to different motion cases. In this chapter first the superposition of the FEM friction simulation results of the single friction points is compared to the unit-level damper friction measurement discussed in Chapter 5.4. Second, it is investigated if the transferability of the LuGre parameters and the inverse normal force sensitivity Ω is also maintained for varying seal geometries. Thus, this chapter aims to validate this dissertation's methodology of damper friction simulation introduced in Chapter 7, on the basis of the friction measurement methodology discussed in Chapter 4.

8.4.1 Comparison of FEM Simulations and Unit-Level Measurements

As already shown, separating the overall damper friction into the respective contributions of the single friction points is valid. This conclusion is tested in Chapter 5.4 based on the two single friction point test rigs SFP1 and SFP2, for which the superposed single friction point measurements resemble the unit level measurement with only minor deviations. These minor deviations are most probably caused by the unknown motion behavior of the O-ring in the floating piston's groove. This section follows the same approach and compares the superposition of the three FEM single friction point simulations as discussed in the Chapters 8.3.1 to 8.3.3 with the unit-level measurement from Chapter 5.4. It should be noted that the FEM simulations and their friction model parameters are based on single friction point measurements that contain different friction related parts than the unit-level measurement, namely a different piston and piston band, a different rod guide assembly with the related oil seal / static seal / scraper combination, and a different floating piston and O-ring. Both qualitative and quantitative deviations are therefore expected, mainly because of geometry deviations, but also because of various other uncertainties such as misalignments through the mounting process, differing lubrication states, differing seal material and surface properties. However, to prove the overall applicability of the friction simulation method in this dissertation, these deviations should be sufficiently small.

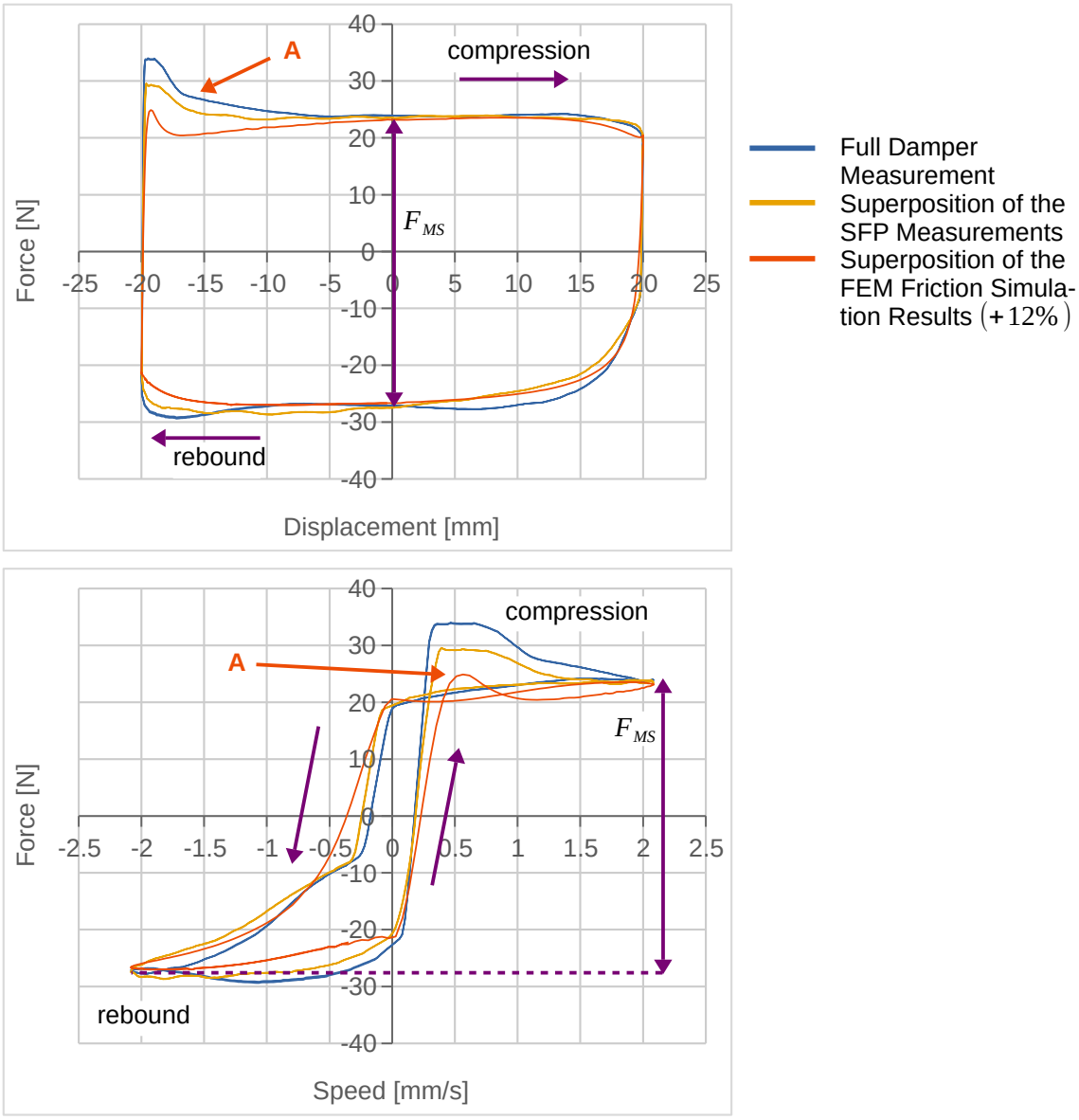

Illustration 8.14: Comparison of the full take-apart damper friction measurement, the superposition of the SFP measurements, and the super-positioned FEM friction simulation results; floating piston / tube friction contribution with regard to equation (29)

The results of the superposition of all three single friction point FEM simulations as compared to the superposition of all three single friction point measurements and to the full damper friction measurement are shown in 8.14. It should be noted that the contributing floating piston / tube friction is weakened with regard to equation (29), due to the hydraulic amplification discussed in Chapter 4.3.2. Since the midstroke friction of the superpositioned FEM data is too low compared to the measured data, 8.14 shows the FEM friction graph amplified by +12 % , which enables matching midstroke friction and thus a better qualitative comparison. This quantitative midstroke friction deviation of 12 % is acceptably low, especially considering the above-mentioned uncertainties. In contrast, the qualitative deviations are quite large, especially during the acceleration phase after the rebound-compression turn-around (8.14 (A)). At

this point, the expected significant overshoot peak is only very small and is almost comparable in its magnitude to the maximum friction force near midstroke. The most likely reason for this behavior is the unknown motion behavior of the floating piston / tube friction point, caused by the design and measurement principle of SFP2 as already discussed in Chapter 5.4. Given that the LuGre parameterization is aiming for perfect reproduction of this uncertain friction behavior, the characteristics and uncertainties of the SFP2 measurements are also transferred to the FEM friction simulation, in which the LuGre parameter set is applied.

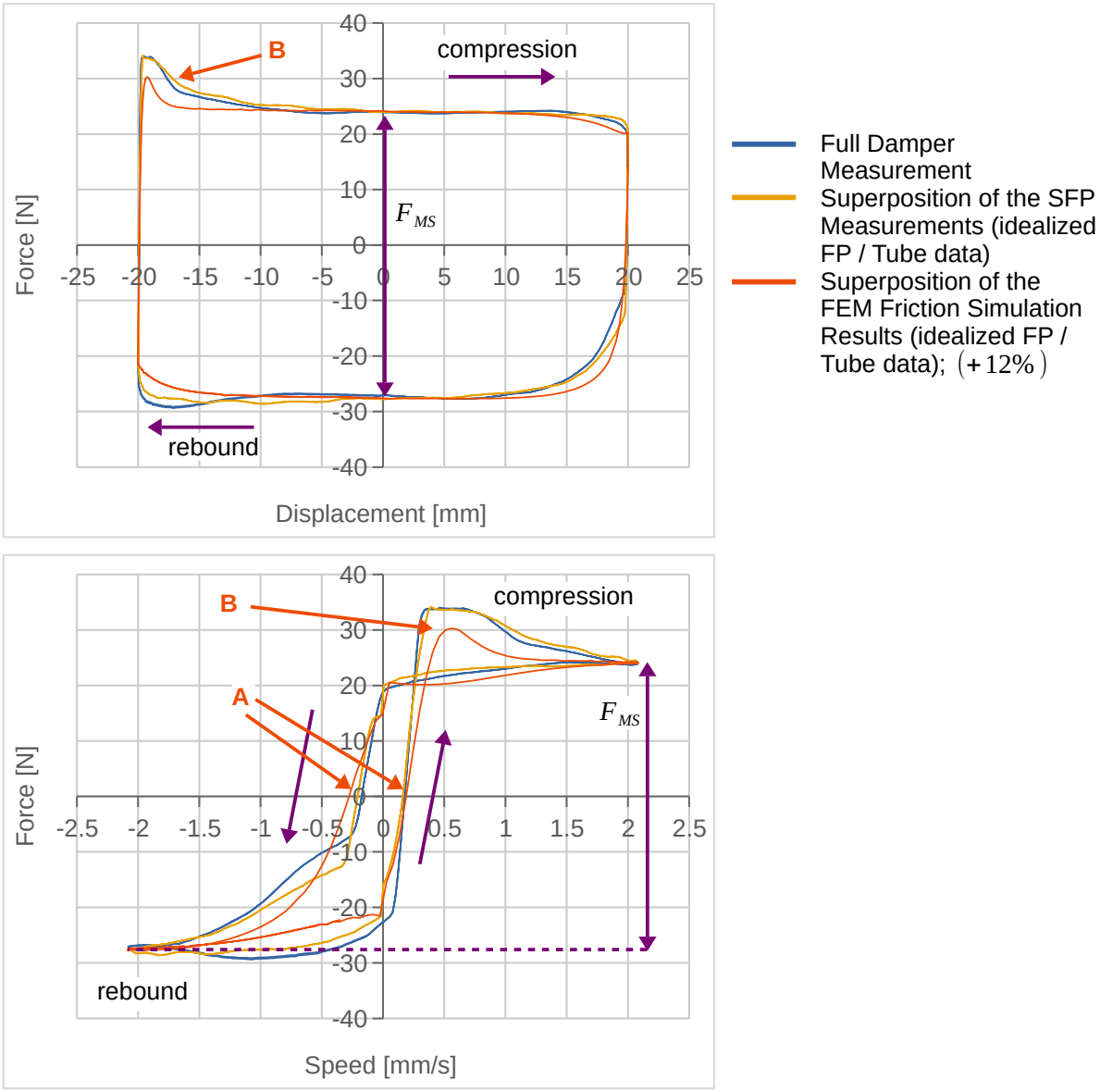

Illustration 8.15: Comparison of the take-apart full damper friction measurement, the superposition of the SFP measurements, and the super-positioned FEM friction simulation results

To prove this assumption, the contribution of the floating piston / tube FEM friction simulation is replaced by an artificial and idealized Coulomb-like friction behavior, coincident to

Chapter 5.4. The resulting force-displacement and force-speed friction graphs are depicted in 8.15 with a +12 % amplified FEM friction graph to achieve matching midstroke friction. The change in friction behavior is as expected: While the accuracy of the midstroke friction is not altered, the qualitative friction behavior shows a much better match. The remaining deviations match the expectations from the findings about the qualitative deviations of the FEM friction graphs compared to the SFP friction graphs in Chapter 8.3.1 and 8.3.2. Because of the systematically underestimated tangential contact stiffness and tangential contact damping, the width of the pre-sliding hysteresis in 8.15 is slightly smaller (A), and the height of the overshoot peak after the rebound-compression turn-around is significantly lower (B) than in the full damper measurement.

In summary, the friction simulation methodology proves to be sufficiently robust against small variations of geometry and material data, as they occur when replacing similar parts. The resulting quantitative deviation is within the acceptable measurement deviation, and therefore sufficiently small. The qualitative deviations mainly result from the uncertainties of SFP2 and the already discussed underestimation of tangential contact stiffness and tangential contact damping, which is caused by the imperfect separability of microscopic and macroscopic seal deformation due to friction.

8.4.2 Friction Model Parameter Transfer to Different Geometry

The main target of this section is to demonstrate the transferability of the friction model parameters to a target geometry that is different from the source geometry originally used for the parameter estimation. Since all friction model parameters describe the microscopic properties of the friction contact of the source geometry, these properties have to be similar between the source geometry and the target geometry. For this test, the reference damper introduced in Chapter 4.1 is investigated with an alternative geometry. In this alternative geometry, the diameter of the rod and the related rod guide assembly is increased for applications with increased lateral load. While the outer rod diameter and the inner rod guide assembly diameter is increased to $d = 14\,mm$, the design principle of this part assembly remains equal to the original $11\,mm$ setup. The $14\,mm$ geometry still consists of a scraper, a bearing, and an oil seal showing three seal lips, while all applied material is the same as for the $11\,mm$ setup. Consequently, the microscopic properties in the friction contact of the $14\,mm$ setup can be assumed to be similar to the $11\,mm$ geometry, thus allowing for the transfer of the $11\,mm$ (source) friction model parameter set to the $14\,mm$ (target) geometry.

The geometry of the simulation setup is abstracted from the real $14\,mm$ geometry and is subsequently discretized following the pre-processing methodology introduced in Chapter 7.2. The resulting mesh is depicted in 8.16 (left). In comparison to the $11\,mm$ geometry (8.16 center and right) it becomes apparent that the scraper's contact geometry is quite similar, even if the back sides of the scrapers are differently shaped. The contact zone of the $14\,mm$ oil seal shows initial penetration only between the lower seal lip and the rod (A), while the $11\,mm$ oil seal shows additional initial penetration of the center lip (B). As a consequence, the contact zone of the $11\,mm$ and the $14\,mm$ oil seal / rod contact is expected to be shaped differently.

The application of the material models, the contact modeling, the friction modeling, and the boundary conditions remains similar to the 11 *mm* setup, as do the solver choice and solver settings (see Chapter 7). The applied friction model parameter set consists of the LuGre parameters of the 11 *mm* rod guide assembly rod contact (see 7.14) and the inverse normal force sensitivity $\Omega_{RGA\,R} = 187.1\,N$ determined in Chapter 8.3.2.

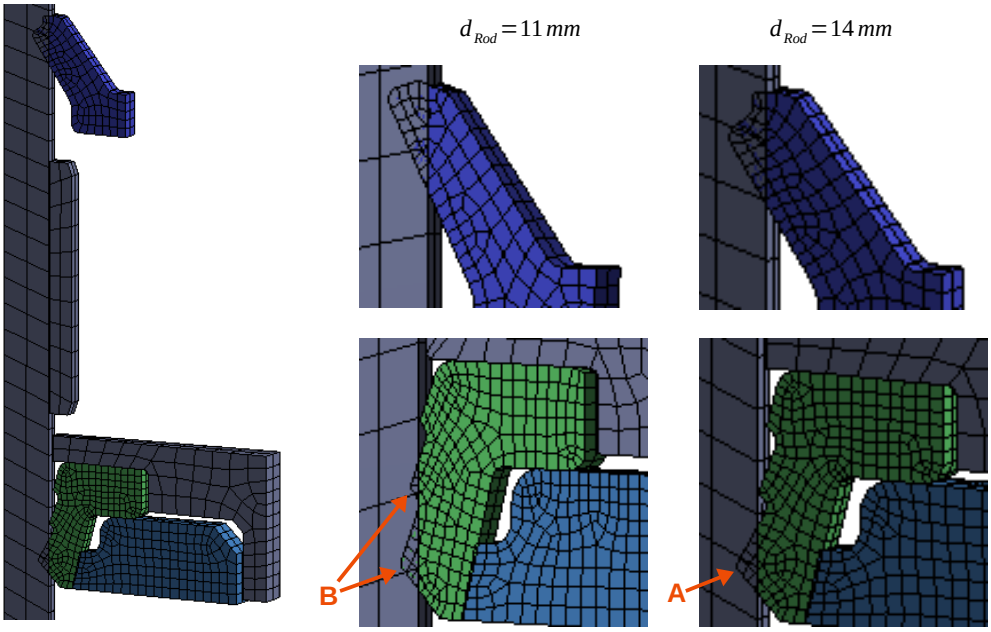

Illustration 8.16: Mesh overview of the 14 *mm rod diameter geometry (left); comparison of mesh details of the* 11 *mm (center) and the* 14 *mm rod diameter geometry (right)*

The resulting equivalent stress distribution is depicted in 8.17 just after mounting (left panel) and after additional 30 *min* of standstill to ensure proper material relaxation. Generally, the scraper behavior is observed to be similar as compared to the 11 *mm* setup: The highest equivalent stress level occurs near the contact zone (A) and the material relaxation is best visible by comparing this area (A) and through the increase of blue shaded area in the middle part of the scraper (B). While the contact area remains almost unchanged during the relaxation phase $(+0.1\,\%)$, the contact normal force decreases significantly $(-23.9\,\%)$. In contrast, the behavior of the oil seal / rod coupling of the 14 *mm* setup differs from the 11 *mm* setup more significantly because of the initially non-penetrating center lip of the oil seal. Since the static seal and the oil seal experience further deformation during the relaxation phase, this center lip comes into contact, which can be noticed by the slightly increased equivalent stress level near this seal lip contact (C), and by the even larger increase of the contact area $(+45.6\,\%)$ during the relaxation phase as compared to the 11 *mm* setup (see Chapter 8.2). The equivalent stress level of the 14 *mm* oil seal and static seal is decreasing during the relaxation phase similar to the 11 *mm* setup, as expected, which is best visible at the contact zones and by the more pronounced blue shading within the less deformed parts of the seals. Due to the ongoing static seal deformation and the static operating pressure of 25 *bar* , the contact normal force also in-

creases slightly during the relaxation phase $(+3.4\,\%)$, which is counter-intuitive, but possible, as already discussed in Chapter 8.2.

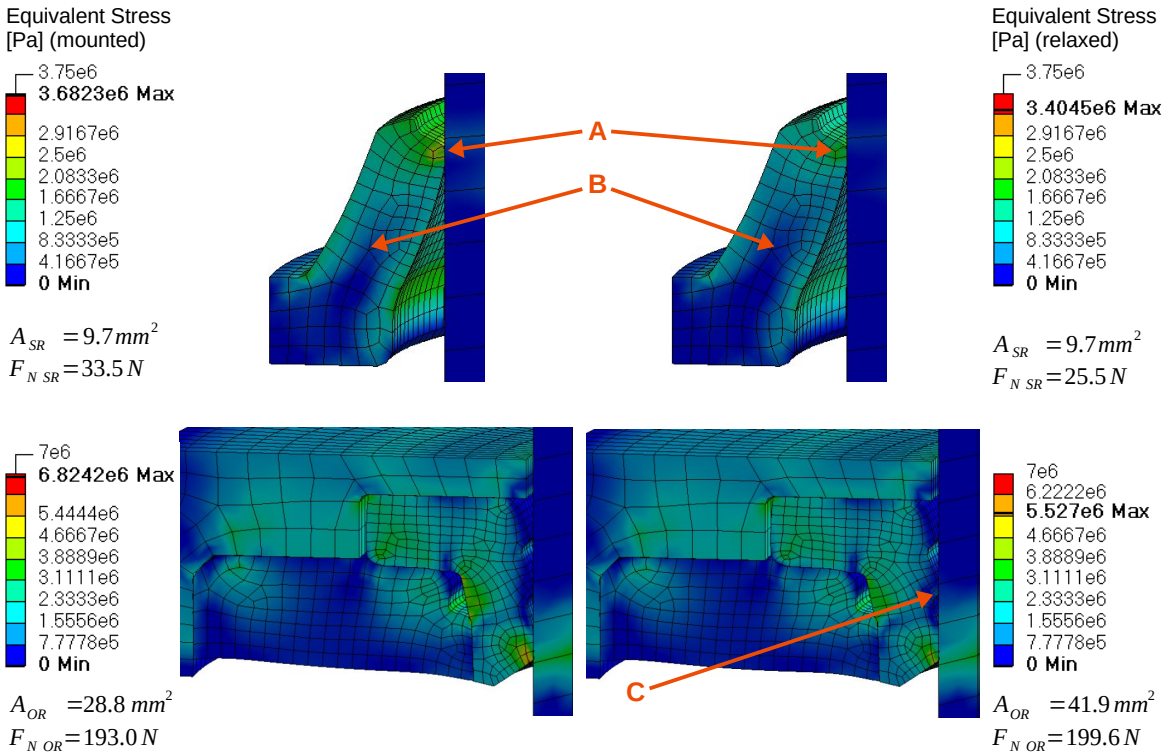

Illustration 8.17: Comparison of the equivalent stress distribution of the 14 mm rod guide assembly / rod FEM setup, divided into the scraper / rod contact (top) and the oil seal / rod contact (bottom) before (left) and after (right) material relaxation time with the resulting contact areas A_{SR} ; A_{OR} and the circumferential scraper / rod and oil seal / rod contact normal forces $F_{N\,SR}$; $F_{N\,OR}$

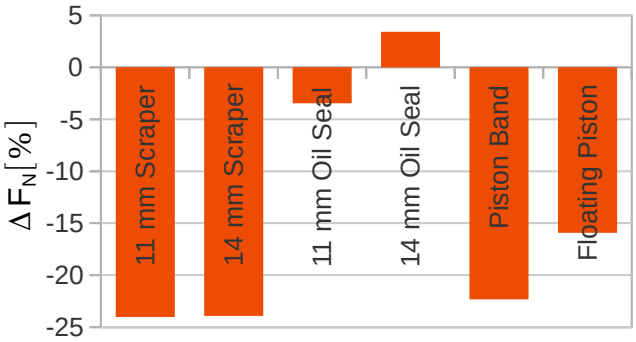

Illustration 8.18: Contact normal force change (in percentage) during the material relaxation phase, depicted for each seal / counterpart FEM contact

To put the changes in the contact normal forces during the relaxation phase into relation to the previously investigated FEM setups, 8.18 compares all of them in one diagram. While the

14 *mm* scraper behaves as expected with almost zero difference to its 11 *mm* equivalent, the increase in contact normal force during the relaxation phase of the 14 *mm* oil seal / rod contact is unique for all friction contacts within this dissertation.

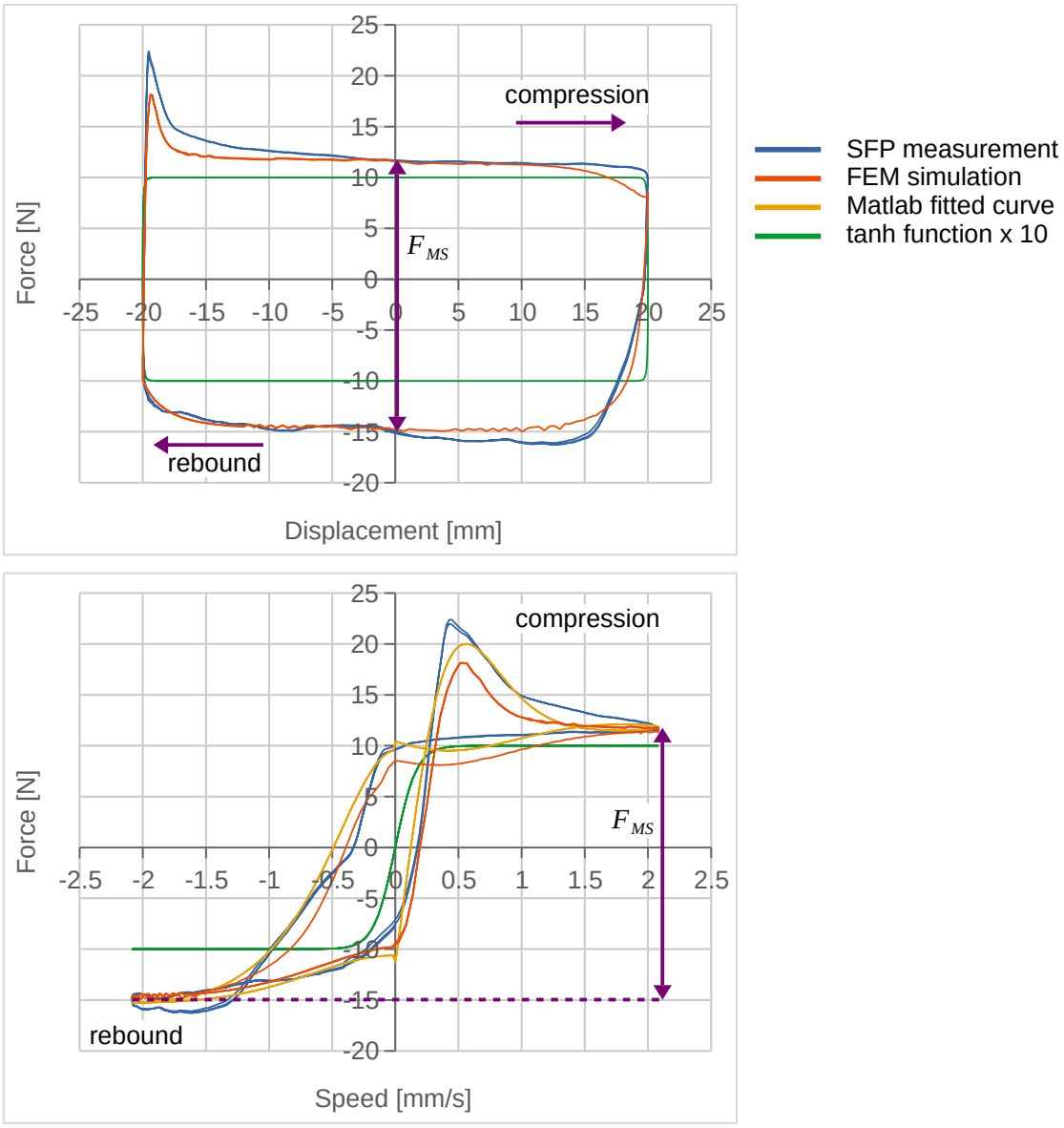

Illustration 8.19: Comparison of the 14 *mm rod FEM simulation and SFP measurement of the friction behavior of the rod guide assembly / rod single friction point*

The friction simulation results from the 14 *mm* rod guide assembly / rod FEM setup compared to the respective 14 *mm* SFP measurements are shown in 8.19. These 14 *mm* SFP measurements are easily obtainable, since the tube diameter remains the same for both the 14 *mm* and 11 *mm* rod guide assembly / rod coupling, as already introduced above. Consequently, the existing single friction point test rig SFP1 can be used for the 14 *mm* friction measurement by simply replacing the rod and the rod guide assembly (see Chapter 4.3.1). The pre-conditioning

sequence and the friction recording sequence remain identical to the 11 *mm* reference damper (see Chapter 4.2), as do the methods to determine the friction point's speed, the shifting of the raw measurement data to an average zero, and the investigation of only cycle two and three of the three recorded friction cycles (see Chapter 5). The qualitative shape of the force-displacement and the force-speed graphs in 8.19 are similar to the reference SFP1 graphs in 5.4. The quantitative characteristics are similar as well, e.g. the pre-sliding hysteresis width, the width of the overshoot peak shortly after the rebound-compression turn-around, and the generation of an almost constant friction level at midstroke. Only the height of the mentioned overshoot peak is significantly higher at the 14 *mm* rod guide assembly / rod friction point, namely 7.7 *pps* higher force peak deviation to midstroke friction compared to the 11 *mm* measurement. The midstroke friction of the 14 *mm* friction measurement of the rod guide assembly / rod friction point is almost equal to the equivalent 11 *mm* measurement $(-0.74\,\%)$, which is of course within the measurement uncertainty.

In a rubber-metal pairing, a larger contact area is expected to lead to a higher friction (see Chapter 2.1.2), under the assumption of similar contact pressure. Additionally, due to the similar initial penetration of the seals into the rod visible in 8.16, higher contact normal forces are expected in the 14 *mm* setup, since the seal-deforming rod perimeter is larger. As expected, the achieved 14 *mm* FEM contact normal forces are +8.9 % higher than the 11 *mm* equivalent, suggesting an increased friction force. In contrast to this expectation, as mentioned above, practically identical midstroke friction occurs in both the 11 *mm* and the 14 *mm* measurements, and practically identical midstroke friction is derived from the FEM simulation setup ($-1.5\,\%$ compared to the 14 *mm* measurement). Consequently, simply implementing normal force sensitivity to a LuGre model is not sufficient for this complex kind of friction simulations. To illustrate this complication, an accordingly simplified friction simulation approach would be set up as follows: The motionless FEM simulation of the single friction point would be used only to determine its related circumferential contact normal force, while the inverse contact normal force sensitivity derived thereof would be implemented into a therefor modified LuGre model, solved for instance in Matlab. This simplified approach would significantly reduce the setup and simulation effort, but it would lead to deviating friction results (expected +8.9 % in this example as mentioned above). It has to be noted that the contact normal forces presented within the equivalent stress depictions (e.g. 8.17) represent the sum of all contact normal forces derived in each contact element in the contact zone of the single friction point. These per-element contact forces are derived from the back-substituted element stresses and the contact area, which is estimated by the number and location of contacting element integration points on the contact side (see Chapter 7.2.3). Especially for round geometries, such as in the friction contacts of this dissertation, the accuracy of the contact area estimation is highly dependent on the quality of the local spatial discretization. Consequently, comparing contact normal forces obtained for friction contacts with different geometry and discretization is sensitive to discretization errors.

Despite these complications, the comparison of contact normal forces of unvarying discretization, as performed within this dissertation is – at least qualitatively – valid. Nevertheless, the

quantitative investigation of results that are dependent on the contact area should be used with caution. This limitation applies the above-mentioned contact force deviation of +8.9 % between the 11 *mm* setup and the 14 *mm* setup, since setups with different geometries and thus different spatial discretizations are compared. However, the overall force equilibrium is reached with good convergence for both setups. Thus, the force reactions to the displacement boundary conditions of the rod actuation, which represent the overall friction of the single friction point, are much more reliable, and additionally more similar to each other.

Two important results have therefore been presented in this section. First, it has been proven that the friction simulation methodology introduced within this dissertation allows for a friction model parameter transfer to a different geometry, under the assumption that the microscopic material behavior and lubrication state is similar. The resulting midstroke friction deviation is negligible, while the qualitative friction behavior is resembled with sufficient accuracy. Second, it has been discussed that the investigation of contact area dependent variables should be performed with caution, since the contact area determination is highly dependent on the local spatial discretization. Consequently, the direct use of the FEM-determined contact normal force as an input parameter to a dynamic friction model is not recommended.

9 Summary and Outlook

9.1 Summary of Achievements

This dissertation seeks to better understand and model friction in automotive shock absorbers with the specific aim of identifying friction relevant parameters, and sufficiently accurate friction prediction early in the design stage. To achieve this, the friction generating contact zones in the automotive shock absorber are first identified, followed by an investigation into the state of the art of simulating lubricated friction in rubber / metal contacts. Out of the general modeling approaches “static friction modeling”, “dynamic friction modeling” and “physics-based friction modeling”, a hybrid approach is chosen, which physically models the macroscopic friction-related properties in a structural FEM simulation, while covering the microscopic friction-related properties via a dynamic friction model in the FEM contact zone. Macroscopic properties are the geometry of seals and counterparts (tube and rod), the related material data, and the operating conditions like static pressure and motion actuation. The microscopic properties address all friction-related influences in the contact zone, e.g. evolution of lubrication state, asperity interaction as a result of roughness height, actuation, stiffness and solid material damping, or viscous lubricant damping. This hybrid approach of combining structural FEM with dynamic friction modeling in the contact zone enables the consideration of the most friction-relevant physical parameters, while maintaining ease-of-use and acceptable simulation time. In modern engineering, accurate results have to be obtained in tightly timed design cycles. Since this dissertation’s friction modeling approach aims for applicability in common engineering, both sufficient accuracy and acceptably low simulation time are crucial.

The above-mentioned hybrid friction simulation approach has to be parameterized with material data and a parameter set for the dynamic friction model in the contact zone. While the material data can be obtained on a standard tensile tester, the friction model parameter sets are unique for each single friction point. Consequently, single friction point test rigs have to be developed and set up for both the independent analysis of the friction point’s behavior, and the determination of the dynamic friction model’s parameter set. The results of the test rig design process are two single friction point test rigs, where one allows to independently investigate the friction behavior of the rod guide assembly / rod friction point and the piston / tube friction point (SFP1), while the second allows to independently investigate the floating piston / tube friction point (SPF2). SFP1 uses a direct actuation principle, allowing for direct force estimation via two strain-gauge force sensors. Key features of SFP1 are the perfect reproduction of the friction-relevant circumstances in the original damper, the easy exchangeability of the friction related parts, and the possibility of friction investigation under constant and stroke-independent static operation pressure. Because SFP2 aims to perfectly reproduce the friction-relevant circumstances of the full damper in the floating piston / tube friction point, it requires an indirect actuation of the floating piston via pressure differences. Consequently, only an indirect friction measurement principle can be used, which is achieved by the use of a pressure

difference sensor. The other key features of SFP2 – easy exchangeability of the friction-related parts, and the possibility of friction investigation under constant and stroke-independent static operation pressure – are similar to SFP1. The results of the investigation of the single friction points show first a relatively simple and controllable friction behavior with typical pre-sliding displacement for the piston / tube friction point. Second, the related rod guide assembly / rod friction point behavior is distinctly asymmetric and direction-dependent, and shows pronounced frictional lag and non-reversible friction behavior during the compression-rebound motion direction turn-around. Finally, even though the friction behavior of the floating piston / tube friction point is symmetric, its motion turn-around behavior leaves some uncertainties, given that the location of the floating piston's O-ring according to its groove is not fixed, and the subsequently performed comparison to a full damper measurement suggests a more piston / tube like friction behavior. However, the discussed comparison of all superpositioned single friction point measurements with a full damper measurement containing all three single friction points proves very accurate reproduction of the midstroke friction of all three single friction points, and very accurate (rod guide assembly / rod and piston / tube friction point) to still sufficiently accurate (floating piston / tube) reproduction of the qualitative friction behavior. The development of a robust, reliable, reproducible and modifiable platform for single friction point measurements is therefore achieved. The material characterization required for the subsequent material modeling within the FEM simulation shows a significantly viscoelastic and viscoplastic material behavior.

The setup of the above-mentioned overall simulation approach consists of the macro-scale FEM setup and the micro-scale dynamic friction modeling. The geometry abstraction follows a compromise of robust simulation, actual part shape and preferably straightforward transfer of CAD data. The material modeling follows the Prony Shear Relaxation modeling approach, allowing for the consideration of viscoelasticity, which results in distinct relaxation and creeping behavior. The viscoplastic material behavior during loading can be described by this modeling approach with sufficient accuracy, and the material behavior during full unloading is not of interest during friction simulation. Consequently, a very accurate reproduction of the actual material behavior is achieved with a low measurement and parameterization effort. The contact setup requires special caution, since its modeling significantly influences both the appropriate application of the friction model, and the convergence of the FEM simulation. In general, an enhanced penetration-based contact detection and modeling approach is used for all contact zones. The friction model application to the contact zone uses the Ansys *userfric* interface and applies a dynamic LuGre friction model with controllable normal force sensitivity. The spatial discretization results in a mesh, which balances the requirements of a fast and stable solution process, sufficiently fine contact resolution, and an appropriate element type choice. The choice of time-dependent boundary conditions and initial conditions aims to reproduce the initial conditions of the friction measurements as well as the friction measurement itself, which results in three main simulation phases: The mounting phase ends with a simulation state that represents a freshly mounted damper, the relaxation phase ensures proper material relaxation, and the friction recording phase simulates the actual friction measurement.

The parameterization of the dynamic LuGre friction model applied to the contact zones of the FEM setup is achieved through a Matlab script, which performs a parameter optimization based on friction measurement data from the related single friction points. While the parameterization of the piston / tube and the floating piston / tube friction point is quite straightforward, the significantly asymmetric friction behavior of the rod guide assembly / rod friction point results in the separation of two of the friction model parameters in speed-direction dependent equivalents, connected by a tanh blending function, which ensures smooth transition between the parameter sets near zero speed. The solver settings mainly aim for robust convergence, which is achieved by the selection of the fully asymmetric Sparse Direct Equation Solver of Ansys Mechanical with enforced use of line search algorithms. The so achieved calculation time per single friction point simulation is on the order of one hour on standard hardware.

The analysis of the friction simulations results in the depiction of appropriate part deformation and contact resolution with interesting insights into the seal behavior during relaxation and stroking. The reproduction of the friction behavior from the reference measurements is good, as could be expected from the accuracy of the friction model parameterization. The friction simulation slightly underestimates contact stiffness and contact damping, which is model-immanent due to the non-separability of microscopic and macroscopic seal deformation behavior. It is shown that the developed friction model parameters based on single friction point measurements can be transferred to the friction behavior of unit-level measurements. The validation of the methodology is further supported by the transfer of the dynamic friction model parameters to different friction point geometry, which results in remarkably small quantitative and sufficiently small qualitative deviations.

Therefore, the main research target defined in Chapter 3 is achieved, and valuable insights into the mechanisms which define the friction behavior of an automotive shock absorber are gathered. Even if not all of these friction mechanisms are fully understood or implemented into the friction simulation model, the findings can be summarized in three main achievements:

1. The measurement and characterization of the friction behavior of the single friction points is now possible with as yet unmatched accuracy, repeatability and ease of exchangeability. The respective contribution of each single friction point to the overall friction behavior is therefore easily analyzable.

2. The simulation of damper friction is now possible with high qualitative and quantitative accuracy, while requiring a reasonably small amount of parameterization and validation measurements, and remarkably low calculation time compared to the large number of considered friction-influencing parameters.

3. The investigations into the type and number of friction influencing parameters open a wide field for further optimization of automotive shock absorbers regarding friction. The most promising approaches address three topics: The general avoidance of misalignment-induced lateral forces in the single friction points, the need to reduce manu-

facturing tolerance induced geometry spread, especially of the seals, and the optimization of micro-scale properties in the contact zone, e.g. solid surface roughness and solid free energy, or fluid surface tension and viscosity.

9.2 Outlook

Given that the research performed in the context of this dissertation takes both measurement methodology and simulation into account, both of these fields of investigation allow further possibilities of improvement. These improvements can be separated into enhancements of the developed friction measurement and friction simulation methodology, and into further research on friction-influencing properties and parameters with subsequent implementation into the friction model. Most of the following research topics cover several of these fields, since the consideration of a new friction-influencing parameter usually leads to necessary changes in both the measurement and the simulation methodology, and vice-versa.

The most important advancement of the experimental part of this dissertation is the uncertainty of the measurement results of the floating piston / tube friction point near zero speed, i.e. at the motion direction turn-around points. Since they are most probably caused by the clearance between the groove flanks and the O-ring, enhancements here require either a quite pervasive change of the measurement principle, or a rejection of the indirect actuation principle. However, improving this aspect of the single friction point measurement methodology would probably remove the remaining deviations in the reproduction of the friction behavior of the full damper. First experiments with the replacement of the O-ring by an X-ring lead to promising results, but did not solve the actual problem. The uncertainty of the O-ring's location within the groove of the floating piston also causes the instability of the floating piston / tube FEM simulation setup, which was mitigated in the simulation by the use of additional O-ring stabilization via a motion restricting remote point. Investigations in the actual O-ring behavior can also lead to new solution attempts for the related FEM friction simulation.

During the analysis of the simulation results, it turned out that the non-separability of microscopic and macroscopic seal deformation during stroking leads to an underestimated contact stiffness and contact damping. To solve this inaccuracy, an iteration loop could be developed, which adjusts the parameter set of the dynamic LuGre friction model in the contact zone. This iteration loop setup is quite simple, given that the most relevant parameters are known $(\sigma_0$ and $\sigma_1)$. It could be additionally accelerated by an appropriate initial guess of σ_0 and σ_1 based on the related seal material data. Since the impact on the near-zero friction behavior is rather small, the required number of FEM simulation runs is quite large. Because the overall interest in near zero-speed friction behavior is much smaller than in midstroke friction behavior, the implementation of such an iteration loop was considered unnecessary within this dissertation. However, the inclusion of such an iteration loop would provide a further improvement in friction simulation accuracy.

Since automotive shock absorbers often have to support lateral loads, especially during their application as a wheel-guide at the front axle, friction behavior under lateral load is an impor-

tant and highly demanding topic for suppliers, OEMs and customers alike. The consideration of lateral forces to the damper's friction points therefore has to be implemented in both the single friction point test rig and the FEM friction simulation. Lateral loads have already been implemented for the simulation part during a follow-up project, as presented in 9.1. In order to release the rotational symmetry enforced by the related symmetry boundary condition, the modeling of an area-symmetric half model (or an 180 ° wedge) of both the piston / tube and the rod guide assembly / rod friction point is required, as mentioned in Chapter 7.2.1. To link both single friction point simulations via a bendable rod while keeping the FEM setup stable and fully determined, the boundary conditions of these single friction points are enhanced by additional boundary conditions, which are pre-calculated based on the principle depicted in 9.1 (left). These additional boundary conditions are the tilting angle of the piston α due to the rod tilting and bending, the horizontal displacement of the piston Δs due to the piston band deformation, and the resulting piston lateral force F_P and the applied lateral force F_L itself. F_A and F_B represent the idealized reaction forces in the bearing. While the simulated stress levels and stress distributions depicted in 9.1 (center and right) are reasonable through the observed contact resolution and solid body deformation, the validation of the simulated friction forces via SFP1 proved to be difficult. This experimental setup is bound to the application of only very-small lateral forces by the small lateral load capabilities of the inner force sensor. First results have been achieved by the use of a bearing-only test rig, which has shown that not only the quantitative amount of friction, but also the qualitative shape of the friction behavior changes under lateral load. Consequently, further investigations are needed, which include test rig design changes as well as the determination of lateral load dependent changes to the friction model parameters for each friction point.

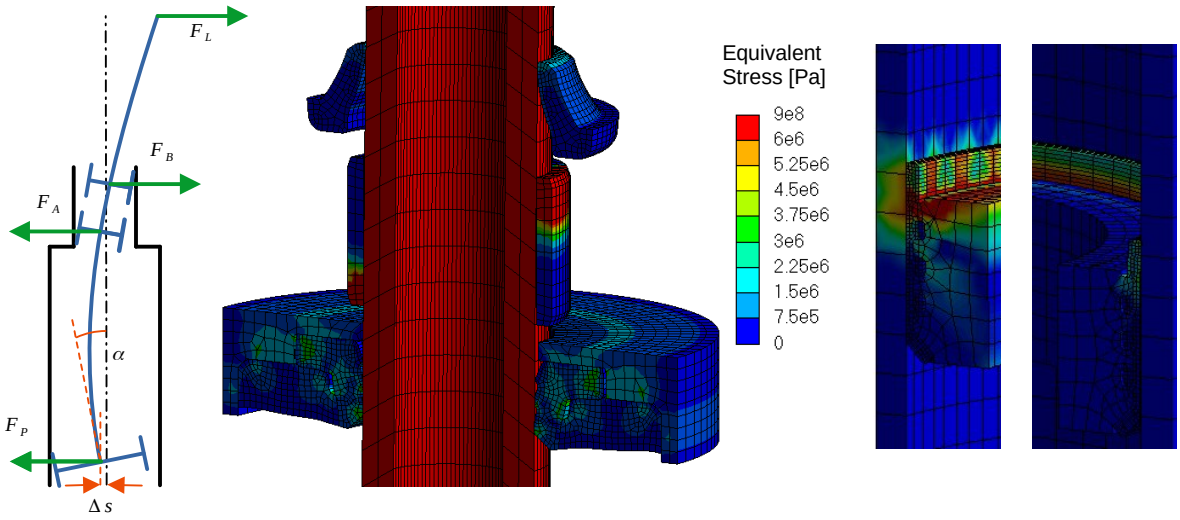

Illustration 9.1: Simulation approach for setups with lateral load application; boundary condition pre-calculation principle (left); equivalent stress distribution immediately prior to the friction recording phase of the rod guide assembly / rod friction point (center) and of the piston / tube friction point (right)

Since double tube dampers as the second common type of automotive shock absorbers share the same friction challenges, but also the same general type of friction points, the friction measurement and friction simulation methodologies developed within this dissertation should be transferable. However, this transferability hat not been proven so far, and requires modified single friction point test rigs and subsequent parameterizations. Given that this methodology is not limited to the analysis of automotive shock absorbers, but should be applicable to most types of friction investigations of hydraulic seals, a wide field of further application and specific adaptation lies open and could be explored in future work.

Bibliography

[1] Manfred Mitschke, Henning Wallentowitz - Dynamik der Kraftfahrzeuge, Springer Vieweg, 2014

[2] John C. Dixon - The Shock Absorber Handbook, John Wiley & Sons, Ltd; Professional Engineering Publishing Ltd, 2007

[3] Bernd Heißing, Metin Ersoy, Stefan Gies - Fahrwerkhandbuch, Vieweg & Sohn Verlag | GWV Fachverlage GmbH, 2007

[4] Tenneco Inc. - Internal friction specification data to comply with various customer requirements, confidential

[5] Dieter Muhs, Herbert Wittel, Dieter Jannasch, Joachim Voßiek - Roloff / Matek Maschinenelemente - Normung, Berechnung, Gestaltung, Viewegs Fachbücher der Technik, 2007

[6] Mohammadreza Mofidi - Tribology of elastomeric seal materials - Dissertation, Department of Applied Physics and Mechanical Engineering, Division of Machine Elements, Luleå University of Technology, 2009

[7] Oliver Pascal Heipl - Experimentelle und numerische Modellbildung zur Bestimmung der Reibkraft translatorischer Dichtungen - Dissertation, Fakultät für Maschinenwesen, RWTH Aachen, 2013

[8] A. Schallamach - Abrasion, Fatigue, and Smearing of Rubber - The Natural Rubber Producer's Research Association, Welwyn Garden City, Herts., England, Journal of Applied Polymer Science Vol. 12, 1968

[9] Gottfried Wilhelm Ehrenstein - Mit Kunststoffen konstruieren - Eine Einführung, Hanser Verlag, 2007

[10] Matthias Wangenheim - Untersuchungen zu Reibmechanismen an Pneumatikdichtungen - Dissertation, Institut für Dynamik und Schwingungen, Gottfried Wilhelm Leibniz Universität Hannover, 2012

[11] Richard Stribeck - Die wesentlichen Eigenschaften der Gleit- und Rollenlager - Zentralstelle für wissenschaftlich-technische Untersuchungen in Neubabelsberg, Zeitschrift des VDI 46, 1902

[12] Erich Santner - Reibung und Verschleiß von Werkstoffen, Bauteilen und Konstruktionen, Expert Verlag, 2004

[13] Maik Hoppert - Analytische und experimentelle Untersuchungen zum Wirkungsgradverhalten von Achsgetrieben - Dissertation, Fakultät für Maschinenbau, Fachgebiet Kraftfahrzeugtechnik, TU Ilmenau, 2015

[14] Farid Al-Bender - Fundamentals of Friction Modeling - Department of Mechanical Engineering, Division PMA Katholieke Universiteit Leuven, Belgium, 2010

[15] P. R. Dahl - A Solid Friction Model - The Aerospace Corporation, El Segundo, CA, 1968

[16] E. Roos, K. Maile, M. Seidenfuß - Werkstoffkunde für Ingenieure - Grundlagen, Anwendung, Prüfung, Springer Vieweg, 2017

[17] J. Wojewoda, A. Stefanski, M. Wiercigroch, T. Kapitaniak - Hysteretic effects of dry friction: modelling and experimental studies - Division of Dynamics, Technical University of Łódź; Centre for Applied Dynamics Research, School of Engineering, University of Aberdeen, King's College Aberdeen, Philosophical Transactions of the Royal Society A | Mathematical, Physical & Engineering Sciences, 2008

[18] D.P. Hess, A. Soom - Friction at a Lubricated Line Contact Operating at Oscillating Sliding Velocities - University at Buffalo, Buffalo, NY 14260, Department of Mechanical and Aerospace Engineering, Journal of Tribology Vol. 112/147, 1990

[19] B. Armstrong-Hélouvry, P. Dupont, C. Canudas de Wit - A Survey of Models, Analysis Tools and Compensation Methods for the Control of Machines with Friction - University of Wisconsin, Milwaukee, Elsevier Science Ltd, 1994

[20] Schröder, Dierk - Elektrische Antriebe - Regelung von Antriebssystemen, Springer-Verlag, 2015

[21] C. Canudas de Wit, V. Seront - Robust Adaptive Friction Compensation - Cincinnati, Ohio, Proceedings of the IEEE International Conference on Robotics and Automation, 1990

[22] M. R. Popovic, G. Liu, A- A. Goldberg - Experimental Study on Low Velocity Friction Compensation and Tracking Control - University of Belgrade, Journal of Automatic Control Vol. 13(2):17-22, 2003

[23] A. Krämer, J. Kempkes - Modellierung und Simulation von nichtlinearen Reibungseffekten bei der Lageregelung von Servomotoren - Hochschule für angewandte Wissenschaften Würzburg-Schweinfurt, FHWS Science Journal Jg. 1, Nr. 2, 2013

[24] K. C. Ludema - Friction, Wear, Lubrication, CRC Press LLC, 1996

[25] Charles Augustin de Coulomb - Théorie des machines simple - (Nouv. éd.), Bachelier, 1821

[26] A. J. Morin - New friction experiments carried out at Metz in 1831-1833 - French Royal Acadamy of Science, Proceedings of the French Royal Acadamy of Science, 1833

[27] Osborne Reynolds - On the theory of lubrication and its application to Mr. Beauchamp Tower's experiments, including an experimental determination of the viscosity of olive oil - Owens College Manchester, Philosophical Transactions of the Royal Society, 1886

[28] Dean Karnopp - Computer Simulation of Stick-Slip Friction in Mechanical Dynamic Systems - Universiy of California, Journal of Dynamic Systems, Measurement and Control, 1985

[29] Michael Rudermann - Zur Modellierung und Kompensation dynamischer Reibung in Aktuatorsystemen - Dissertation, Fakultät für Elektrotechnik und Informationstechnik, Lehrstuhl für Regelungssystemtechnik, Technische Universität Dortmund, 2012

[30] C. Canudas de Wit, H. Olsson, K. J. Åström, P. Lischinsky - A New Model for Control of Systems with Friction - L'école polytechnique de l'Université Grenoble Alpes, IEEE Transactions on Automatic Control vol. 40, 1995

[31] P. R. Dahl - Measurements of solid friction parameters of ball bearings - The Aerospace Corporation, El Segundo, CA, 1977

[32] V. van Geffen - A study of friction models and friction compensation - Technische Universiteit Eindhoven, Department Mechanical Engineering, Dynamics and Control Technology Group, 2009

[33] K. J. Åström, C. Canudas de Wit - Revisiting the LuGre friction model - Institute of Electrical and Electronics Engineers, IEEE Control Systems Magazine, 2008

[34] Farid Al-Bender, Jan Swevers - Characterization of Friction Force Dynamics - IEEE Control Systems Magazine, 28(6):64:81, 2008

[35] M. Ruderman, T. Bertram - Modified Maxwell-Slip model of presliding friction - Milan, Italy, Proceedings of the 18th IFAC World Congress, 2011

[36] P. Dupont, V. Hayward, B. Armstrong - Single State Elasto-Plastic Models for Friction Compensation - Aerospace & Mechanical Engineering, Boston University, IEEE Transactions on Automatic Control, 1999

[37] P. Dupont, B. Armstrong, V. Hayward - Elasto-Plastic Friction Model: Contact Compliance and Stiction - Aerospace & Mechanical Engineering, Boston University, Proceedings of the American Control Conference, Chicago, Illinois, 2000

[38] J. Swevers, F. Al-Bender, C. G. Ganseman, T. Prajogo - An Integrated Friction Model Structure with Improved Presliding Behavior for Accurate Friction Compensation - Katholieke Universiteit Leuven, IEEE Transactions on Automatic Control Vol. 45 No. 4, 2000

[39] V. Lampaert, J. Swevers, F. Al-Bender - Modification of the Leuven Integrated Friction Model Structure - Katholieke Universiteit Leuven, IEEE Transactions on Automatic Control Vol. 47 No. 4, 2002

[40] V. Lampaert, F. Al-Bender, J. Swevers - A generalized Maxwell-slip friction model appropriate for control purposes - Department of Mechanical Engineering, Katholieke Universiteit Leuven, IEEE International Workshop on Workload Characterization (IEEE Cat. No.03EX775), Saint Petersburg, 2003

[41] F. Al-Bender, V. Lampaert, J. Swevers - A novel generic model at asperity level for dry friction force dynamics - Department of Mechanical Engineering, Katholieke Universiteit Leuven, Tribology Letters, Vol. 16, No.1, 2003

[42] Hermann Schlichting, Klaus Gersten - Grenzschicht-Theorie, Springer-Verlag, 2006

[43] Dirk Bartel - Simulation von Tribosystemen - Grundlagen und Anwendungen, Vieweg + Teubner | GWV Fachverlage GmbH, 2010

[44] Timo Schmidt - Mischreibung und Verschleiß in Hydraulikdichtsystemen - Modellbildung, Simulation und experimentelle Analyse - Dissertation, Fakultät für Maschinenbau, Institut für Maschinenelemente, Konstruktionstechnik und Tribologie, Gottfried Wilhelm Leibniz Universität Hannover, 2011

[45] H.J. Van Leeuwen, M.J.W Schouten - Die Elastohydrodynamik: Geschichte und Neuentwicklungen - Eindhoven University of Technology, VDI Berichte Nr. 1207, 1995

[46] H. Blok - Inverse problems in hydrodynamic lubrication and design directives for lubricated flexible surfaces - Houston, Proceedings of the International Symposium on Lubrication and Wear, 1963

[47] Fabian Kaiser - Ein Simulationsmodell zur Analyse des Schmierfilms von Stangendichtungen - Dissertation, Lehrstuhl für Maschinenelemente und Getriebetechnik, TU Kaiserslautern, 2015

[48] Yekta Öngün - Finite Element Simulation of Mixed Lubrication of Highly Deformable Elastomeric Seals - Dissertation, Institut für Maschinenkonstruktion , Universität Magdeburg, 2010

[49] Eckart Laurien, Herbert Oertel jr. - Numerische Strömungsmechanik - Grundgleichungen und Modelle,Lösungsmethoden, Qualität und Genauigkeit, Springer Vieweg, 2013

[50] ANSYS, Inc. - ANSYS Fluent User's Guide Version 2020 R1, 2020

[51] ANSYS Inc. - Solving FSI Application Using ANSYS Mechanical and ANSYS Fluent, FSI Training, 2015

[52] K. H. Grote, J. Feldhusen - Dubbel - Taschenbuch für den Maschinenbau, Springer-Verlag, 2007

[53] Bernd Klein - FEM - Grundlagen und Anwendungen der Finite-Elemente-Methode im Maschinen- und Fahrzeugbau, Springer Vieweg, 2015

[54] Peter Steinke - Finite Elemente Methode - Rechnergestützte Einführung, Springer Vieweg, 2012

[55] Wilhelm Rust - Nichtlineare Finite-Elemente-Berechnungen, Springer Vieweg, 2016

[56] ANSYS, Inc. - ANSYS Mechanical User's Guide Version 2020 R1, 2020

[57] ANSYS, Inc. - ANSYS Mechanical APDL Theory Reference Version 2020 R1, 2020

[58] Viktor Hein - Untersuchung des Einflusses von Oberflächenmodifikationen auf das Reibverhalten von Metall-Elastomer-Kontakten - Master Thesis, Automotive Engineering Group, TU Ilmenau, 2017

[59] Florian Güth - Entwicklung eines Dauer-Einzelreibstellenprüfstandes von Automobil-Schwingungsdämpfern - Master Thesis, Automotive Engineering Group, TU Ilmenau, 2018

[60] Matthias Wicha - Untersuchung reibungsrelevanter Einflussfaktoren am Trennkolben von Automobilschwingungsdämpfern - Master Thesis, Automotive Engineering Group, TU Ilmenau, 2017

[61] Jonas Vogel - Untersuchung der Traversenschwingungen am Reibkraftprüfstand für Automobil-Schwingungsdämpfer - Bachelor Thesis, Automotive Engineering Group, TU Ilmenau, 2017

[62] Florian Güth - Optische Untersuchungen an den Einzelreibstellen eines Automobil-Schwingungsdämpfers - Project Seminar Documentation, Automotive Engineering Group, TU Ilmenau, 2018

[63] DIN ISO 3408-3:2011-04 - Ball screws - Part 3: Acceptance conditions and acceptance tests, same as ISO 3408-3:2006

[64] Tenneco Inc. - Internal findings, Personal communication

[65] Achim Frick, Claudia Stern - Einführung in die Kunststoffprüfung - Prüfmethoden und Anwendungen, Carl Hanser Verlag, München, 2017

[66] DIN EN ISO 3167:2014-11 - Plastics - Multipurpose test specimens, 2014

[67] Christoph Mock - Materialmodellierung in FEM-Analysen zur Simulation von Automobil-Schwingungsdämpfern - Bachelor Thesis, Automotive Engineering Group, TU Ilmenau, 2016

[68] Philipp Claus - Programmierung von Reibmodellen in Finite Elemente Analysen - Master Thesis, Automotive Engineering Group, TU Ilmenau, 2016

[69] Tribo Technologies GmbH - Tribo-X THED Simulation Software, Website: https://www.tribo-technologies.com/de/tribo-x - visited 2020/01/09

[70] Christoph Mock - Entwicklung einer Methodik zur zielführenden Wahl der Materialmodelle zur Simulation von Metall-Elastomer-Kontakten - Master Thesis, Automotive Engineering Group, TU Ilmenau, 2018

[71] DIN EN ISO 527-1:2012 - Plastics - Determination of tensile properties - Part 1: General principles, 2012

[72] Dennis Ritter - Simulative Untersuchung der gegenseitigen Beeinflussung zweier Reibstellen in einem Automobil-Schwingungsdämpfer - Master Thesis, Automotive Engineering Group, TU Ilmenau, 2018

[73] ANSYS, Inc. - Ansys Meshing User's Guide Version 2020 R1, 2020

[74] The MathWorks, Inc. - Optimization Toolbox User's Guide in Matlab R2020a, 2020

[75] Yuqin Wei - Entwicklung einer Methodik für die automatisierte Parametrierung dynamischer Reibmodelle zur Simulation des Reibverhaltens von Automobil-Schwingungsdämpfern - Master Thesis, Automotive Engineering Group, TU Ilmenau, 2018

[76] Christopher Naser - Modellierung des dynamischen Reibmodells von Trennkolben und Rohr eines Automobil-Schwingungsdämpfers - Master Thesis, Automotive Engineering Group, TU Ilmenau, 2019

Illustrations

Erklärung

Ich versichere, dass ich die vorliegende Arbeit ohne unzulässige Hilfe Dritter und ohne Benutzung anderer als der angegebenen Hilfsmittel angefertigt habe. Die aus anderen Quellen direkt oder indirekt übernommenen Daten und Konzepte sind unter Angabe der Quelle gekennzeichnet.

Bei der Auswahl und Auswertung folgenden Materials haben mir die nachstehend aufgeführten Personen in der jeweils beschriebenen Weise ~~entgeltlich~~ / unentgeltlich[1)] geholfen:

1. Philipp Claus im Rahmen der Anfertigung seiner Masterarbeit mit dem Thema „Programmierung von Reibmodellen in Finite Elemente Analysen“: Analyse der *userfric* Schnittstelle von Ansys Mechanical sowie erste Implementierungen von selbst geschriebenen Reibmodellen (siehe Bibliography [68])
2. Robert Bodenstab im Rahmen seines Projektseminars mit dem Titel „Untersuchung des Einflusses der Vorkonditionierung von Kraftfahrzeug-Schwingungsdämpfern auf ihr Reibverhalten“: Ausarbeitung einer ersten Vorkonditionierungsstrategie
3. Dennis Ritter im Rahmen seines Projektseminars mit dem Titel „Erweiterung eines FEM-Simulationsmodells für das Reibverhalten von Kolben-Rohr-Kontakten um äußere Einflüsse“: Debugging und Optimierung der Reibmodell-Implementierung in Ansys Mechanical
4. Viktor Hein im Rahmen der Anfertigung seiner Masterarbeit mit dem Thema „Untersuchung des Einflusses von Oberflächenmodifikationen auf das Reibverhalten von Metall-Elastomer-Kontakten“: Auskonstruktion und Inbetriebnahme von SFP1 (siehe Bibliography [58])
5. Matthias Wicha im Rahmen der Anfertigung seiner Masterarbeit mit dem Thema „Untersuchung reibungsrelevanter Einflussfaktoren am Trennkolben von Automobil-Schwingungsdämpfern“: Auskonstruktion und Inbetriebnahme von SFP2 (siehe Bibliography [60])
6. Yuqin Wei im Rahmen der Anfertigung ihrer Masterarbeit mit dem Thema „Entwicklung einer Methodik für die automatisierte Parametrierung dynamischer Reibmodelle zur Simulation des Reibverhaltens von Automobil-Schwingungsdämpfern“: Entwicklung der Parameter-Optimierungsstrategie mittels Matlab (siehe Bibliography [75])
7. Florian Güth im Rahmen der Anfertigung seiner Masterarbeit mit dem Thema „Entwicklung eines Dauer-Einzelreibstellenprüfstandes von Automobil-Schwingungsdämpfern“: Optimierungen an SFP1 sowie Durchführung zahlreicher Einzelreibstellenmessungen (siehe Bibliography [59])
8. Christoph Mock im Rahmen der Anfertigung seiner Bachelorarbeit mit dem Thema „Materialmodellierung in FEM-Analysen zur Simulation von Automobil-Schwingungsdämpfern“, seinem Projektseminar mit dem Thema „Materialmodellierung in FEM-Analysen zur Simulation des Reibverhaltens von Automobil-Schwingungsdämpfern“ sowie seiner Masterarbeit mit dem Thema „Entwicklung einer Methodik zur zielführenden Wahl der Materialmodelle zur Simulation von Metall-Elastomer-Kontakten“: Analyse verschiedener Methoden zur Materialmodellierung in FEM, Durchführung zahlreicher Materialprüfungen (siehe Bibliography [67] [70])

9. Philipp Schappke im Rahmen seines Projektseminars mit dem Titel „Entwicklung einer Methodik zur Parametrierung von Elastomer-Materialmodellen unter Nutzung ungünstiger Materialprobenformen“: Durchführung der Materialprüfungen der Trennkolben-Dichtringe
10. Paul Schulze-Eckel im Rahmen seines Projektseminars mit dem Titel „Setup eines Gesamtdämpfer-Simulationsmodells basierend auf Einzelreibstellenmodellen“: Optimierungen an SFP2, Konzeptentwicklung zur Vorberechnung der lagerindividuellen Reaktionskräfte auf Lateralkräfte sowie Durchführung zahlreicher Einzelreibstellenmessungen
11. Mechthild Herzog und René Gassmöller: Hinweise und Anregungen zu Rechtschreibung, Grammatik, Ausdruck und Argumentationsweise

Weitere Personen waren an der inhaltlich-materiellen Erstellung der vorliegenden Arbeit nicht beteiligt. Insbesondere habe ich hierfür nicht die entgeltliche Hilfe von Vermittlungs- bzw. Beratungsdiensten (Promotionsberater oder anderer Personen) in Anspruch genommen. Niemand hat von mir unmittelbar oder mittelbar geldwerte Leistungen für Arbeiten erhalten, die im Zusammenhang mit dem Inhalt der vorgelegten Dissertation stehen.

Die Arbeit wurde bisher weder im In- noch im Ausland in gleicher oder ähnlicher Form einer Prüfungsbehörde vorgelegt.

Ich bin darauf hingewiesen worden, dass die Unrichtigkeit der vorstehenden Erklärung als Täuschungsversuch bewertet wird und gemäß § 7 Abs. 10 der Promotionsordnung den Abbruch des Promotionsverfahrens zur Folge hat.

(Ort, Datum) (Unterschrift)

[1)] Unzutreffendes bitte streichen.

Annex

A. Material Modeling

Prony Shear Relaxation Material Model Formulation

$$G(t) = G_0 \cdot \left(\frac{G_\infty}{G_0} + \sum_{i=1}^{k_G} \alpha_i^G \cdot e^{-\frac{t}{\tau_i^G}} \right)$$

with

$$G_0 = \frac{E_0}{2 \cdot (1 + \nu)}$$

Material Data

Material	**Density** $\rho\ [kg/m^3]$	**Young's Modulus** $E;E_0\ [MPa]$	**Poisson's Ratio** $\nu\ [1]$	**Relative Moduli** $\alpha_i^G\ [1]$	**Relaxation Time** $\tau_i^G\ [s]$
NBR70	1214	7.78	0.49	(1) 0.0707 (2) 0.0735 (3) 0.0395	(1) 1448.6 (2) 130.2 (3) 8.8
NBR75	1275	8.24	0.49	(1) 0.0339 (2) 0.0148 (3) 0.0689	(1) 470.2 (2) 161.3 (3) 11.7
NBR82	1448	15.87	0.49	(1) 0.0787 (2) 0.0827 (3) 0.1321	(1) 1860.2 (2) 216.8 (3) 8.7
FKM88	2010	26.47	0.49	(1) 0.1336 (2) 0.0834 (3) 0.0694	(1) 1655.2 (2) 103.8 (3) 7.2
PTFE	2300	680.97	0.49	(1) 0.1167 (2) 0.2027	(1) 149.0 (2) 1748.9
Steel	7850	200000	0.30	-	-

B. Friction Model Implementation

LuGre Model Formulation

$$\begin{aligned} F_{fric} &= \sigma_0 \cdot z + \sigma_1 \cdot \dot{z} + \sigma_2 \cdot v \\ \dot{z} &= v - \sigma_0 \cdot \frac{|v|}{g(v)} \cdot z \\ g(v) &= F_C + (F_S - F_C) e^{-(v/v_S)^2} \end{aligned}$$

Rod Guide Assembly / Rod Parameter Blending

$$\sigma_1 = \frac{\sigma_{1+} + \sigma_{1-}}{2} + \left(\sigma_{1+} - \frac{\sigma_{1+} + \sigma_{1-}}{2} \right) \cdot \tanh\left(v \cdot 10^6\right)$$

$$F_C = \frac{F_{C+} + F_{C-}}{2} + \left(F_{C+} - \frac{F_{C+} + F_{C-}}{2} \right) \cdot \tanh\left(v \cdot 10^6\right)$$

Friction Model Parameters

Parameter	Piston / Tube	RGA / Rod		Floating Piston / Tube
$\sigma_0\,[N/m]$	20.643E+03		5.577R+03	7.414E+03
$\sigma_1\,[Ns/m]$	10.010E-06	(-)	3.107E+00	10.005E-06
		(+)	40.670E+03	
$\sigma_2\,[Ns/m]$	10.004E-06		10.000E-06	12.385E+03
$F_C\,[N]$	7.100E+00	(-)	15.354E+00	10.010E-03
		(+)	11.862E+00	
$F_S\,[N]$	6.893E+00		8.716E+00	31.748E+00
$v_S\,[m/s]$	1.432E-03		976.013E-06	2.552E-03
$\Omega\,[1/N]$	92.790E+00		187.068E+00	225.185E+00

C. Supervised Theses

While some of the Bachelor Theses and Master Theses related to the dissertation's research topic are already mentioned in the bibliography, a complete list of the students supervised by me during the damper friction project is provided as follows:

Type	Student's Name
Bachelor Thesis	Lukas Edel
Bachelor Thesis	Fabio Messina
Bachelor Thesis	Christoph Mock
Bachelor Thesis	Dennis Ritter
Bachelor Thesis	Jonas Vogel
Master Thesis	Philipp Claus
Master Thesis	Florian Güth
Master Thesis	Viktor Hein
Master Thesis	Martin Kahl
Master Thesis	Christoph Mock
Master Thesis	Christopher Naser
Master Thesis	Dennis Ritter
Master Thesis	Ahmad Saleh
Master Thesis	Philipp Schappke
Master Thesis	Yuqin Wei
Master Thesis	Matthias Wicha